UNIVERSITY OF CALIFORNIA
IRVINE

Search for a TeV Component of Gamma-Ray Bursts Using the Milagrito Detector

A dissertation submitted in partial satisfaction
of the requirements for the degree of

DOCTOR OF PHILOSOPHY

in

PHYSICS

by

Maria Isabel R. Leonor

Dissertation Committee:
Professor Gaurang Yodh, Chair
Todd Haines
Clare Yu
Gary Chanan
Anthony Shoup

2000

© 2000 Maria Isabel R. Leonor

The dissertation of Maria Isabel R. Leonor is approved
and is acceptable in quality and form
for publication on microfilm:

Committee Chair

University of California, Irvine
2000

Dedication

I lovingly dedicate this work to my parents,
Vicente and Cristina Leonor.

Contents

List of Figures

List of Tables

Acknowledgements

I feel fortunate that I was able to see the fulfillment of a personal goal that, many years ago, was merely a pipe dream. This was possible only because I was equally fortunate to encounter people who would help me turn my goal into a reality. To these people, I would like to convey my heartfelt gratitude, and to promise to return their kindness by leading a life that would reflect the influence of their generosity. More or less in order of their appearance in my graduate study career:

I would like to thank my UCI adviser, Gaurang Yodh, who was generous and courageous enough to hire a student who knew next to nothing about astrophysics. Since I am a foreign national as well, Gaurang's generosity verged on being philanthropic. I truly appreciate his patience and support through all those years – many, many years – of graduate study. I also have to mention that this is a person who took the time to attend and chair my advancement to candidacy during a difficult time when his wonderful wife, Kanwal, who has also been unselfish with her support and encouragement, was recovering from major surgery. I will never forget that.

I would also like to express my thanks to Anthony Shoup, who also took a big chance on me and taught me countless things about research work, as if he didn't have enough work to do already. The experience I gained by working with you has really been pivotal in encouraging me and in giving me confidence that I could learn to do research work. Thank you for sharing all those things with me and for being a patient teacher. I still have a lot to learn, but what you have taught me will serve me well.

I would like to thank Todd Haines who served as my adviser when I was in Los Alamos. Thank you for all your support, encouragement, and for taking the time to sit down to discuss things with me, even if that meant explaining things step by step before I finally understood what you were talking about. My brain always hurt after those discussions, not only because I had a difficult time deciphering what you scribbled on paper, but also because you gave me things to think about. You could be difficult to work with, but in the end, I understood that your heart was in the right place, and this was reflected in your professional concern not only for me but for other students as well. I was never very comfortable working with people who were too polite, anyway.

My colleagues from New York University – Peter Nemethy, Lazar Fleysher, and Roman Fleysher – have also been a big help along the way. Thank you for your support and for what you have taught me.

I don't think I could have survived living in Los Alamos without my good friend, Kelin Wang. Thanks for everything, Kelin. I look forward to the day when I will be reading your thesis. I wish you success in all your future endeavors.

I also wish to thank all the members of the Milagro Collaboration. Thank you for the long hours and hard work that all of you put in, that have made this experiment possible, and for accommodating me.

I would like to thank Gary Chanan and Clare Yu for taking precious time from their busy schedules to be members of my dissertation committee. I feel happy and privileged that you could be part of this important occasion in my graduate career.

I thank the BATSE Collaboration for doing a good job, and for making their data public and easily accessible through the Internet. This was no doubt a big help to me. The Internet era has also made it possible for a desperate graduate student to harass and seek assistance from complete strangers through e-mail. Among these people were Ken Watanabe who helped me with FTOOLS and XSPEC, and Scott Barthelmy who added me to the GCN mailing list. I wish to thank them as well.

I also like to thank UCI staff who have been very helpful as well as very nice people. In particular, Rita Viner was always there for me when I needed her help, and never made me feel like I was giving her more work to do, even when I was. It was a real pleasure working with you. My thanks also goes to Lorna Martinez for all her help with making copies of this work. And what would I do without the staff of the UCI International Center? My special thanks goes to Zara Syed who does a very good job of taking care of international students.

The drudgery which sometimes managed to sneak up on me while I was writing my dissertation in Irvine was made manageable with the support of good friends who have been too generous to give up on me. Cheryl Young, I will never forget your friendship and all the wonderful things you did for me. Nitin Pandya, thank you for all your help, your encouragement, and for dragging me from my computer from time to time to remind me of the existence of a form of entertainment called movies. Margie Zuniga, thanks for all your help and your friendship. Swarupa Kamat, you have been too patient with me – thank you for your friendship and support. Tita Carol, thank you for always being there for me.

Being away from family is difficult, but I was fortunate to be around people whom I considered to be my family during this dissertation-writing phase of my life. Kathleen Green and Judy Sjodin, thank you for giving me a home. I wish only the best for you.

And last, but obviously not least, I would like to thank my brother, Ferdie, and his family, my sister, Jojie, and her family, and most especially my parents, Vicente and Cristina. When things got tough, I only had to think of you. This would not have been possible without you. Thank you.

Curriculum Vitae

Maria Isabel R. Leonor

December 2000	Ph.D. in Physics, University of California, Irvine
1995	M.S. in Physics, University of California, Irvine
1994-2000	Graduate Student Researcher, University of California, Irvine
1991-1995	Teaching Assistant, University of California, Irvine
1986	B.S. in Physics, Cum Laude, University of the Philippines, Diliman, Philippines

Publications

Evidence for TeV Emission from GRB 970417a, Atkins, R., et. al. 2000, ApJ, 533, L119.

Search for a TeV Component of GRBs Using the Milagrito Detector, Leonor, I.R., et. al. 1999, in Proceedings of the 26th International Cosmic Ray Conference, ed. D. Kieda, M. Salamon, & B. Dingus, v. 4, p. 12.

TeV Observations of Markarian 501 with the Milagrito Water Cerenkov Detector, Atkins, R., et. al. 1999, ApJ, 525, L25.

Milagrito, a TeV Air-Shower Array, Atkins, R., et. al. 2000, NIMPA, 449, 478.

Conferences Attended

Apri 2000	American Physical Society Meeting, Long Beach, LA
August 1999	26th International Cosmic Ray Conference, Salt Lake City, UT
March 1999	Frederick Reines Symposium: A Celebration, Irvine, CA
June 1998	5th International WEIN Symposium: Physics Beyond the Standard Model, Santa Fe, NM
April 1998	Los Alamos Astrophysics/University of New Mexico Astrophysics Annual Meeting, Santa Fe, NM
April 1998	American Physical Society Four Corneers Meeting, Albuquerque, NM

Abstract of the Dissertation

Search for a TeV Component of Gamma-Ray Bursts
Using the
Milagrito Detector

by

Maria Isabel R. Leonor

Doctor of Philosophy in Physics

University of California, Irvine, 2000

Professor Gaurang Yodh, Chair

The past decade has seen an explosion in our understanding of gamma-ray bursts (GRBs). Due mainly to recent progress made in the fast and precise localizations of GRBs, multiwavelength studies of these astrophysical objects are now a reality. These studies at radio, optical, x-ray, and gamma-ray wavelengths, have led to a good, though incomplete, understanding of the distance scale to GRBs, their energetics, and the physical processes which give rise to the radiation which we eventually detect on Earth. The goal of the work presented here was to contribute to the present understanding of GRBs by observing them through an energy window – the TeV energy regime – which had been searched in the past by other experiments but which had failed to reveal any convincing TeV signals from GRBs, and by using Milagrito, an instrument which was sensitive to TeV gamma-rays and which was well-suited for catching a glimpse of these ephemeral objects. The search was made by examining 54 BATSE GRBs for TeV emission which was coincident with emission in the keV-MeV regime. The search revealed one candidate for a TeV GRB. Implications of a TeV detection on the GRB distance scale and energetics are discussed.

Chapter 1

Introduction

I find amazing the extent of what mankind has learned about the Universe of which it is a part without escaping the gravitational confines of the Earth. It has been enough that man's ingenuity has produced tools with which he could see beyond where he could journey, and gaze before when he existed, and that he has boldly and tenaciously labored to understand what he has seen. Gravity does not confine his mind, nor his imagination. Today, man meets the self-imposed challenge of continuing this exploration using an impressive array of instruments which can watch the electromagnetic Universe at wavelengths and energies spanning 19 orders of magnitude – from radio waves to very high energy gamma-rays.

The picture that is outlined in the pages that follow is but one example of the rewards that have been possible because of the collaborative effort at a multiwavelength exploration of the Universe. Gamma-ray astronomy, concerned with the study of the Universe at energies $\gtrsim 50\ keV$, has been contributing to this effort for only about three decades past – fairly recent compared to more traditional ways of seeing what's out there. Highly successful satellite missions launched in the 1990s and ground-based air Cherenkov telescopes, in particular, have contributed much to the rapid growth of gamma-ray astronomy in the past decade with their prolific detections of previously unknown sources of keV to TeV gamma-rays. Today, the observed gamma-ray sky consists of about 309 astrophysical objects [1]. These gamma-ray sources include diffuse galactic emission, pulsars, supernova remnants, active galactic nuclei, and accreting binary systems, to name some. A big fraction of these gamma-ray sources have unknown origins.

In contrast, traditional ground-based air shower particle detectors, studying the sky at energies higher than $\gtrsim 1\ TeV$, have not yielded a single undisputed detection of gamma-rays from an astrophysical source at these energies. The wide field-of-view and high duty cycle of these types of detectors are desirable characteristics in the task of observing the gamma-ray sky, but it is clear that ways have to be found to increase the sensitivity of such detectors.

In this light, Milagrito and its successor, Milagro, the first ground-based water Cherenkov detectors for observing astrophysical gamma-ray sources, occupy a unique place in very high energy gamma-ray astronomy. This type of detector has an energy threshold $\lesssim 1\ TeV$, comparable to that of air Cherenkov telescopes, as well as a wide aperture and the ability to continuously monitor the sky during both daytime and night-time. The results from the Milagrito experiment were promising but, as with most novel experimental techniques, also made clear that more work and refinements had to be done to extract the best sensitivity from this type of detector, and to bring out its full potential.

The collaborative efforts among the different disciplines of astrophysics to explore the Universe at different wavelengths are perhaps best exemplified in the study of gamma-ray bursts. This work is in keeping with those efforts. Quite possibly, the contribution of this work to the understanding of gamma-ray bursts will be modest, if that. But as with most collaborative undertakings, efforts big and small are needed to get the job done.

The multiwavelength Universe is revealing itself to us, and our reward for paying attention is a better understanding of that which we are a part of, and of ourselves.

Chapter 2

Gamma-Ray Bursts: Observations and Theories

Before 1969, no human had been aware of the existence of gamma-ray bursts. Humankind had not been knowing of the message which the Universe seemed to be conveying in GRBese. Like most of the interesting discoveries of the 20th century, the discovery of gamma-ray bursts has a good story behind it. Yes, these fleeting bursts of highly energetic photons were discovered three decades ago, but the origin of these bursts, the message the Universe wants to convey, confounds to this day. The story of GRBs is therefore an evolving story and, like all good stories, it has its share of plot twists and turns which keep its readers on their toes and coming back for more. This chapter will tell the unfinished story of GRBs, from their discovery to present-day detections, as well as the current, widely accepted model of GRBs. (See reference [2] for a review of gamma-ray bursts.)

In 1967, Jocelyn Bell noticed a bit of scruff traced in the paper roll on which was recorded the output from a radio telescope; this signal was later confirmed to be from a pulsar, a supernova remnant. In 1965, Arno Penzias and Robert Wilson couldn't seem to get rid of an annoying noise picked up by their radio antenna; this signal was interpreted as the 3-K microwave background radiation, a remnant of the radiation produced in the Big Bang. The story of GRBs, likewise, has an unexpected and unassuming beginning.

2.1 The Vela Satellites

The story of GRBs begins here. The 1960s was a time in history when the threat of a nuclear war was very real and foremost in the collective consciousness of man. The

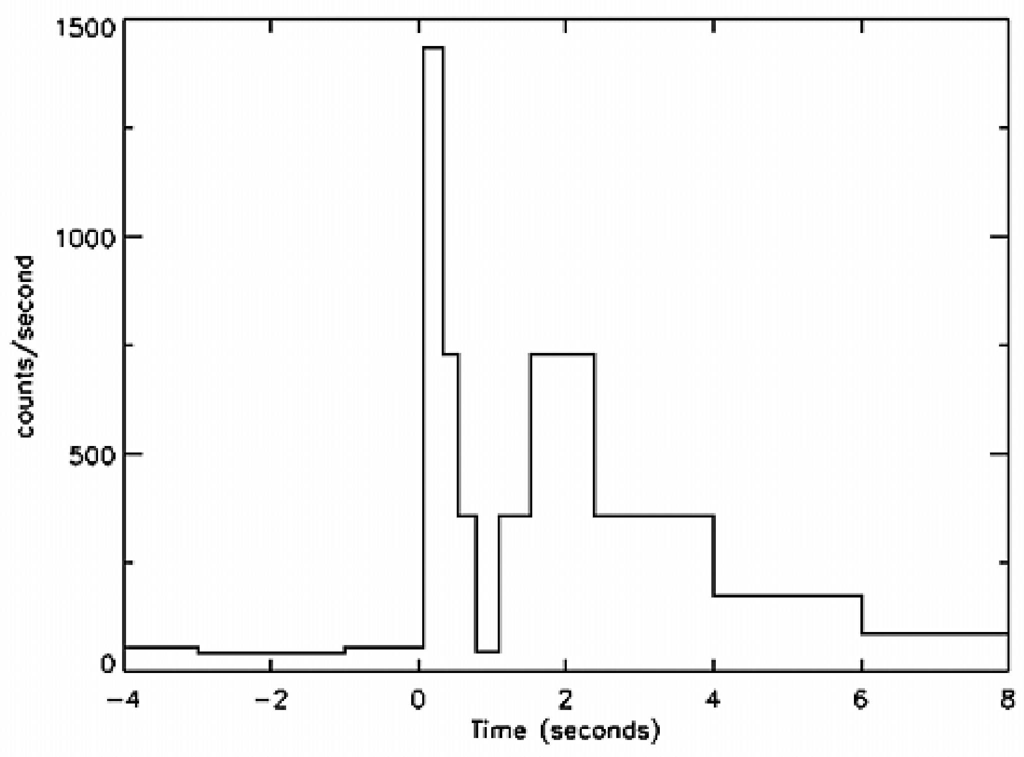

Figure 2.1: The time profile of the first gamma-ray burst observed by Earthlings [5, 6].

Limited Nuclear Test Ban Treaty of 1963 prohibited all nuclear weapons testing in the atmosphere, in outer space, and under water [3]. It was in this atmosphere that the first pair of satellites designed to directly detect the x-rays, gamma-rays, neutrons, radio and optical signals from nuclear explosions, was launched in October 16, 1963 by the United States Air Force [4]. From 1963 to 1970, a total of 12 Vela satellites were launched to take part in a United States unclassified program to develop technology for monitoring nuclear tests from space, and to verify compliance to the treaty, presumably by other signatory countries.

With each launch, the instrumention on the satellites improved. Specifically, Vela 5A and 5B (launched in May 23, 1969), and Vela 6A and 6B (the last pair, launched on April 8, 1970), had timing resolutions which were smaller than the difference in arrival time which would be caused by photons from a single source traversing different distances to the different satellites [5, 6]. (The four satellites were almost equally spaced in a circular orbit with a geocentric radius of $\sim 1.2 \times 10^5$ km [7].) This meant that the direction of the source of the photons could be confined to specific areas using the differences in detection time of the photons recorded by the different satellites.

Each satellite was instrumented with six gamma-ray detectors [5, 7], each consisting of a 10-cm^3 CsI scintillation counter, which were arranged so that photons coming from almost any direction could be detected. The detectors were sensitive to photons in the energy range between 0.2 MeV and 1.5 MeV. The passage of a gamma-ray photon through a scintillator liberates electrons in the scintillator, at this energy range mostly through multiple Compton scatterings of the photon, and these electrons in turn cause ionization and subsequent emission of light in the scintillator. This light is collected by a photomultiplier tube and serves as an indication of the passage of a photon. The amount of light collected also serves as a measure of the amount of energy deposited in the scintillator by the photon. The output from the six detectors were summed, and a rapid, statistically significant rise in count rate above background initiated a recording of the event counts.

Then it happened. On July 2, 1967, Vela 4A and 4B recorded what is now accepted as the first gamma-ray burst observed [5, 6]. But the discovery of what lay hidden in the data did not happen until 1969, when Ray Klebesadel and Roy Olsen, both of the Los Alamos Scientific Laboratory (now Los Alamos National Laboratory), perused the Vela 4 data. However, since the older satellites did not have the necessary timing resolution, the general direction of the burst could not be determined, and nearby sources such as the Sun could not be ruled out. Only in retrospect was this phenomenon recognized as a gamma-ray burst, due to its time history's similarity to those of gamma-ray bursts which were observed after this initial GRB. The plot of event count rate as a function of time for this burst is shown in Fig. 2.1.

For Klebesadel, Olsen, and another Los Alamos colleague, Ian Strong, the convincing proof for the existence of gamma-ray bursts whose origin was beyond the neighborhood of the Earth and the Sun came in 1972, when they perused data from the more technologically advanced Vela 5 and Vela 6. The three scientists analyzed data recorded by the four satellites between July 1969 and July 1972, and their efforts were handsomely rewarded: Derived from the data was evidence for 16 gamma-ray bursts which they inferred to be of cosmic origin [7].

The time durations of the 16 gamma-ray bursts observed by the Los Alamos trio ranged from less than a second to $\sim$30 seconds. The count rate time history, i.e. the plot of count rate as a function of time, had a number of clearly resolved peaks for some GRBs, while those of other GRBs displayed no structure. The measured fluence in the energy range to which the scintillation counters were sensitive ranged from the threshold of $\sim 10^{-5}\ ergs/cm^2$ to more than $2 \times 10^{-4}\ ergs/cm^2$. The fact that the measured fluence for a GRB was independent of the recording spacecraft, and the measured differences in arrival time of the photons at the different spacecraft, led them to conclude that the sources of these gamma-rays were at a distance of at least several million kilometers.

In June 1973, the scientific community was made aware of the existence of this class of astrophysical objects through the publication of Klebesadel, Strong, and Olson's work in reference [7]. However, unlike the almost immediate and unequivocal identification of the sources responsible for the signals that were observed by Jocelyn Bell and by Penzias and Wilson, the ultimate origin of GRBs remains unknown almost 30 years after the puzzle was presented to the scientific community and the best minds therein. GRBese is turning out to be a hard language to learn.

2.2 The Compton Gamma-Ray Observatory

Fast forward to the 1990s. The Cold War is over. This is a good place to start the second chapter of the GRB story.

On April 5, 1991, the Compton Gamma-Ray Observatory (CGRO) was launched by the space shuttle Atlantis [8]. On board this satellite were four distinct experiments whose

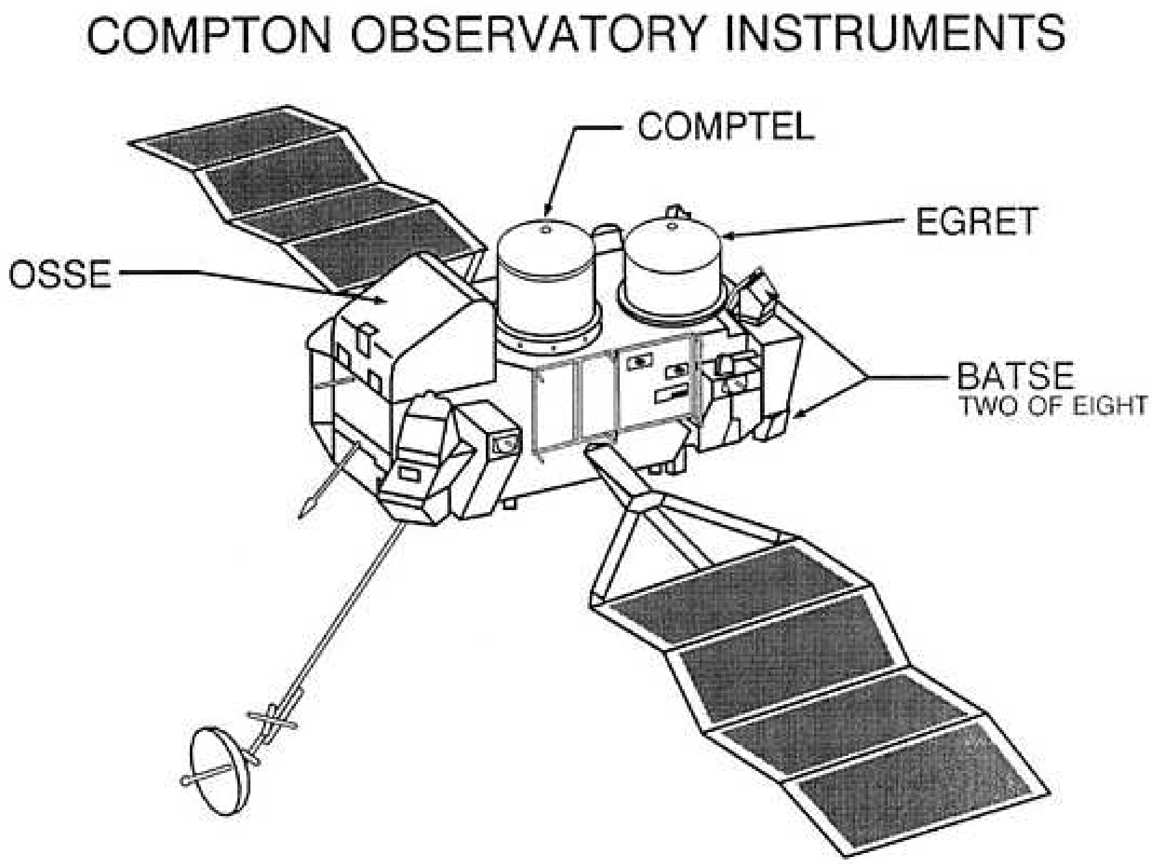

Figure 2.2: Sketch of the Compton Gamma-Ray Observatory showing the locations of the four experiments [8].

primary mission was to monitor the Universe for gamma-ray sources. Together, these four experiments served as a window through which gamma-rays from 10 keV to 30 GeV could be observed. And the scenery viewed through this window would truly be breathtaking: Supernovae, pulsars, x-ray binaries, galaxies, quasars, blazars, diffuse emission from the Milky Way, solar flares, astrophysical objects previously unknown and undetected. And of course, gamma-ray bursts.

One experiment on board CGRO would single-handedly provide the information which would revolutionize the way GRBs were thought of. This experiment was the Burst and Transient Source Experiment (BATSE). But this is getting ahead of the story.

The CGRO was about the size of a school bus, and weighed about 16 tons [8].

Figure 2.2 is a sketch of the observatory and of the locations of the four experiments which comprised it. Briefly, the four experiments on board CGRO were [8, 9]:

(a) Oriented Scintillation Spectrometer Experiment (OSSE)

The goal of OSSE was to conduct comprehensive observations of astrophysical gamma-ray sources, primarily in the 0.05 to 10 MeV energy range. It consisted of four detector systems, the primary detecting element of each being a 330-mm diameter, 102-mm thick NaI(Tl) scintillation crystal optically coupled to a 76-mm thick CsI(Na) crystal (a so-called phoswich), which was viewed by seven photomultiplier tubes (PMTs). As in all scintillation counters, a gamma-ray is detected through the detection of light emitted in the scintillator as a result of ionizations caused by electrons liberated by the passage of the gamma-ray photon, and the energy of the incident gamma-ray is deduced from the total amount of light observed. OSSE had a field-of-view of 3.8^o by 11.4^o.

(b) Compton Telescope (COMPTEL)

COMPTEL observed astrophysical sources which emitted gamma-rays in the 0.8 to 30 MeV energy range. The base detector system consisted of an upper detector made of a liquid scintillator (NE 213A) viewed by 56 PMTs, and a lower detector of NaI(Tl) scintillation crystals viewed by 98 PMTs. An incident gamma-ray gets Compton-scattered in the upper liquid detector, and then is absorbed in the lower NaI detector. Measurements of the positions of interactions and of energies at these two detectors enable the determination of the direction of the incident photon. COMPTEL had a field-of-fiew of ~ 1 sr and an angular resolution of 0.5^o to 1.0^o.

(c) Energetic Gamma Ray Experiment Telescope (EGRET)

The atrophysical objects observed by EGRET were in the 20 MeV to 30 GeV energy range. Its detection system consisted of an upper and a lower spark chamber system, two levels (one above and one below the lower spark chamber) of scintillation arrays used as a directional time-of-flight coincidence detector, and an eight radiation length thick NaI(Tl) scintillation crystal below all of these. (A spark chamber is basically made up of parallel metal plates in a chamber of gas. Alternate layers of plates are at ground potential. The interleaving plates are also at ground potential when no particle is being tracked; however, when the spark chamber is triggered, a big potential is momentarily applied to these plates, causing sparks along the trails of ionizations left by an electron-positron pair produced by an incident gamma-ray.) A gamma-ray incident on the upper spark chamber can produce an electron-positron pair. When one or both of these pass through the directional time-of-flight coincidence detector, the two spark chambers are triggered, allowing the electron-positron tracks to be imaged and, hence, the direction of the incident gamma-ray to be determined. The energy of the incident gamma-ray is determined in large part by the NaI scintillator at the bottom of the detector assembly. This crystal is also used for spectroscopy in the 0.6 to 140 MeV range, and is referred to as the Total Absorption Shower Counter (TASC). EGRET's field-of-view was ~ 0.6 sr, and its angular resolution was 5 to 10 arcminutes.

(d) Burst and Transient Source Experiment (BATSE)

BATSE's primary objective was the detection, location, and study of gamma-ray bursts. It consisted of eight detector modules located at the corners of the CGRO satellite, their faces parallel to those of an octahedron, and having an unobstructed view of the heavens. Each detector module had a 50.8-cm diameter, 1.27-cm thick disk of NaI(Tl) scintillation crystal, called a Large Area Detector (LAD), which was optimized for sensitivity and directional response, and a 13.03-cm diameter, 7.195-cm thick NaI(Tl) scintillation crystal, called a Spectroscopy Detector (SD), optimized for broad energy coverage and energy resolution. Figure 2.3 gives a close-up view of a BATSE detector module. In front of the LAD was a thin plastic scintillation detector which served as an anticoincidence shield which reduced the background count due to charged particles. Particles which registered a signal in the LAD as well as in the plastic scintillator shield were vetoed. Each LAD detected incident gamma-rays in the 20 keV to 1.9 MeV energy range, with the maximum response being in the 50 keV to 300 keV range, while each SD detected gamma-rays in the

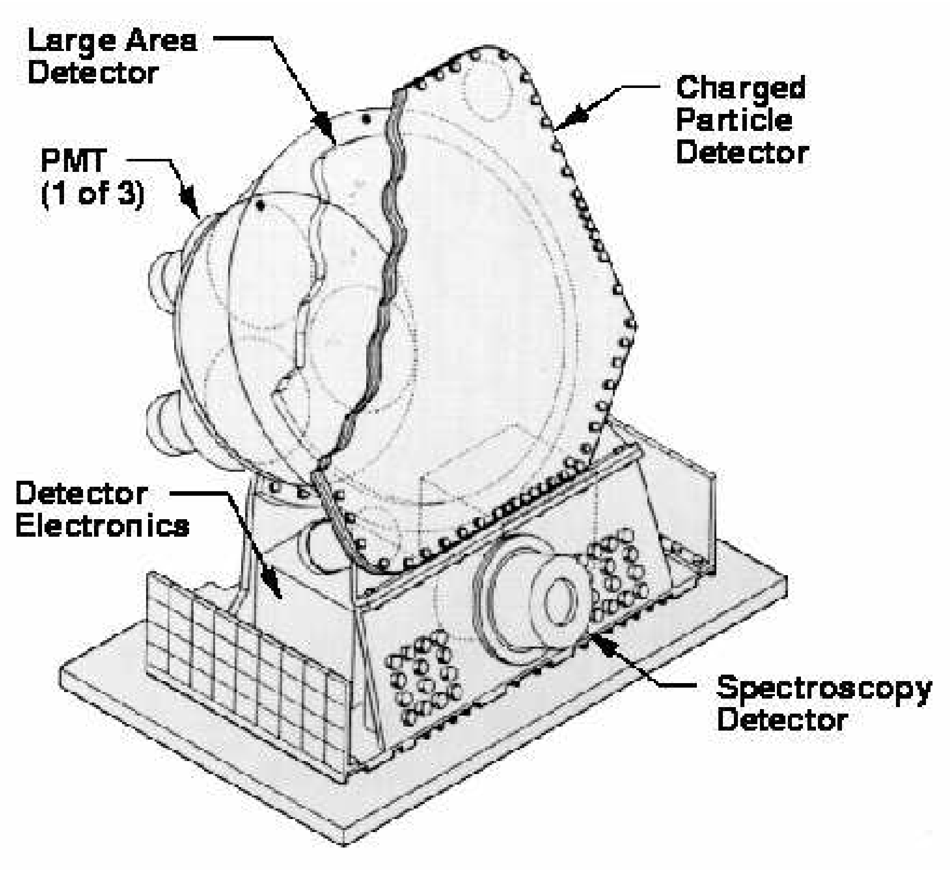

Figure 2.3: Close-up view of a BATSE module [9].

10 keV to 100 MeV energy range. The direction to a source was determined by comparing the relative count rates from the four or six brightest LADs (see Section 5.2). This method resulted in deduced GRB locations with large error radii. The statistical error radius ranged from $\sim 1^o$ to $\sim 25^o$, and strong bursts generally had smaller error radii than weak bursts. BATSE also served as a gamma-ray burst trigger for the other experiments on CGRO.

BATSE was triggered by a gamma-ray burst when the count rate increased by at least 5.5 standard deviations in at least two of the LAD detectors simultaneously. Gamma-ray events which deposited energies in the 50 to 300 keV range in a LAD were used for this purpose. BATSE was sensitive to gamma-ray fluences larger than $\sim 10^{-7}\ ergs/cm^2$. Figure 2.4 shows a histogram of the fluences measured for 2138 BATSE GRBs, using the

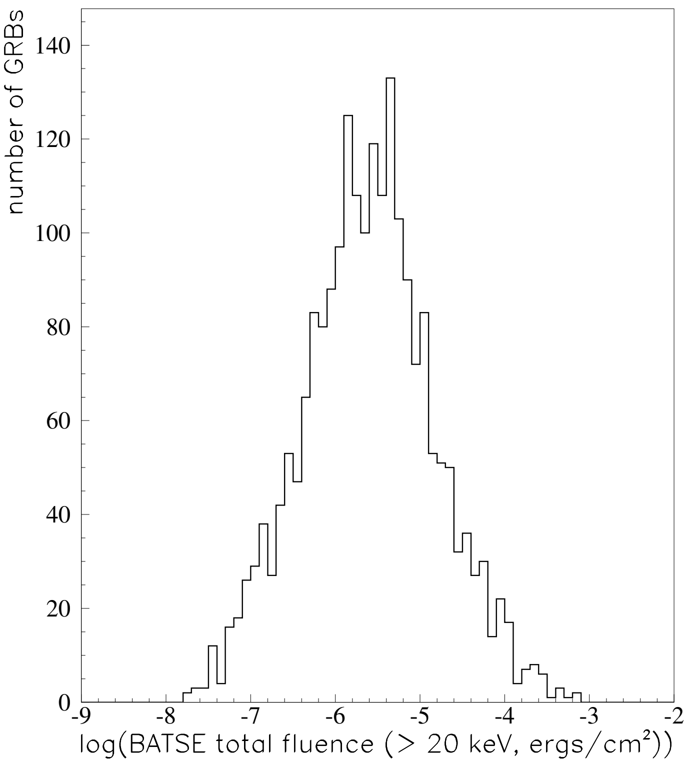

Figure 2.4: Distribution of total fluence ($E > 20$ keV) measured by BATSE, using fluence measurements for 2138 GRBs obtained from the BATSE current catalog [10].

sum of the fluences measured in four LAD energy channels. The approximate boundaries of these four energy channels were: 20 to 50 keV, 50 to 100 keV, 100 to 300 keV, and > 300 keV.

2.3 BATSE's Contributions

The combination of BATSE's sensitivity to weak bursts and its full sky field-of-view made possible its prolificness. From its activation in April 21, 1991 to its termination in June 2000, BATSE detected a total of 2704 gamma-ray bursts, or a detection rate of ~ 0.85 burst per day. Correcting for Earth occultation and experiment dead time, it is estimated that this translates to a full sky GRB rate of ~ 800 GRBs per year at BATSE's sensitivity.

The large number of GRBs detected by BATSE meant that, for the first time, there was enough statistics to allow a study of GRB global properties with more certitude than was possible in the past. Among these global properties are: Spatial distribution, time duration, light curve, and energy spectrum.

2.3.1 Spatial distribution of GRBs Before CGRO's launch, there had been nagging questions about GRBs which had, for two decades, remained unanswered. Questions the answers to which were central to understanding the origin of GRBs. Foremost among these questions were: What is the spatial distribution of GRBs? Is the distribution isotropic? Is the distribution homogeneous? What is the distance scale to GRBs? Are GRBs located at cosmological distances, or are they Galactic objects? To be sure, satellite and balloon experiments of the day already hinted at the answers to some of these questions. BATSE's results, however, would provide the first bold articulation of the answers to these questions.

Figure 2.5 is an all-sky map of the 2704 GRBs detected by BATSE during its 10-year mission. Each dot on the map represents the measured location of a GRB in Galactic coordinates. In this system of coordinates, latitude and longitude are measured with the Earth at the origin, and the Milky Way (see Fig. 2.6) would be centered around the 0th latitude, and extend from left to right. The center of the Milky Way would be located at 0th latitude and 0th longitude. It can be seen from the BATSE all-sky map that the angular distribution of GRBs is isotropic, with no clustering along the Galactic plane or toward the Galactic center. Neither is there evidence for clustering in the direction of known nearby galaxies or galaxy clusters [11].

Knowledge of the isotropy of GRB locations does not, by itself, unequivocally give an answer to the question about the distance scale of GRBs. GRB sources which are nearby and Galactic could display isotropy, as would GRB sources which are at cosmological distances. The question of whether the detected bursts are nearby or at cosmological distances can be answered by investigating if the detected bursts conform to Euclidean geometry.

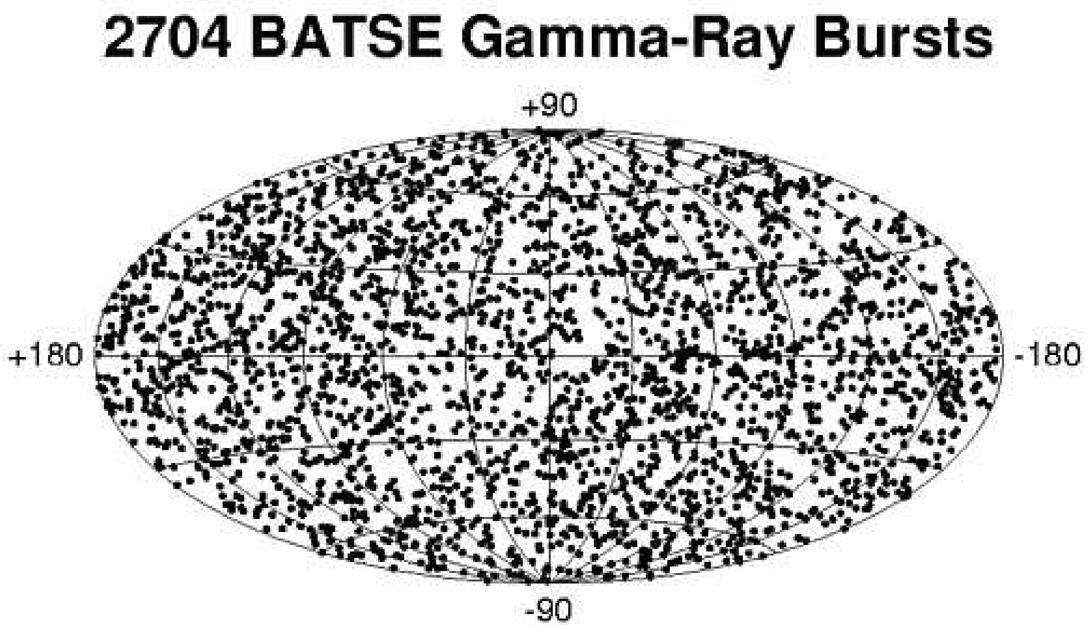

Figure 2.5: Sky map of GRBs detected by BATSE, in Galactic coordinates [10]. Plot labels are in degrees.

Nearby bursts will. Cosmological bursts, because of the expansion of the Universe, will not.

Assuming that GRBs are standard candles, i.e. that they have approximately the same intrinsic luminosities (energy released per second), then a test of the homogeneity of GRB locations could be made using BATSE's flux measurements. If GRBs have the same intrinsic luminosities, then the flux (gamma-ray count per unit area per unit time) measured by BATSE for a certain GRB would be inversely proportional to the square of the distance between BATSE and the GRB,

$$F(R) \propto \frac{1}{R^2} \quad , \tag{2.1}$$

where R is the distance, and $F(R)$ is the measured flux. A homogeneous distribution of GRBs, wherein the number of GRBs per unit volume is constant, on the other hand, would mean that the number of GRBs located within a spherical volume of radius R is,

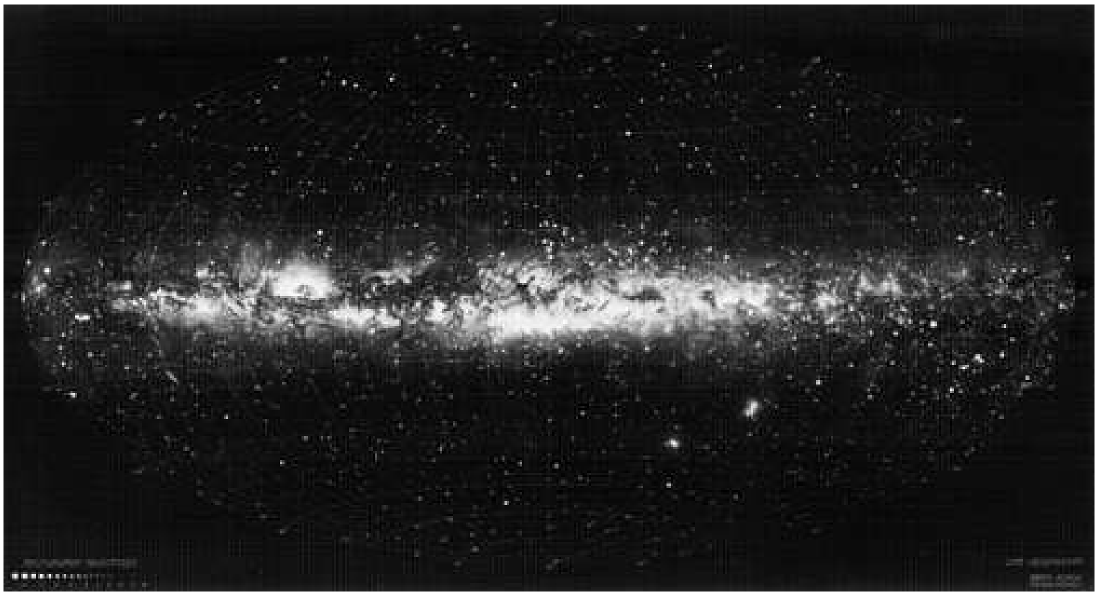

Figure 2.6: The Milky Way galaxy in Galactic coordinates [12].

$$N(< R) \propto R^3 \quad . \tag{2.2}$$

Since, assuming equal intrinsic luminosities, a measured flux is an indication of the GRB distance, equation (2.2) can be written,

$$N(< R) = N(> F(R)) \propto R^3 \quad . \tag{2.3}$$

From equations (2.1) and (2.3), it follows that,

$$N(> F(R))^2 \propto F(R)^{-3} \quad , \tag{2.4}$$

$$\implies \quad log[N(> F(R))] \propto -\frac{3}{2} log[F(R)] \quad . \tag{2.5}$$

This test for homogeneity in Euclidean space is called the *Hubble test*.

Figure 2.7 plots the number of GRBs with corresponding BATSE measured fluxes larger than a given flux, using data obtained with 1.024-second integration time. Gamma-ray events which deposited energies in the LADs in the 50 to 300 keV range, the range

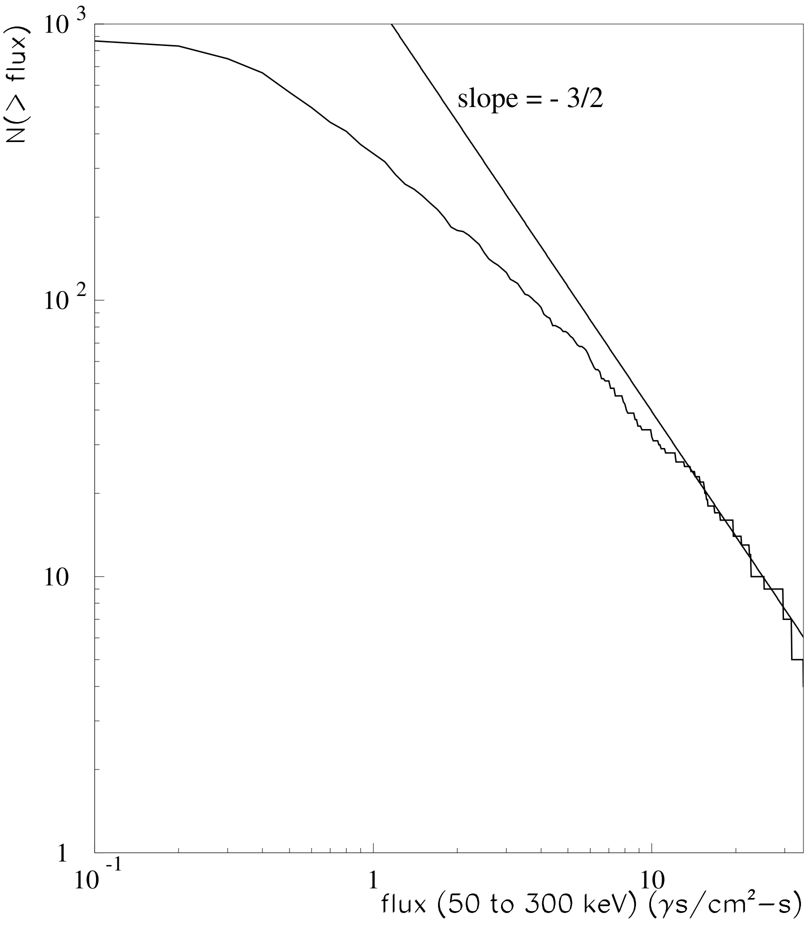

Figure 2.7: BATSE measured flux integral distribution, using data obtained with 1.024-second integration time. The line with the slope of $-3/2$ is the expected distribution for a homogeneous distribution of GRB locations.

where the LADs' sensitivity peaked, were used in the flux measurements. Also shown is the distribution given by equation (2.5) for a homogeneous distribution of GRB locations. Clearly, the BATSE measured distribution shows a rollover, so that at low fluxes the distribution is flatter than that expected from a homogeneous distribution. In other words, there is a paucity in the number of weak bursts seen compared to the number of weak bursts expected from a homogeneous distribution.

Thus, BATSE's results showed that GRBs were isotropically distributed, but did not seem to conform to a homogeneous spatial distribution in Euclidean space. This conclusion essentially ruled out the Galactic disk origin of GRBs, i.e. the detected GRBs could not have been located within the Galactic disk. The observations, however, still allowed a Galactic halo model, in which the GRBs are located in a Galactic halo extending beyond 100 kpc, and in which the GRB spatial density falls with distance from the Galactic center [13]. On the other hand, the observed spatial distribution of GRBs was also consistent with a cosmological origin, since the geometry of an expanding Universe would be able to explain the rollover found in the BATSE flux distribution.

2.3.2 Temporal properties of GRBs A gamma-ray burst can be characterized by its time duration, i.e. how long the burst lasted. GRBs are ephemeral phenomena, universal transients which last a fraction of a second in some cases, tens to hundreds of seconds in others. For each burst, BATSE measured a parameter, called T90, which quantified that burst's duration. T90 is defined as the time interval during which 90% of the total measured gamma-ray event count were detected. The start of the T90 interval is defined by the time when the first 5% of the total count have been detected, and the end of the interval is set by the time when the first 95% of the count have been detected [10]. Figure 2.8 is the distribution of measured T90 intervals of the GRBs in the BATSE 4B catalog. It is quite evident from the plot that burst durations can be grouped into two classes: Durations which are shorter than ~ 2 seconds, and those which are longer than ~ 2 seconds. Suggestions have also been made of a possible intermediate class of GRB durations, consisting of burst durations lasting from ~ 2 seconds to ~ 10 seconds. The time duration of a GRB reflects the time during which the object which powers the burst remains active, and a popular interpretation for the observed grouping of burst durations into two is that there are two types of astrophysical events responsible for the generation of GRBs. These so-called *inner engines* are discussed further in Section 2.5.5.

The time profiles – plots of count rate as a function of time, also called light curves – of GRBs exhibit remarkable diversity. In a GRB era when thousands have been detected, it is usual to hear the quip, "Once you've seen one GRB, you've seen one GRB," referring

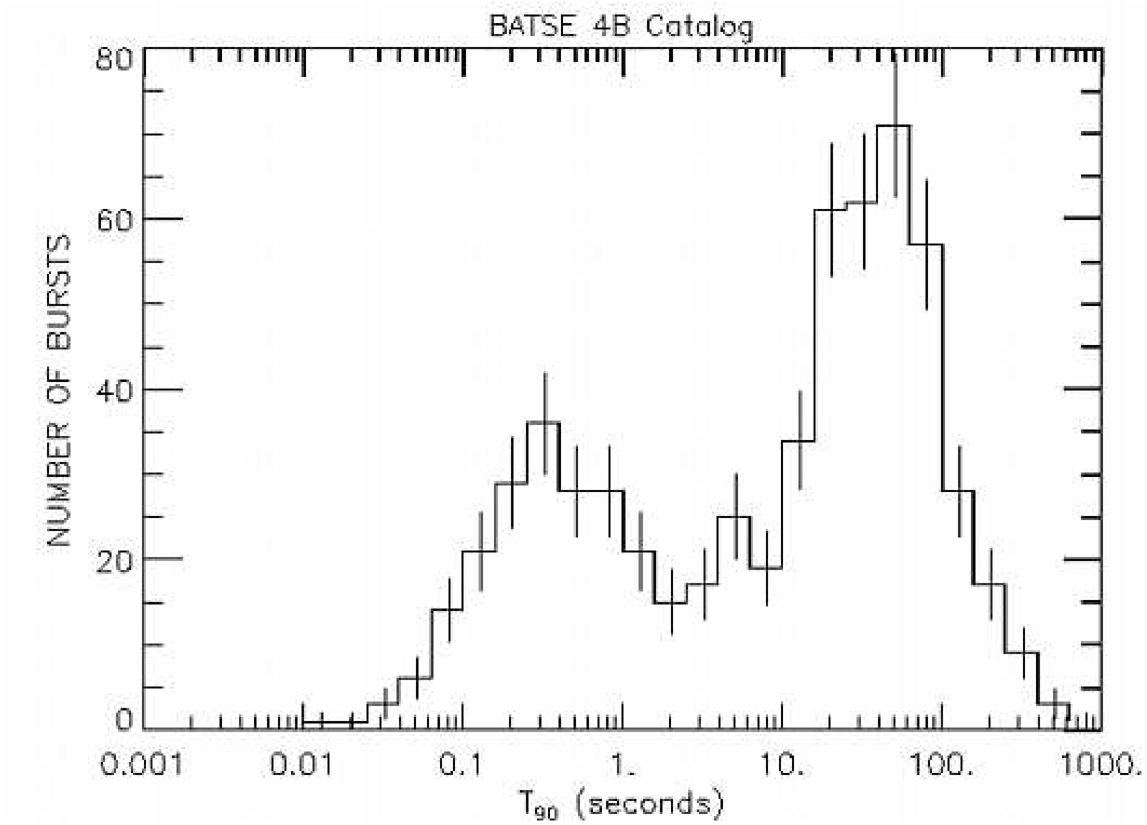

Figure 2.8: BATSE T90 distribution [10].

to the uniqueness of each GRB time profile. Figure 2.9 shows the BATSE time profiles of some of the GRBs used in this analysis, using the sum of the count rates in the four LAD energy channels (i.e. $E > 20$ keV) of all the triggered LADs. (More time profiles can be found in the Appendix.) Some time profiles display no structure, having only a single peak, while others display a few or several peaks within T90, with the width of the peaks being fractions of a second to several seconds long. If T90 reflects the duration of the activity of the GRB engine, then, according to the current model of GRBs, the time structure within T90 gives an indication of the radiation mechanism in a GRB source. This is elaborated on in Section 2.5.2.

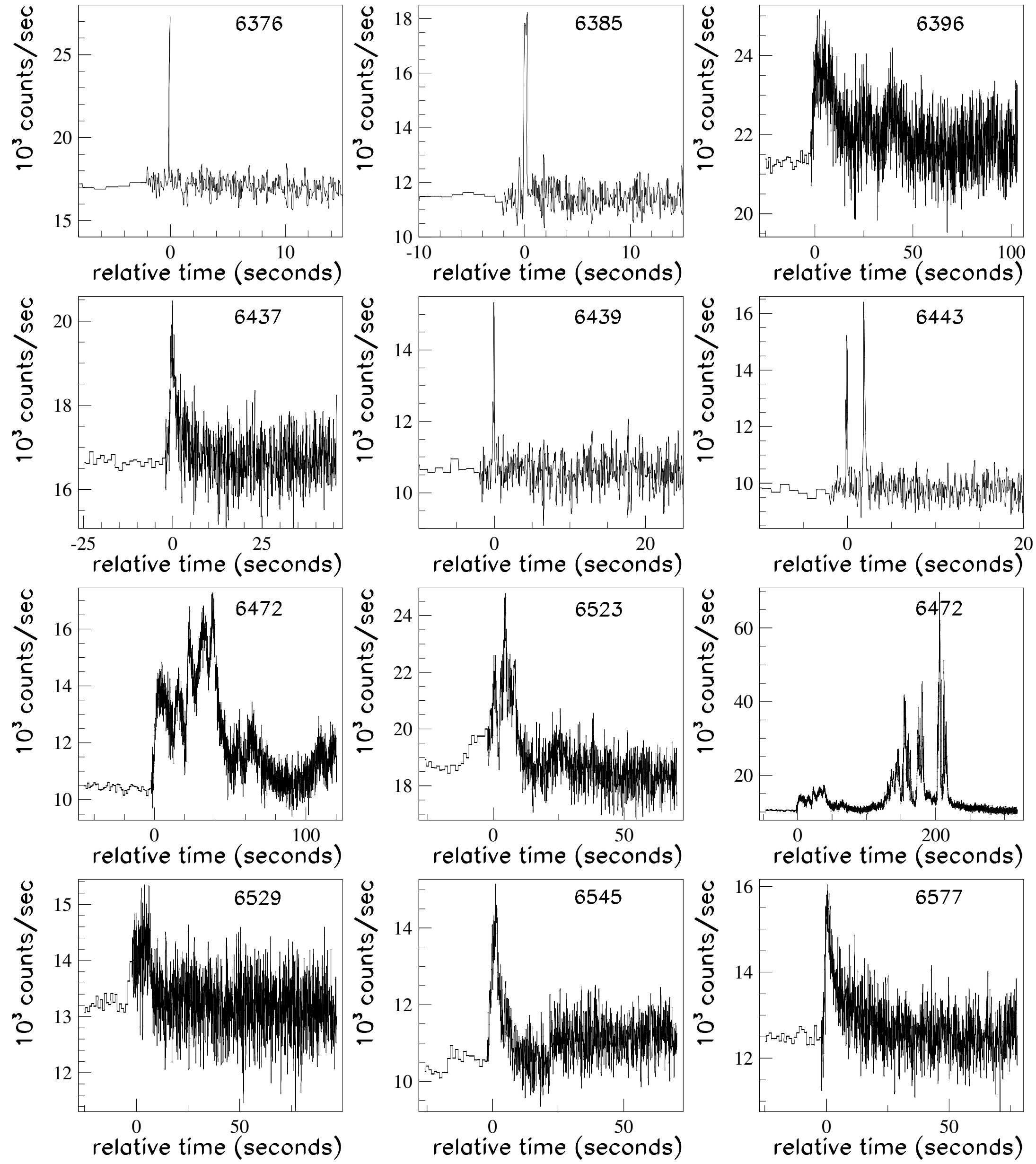

Figure 2.9: Some BATSE GRB time profiles [14]. The count rate is for $E > 20$ keV, and is the sum of the count rates from all the triggered LADs. The time is relative to the BATSE trigger time for each GRB. The numbers at the top are the BATSE trigger numbers.

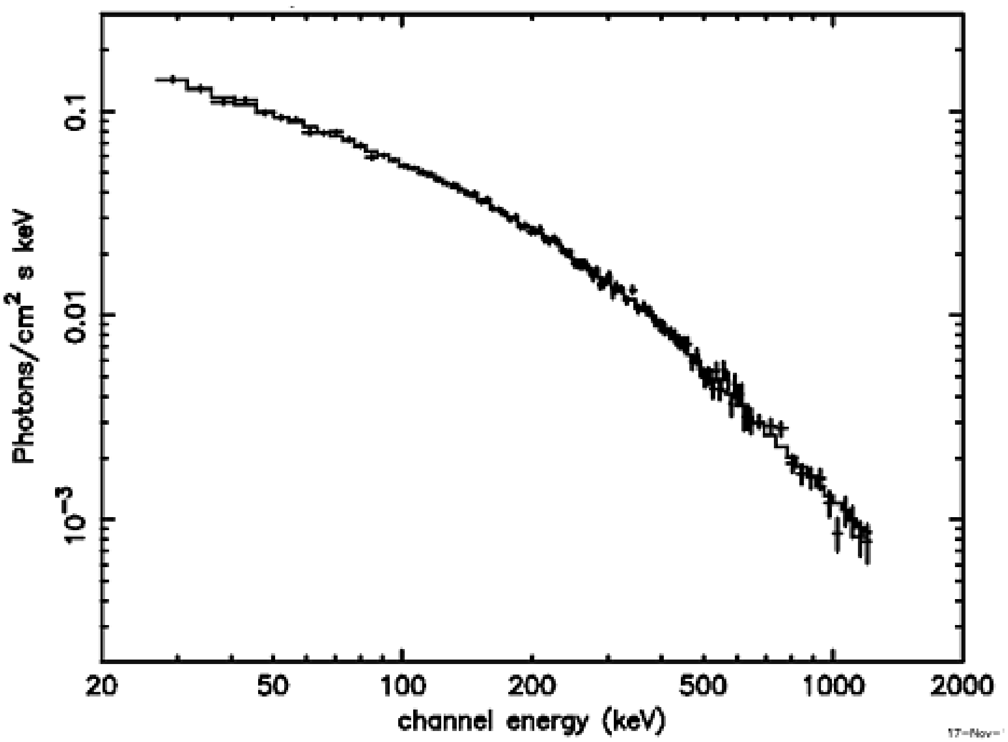

Figure 2.10: A GRB spectrum.

2.3.3 Energy spectrum of GRBs The GRBs detected by BATSE are observed to emit the bulk of the gamma-rays in the energy range of a few hundred keV. GRB spectra are nonthermal, most having a high-energy tail extending up to ~ 1 MeV. Some GRBs which were observed by EGRET, which was sensitive to gamma-rays of higher energies than that covered by BATSE, coincidentally with BATSE observations, diplayed high-energy tails which extended to a few hundred MeV [15]. One GRB observed by both BATSE and EGRET, GRB 940217b (nicknamed the "Superbowl burst" as it happened on Superbowl Sunday, 1994), was observed by EGRET to emit an 18-GeV photon hours after the lower-energy emission detected by BATSE [16], evidence that GRBs are capable of emitting gamma-rays of energies much higher than that to which BATSE was sensitive.

BATSE GRB spectra are found to be fitted well by a so-called GRB model, a four-parameter model in which the differential flux (in units of $photons\ cm^{-2}\ s^{-1}\ keV^{-1}$) is given by [17]:

$$\frac{dF(E)}{dE} = \begin{cases} A\left(\frac{E}{100\,keV}\right)^{\alpha} exp\left(-\frac{E}{E_o}\right) \,, & E \leq (\alpha-\beta)E_o \,, \\ A\left[\frac{(\alpha-\beta)E_o}{100\,keV}\right]^{\alpha-\beta} exp(\beta-\alpha)\left(\frac{E}{100\,keV}\right)^{\beta} \,, & E \geq (\alpha-\beta)E_o \,, \end{cases} \tag{2.6}$$

where A is a normalization constant for the flux, and α, β, and E_o are constants which define the shape of the spectrum. This model consists of two smoothly connected power laws, with α being the slope of the low-energy part of the spectrum ($E \leq (\alpha-\beta)E_o$), and β the slope of the high-energy part ($E \geq (\alpha-\beta)E_o$). The spectrum is concave downward, with $\alpha > \beta$. Figure 2.10 shows an example of a GRB time-averaged spectrum showing the data points fitted with the GRB model, equation (2.6).

A majority of GRB spectra can be fitted well with the GRB model. Other GRBs which are poorly fitted with the GRB model can be fitted with a broken power law in which the transition from the low-energy component to the high-energy component is abrupt. For cases in which the fitted high-energy power-law index, β, is too negative, the high-energy power law can be omitted, leaving only the low-energy power law with an exponential cutoff. BATSE's fits to the spectra of bright GRBs reveal the range of values of the model parameters which define the shape of the spectra [18]. These studies have shown that the distribution of the fitted low-energy power-law index, α, is centered at -1, with a majority of the fitted values falling between ~ -0.5 and ~ -1.5. The distribution of the high-energy power-law index, β, has a peak at -2.25, with a majority of the fitted values falling between ~ -1.8 and ~ -2.8. The break energy, E_{break}, which is the energy at which the spectrum turns over from the low-energy component to the high-energy component, is found to have a distribution which has a full-width at half-maximum less than a decade in energy, and which peaks at ~ 200 keV. For fits which result in $\beta < -2$, the parameter given by $E_{peak} \equiv E_{break}(\alpha+2)/(\alpha-\beta)$ gives the energy at which the spectrum of $E^2 dF(E)/dE$ peaks, i.e. the energy at which most of the GRB energy is emitted. Time-resolved studies of GRB spectra also show the evolution of the spectral parameters with time.

The GRB models used in fitting GRB spectra are phenomenological models, wherein no assumptions are made regarding the physics of the radiation mechanisms responsible for the generation of the observed gamma-ray bursts. However, the general characteristics of the spectra and the derived distributions of the spectral fit parameters have to be explained by any valid theoretical model which claims to have unravelled the process by which gamma-ray bursts are produced. So far, no theoretical model has done so [2].

2.4 First Light of Multiwavelength Counterparts

Before BATSE's launch, there was a tendency for some, if not most, members of the GRB scientific community to favor a nearby, local origin of GRBs, as opposed to an extragalactic, cosmological origin [19]. After BATSE's discovery of the isotropic but inhomogeneous distribution of GRB locations, there were still considerable efforts to account for such observations using a Galactic halo model, wherein the GRBs are located in a Galactic halo extending up to 100 kpc [13]. The main reason for this bias against a cosmological origin of GRBs was the energetics implied by the assumption of cosmological distances. Given the GRB fluences measured by various satellite and balloon experiments, putting GRBs at cosmological distances, with redshifts of $z \sim 1$, would amount to a total isotropic energy release of $\sim 10^{53}$ ergs. This is a tremendous amount of energy to release in just tens, or even hundreds, of seconds.

Efforts to detect GRB sources at other astronomical wavelengths – x-ray, optical, and radio wavelengths – had remained unsuccessful before 1997. The poor GRB localization capability of gamma-ray satellite experiments and the fleeting nature of GRB phenomena, coupled with the small field of view of x-ray, optical, and radio telescopes, made the success of these endeavors difficult, if not impossible, to realize. In contrast, the current imaging technologies available for astronomy at these longer wavelengths provide a location accuracy of a few arcminutes in the case of x-ray astronomy, to fractions of an arcsecond in the case of optical astronomy, much more accurate than that which can be provided by contemporaneous satellite-based gamma-ray observatories, which have pointing accuracies of the order of a few degrees. Detecting emission from a GRB source at such wavelengths would not only greatly improve the accuracy of measured GRB locations but would also, in the case of optical astronomy, afford the opportunity to unambiguously measure the distance to the GRB source through spectroscopic redshift measurements. However, for such measurements to be possible, the multiwavelength counterparts to the gamma-ray burst would have to last more than a few minutes. What was needed was a prompt (for temporal association with the gamma-ray burst) but long-lived emission from the GRB source at other wavelengths, and the detection of these so-called GRB *afterglows* by a complement of astronomical instruments.

2.4.1 BeppoSAX and the first multiwavelength counterpart detections On April 30, 1996, the *Satellite italiano per Astronomia X (BeppoSAX)*, an Italian/Dutch satellite mission for x-ray astronomy, was launched from Cape Canaveral [20]. On board BeppoSAX is a collection of instruments designed to detect x-rays in the 0.1 to 300 keV energy range, and a gamma-ray burst monitor (GRBM) for detecting gamma-rays in the 60 to 600 keV energy range. The x-ray instruments consist of four narrow field-of-view instruments (NFI) covering the energy range from 0.1 to 300 keV, and two wide field cameras (WFC) which are sensitive to x-rays with energies of 2 to 30 keV. The two WFCs face opposite directions, and each has a field of view of $20^o \times 20^o$, and an angular resolution of 5 arcminutes. The gamma-ray burst monitor consists of four slabs of CsI(Na) scintillators, each 10-mm thick, 275-mm high, and 402-mm wide [21]. A GRB triggers the gamma-ray burst monitor when at least two of the CsI slabs register photon events which meet the energy trigger requirement.

A GRB which triggers GRBM, or other satellites equipped with gamma-ray burst detectors, and which also happens to be in the field of view of one of the WFCs, and which emits x-rays coincidentally with the gamma-rays, will be imaged by the WFC and its location determined to within a few arcminutes within a matter of hours from the trigger [22], paving the way for complementary astronomical observations at x-ray, optical, and radio wavelengths.

On February 28, 1997 (UT), this happened precisely. GRB 970228 was simultaneously detected in gamma-rays by GRBM, and in x-rays by one WFC [23]. Within a few hours, analysis of the WFC data resulted in a localization of the GRB with an error circle of 3-arcminute radius. Given this small patch of sky to patrol, other astronomical experiments and instruments joined the hunt for multiwavelength counterparts to GRB 970228. About 21 hours after the GRB trigger, an optical counterpart was found in the WFC error circle using a ground-based optical telescope, and its position determined to within 0.2 of an arcsecond [24]. The optical object exhibited a rapid decline in brightness and, four days later, was no longer visible to ground-based optical telescopes. The first optical transient (OT) directly associated with a GRB had just been discovered. Observations made with the Hubble Space Telescope (HST) further revealed that the optical transient was embedded in a faint galaxy [25], proof that this GRB had an extragalactic origin. Further, the OT was observed to be offset from the center of the galaxy. Efforts to determine the redshift of the OT through spectroscopy, however, yielded no immediate results [25].

Follow-up observations by BeppoSAX's NFIs revealed a similar temporal behavior by the x-ray source which was spatially coincident with the optical transient. About 8 hours after the GRB trigger, the measured fluence from the x-ray source had declined to $\sim 1/3600$ of the initial fluence measured by the WFC, and about three days later, the fluence had dropped to $\sim 1/67000$ of the initial fluence [23].

Efforts were also made to detect radio emission from GRB 970228, but none was found [24, 25].

Since this initial success at detecting GRB counterparts at both x-ray and optical wavelengths, rapid and precise localizations by BeppoSAX, the Third Interplanetary Network (IPN3), and the Rossi X-Ray Timing Explorer (RXTE), of about 76 GRB positions (as of this writing) [26] have made possible follow-up observations of multiwavelength afterglow emission from these GRBs. IPN3 consists of the satellite missions Ulysses and the Near Earth Asteroid Rendezvous (NEAR), which are located in interplanetary space, as well as several near-Earth missions including KONUS, BeppoSAX, and RXTE [22]. IPN3 localizes bursts through the triangulation method using the time of arrival of the burst signal at the different satellites. RXTE is an x-ray satellite mission, whose all-sky monitor (ASM) has a field of view of $6^o \times 90^o$, and is sensitive to x-rays of energies 1.5 to 12 keV [27].

Out of the approximately 76 GRBs which were examined for afterglow emission, 34 GRBs had an x-ray afterglow, 20 had an optical afterglow, and 13 had a radio afterglow [26]. For about one-half of the GRBs studied, no afterglow emission was detected at any wavelength [22].

2.4.2 Pinning down GRBs: Redshift measurements and host galaxies On May 8, 1997 (UT), a GRB was detected by BATSE and by the GRBM in BeppoSAX, and was localized by a WFC within a 5-arcminute radius error circle [28, 29]. Follow-up observations revealed afterglows in the x-ray, optical, and radio wavelengths associated with GRB 970508 [30, 31, 32, 33, 34]. About two days after the burst trigger, spectroscopy of the optical transient made with the Keck II 10-m telescope in Hawaii revealed absorption features consistent with a redshift of $z = 0.835$ [35]. Spectroscopic observations made by different groups at the position of the OT one month, and then about 5 months later, uncovered emission lines which were consistent with the absorption system redshift [36, 37]. For the first time, the distance to a GRB source was directly measured, and it was of cosmological proportions.

The measured optical light curve (plot of magnitude vs. log(time)) of the optical transient associated with GRB 970508 showed that the transient exhibited an initial brightening after the gamma-ray burst, which reached a maximum ~ 1.5 days after the GRB trigger. The transient then faded, with the light curve exhibiting a power law decay with a slope of -1.141 ± 0.014, i.e. $F \propto t^{-1.141}$, where F is the flux, over the first 100 days after the burst [29]. Late-time optical observations made roughly 200 to 300 days after the burst then revealed a subsequent flattening of the light curve, leading to the interpretation that the OT had faded to reveal a faint but constant optical source $-$ the host galaxy of GRB 970508 [37].

Some three years after GRB 970508, redshifts have been measured or estimated for at least 16 GRB sources, with the median redshift for the sample being $z \approx 1$ (see Table 2.1). For most of these GRBs, a corresponding host galaxy has been detected. The optical transients were observed to be offset from the respective host galaxy's center, leading to the conclusion that GRBs are not associated with central black holes nor with active galactic nuclei. Evidence have also been put forward that the observed optical transients resided in star-forming regions of the host galaxies.

Thus, the distances to at least some GRBs have been proven to be cosmological, and the bursts of photons these GRBs sent our way turned out to be quite old, carrying messages from earlier times when the Universe was younger. Seems like GRBese is an ancient language.

2.4.3 Briefly the brightest being The measured redshifts to GRBs range from $z \approx 1$ to $z \approx 4$. Combine these with the fact that the measured fluences in gamma-rays, where a GRB seems to emit most of its energy, range from $\sim 10^{-6}$ to $\sim 10^{-4}$ $ergs/cm^2$, and it is easily figured using inverse square distance considerations that these GRBs release energies roughly equivalent to the rest mass energy of the Sun, in mere tens to hundreds of seconds. This is a luminosity in gamma-rays of $\sim 10^{50}$ to $\sim 10^{53}$ $ergs/s$, or $\sim 10^{17} L_\odot$ to $\sim 10^{20} L_\odot$, where $L_\odot$ is the bolometric luminosity of the Sun, $L_\odot \approx 3.9 \times 10^{33}$ $ergs/s$. The mean luminosity of galaxies is $\sim 10^{10} L_\odot$, and active galactic nuclei have luminosities of $\sim 10^{10} L_\odot$ to $\sim 10^{15} L_\odot$. Thus, as far as humans know, when a GRB comes into being, it becomes, for a few moments, the electromagnetically brightest object in the Universe.

Table 2.1 lists the GRBs with a measured or estimated redshift, and the corresponding isotropic energy release implied by the redshift and fluence measurements. The energy released was calculated assuming a flat, Einstein-de Sitter Universe ($\Omega = 1$, $\Lambda = 0$, $q_o = 0.5$), and Hubble constant $H_o = 65\ km\ s^{-1}\ Mpc^{-1}$:

$$E_{iso} = \frac{4\pi d_L^2 \Phi_o}{1+z} \quad , \tag{2.7}$$

where Φ_o is the measured fluence in gamma-rays, z is the redshift, and d_L is the luminosity distance which, for the assumed cosmology, is given by,

$$d_L = \frac{2c}{H_o}\left(1 + z - \sqrt{1+z}\right) \quad . \tag{2.8}$$

The implied energies for isotropic release range from $\sim 10^{48}$ to $\sim 10^{54}\ ergs$. The wide spread of energies and luminosities demonstrates that GRBs are not standard candles.

The total isotropic energy released in GRBs is similar to the total energy released in supernovae [2, 38]. However, while GRBs release the bulk of this energy in the form of electromagnetic radiation, mostly as gamma-rays, in a time span of fractions of a second to tens of seconds, 99% of the energy released in supernovae is released as neutrinos, the rest of the energy being converted into kinetic energy of ejected particles. Only about 10^{-4} of the total energy released in a supernova is emitted in the form of electromagnetic radiation, mostly in the optical region, within a few months, and the rest of the kinetic energy is converted into radiation over a period of thousands of years [38]. The gamma-rays observed from GRBs, as will be seen in Section 2.5, and the optical emission from supernovae, are the result of the conversion of the kinetic energy of ejected particles into radiation. However, in the case of GRBs, the mass of the ejecta is of the order of 10^{-5} of a solar mass, and the ejected particles attain relativistic speeds, whereas in the case of typical supernovae, the mass of the ejecta is of the order of a solar mass, and the particles attain speeds which are nonrelativistic.

Table 2.1: GRBs with a measured or estimated redshift.

GRB	burst[a] duration (*seconds*)	fluence in[b] gamma-rays ($ergs/cm^2$)	z[c]	implied[d] isotropic energy release (*ergs*)	References (with useful references therein)
970228	80	1.1×10^{-5}	0.6950 ± 0.0003	1.0×10^{52}	[23,25]
970508	23	3.1×10^{-6}	0.8349 ± 0.0003	4.0×10^{51}	[10,29,35,36,37]
971214	31	1.1×10^{-5}	3.418 ± 0.010	1.4×10^{53}	[10,39]
980326	5	1.4×10^{-6}	≈ 1[e]	2.4×10^{51}	[40,41]
980425	23	4.4×10^{-6}	0.0085 ± 0.0002	8.1×10^{47}	[42,43,38]
980613	20	1.7×10^{-6}	1.0969 ± 0.0002	3.5×10^{51}	[44]
980703	412	4.6×10^{-5}	0.9662 ± 0.0002	7.6×10^{52}	[10,45,46]
990123	63	5.1×10^{-4}	1.6004 ± 0.0008	2.0×10^{54}	[10,47]
990510	68	2.3×10^{-5}	1.619 ± 0.002	9.0×10^{52}	[10,48]
990712	30	–	0.4337 ± 0.0004	–	[49,50]
991208	68	$\sim 10^{-4}$	0.707 ± 0.002	9.6×10^{52}	[51,52]
991216	15	2.6×10^{-4}	1.02	4.7×10^{53}	[10,53]
000131	96	3.5×10^{-5}	4.500 ± 0.015	6.5×10^{53}	[54]
000301c	2	2.0×10^{-6}	2.0404 ± 0.0008	1.1×10^{52}	[55]
000418	30	1.3×10^{-5}	1.11854 ± 0.0007	2.8×10^{52}	[56,57]
000926	25	2.2×10^{-5}	2.0369 ± 0.0007	1.2×10^{53}	[58,59,60]

[a] Duration of gamma-rays measured by one of the following satellite experiments: BATSE, Ulysses, NEAR, or GRBM on board BeppoSAX.

[b] Fluence in gamma-rays measured by one of the satellite experiments mentioned above.

[c] Measured or estimated redshift. Measured redshifts are either from observed emission lines from the host galaxy, or from observed absorption lines from the OT.

[d] Calculated assuming a flat, Einstein-de Sitter Universe ($\Omega = 1$, $\Lambda = 0$), and $H_o = 65\ km\ s^{-1}\ Mpc^{-1}$.

[e] Estimated from model fits to the observed optical light curve assuming an underlying supernova.

2.4.4 The supernova twist As was forewarned at the beginning of this chapter, the GRB story does not lack in plot twists and turns. On April 25, 1998 (UT), the turn led to a supernova. GRB 980425 was observed by BATSE and by GRBM, and was localized by a WFC within an 8-arcminute error circle. Optical observations of the WFC error circle about two days later revealed a type Ic supernova, SN 1998bw, located 1.6 arcminutes away from the center of the error box, with a positional uncertainty of about 0.2 of an arcsecond in radius [42]. The time of core collapse was estimated to coincide with GRB 980425 to within +0.7/-2 days [43]. The probability for finding a supernova within the GRB error circle coincident within days of the burst was estimated to be 9×10^{-5} [42], small enough to lead to a cautious consideration of the association of SN 1998bw with GRB 980425.

Radio observations also revealed a radio source spatially and temporally coincident with the optical object and which was consistent with a type Ib/c radio supernova [38]. SN 1998bw was located in a spiral arm of the barred spiral galaxy ESO184-G82 at a redshift of $z \approx 0.0085$ [43, 42]. If the source responsible for GRB 980425 was truly the same source responsible for the supernova, then it was at the nearest distance yet measured for a GRB (cf. Table 2.1).

Analyses of archival data have led to claims of a supernova connection for at least three other GRBs: GRB 970228 [61, 62], GRB 970514 [63, 64], and GRB 980326 [41]. In the cases of GRBs 970228 and 980326, an initial steep power law decay of the respective OT light curves during early times, followed by a plateau at later times, and then a subsequent resumption of the steep decay, coupled with the reddening of the observed OT spectra with time, has been interpreted as due to a supernova being revealed only after the initial optical afterglow, dominant during early times, had faded. In the case of GRB 970514, its location as determined by BATSE was found to be 0.88^o away from supernova SN 1997cy, described as the brightest supernova yet discovered, and possessing a peculiar type II spectrum. The probability of a chance association between SN 1997cy and GRB 970514 was estimated to be 0.7%. The supernova, which exploded between 1997 March

12 and 1997 July 15, was found in a faint galaxy at a redshift of $z = 0.063$.

2.5 Interpreting GRB and GRB Afterglow Observations

The previous sections presented a summary of GRB observations which, though far from complete, gives a good idea of the progress which has been made during the past three decades in gathering empirical information about GRBs − information which are revealing clues about the nature of GRBs. The discovery of GRB counterparts at x-ray, optical, and radio wavelengths, especially, has made GRB science into a multi-disciplinary endeavor, and has led to a multifold increase in the amount of literature published on the subject. Expectedly, interpretations of the observations have increased proportionally and, for the most part, serve as a testament not only to humankind's reasoning abilities, but also to its ability to allow the mind to triumph and to imagine things well beyond the purview of daily existence. That these interpretations are sometimes conflicting is a reassuring sign of an ongoing healthy debate, and that none who wish to claim the role of sole gatekeeper to the nature of GRBs could do so.

2.5.1 Summary of observations A more apt appellation for this phenomenon is hard to contrive. Gamma-ray bursts are observed flashes of gamma-rays of cosmic origin. Data from satellite experiments have revealed that the energy spectra of GRBs are nonthermal, with the bulk of the energy detected being carried by photons with energies of a few hundred keV, and with most spectra having a high-energy tail extending to MeV energies, some to GeV energies. These bursts of gamma-rays last anywhere from a few milliseconds to a thousand seconds. Within these durations, some GRB time histories exhibit highly variable features, with the widths of the features being fractions of a second to a few seconds long, while others consist only of a single peak. GRB time durations can be grouped into two: those which are shorter than two seconds, and those which are longer.

BATSE's data show that the spatial distribution of GRBs is isotropic but not homogeneous in Euclidean space, giving circumstantial evidence that GRB sources are located at cosmological distances. Since 1997, x-ray, optical, and radio afterglows have been observed from some GRB sources. These long-lived afterglows persist hours, days, or even months after the main gamma-ray burst. Observations of optical counterparts to a few GRBs have provided opportunities to directly measure the distances to some of these GRBs through redshift measurements. It is now known that some GRBs are located at redshifts of $z \approx 1$ to $z \approx 4$. The measured gamma-ray fluences and redshifts for these bursts imply an isotropic energy release of $\sim 10^{51}$ to $\sim 10^{54}$ $ergs$ during the GRBs' short lifetimes. For most of the optical transients found, a corresponding host galaxy was also observed, with the optical transient's position found to be offset from the center of its host galaxy. It should also be noted that the GRBs for which afterglows have been found had main burst time durations of ~ 2 seconds or longer. There has been no afterglow found for a GRB whose time duration was in the subsecond range, quite possibly due to the difficulty involved in accurately locating short-duration bursts.

Using BATSE's measured GRB flux distribution, Schmidt [65] inferred for the sample studied a GRB comoving space density of ~ 0.18 to ~ 0.45 yr^{-1} Gpc^{-3} for $z = 0$, depending on the assumed cosmology, a GRB redshift distribution which peaks a little above $z = 1$, and a characteristic GRB energy release of $\sim 1.2 \times 10^{53}$ $ergs$ in the 10-1000 keV photon energy range.

2.5.2 The fireball model of GRBs The relativistic fireball model of GRBs [2, 66, 67], also called the internal-external shocks model for reasons which will become apparent a few sentences from now, is currently the popular model for explaining the physical mechanisms which give rise to the observed GRB phenomena. This model is schematically illustrated in Fig. 2.11. In the fireball model, there is an inner engine which acts as the GRB progenitor. This engine is not observed directly, and its real nature is still unknown, though possible candidates have been suggested. From the observed temporal variability, ΔT, in GRBs' time histories, which can be of the order of a few milliseconds, it is inferred that the size of this inner engine is $R \sim c\Delta T \sim 10^5 - 10^6$ m. Somehow, this engine, which is active during the observed GRB duration, T, is able to release a tremendous amount of energy in the form of a radiation-plasma fireball. The pressure of this fireball causes it to expand relativistically, thus accelerating baryonic matter which may have been ejected together with the fireball, and resulting in a particle wind (Fig. 2.11, top panel). Eventually, most of the initial fireball energy is converted into bulk kinetic energy of the matter, with the baryonic matter attaining a relativistic velocity, corresponding to a bulk relativistic Lorentz factor, Γ, if the baryonic load is small enough. The engine activity could be highly variable, giving rise to multiple fireballs and highly variable particle winds, and thus to multiple shells with different Lorentz factors (middle panel). This characteristic is necessary to explain the multiple peaks observed in some of the GRB time histories.

The nonthermal energy spectra of GRBs indicate that the radiation is emitted from an optically thin region. A region with a large optical depth would result in thermalization and a blackbody spectrum [2]. The consideration that the emitting region is optically thin leads to the conclusion that the shells of matter attain ultrarelativistic velocities, with bulk Lorentz factors of at least ~ 100. Different shells will have different Lorentz factors, and when a fast shell catches up with a slow shell, the two shells collide inelastically, forming a shock. The shock accelerates the electrons coupled to the baryonic matter, and this acceleration of electrons in an ambient magnetic field causes the emission of synchrotron radiation which is observed on Earth (middle panel). It is also possible that gamma-rays are produced through inverse Compton scattering of synchrotron radiation off the shock-accelerated electrons. These collisions take place at an optically thin region which is $R \sim 10^{12}\ m$ from the engine. In this scenario, the generation of internal shocks through multiple collisions of relativistic shells explains the multiple peaks found in some GRB time histories. Thus, in this model, the time duration of the burst, T, is the time during which the inner engine is active, and the temporal variability, ΔT, reflects the variability of the engine activity.

The final stage of this model involves the expansion of the relativistic shells into an interstellar, ambient medium of low-density gas. Alternatively, this could be stellar

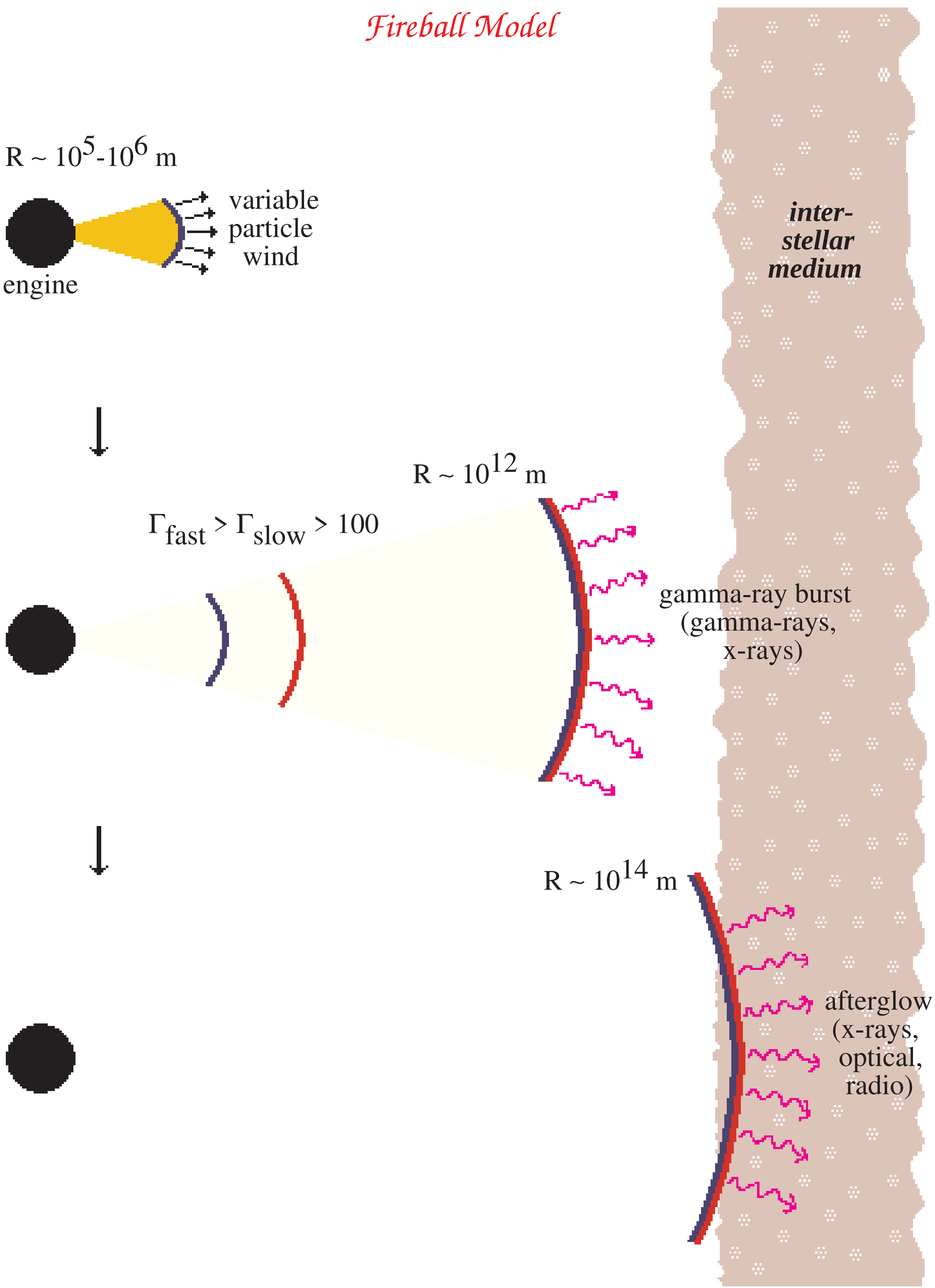

Figure 2.11: Relativistic fireball model of GRBs. Parameter values given are relative to the observer's reference frame.

wind associated with the GRB progenitor. The expansion of the relativistic shells into this medium causes the slowing down of the shells and the production of external shocks, which again accelerate electrons and give rise to synchrotron radiation, but at longer wavelengths than those produced in the internal shocks. This radiation is observed as the GRB afterglow (bottom panel).

2.5.3 Emission of TeV photons from GRBs A handful of astrophysical sources have been detected in the TeV waveband [68, 69]. These sources include the Crab nebula, the Vela pulsar, the active galactic nuclei Markarian 421 and Markarian 501, and the PSR 1706-44 supernova remnant. For some of these sources, the observed energy spectrum spans a wide range of energies, from radio to TeV energies. In the cases of the Crab nebula [70-74] and the blazars Mrk 421 and Mrk 501 [75-89], the observed low-energy emission is commonly believed to be due to synchrotron radiation from relativistic electrons accelerated in the astrophysical sources, while the high-energy TeV component is believed to be due to inverse Compton scattering of the synchrotron photons off the same population of relativistic electrons.

Calculations by Pilla and Loeb [90] have shown that, considering both synchrotron and inverse Compton processes, and for shell Lorentz factors of $\Gamma \sim 3 \times 10^3$, the emission spectra of GRBs due to internal shocks would be observed to extend to GeV-TeV energies (assuming a redshift of $z \approx 1$), with the synchrotron process producing radiation which would be observed in the keV-MeV range, and the inverse Compton process producing radiation which would be observed in the GeV-TeV range. The emergence of the GeV-TeV component is expected to be prompt, coincident with synchrotron radiation seen in the keV-MeV range.

The observed characteristic energy due to inverse Compton scattering of synchrotron radiation off the shocked electrons is expected to be [2] (e is electron charge, B is magnetic field, m_e is electron mass, c is speed of light, all in *cgs* units),

$$E_{IC} \approx \left(\frac{\hbar e B}{m_e c} \, \gamma_e^2 \, \Gamma \right) \gamma_e^2 \quad , \tag{2.9}$$

$$E_{IC} \approx E_{sync} \gamma_e^2 \quad , \tag{2.10}$$

where E_{sync} is the observed characteristic energy due to the synchrotron process, and γ_e is the Lorentz factor of the shocked electrons in the comoving frame, $\gamma_e \sim m_p/m_e$, the ratio of proton mass to electron mass. If the observed GRB spectra in the soft gamma-rays is due to synchrotron radiation, then $E_{sync} \approx 200\ keV$, and the characteristic energy due to synchrotron self-Compton would be observed to be,

$$E_{IC} \approx 1\ TeV \quad . \tag{2.11}$$

Thus, the production of TeV photons, as seen in the observer's frame, through internal shocks in the context of the relativistic fireball model is possible, and searching for TeV photons from GRBs using ground-based gamma-ray observatories is a worthwhile effort, the result of which, whether null or positive, would have an impact on modelling GRB radiation mechanisms.

Of course, the ability to positively detect such photons would depend on the sensitivity of the gamma-ray instrument. At TeV energies, absorption of high-energy gamma-ray photons by cosmic infrared radiation (IR) has a big effect on the incoming flux of photons, and the observed flux is expected to be a fraction of the unattenuated flux due to attenuation by the cosmic infrared radiation (see Chapter 8 for a discussion). Since GRBs have very short durations, and TeV emission is expected to be prompt, it is also necessary that the gamma-ray detector have a wide field of view, that is, is able to monitor simultaneously different parts of a wide patch of sky. Gamma-ray telescopes which have to move mechanically so as to point to a GRB direction in real time might be too slow to catch a glimpse of the ephemeral objects. Moreover, a detector which is able to monitor the sky during the day as well as during the night will have twice the chance for detecting TeV emission as one which is restricted to making observations at nighttime only.

There have been searches made for TeV emission from GRBs by various experiments [91-95]. Some of these have resulted in tentative evidence for TeV emission [91, 92], but none of the searches have resulted in convincing evidence for such emission.

2.5.4 GRB geometry: To beam or not to beam? Beaming, or a jet, descriptive of matter being ejected into a collimated direction, is a common astrophysical phenomenon. *Radio quasars*, *optically violently variable quasars*, *BL Lac objects*, all falling under the general category of *active galactic nuclei*, are some astrophysical objects which are known to eject relativistic plasma into a jet geometry. It has been suggested that GRB sources likewise eject baryonic matter in a beamed direction instead of isotropically [96, 66]. If the beaming angle of a GRB is θ_o, then the total energy requirement for the GRB would be reduced from that required if an isotropic emission is assumed:

$$E_{beam} = 2\,\frac{\theta_o^2}{4} E_{iso} \quad , \tag{2.12}$$

where the factor $\theta_o^2/4$ is the ratio of beamed solid angle to isotropic solid angle, and the factor of two comes from assuming that there are two oppositely directed beams produced. A beaming angle of $\theta_o = 0.1\ rad$ ($\approx 6^o$), for example, would reduce the energy requirement by a factor of 200, or by two orders of magnitude. In other words, beaming would ease the GRB energy requirement to a magnitude which would be easier to reconcile theoretically with suggested astrophysical GRB progenitors and energy conversion mechanisms (see next subsection). Beaming would also mean that the actual GRB rate is higher than the rate at which GRBs are observed.

Radiation produced by a relativistically moving charged particle is strongly beamed within an angle Γ^{-1} centered along the particle's direction of motion, where Γ is the Lorentz factor associated with the particle's motion. Thus, in the context of the relativistic fireball model, observers on Earth see only GRB radiation produced by electrons confined within the angle Γ^{-1} from the observer's line of sight, where Γ is the shell's bulk Lorentz factor. If the GRB's initial beaming angle is large in relation to this relativistic effect, $\theta_o > \Gamma^{-1}$, then observers on Earth would not be aware of the jet, and would not be able to tell that they are not observing isotropic emission from an expanding spherical shell [66]. As the relativistic shell of matter expands into the interstellar medium (ISM), however, the shell slows down and Γ decreases until $\theta_o \sim \Gamma^{-1}$. At this point, the jet geometry becomes apparent to the observer, since radiation from the entire emitting region of the shell can be seen by the observer. Also at this point, it is suggested that the matter begins to expand sideways relativistically [96, 66]. The combination of this rapid sideways expansion and the larger radiation angle, Γ^{-1}, is expected to result in a break in the observed afterglow light curve, with the time of the break relative to the main burst depending on the initial beaming angle, θ_o, and on the density of the ISM [96].

Possible beaming evidence from optical afterglow light curves have been claimed for at least seven GRBs: GRBs 980326, 980519, 990123, 990510, 991216, 000131, and 000301c. Typically, GRB optical light curves are observed to decay according to a power law: $F \propto t^{-a}$, where a is typically $a \approx 1$ (see Table 2.2). However, in the cases of GRBs 980326 [40, 41, 96], 980519 [100, 96], and 000131 [54], the observed decay was steeper than usual, with $a \approx 2$. These steep light curves have been interpreted as due to the sideways expansion of beamed matter [96, 66]. In the cases of GRBs 990123 [47, 96], 990510 [101, 102], 991216 [53], and 000301c [55], an observed transition from an initial slope of $a_1 \approx 1$ to $a_2 \approx 2$, with the break in the light curve occurring on a time scale of a few days after the main burst, has been interpreted as due to a transition from a phase when the jet was not apparent to the observer (spherical-like phase) to a phase when the jet and its sideways expansion became apparent [96, 66].

The implied beaming angles for some GRBs, derived from information extracted from their respective optical afterglow light curves, are given in Table 2.2. Using equation (2.12) and the implied isotropic energies given in Table 2.1, the total energy release for some of the GRBs, assuming beamed emission, would be:

GRB 990123: $E_{beam} \approx 2.0 \times 10^{54}\ ergs/200 \approx 1.0 \times 10^{52}\ ergs$

GRB 990510: $E_{beam} \approx 9.0 \times 10^{52}\ ergs/300 \approx 3.0 \times 10^{50}\ ergs$

GRB 991216: $E_{beam} \approx 4.7 \times 10^{53}\ ergs/200 \approx 2.3 \times 10^{51}\ ergs$

GRB 000131: $E_{beam} \approx 6.5 \times 10^{53}\ ergs/140 \approx 4.6 \times 10^{51}\ ergs$

GRB 000301c: $E_{beam} \approx 1.1 \times 10^{52}\ ergs/30 \approx 3.7 \times 10^{50}\ ergs$

On the other hand, GRBs 970228 and 970508 showed no evidence of a beaming break, since their respective light curves obeyed a single power law even months after the initial observations [96, 66]. This sets a lower limit, $\theta_o \geq 1\ rad$, to the beaming angle of these GRBs, corresponding to a reduction of less than an order of magnitude to the isotropic energy emission [96].

2.5.5 The inner engine There are four most commonly enumerated astrophysical modes for the formation of a GRB inner engine. All four progenitors suggested are described to have a single outcome: matter accreting into a black hole. A fraction of the energy produced in the accretion of matter into the black hole would then supply the energy needed to produce a GRB. Each of the four astrophysical pathways is estimated to be capable of releasing at least $\sim 10^{53}$ ergs [2]. Since all of the models involve massive stars, it is expected that GRBs trace the star formation history of the Universe [105-109]. Briefly, the four modes are:

> *Neutron star - neutron star merger* Binary neutron stars which are orbiting each other lose rotational energy through the emission of gravitational radiation, so that they eventually spiral into each other and collide. The median merger time is $\sim 10^8\ years$. Several binary neutron star (NS) systems have been discovered. The two supernova events giving rise to the two neutron stars are expected to give the binary neutron star system a "kick" velocity, so that the merger takes place a few kpc from the pair's birthplace. It has been estimated that at a redshift of $z = 1$, 90 percent of these mergers occur within $\sim 4\ arcseconds$ from the host galaxy, still consistent with current afterglow and host galaxy observations. But if NS-NS mergers give

rise to GRBs, it is also expected that a non-negligible fraction of these GRBs should occur well outside dwarf galaxy hosts [110]. The NS-NS merger comoving rate is estimated to be $\sim 10^2 - 10^3\ yr^{-1}\ Gpc^{-3}$ for $z = 0$ [109, 105].

Neutron star - black hole merger For this proposed progenitor, tidal disruption of the neutron star by the black hole (BH) in a NS-BH binary leads to accretion of the neutron star debris into the black hole. Unlike a binary neutron star system, however, no neutron star - black hole binary has been found in nature. Nevertheless, it has been suggested that the NS-BH merger rate would be comparable to the NS-NS merger rate [2, 66], and that a NS-BH system would have smaller system velocities than NS-NS binaries, so that NS-BH mergers would take place closer to their host galaxies [110].

Collapsar or failed Type Ib supernova A Type Ib supernova is believed to be caused by the iron core collapse and subsequent explosion of a massive star which has lost its hydrogen envelope [111]. Very massive stars of $\gtrsim 35 M_\odot$ undergoing iron core collapse would be more difficult to explode, and continued mass accretion from the star's mantle and helium core into the iron core would cause the core to collapse into a black hole. In this scenario, it is still possible for a supernova to occur, but a considerable amount of material would still accrete into the black hole. The accretion time scale is estimated to be of the order of several seconds to several tens of seconds. The rate of Type Ib/c supernovae is $\sim 3 \times 10^4\ yr^{-1}\ Gpc^{-3}$ [105].

Hypernova or microquasar As in the collapsar model, a hypernova/microquasar is envisioned to result from the violent end of a massive star's evolution. In this scenario, the collapse of the iron core of a massive, rapidly rotating star which is a member of a massive binary, results in an accretion disk surrounding a rapidly spinning Kerr black hole. The presence of a superstrong magnetic field could possibly extract the rotational energy of the Kerr black hole and generate a GRB [112].

Several authors have suggested that the afterglow observations which link some GRBs to supernovae, as well as evidence which associate GRBs with star forming regions of the host galaxies, tend to support the collapsar or hypernova models over the stellar remnant merger models. It has also been suggested that the star collapse models give rise to the long-duration population of GRBs, while the stellar remnant merger models give rise to the observed population of short-duration GRBs, for which no representative afterglow has been observed. While these suggestions have merit, it is premature to make any firm conclusions, based on the current data, regarding the real nature of GRB progenitors. Further observations at all wavelengths are necessary before one can completely embrace, or thoroughly discard, a GRB progenitor model. Detections of gravitational radiation as well as neutrino signals coincident with GRBs are some of the additional tasks which have been put forward [2]. Valiant efforts are being made to use computers to simulate these progenitor models to test their validity [113, 114, 115]. However, it is this author's opinion that the next big clue which will lead to the denouement of the GRB story will fall on the lap of an unsuspecting but watchful experimentalist.

Table 2.2: Measured power law indices of GRB optical afterglow light curves.

GRB	a_1 [a]	a_2 [a]	t_{break} [a] (*days*)	θ_o [b] (*rad*)	References (with useful references therein)
970228	1.51 ± 0.06				[62, 61, 96]
970508	1.141 ± 0.014				[29, 96]
971214	1.22 ± 0.2				[39, 97, 98]
980326	2.10 ± 0.13				[40, 41, 96]
980329	1.1 ± 0.4				[99]
980519	2.05 ± 0.04			< 0.1	[100, 96]
990123	1.10 ± 0.03	1.65 ± 0.06	2.04 ± 0.46	~ 0.1	[47, 96]
990510	0.82 ± 0.02	2.18 ± 0.05	1.20 ± 0.08	~ 0.08	[101]
	0.76 ± 0.01	2.40 ± 0.02	1.57 ± 0.03		[102]
990712	0.97 ± 0.05				[49]
991208	2.15				[103]
991216	1.219 ± 0.036	1.53 ± 0.05	~ 1	~ 0.1	[53]
000131	2.25 ± 0.19		< 3.5	< 0.12	[54]
000301c	0.72 ± 0.34	2.29 ± 1.00	4.39 ± 1.52	~ 0.26	[55]
000418	1.22				[56]
000630	1.1 ± 0.3				[104]

[a] Some light curves have only a single slope, in which case the flux is $F \propto t^{-a_1}$, while others have two slopes, with the early part being described by $F \propto t^{-a_1}$, and the late part being described by $F \propto t^{-a_2}$, and the time when the transition occurred given by t_{break} (relative to the time of the main burst).

[b] Implied beaming angle.

Chapter 3

Extensive Air Showers

At TeV energies, gamma-ray astronomy is conducted on terra firma, that is to say, within the Earth's atmosphere, instead of without. This is so since, for TeV astronomy experiments, the Earth's atmosphere is an integral component of the particle detector. A high-energy primary gamma-ray passing through the atmosphere interacts with this medium, initiating the production of secondary particles and photons which could be detected by ground-based particle detectors or Cherenkov telescopes. The small physical sizes of satellite-based detectors make these instruments ill-equipped for detecting small fluxes of gamma-rays. Thus, the study of astrophysical, high-energy gamma-ray sources benefits from the complementary techniques of satellite-based and ground-based experiments. This chapter elaborates, in particular, on the production of extensive air showers initiated by high-energy gamma-rays incident on top of the atmosphere.

3.1 Longitudinal Development of an Extensive Air Shower

The qualitative outline for the longitudinal development of an extensive air shower (EAS) is as follows. A high-energy primary gamma-ray entering the Earth's atmosphere interacts with the electromagnetic field of a nitrogen or oxygen nucleus, thus producing an electron-positron pair moving at ultrarelativistic speeds. Each of these ultrarelativistic particles, in turn, suffers dramatic energy losses through emission of *bremsstrahlung radiation* as it passes through the atmosphere. The bremsstrahlung photons emitted in this process subsequently interact with air nuclei to produce electron-positron pairs. The process continues in this manner, with the passage of ultrarelativistic electrons and positrons in the atmosphere causing the production of bremsstrahlung radiation, and the radiation producing electron-positron pairs.

For ultrarelativistic particles, the radiation length for the bremsstrahlung process, the distance traversed in a material over which a particle loses 63% of its energy through emission of bremsstrahlung radiation, is approximately equal to the radiation length for electron-positron pair production [116, 117]. Equivalently, this distance can be expressed in terms of the amount of material traversed. For air, this radiation length is about $X_o \approx 37\ g\ cm^{-2}$. On the average, an electron or positron loses half of its energy through bremsstrahlung after traversing a distance equal to $X_o ln2$, producing a photon with an energy approximately one-half the energy of the electron or positron. Similarly, a photon will produce an electron-positron pair after traversing, on the average, the same distance. The electron and the positron produced will, on the average, each have an energy approximately one-half the energy of the photon. The electromagnetic cascade ceases when the average energy per particle is less than the critical energy of $E_c \approx 80\ MeV$. At energies below this critical energy, the main mechanism by which the charged particles lose energy is through ionization losses rather than bremsstrahlung, so that additional photons are no longer produced.

Qualitatively, the outcome of this process is the production of a multitude of secondary particles – photons, electrons, and positrons – cascading down through the atmosphere near the speed of light, and the number of which increases exponentially with distance traversed in the atmosphere, until a depth in the atmosphere is reached where the number of particles reaches a maximum, and the average energy per particle is approximately equal to the critical energy, E_c. This stage in the development of an EAS is called *shower maximum*. At a given depth in the atmosphere, the number of secondary particles produced is proportional to the energy of the initiating primary gamma-ray. After shower maximum, the number of secondary particles in the EAS decreases with depth in the atmosphere as the energy of the secondary particles is absorbed by the atmosphere through ionizations and scattering.

Figure 3.1 shows the average number of secondary particles in an EAS as a function of depth in the atmosphere for different primary gamma-ray energies, from Monte Carlo simulations made by Di Sciascio, et. al. [118]. The depth which has been traversed by the EAS is given in units of radiation lengths, i.e. $depth = x/X_o$, where x is the amount of material, in $g\ cm^{-2}$, and $X_o \approx 37\ g\ cm^{-2}$ is the radiation length in air. The total depth of the atmosphere is $\sim 1,000\ g\ cm^{-2}$, which is ~ 27 radiation lengths. Fig. 3.1(a) gives the average number of electrons, and Fig. 3.1(b) gives the average number of photons. The general trend for the shower size as a function of depth discussed above, i.e. the exponential increase, the shower maximum, and the decrease after shower maximum, can be seen in these plots. It can also be seen that, after shower maximum, the decrease in the number of photons with depth is less severe than the decrease in the number of electrons. At a depth of about 20 radiation lengths, where Milagrito is situated, the average number of photons is about 3 to 4 times larger than the average number of charged particles in extensive air showers initiated by gamma-rays of TeV energies.

Occasionally, an extensive air shower initiated by a high-energy gamma-ray will also contain some muons, since muons can be produced via $\gamma \rightarrow \mu^+\mu^-$. The fraction of showers which contain muons increases as the energy of the initiating primary gamma-ray increases.

3.2 Lateral Distribution of Air Shower Particles

The ultrarelativistic particles and photons in an EAS are produced in a mostly forward direction. However, the electrons and positrons suffer multiple Coulomb scattering off the electric field of nuclei. Low-energy particles get scattered more than high-energy particles. Because of this multiple scattering, the shower particles and photons are spread out over an area and attain a lateral distribution. The density of shower particles is greatest near the *shower core*, which is the trajectory that the primary gamma-ray would have if it did not interact with the atmosphere, and decreases with increasing distance from the

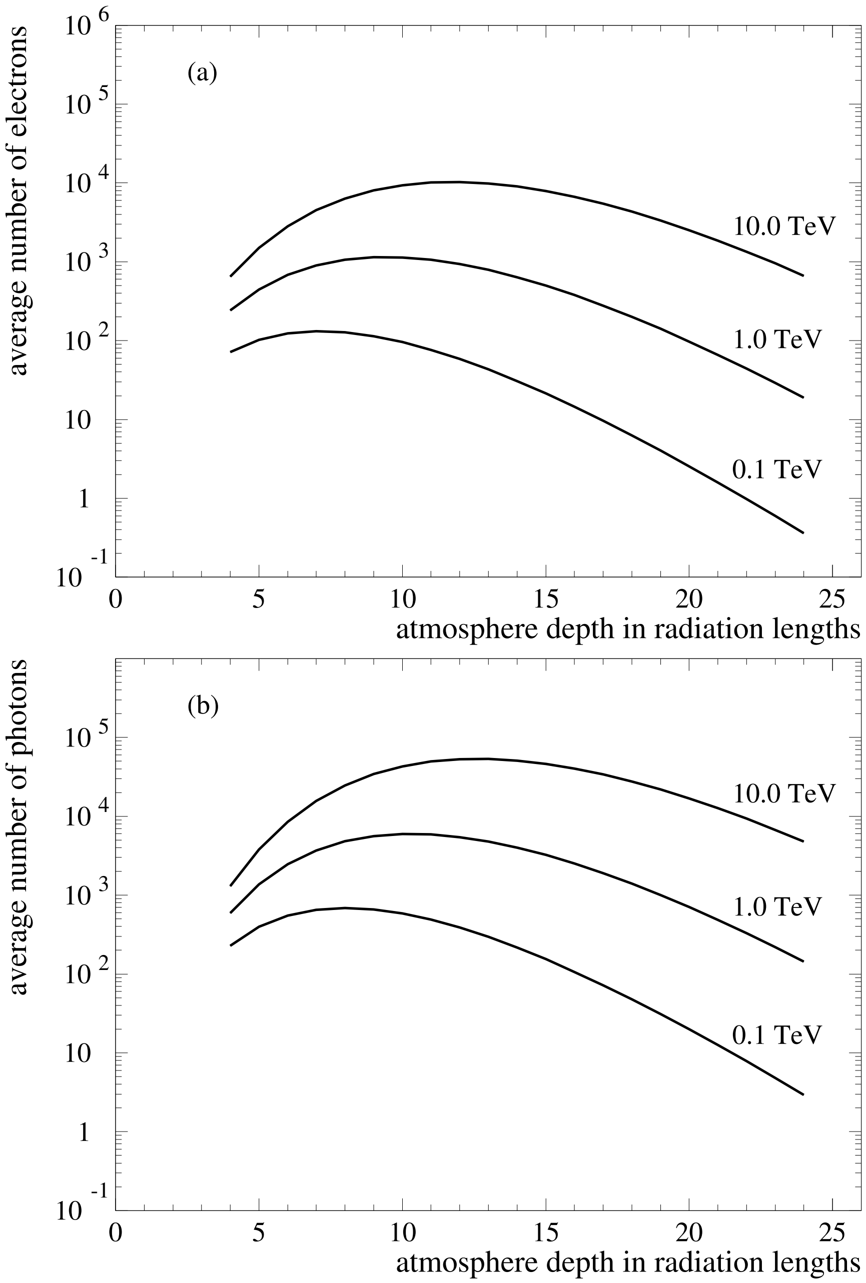

Figure 3.1: Average number of air shower particles as a function of atmosphere depth for different primary gamma-ray energies. Plot (a) gives the average number of electrons, while plot (b) gives the average number of photons.

shower core. Because high-energy particles get scattered less, the highest-energy particles in an EAS are found nearest the core, and the lowest-energy particles are found farthest from the core.

As a consequence of the fact that photons do not lose energy through ionizations like electrons and positrons do, shower photons spread out farther from the core than electrons or positrons do [118]. Thus, the ratio of the average number of photons to the average number of electrons increases with increasing distance from the shower core. Figure 3.2(a) plots the density of electrons, normalized to the total number of electrons in the shower, as a function of core distance for different primary gamma-ray energies, and for a depth of 22 radiation lengths, and Fig. 3.2(b) plots the equivalent quantity in the case of photons. These plots reflect the fact that most of the particles in an EAS are found within a few hundred meters from the shower core.

3.3 Temporal Distribution of Air Shower Particles

Ground-based air shower arrays generally determine the arrival direction of a cosmic primary particle incident on the atmosphere by using the relative times of arrival on the ground of the generated air shower particles. Knowledge of the temporal characteristics of air shower particles is thus an important factor toward achieving the best possible angular resolution for these types of experiments. There are two important things to consider when thinking about the temporal characteristics of an EAS: The shape of the shower front, and the air shower ”thickness.”

In general, the shower front is defined by the shower particles which hit the ground the earliest at different distances from the location of the shower core on the ground. These particles thus ”lead” the other particles in the air shower and, generally, these will be the higher-energy particles in the shower. Results of Monte Carlo simulations by Di Sciascio, et. al. [118] are shown in Figure 3.3, which plots the average time of arrival on the ground of the earliest particles relative to the time of arrival of the shower core, as a function of

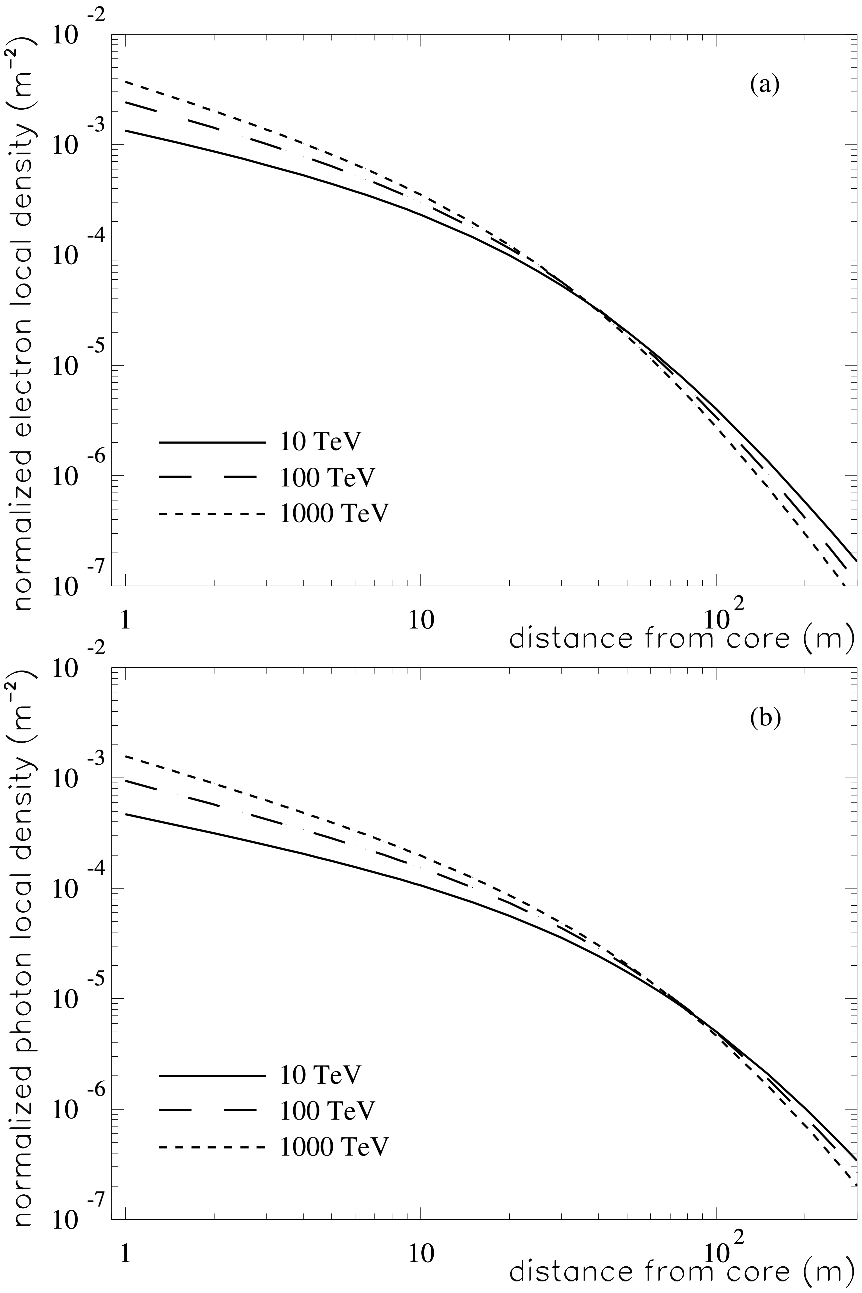

Figure 3.2: Lateral distribution of air shower particles for different primary gamma-ray energies. Plot (a) gives the electron distribution, while plot (b) gives the photon distribution.

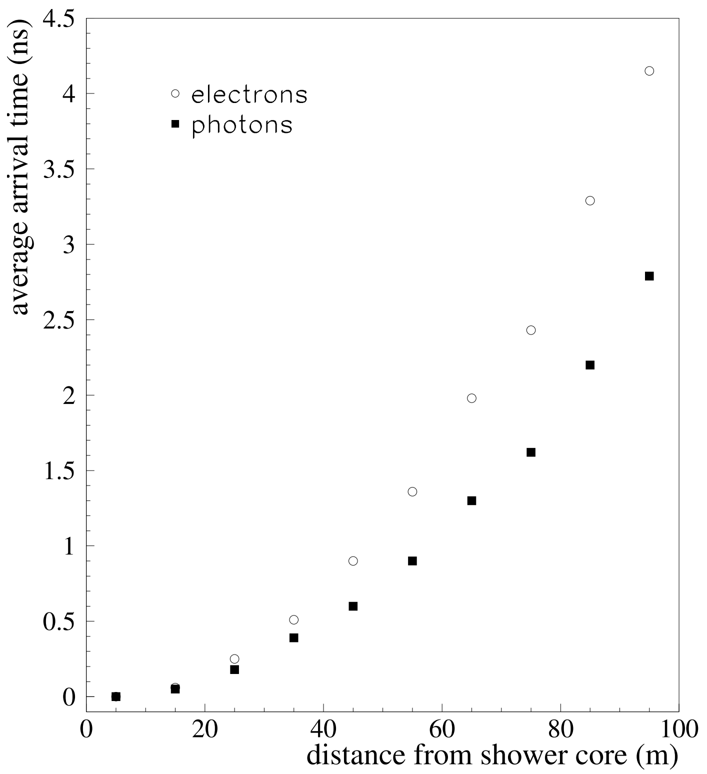

Figure 3.3: Average time of arrival on the ground of air shower particles which define the shower front. The time of arrival is relative to the time of arrival of the shower core on the ground.

distance from the core, for an EAS initiated by a 10-TeV gamma-ray, and for a depth of 22 radiation lengths. The simulations tracked shower particles down to an energy of 1 MeV. The photons are more prompt than the electrons, as expected, since at large depths, the electrons travel at lower speeds than the photons. It can also be seen from the plot that the shower front has a parabolic shape – particles near the core are prompt, and the average arrival time of the earliest particles increases with distance from the core. The plot shows that at about 100 meters from the core, the earliest particles arrive about 3 to 4 ns later than the particles near the core, corresponding to a longitudinal distance of about 1 meter between the shower front particles near the core and the shower front particles at 100 meters from the core.

The thickness of an EAS is defined by the distribution of arrival times of the shower particles which are delayed relative to the prompt particles which make up the shower front. The shower thickness is, therefore, due to the lower-energy particles in a shower. This means that the shower thickness is smallest near the shower core, and increases with increasing distance from the shower core. Also, since, as pointed out in Section 3.2, low energy photons can propagate farther than low energy electrons because these photons do not lose energy through ionizations, the thickness of the photon component at large distances from the core tends to be larger than the thickness of the electron component [118]. At a lateral distance of 50 meters from the core, the average time delay of electrons relative to the time of arrival of the shower core is about 10 ns, corresponding to about 3 meters average thickness, while the average time delay of photons is about 15 ns, corresponding to about 5 meters average thickness. At 100 meters from the core, the average time delay of electrons is about 20 ns, or about 7 meters average thickness, while the average time delay of photons is about 35 ns, or about 12 meters average thickness [118].

3.4 Cherenkov Radiation

Cherenkov radiation [119, 120, 121] is weak radiation which is produced when a relativistic, charged particle passes through a dielectric medium. The passage of a fast, charged particle through a dielectric causes the polarization of atoms near the track of the particle. The atomic electrons are, in effect, shocked. If the speed of the charged particle is larger than the phase velocity of light in the medium, the radiation resulting from this polarization effect would add coherently, and the radiation would be able to escape to infinity. The condition for the production of Cherenkov radiation is thus given by,

$$\beta > \frac{1}{\sqrt{\epsilon(\nu)}} = \frac{1}{n(\nu)} \quad , \tag{3.1}$$

where $\beta = v/c$ is the ratio of the particle speed to the speed of light in vacuum, and $\epsilon(\nu)$ is the dielectric constant of the medium which, in general, is a function of the frequency of light, ν, and $n(\nu)$ is the index of refraction of the medium. Below this particle speed threshold, the energy lost by the energetic particle in polarizing the atoms is deposited near the particle path, and no Cherenkov radiation is produced. In terms of the total energy, E, of a relativistic particle with rest mass m, the threshold condition can be rewritten as,

$$E > \frac{mc^2}{\sqrt{1 - \frac{1}{n(\nu)^2}}} \quad . \tag{3.2}$$

Cherenkov radiation is emitted at an angle with respect to the track of the particle. This angle is given by,

$$cos\,\theta_C = \frac{1}{\beta\, n(\nu)} \quad . \tag{3.3}$$

Thus, the requirement given by equation (3.1) ensures that the angle given by equation (3.3) is a physical angle. For an ultrarelativistic particle, $\beta \approx 1$, and the angle is given by,

$$cos\,\theta_C \approx \frac{1}{n(\nu)} \quad . \tag{3.4}$$

Cherenkov radiation consists mainly of visible and near-visible wavelengths, for which the index of refraction, n, of a medium is approximately constant. The energy lost, through Cherenkov radiation, per unit path length per unit wavelength by a relativistic particle passing through a medium is given approximately by,

$$\frac{dE}{dl\; d\lambda} = 4\pi^2\, (Ze)^2\, sin^2\theta_C\, \frac{1}{\lambda^3} \quad , \tag{3.5}$$

where Ze is the charge of the relativistic particle. That is, Cherenkov radiation is emitted mostly at the violet end of the spectrum.

The index of refraction, at visible wavelengths, of water is $n_{water} = 1.33$, and of air at standard temperature and pressure is $n_{air} = 1.000293$. Thus, for water, the threshold total energy given by equation (3.2) is approximately $0.775\ MeV$ for an electron, $0.16\ GeV$ for a muon, and $1.42\ GeV$ for a proton. For air, the threshold energies are approximately $21.114\ MeV$ for an electron, $4.37\ GeV$ for a muon, and $38.78\ GeV$ for a proton. For ultrarelativistic particles, the Cherenkov angle, given by equation (3.4), is approximately 41^o in water, and 1.4^o in air at standard temperature and pressure. Since the index of refraction of air is a function of altitude, decreasing with increasing altitude, the Cherenkov angle in air decreases with increasing altitude.

The relativistic electrons and positrons in extensive air showers give rise to Cherenkov light as these particles pass through the atmosphere. The intensity of this radiation is small, and the energy emitted is about 0.05% of the energy lost by the particles through ionization [121]. Also, due to the large threshold energies required, muons and nucleons contribute little to the intensity of Cherenkov light which is produced in air. Nevertheless, Cherenkov light produced by the passage of air shower particles in the atmosphere can be detected on the ground by so-called air Cherenkov telescopes.

3.5 Cosmic Rays

The discussion has been limited so far to extensive air showers produced by primary gamma-rays. However, the particles which impinge on the Earth's atmosphere in abundant numbers are *cosmic rays*. Primary cosmic rays, which are produced by astrophysical sources, are composed primarily of protons. Protons constitute 79% of cosmic rays, while helium nuclei make up 70% of the remaining fraction [122]. Carbon, oxygen, iron, and other nuclei are also found in cosmic rays in smaller fractions. The highest-energy cosmic rays which have been found, and which could be extragalactic in origin, have energies of about $10^{20}\ eV$. At energies between a few GeV and about 100 TeV, cosmic rays are believed to originate from the Milky Way galaxy. Because cosmic rays are charged particles and interact with interplanetary and Galactic magnetic fields, information about the original directions of cosmic rays is lost. At energies up to about 100 TeV, the measured arrival directions of cosmic rays on Earth are essentially isotropic. The differential flux of cosmic rays on top of the atmosphere at this energy range is given approximately by [122],

$$\frac{dN(E)}{dA\,dt\,d\Omega\,dE} \approx 1.8\,E^{-2.7}\,\frac{nucleons}{cm^2\;s\;sr\;GeV} \quad , \tag{3.6}$$

where E is the total energy per nucleon.

A collision between an incoming cosmic ray and an air nucleus initiates a cascade of secondary particles in the atmosphere. A collision between an energetic primary proton and an air nucleus will lead to the production primarily of neutral and charged pions. If the collision is between a cosmic ray nucleus and an air nucleus, energetic nucleons which can initiate other cascades are also produced. The pions which are produced can interact with the atmosphere to produce other energetic nucleons. However, neutral pions quickly decay into gamma-rays,

$$\pi^o \longrightarrow \gamma\gamma \quad . \tag{3.7}$$

The generated gamma-rays then initiate electromagnetic air showers as described in Section 3.1. The charged pions also decay to produce muons and neutrinos,

$$\begin{aligned} \pi^- &\longrightarrow \mu^- + \overline{\nu}_\mu \quad , \\ \pi^+ &\longrightarrow \mu^+ + \nu_\mu \quad . \end{aligned} \tag{3.8}$$

The energetic muons which are produced have lifetimes which are dilated to $\gamma_\mu \tau_o$ in the observer's reference frame, where γ_μ is the Lorentz factor of a produced muon, and τ_o is the muon lifetime in the muon rest frame. Because of this relativistic time dilation effect, energetic muons survive to sea level without decaying. Thus, extensive air showers initiated by cosmic rays are characterized by the presence of large numbers of muons, aside from copious electrons, positrons, and photons.

The extensive air showers produced by cosmic rays are the main source of background noise for ground-based gamma-ray detectors. These experiments, thus, must develop methods to discriminate between showers initiated by primary gamma-rays and those initiated by cosmic rays in order to increase their sensitivity to gamma-ray fluxes from astrophysical sources.

3.6 Detecting Extensive Air Showers

Extensive air showers produced in the atmosphere by the transit of primary gamma-rays or cosmic rays can be detected by the use of ground-based detectors generally called *air shower arrays*. An air shower array is commonly made up of discrete scintillation detectors spread over a wide area of land. Each scintillation detector would basically consist of a scintillator material, material wherein light is produced upon the passage of charged particles, and a photomultiplier tube to detect the generated light. It is common practice to exploit the abundance and promptness of photons in extensive air showers by covering the scintillation detectors with an optimal thickness of lead, wherein shower photons could convert into positron-electron pairs. The measured relative times of arrival of the shower particles at the scintillation detectors are then used to determine the angular direction of the primary particle. The size of the shower, which can be inferred from a measurement of the particle density as a function of distance from the shower core, is used to estimate the energy of the primary particle.

Due to the sparseness of discrete scintillation detectors, air shower arrays sample only a small fraction of the particles which make up an air shower. Air shower arrays, thus, tend to have high energy thresholds, since these arrays are able to detect and reconstruct only large air showers. Typically, traditional air shower arrays have energy thresholds of $\sim 10\ TeV$. Milagrito and its successor, Milagro, overcome this weakness by using water as the medium with which the air shower particles interact. By using this single, continuous medium, both the electron and photon components of extensive air showers could be detected through the generation of Cherenkov light in water. In the case of the photon component, this happens after photons are converted in the water into electron-positron pairs, or after Compton scattering of photons. The combination of using a continuous medium to ultimately produce light from the transit of air shower particles, and the large emission angle of Cherenkov light in water, ensures an efficient sampling of air shower particles by the detector, even if a sparse array of photomultiplier tubes is used to detect the Cherenkov light. Thus, small showers which could not be detected by traditional scintillation air shower arrays could be detected by a water Cherenkov detector, resulting in a lower energy threshold. At small zenith angles ($< 25^o$) and using a 100-tube trigger requirement, Milagrito had an energy threshold of $\sim 300\ GeV$.

Another general class of instruments for detecting extensive air showers consists of air Cherenkov telescopes. These telescopes detect air Cherenkov light produced by the passage of ultrarelativistic shower electrons and positrons in the atmosphere. An air Cherenkov telescope basically consists of mirrors which collect the light and which also focus the light onto a light detector, which usually consists of photomultiplier tubes. The resulting orientation of the imaged air Cherenkov light is used to determine the direction of the primary particle, while the shape of the image is used to discriminate primary gamma-rays from primary cosmic rays. The amount of Cherenkov light produced by an air shower is roughly proportional to the primary particle energy. Air Cherenkov telescopes tend to have better sensitivities, lower energy thresholds, and smaller angular resolutions than traditional air shower arrays. However, Cherenkov telescopes have small fields of view and can operate only during dark, moonless nights. Air shower arrays, Milagrito included, on the other hand, have large fields of view and can operate during the day as well as during the night.

For completeness, mention is made of a fourth method of detecting extensive air showers $-$ the air fluorescence technique. This method detects the scintillation light produced as a result of the excitation of N_2 molecules in the atmosphere by ionizing particles in extensive air showers, and is used to detect the highest-energy cosmic rays, i.e. cosmic rays with energies larger than $100\ PeV$ [69].

Chapter 4

The Milagrito Detector

Milagrito was the first functional detector of extensive air showers utilizing the water Cherenkov technique, which has been a widely used technique in particle physics experiments, mostly found buried deep within the protection of the Earth's rocks, shielded from air showers which are considered sources of noise in these experiments. Milagrito's successful operation was a major step toward establishing the potency of the water Cherenkov technique for purposely detecting and reconstructing such air showers. An antithesis to entombed particle physics detectors, the Milagrito detector was nestled in the beautiful Jemez Mountains of northern New Mexico, at an altitude of 2646 meters, with a grand view of the equally beautiful, smog-free New Mexico skies. Milagrito, which was in operation from February 1997 to May 1998, was a precursor to the bigger Milagro experiment which has been in operation at the same site since February 1999. Being a first of its kind, Milagrito afforded valuable learning opportunities which were essential for understanding this type of detector. This chapter presents details of the Milagrito detector and its performance (see also reference [123]).

4.1 Physical Components of the Milagrito Detector

4.1.1 The water pond The Milagrito water pond was located in the complex of what is now known as the Fenton Hill Observatory. The pond's elevation was 2646 meters, which translates to an atmospheric overburden of 750 g/cm^2, or about 20 radiation lengths. The depth of shower maximum for air showers initiated by TeV gamma-rays is roughly 9 to 13 radiation lengths, so the pond was well below shower maximum, rendering the efficient conversion of air shower particles into Cherenkov radiation by the water medium even more essential.

The reservoir, whose profile is in the shape of a trapezoid, has a bottom which is 50 meters long by 30 meters wide, an aperture at the top which is 80 meters long by 60 meters wide, a depth of 8 meters, and sloping sides. It can hold up to 21 million liters of water. Figures 4.1 and 4.2 are depictions of the pond.

A grid of sand-filled, PVC pipes of 7.5-cm diameter was constructed along the bottom and sides of the pond, such that the pipes intersected to form squares of dimensions 2.8 meters by 2.8 meters. This grid served as the structure to which the photomultiplier tubes (PMTs) were anchored. The PMTs were held down near the bottom of the pond at the corners of the formed squares by 1.6-mm diameter Kevlar strings. Since each encapsulated PMT had a buoyancy of about 10 pounds and was bottom heavy, each PMT floated to an upright position, with its photocathode facing upward, with the addition of water. The string lengths were chosen such that, submerged in water, the crests of the PMTs were all at the same horizontal level to within ~ 1 cm. The geometry of the PVC grid ordered these PMTs into 12 columns and 19 rows, for a total of 228 PMTs deployed in the pond. Figures 4.3 and 4.4 depict the PMT arrangement in the water pond.

During most of Milagrito's lifetime, the water level in the pond was such that there was ~ 1 meter of water above the PMTs' photocathodes. During the latter part of the detector's life, the water level was increased so that there was, first 1.5 meters, then 2.0 meters of water above the PMTs. Since the purpose of the PMTs was to detect Cherenkov light produced by air shower particles traversing the water, it was necessary to make the pond lighttight to prevent any extraneous light from being detected by the PMTs. This was accomplished by covering the pond with a 1-mm thick black material made of two layers of polypropylene with an internal layer of polyester scrim. This was the same material which lined the bottom and sides of the pond. Access into the pond was made possible by inflating the pond cover, using fans to blow clean air into the pond.

Figure 4.1: Aerial view of the Milagrito water pond.

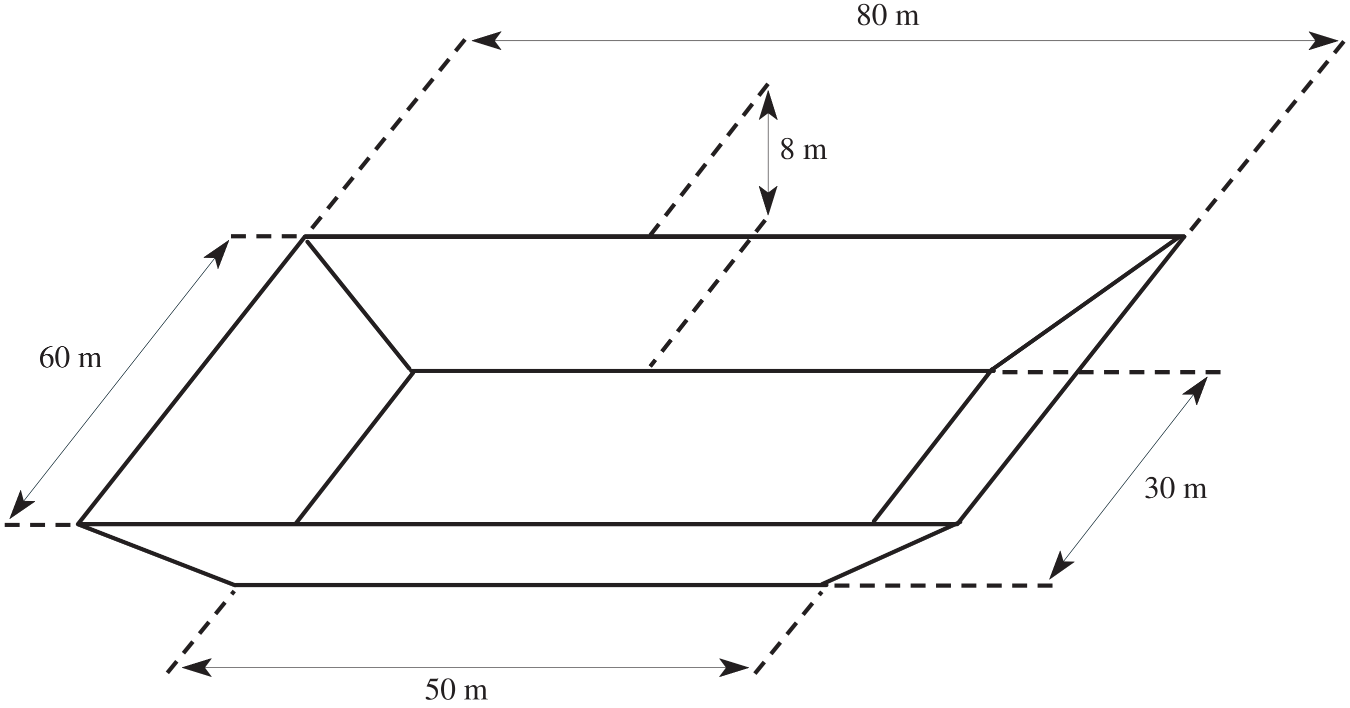

Figure 4.2: Physical dimensions of the water pond. Figure is not to scale.

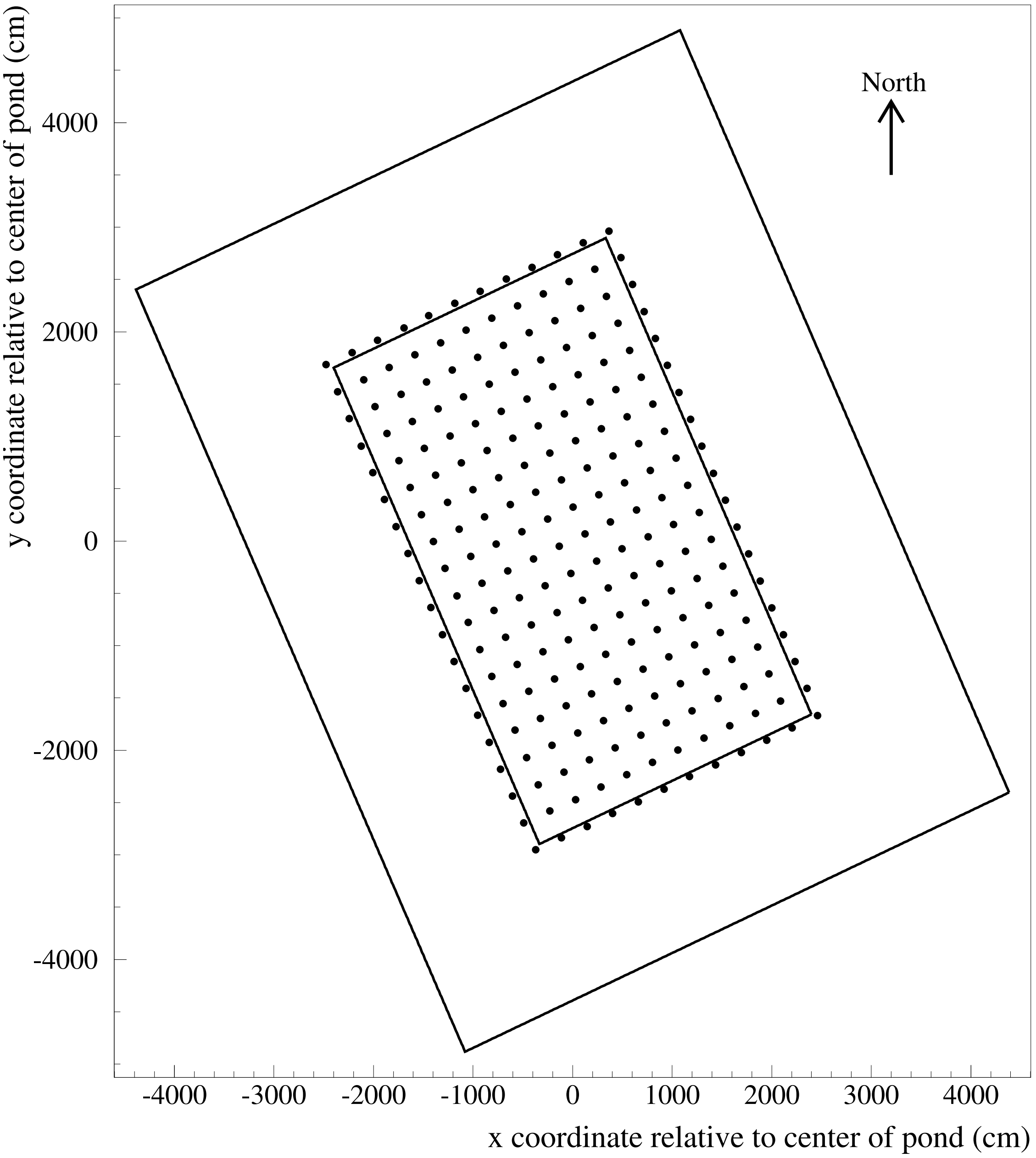

Figure 4.3: Top view of the PMT layout in the Milagrito pond. Each of the 228 dots represents a PMT. The small rectangle delineates the bottom of the pond, and the big rectangle delineates the top of the pond.

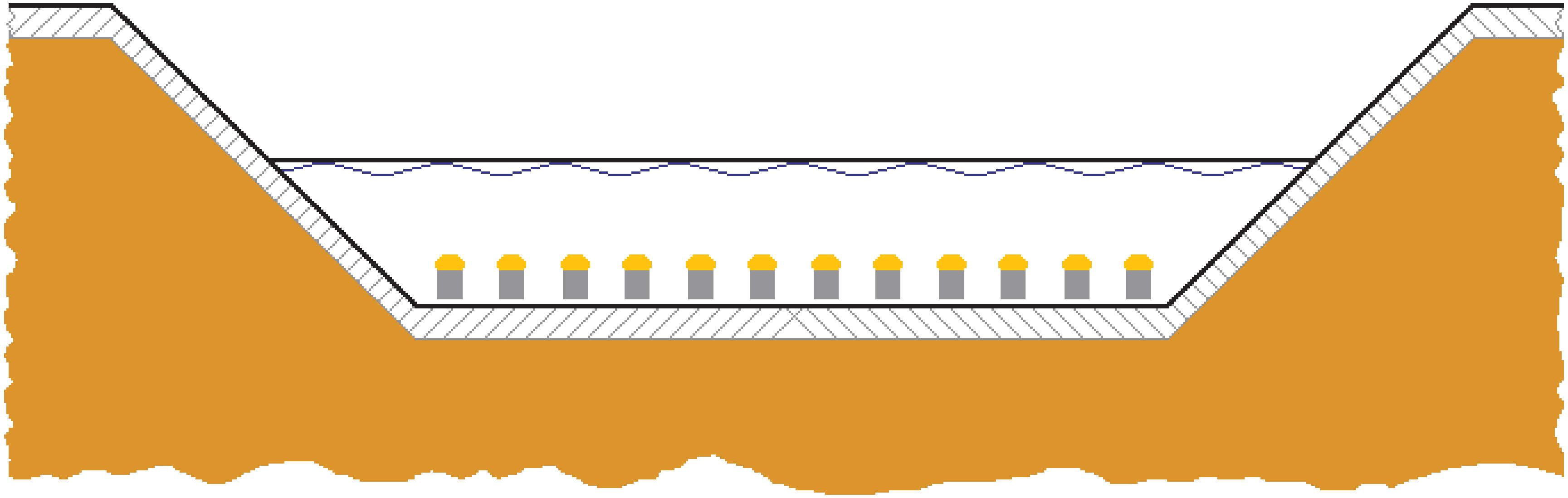

Figure 4.4: Schematic of the Milagrito pond showing three of the important components of the experiment: The PMTs, the water, and the lighttight cover. Figure is not to scale.

The location of the Milagrito experiment placed it at a high risk for being struck by lightning. Thus, it was necessary to construct a lightning protection system around the experiment. The existing lightning protection system is a 12,500 m^2 Faraday cage consisting of a copper wire grid suspended over the water pond and the adjacent auxiliary buildings, and connected to the steel chain link fence surrounding the pond [123].

4.1.2 The photomultiplier tube Milagrito utilized 20.3-cm diameter Hamamatsu PMTs, model R5912. Figure 4.5 shows a schematic of a PMT. A photon incident on the photocathode causes the emission of a photoelectron (PE) into the vacuum tube via the photoelectric effect. The photoelectron is guided toward the dynode assembly through fields set up by focusing electrodes. When this photoelectron hits a dynode, secondary electrons are emitted, which in turn hit the next dynode, causing the emission of more secondary electrons, and so on. The dynodes are at different potentials supplied by a voltage divider. Through this process, an effective multiplication of the number of electrons takes place. The electrons are then collected at the anode where an output current is produced. This particular type of PMT has a 10-stage dynode structure and a gain of $\sim 10^7$, i.e. 10^7 electrons of output at the anode per photoelectron produced at the photocathode.

This PMT model is sensitive to 300 to 650 nm light, with the peak sensitivity occurring at 420 nm. It's quantum efficiency, i.e. the ratio of the number of photoelectrons produced to the number of photons incident on the photocathode, is 20 to 25 percent at 325 to 450 nm, and decreases sharply outside this wavelength range. The anode signal rise time is ~ 4 ns, and the electron transit time, which is the time interval between the time a photon is incident on the photocathode to the time the anode signal reaches its maximum amplitude, is ~ 55 ns [124].

Acceptance testing of the PMTs used in Milagrito confirmed further characteristics of this type of PMT. For these tests, a detection threshold voltage of 1/4 to 1/3 of a single-PE signal amplitude was used. These characteristics are:

operating voltage: The anode to cathode operating voltages of the PMTs ranged

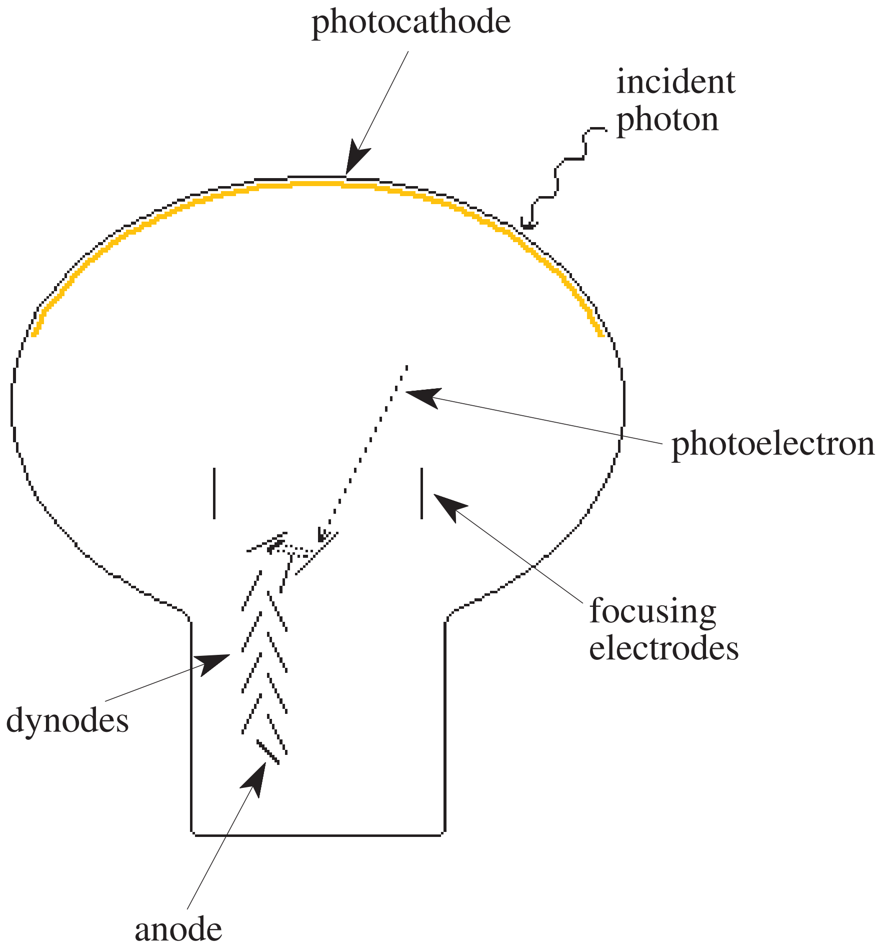

Figure 4.5: Schematic of a photomultiplier tube.

from 1375 V to 2100 V, with 1720 V being the average.

anode dark current rate: Even in the absence of visible light, anode current is produced by a PMT. This so-called dark current is caused by the thermionic emission of electrons from the photocathode and the dynodes. Thermionic electrons from the photocathode and, to a lesser degree, those from the dynodes are multiplied by the dynodes and result in anode dark signals. After dark-adapting the PMTs for ~ 8 hours, the dark signal rate from the PMTs was about 1 to 2 kHz on the average.

single-PE transit time spread: The transit time spread (TTS) is the width of the electron transit time distribution, and is dependent on the light intensity incident on the photocathode. The TTS resulting from a single-PE light intensity incident on the photocathode, that is, incident light intensity which caused single-PE emission from the photocathode, was 2.7 ns on the average.

50-PE transit time spread: The TTS resulting from a 50-PE light intensity incident on the photocathode was 0.65 ns on the average.

single-PE prepulsing: Prepulses are thought to be caused by light directly hitting the first dynode, thereby resulting in an anode signal which precedes the main anode signal which is induced by photoecletrons. A prepulse occurs about 4 ns to 20 ns before the main pulse. The incidence of prepulses, i.e. the ratio of the number of main signal events accompanied by a prepulse to the total number of main signal events, resulting from a single-PE incident light intensity was 0.2 to 0.3 percent on the average.

50-PE prepulsing: The incidence of prepulses resulting from a 50-PE incident light intensity was 0.2 to 0.6 percent on the average. Much larger light intensities should result in an increase in the incidence of prepulses.

late pulsing: Late pulses are believed to be caused by single electrons reflecting off the first dynode and then being guided by the field back into the dynode structure, producing the late signals. A late pulse occurs about 8 ns to 60 ns after the main pulse. The incidence of late pulses resulting from a single-PE incident light intensity was 5.5% on the average.

afterpulsing: Afterpulses are thought to be caused by residual gas molecules in the tube being ionized by photoelectrons, and subsequently hitting the photocathode, thereby causing the emission of electrons. An afterpulse occurs about 100 ns to 16 μs after the main pulse. The incidence of afterpulses resulting from a single-PE incident light intensity was 6% on the average.

peak-to-valley ratio: The peak-to-valley ratio refers to the height of the peak of the single-PE ADC distribution relative to the height of the valley separating the single-PE ADC distribution from the ADC pedestal. It is a measure of how well a PMT is able to resolve single electrons from the photocathode from dynode noise or dark current. The peak-to-valley ratio of the PMTs was 3.0 on the average.

saturation: It is desirable that the anode signal varies linearly with the light intensity incident on the photocathode. For the PMTs used, the anode signal was linear as a function of incident light intensity up to a light level corresponding to ~ 75 PEs. For larger light levels, the anode signal was smaller than that prescribed by a linear response, and the PMT signal was said to saturate.

Overall, the characteristics of this type of PMT was well-suited for the application of indirectly detecting air shower particles and reconstructing primary particle directions using relative times of arrival of Cherenkov light at the PMTs.

The voltage divider circuit connected to the base of each PMT was shielded from the water by encapsulating the lower part of each PMT in a PVC housing. The PMT was sealed to the PVC housing using RTV silicone rubber (Dow Corning). The height of each encapsulated PMT was ~ 35.6 cm. A coaxial bulkhead connector was secured into an aperture in the PVC housing in a watertight manner. The voltage divider circuit was connected to the part of the coaxial connector which was inside the housing, and an RG59 coaxial cable, which had a matching coaxial connector at its end, was connected to the part which was outside the housing. When connected together, the coaxial connector pair was watertight.

4.1.3 The water Water for the Milagrito experiment was provided by a fresh water well located at the site of the experiment. It is plain that an experiment of this nature requires very clean water. This kind of water was approximated by recirculating the pond water and filtering it at each cycle using a carbon filter, a 1-μm filter, a UV lamp, and a 0.2-μm filter. The water was recirculated at a rate of 725 liters/min. Water from the fresh water well also went through a media filter and a water softenener during the filling stages of the pond. The pond was filled at a rate of 300 liters/min. The result of this purification effort was an attenuation length in the water of 5 meters, on the average, for 350-nm wavelength light.

The amount of water in the pond varied from 3×10^6 liters to 4.4×10^6 liters,

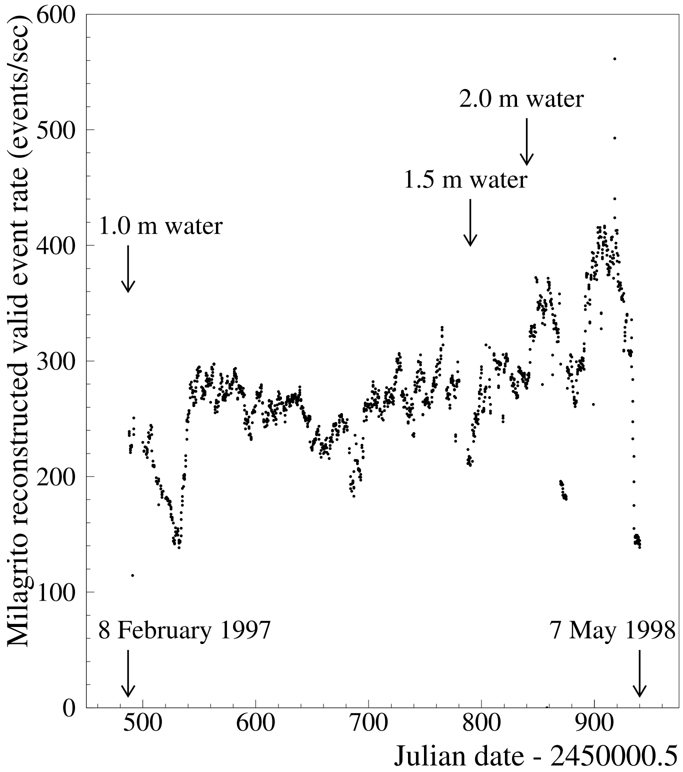

Figure 4.6: Variation of Milagrito daily reconstructed valid event rate over time.

corresponding to 1.0 meter to 2.0 meters of water above the PMT photocathodes. For much of Milagrito's lifetime, the water level was 1.0 meter above the PMTs. Figure 4.6 is a plot of Milagrito daily reconstructed valid event rate as a function of Julian date. Indicated in this plot are the dates of the commencement of the addition of water to the pond to increase the water level to, first 1.5 meters, then 2.0 meters above the PMTs. The increase in event rate after these dates is apparent.

4.1.4 The electronics Figure 4.7 is a schematic of the electronics logic used in Milagrito for one PMT channel. When a PMT is hit by Cherenkov light, causing the emission of photoelectrons from the photocathode, the anode signal is sent to a high gain amplifier and to a low gain amplifier. The output from the high gain amplifier is sent to a discriminator whose threshold is set to $\sim 1/4$ of a single-PE amplitude. If the amplified signal crosses the discriminator threshold, the discriminator generates a pulse whose width reflects the time width of the amplified signal at the discriminator threshold. This time width is called the low *time-over-threshold (TOT)* of the signal, and the leading edge of the pulse is called the low *start time* of the signal (labeled "1" in Fig. 4.7). Figure 4.8 illustrates the definitions of TOT and start time. The output from the low gain amplifier is sent to another discriminator whose threshold is set to ~ 7 PEs. Similarly, if the amplified signal crosses this high threshold, the discriminator generates a pulse whose width reflects the amplified signal's high TOT and whose leading edge is the high start time of the pulse (labeled "3" in Fig. 4.7).

The TOT values, low threshold and high threshold, are used as measures of the anode signal's size, i.e. large TOT values indicate correspondingly large numbers of PEs emitted from a PMTs photocathode. Anode signals which correspond to PEs larger than $\sim 1/4$ PE cross the low discriminator threshold, and anode signals which correspond to PEs larger than ~ 7 PEs cross both the low and high discriminator thresholds. The implementation of the high discriminator threshold, in addition to the low threshold, and the high TOT was necessary because at sufficiently large PEs, the incidence of prepulsing increases and affects the low TOT value as well as the low start time. The high threshold was also necessary to ensure that a measure of the anode signal size would be available even for those signals which were large enough to saturate the high gain amplifier.

The output from the low threshold discriminator and the output from the high threshold discriminater, if any, are then summed to form a single signal with TOT and start time information. This signal is sent to a common stop TDC which digitizes the time edges.

Meanwhile, the analog signal from the low gain amplifier is delayed and then sent to an ADC which digitizes the amount of charge in the anode signal.

A shower event is said to *trigger* Milagrito if at least 100 PMTs each gives rise to an anode signal which crosses the low threshold discriminator, all occurring within a 300-ns time window. This is implemented in the electronics by the generation of a 25-mV, 300-ns pulse for each PMT signal which crosses the low threshold discriminator. The sum of the 25-mV pulses occurring within 300 ns of the first PMT signal is then sent to a discriminator with a threshold corresponding to 100 PMTs being hit by Cherenkov light. If the sum of the pulses crosses this threshold, a trigger pulse is sent to memory boards and data acquisition computers, together with the TDC and ADC output from the other PMT channels which register Cherenkov light hits. A GPS clock is used to put a time stamp on an event which triggers Milagrito.

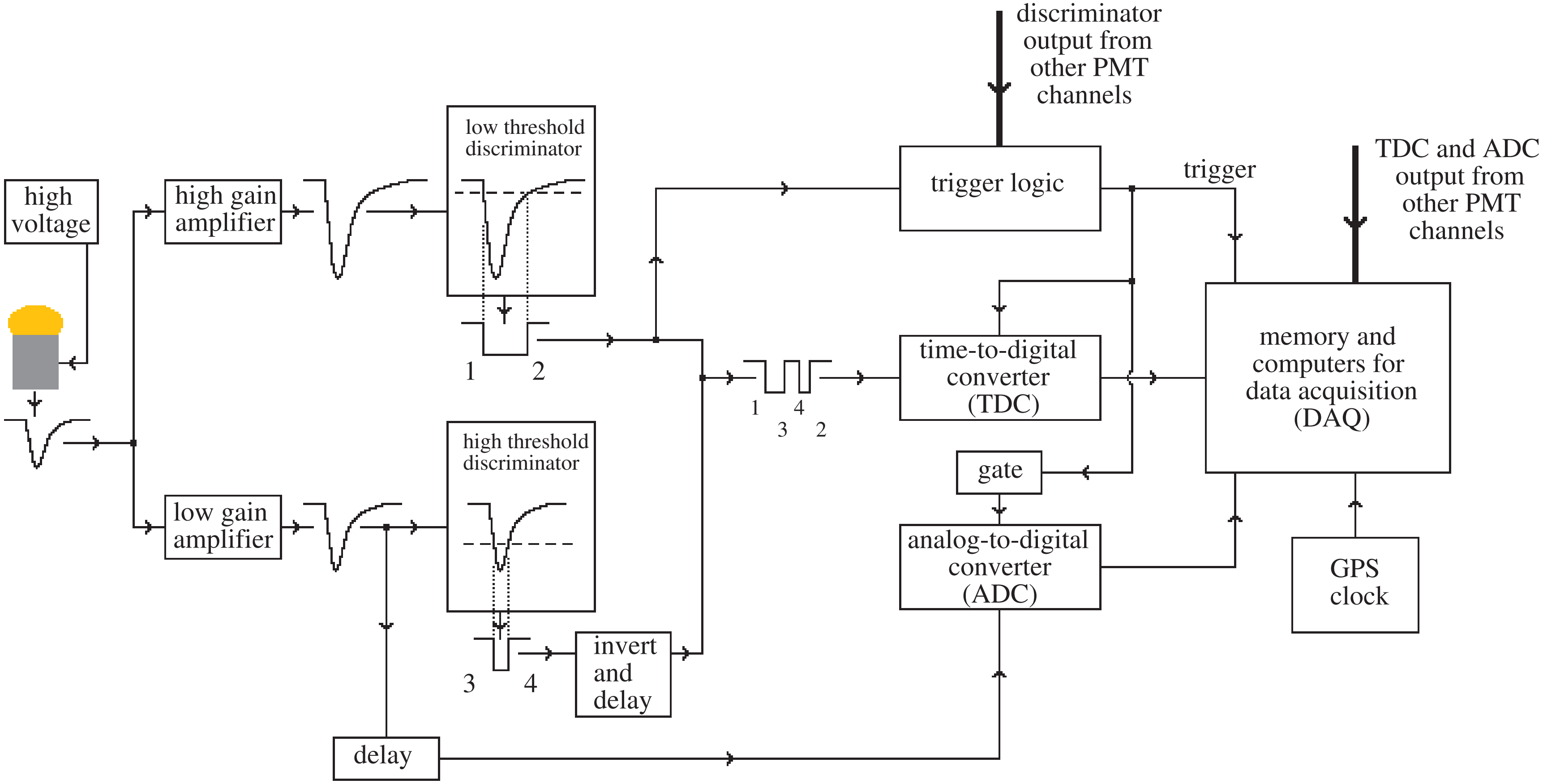

Figure 4.7: Schematic of electronics logic used in Milagrito.

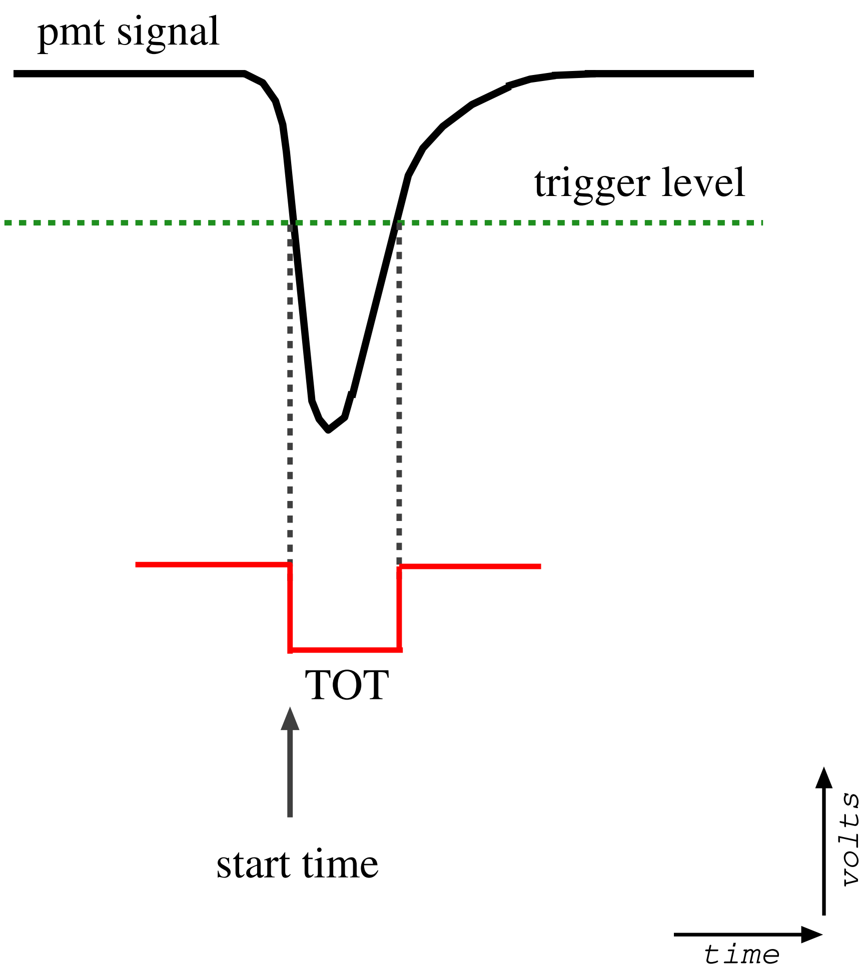

Figure 4.8: Definitions of time-over-threshold (TOT) and start time.

4.2 Reconstructing Air Showers Using the Milagrito Detector

Experiments which are built to indirectly detect primary gamma-rays or cosmic rays incident on the Earth's atmosphere, through detecting the secondary shower particles which are subsequently generated, are ultimately faced with the task of determining the direction from which a primary particle came, and the primary particle's energy. The process through which this task is accomplished is called *reconstructing* the air shower. Knowledge of the general characteristics of extensive air showers, as discussed in Chapter 3, is essential in reconstructing the air shower events detected by Milagrito. Furthermore, knowledge of Milagrito's response to the secondary air shower particles, of Milagrito's inherent limitations, and of the behavior of shower particles and Cherenkov light in the water, is important for qualitatively understanding how well Milagrito determines the reconstructed parameters. The term "*detector response*", as used in this work, basically refers to the effect of having discrete PMT detectors, each with a finite size, to *sample* the secondary air shower particles through the detection of the Cherenkov light produced in water. It is important to know, for example, that Milagrito is efficient at detecting both the electron and photon components, and both the low energy and high energy components of an air shower. Such *sampling* characteristics of the detector directly affect the quality of the reconstructed parameters. A detector's response to secondary particles will also be responsible for the measured characteristics of an air shower – such as the shape of the shower front and the lateral distribution of the shower particle density – looking different from the picture that computer simulations paint.

Among Milagrito's inherent limitations, the most limiting is this: Milagrito cannot determine the location of shower cores which land outside the pond, and it cannot distinguish between cores which land inside the pond and those which land outside the pond. This limitation is a direct consequence of the fact that the physical size of Milagrito is much smaller than the size of air showers, at Milagrito's altitude, initiated by TeV primaries. By the time a TeV-inititated air shower has developed down to Milagrito's depth, the size of the air shower can be four to ten times the size of Milagrito.

Just how limiting a large uncertainty in the shower core position is in reconstructing air shower parameters can be gleaned by considering that an air shower's characteristics – the shape of the shower front, the lateral distribution of the shower particles, the average time delay of late particles relative to the shower front – whether measured or simulated, are all functionally dependent on the distance from the shower core. The shower core limitation most especially impedes any attempt to infer the lateral distribution of particles in an observed air shower. It is almost impossible to determine this distribution without proper knowledge of the shower core location. As a result, the size of the shower and, therefore, the energy of the initiating primary particle, cannot be determined with Milagrito.

Fortunately, Milagrito's efficiency at detecting the photon component and the high-energy secondaries in an air shower, and the PMTs' good timing resolution, make possible the estimation of a primary particle's direction even without an accurate knowledge of the core position. This will be seen in the paragraphs that follow.

4.2.1 Reconstructing the primary particle direction In the Milagrito experiment, the direction of an initiating primary particle was reconstructed by utilizing the relative times of arrival of water Cherenkov light at the PMTs. This is sketched in Fig. 4.9. The figure shows the slope of the relative arrival time as a function of PMT position reflecting the slope of a planar shower front which is perpendicular to the direction of the primary particle direction. However, before the arrival times can be used for this purpose of determining the primary particle direction, some corrections have to be made to the measured raw arrival times. The origin of these corrections can be grouped into two:

(a) time corrections resulting from the characteristics of the air shower, coupled with the detector response; and,

(b) time corrections stemming from the experimental hardware: the PMTs, the cables, and the electronics.

This subsection will deal with item (a), and the next subsection, which discusses the calibration of Milagrito, will deal with item (b).

As discussed in Chapter 3, the shape of a shower front is parabolic, and is said to have a curvature. This front is defined by those secondary particles which lead, or are in front of, the other particles at a given lateral distance from the shower core. Since these leading, or prompt, particles are those secondaries with the highest energies, the shower front is defined by the high-energy secondary particles. It was also noted that the large emission angle of Cherenkov radiation in water assures the efficient sampling of air shower particles by Milagrito, even with the discreteness and finite size of the PMTs. Nevertheless, the PMTs will not always sample the prompt secondaries which make up the shower front. As a result, the effective shower curvature measured by Milagrito will not necessarily be the same as the shower front curvature given by particle times derived directly from air shower simulations.

When these simulated air showers were reconstructed by a simulated Milagrito detector, it was determined that the effective shower curvature measured by the simulated Milagrito was ~ 0.04 ns/m [123]. This quantity gives the slope of the line plotting the average earliest secondary particle time detected by Milagrito as a function of distance from the shower core.

In Milagrito, the location of the shower core was estimated by averaging the coordinates of the PMTs which registered the largest number of photoelectrons among the PMTs hit, using the registered number of photoelectrons as weights. This procedure resulted in core positions which were always inside the pond, regardless of the true location of the real core. Because the location of the shower core was not well determined when using real shower data, shower curvature was not apparent in the real data. Nevertheless, a time correction of 0.04 ns per meter from the reconstructed shower core was applied to the raw arrival times because simulations show that the angular resolution improves with the use of this correction [123].

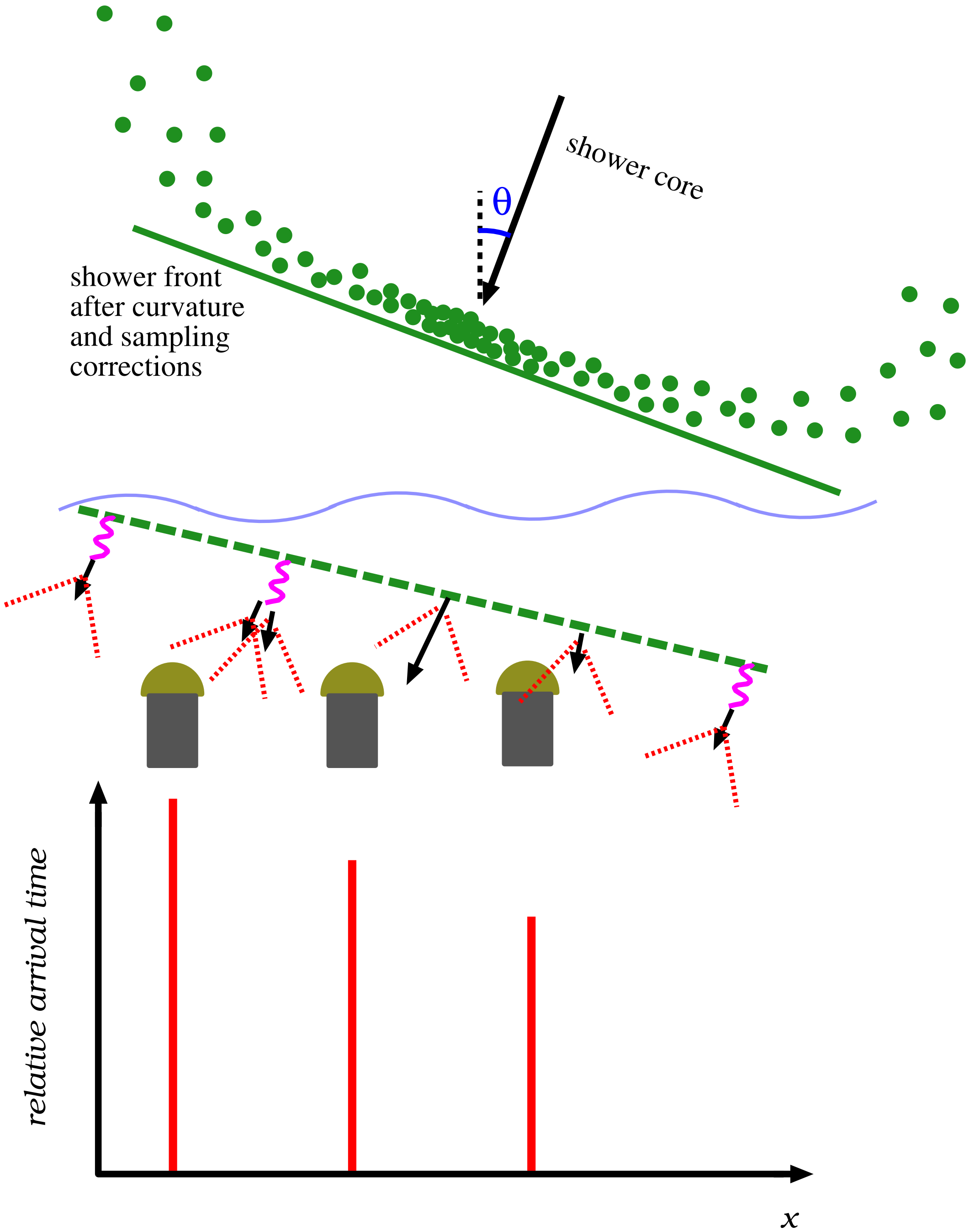

Figure 4.9: Reconstructing a primary particle direction.

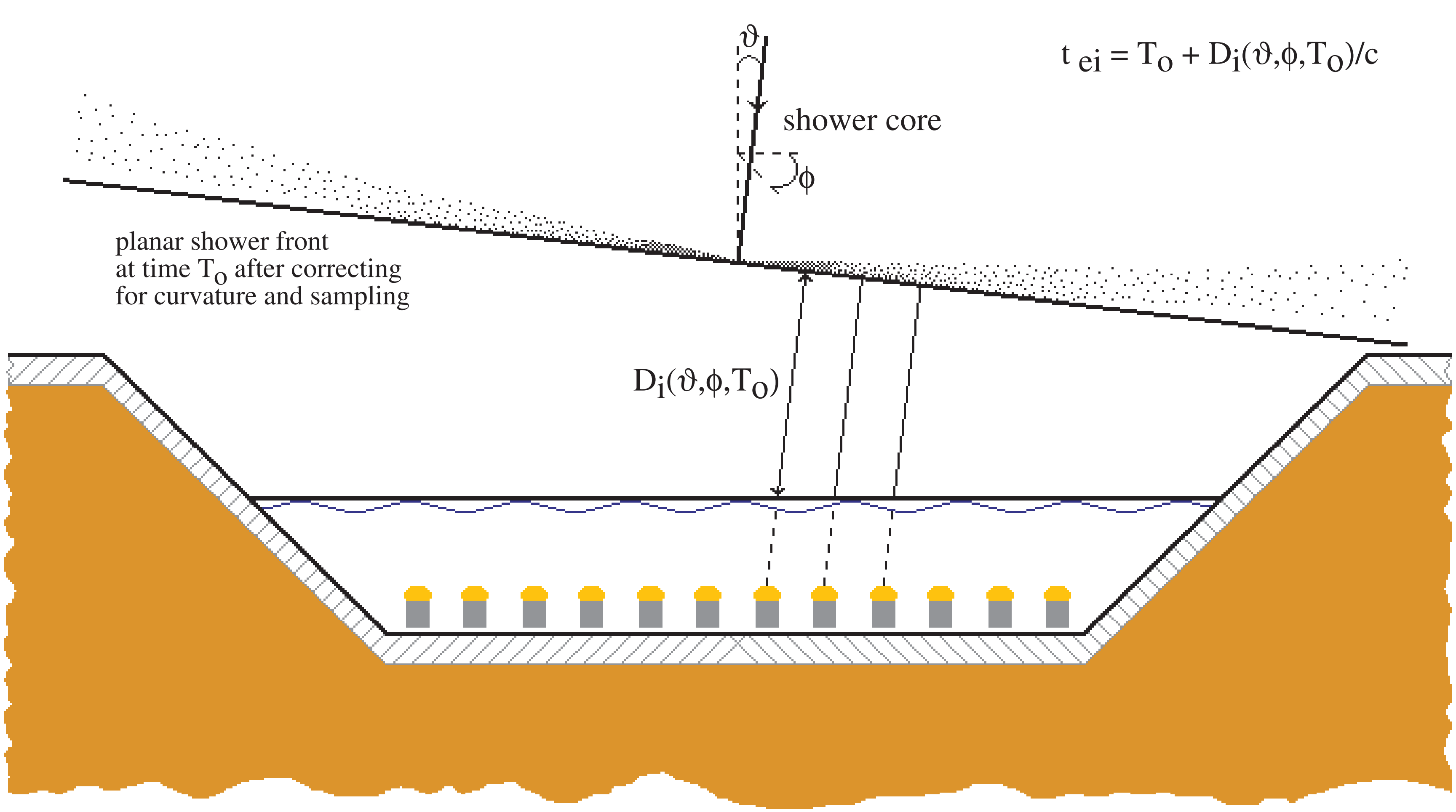

Figure 4.10: Sketch depicting how a primary particle direction is reconstructed. The difference between the expected time of arrival, t_{ei}, and measured time of arrival of Cherenkov light at each PMT hit is used in a χ^2 minimization algorithm to estimate the unknown parameters θ, ϕ, and T_o.

Another correction which was applied to the raw arrival times had its origin in the observation that for air showers initiated by primaries coming from zenith, PMTs hit which registered large numbers of PEs also registered, on the average, earlier times of arrival than those PMTs hit which registered small numbers of PEs. These time corrections are therefore pulse height dependent. This observed dependence of arrival time on pulse height or number of PEs registered, is most probably caused by each PMT sampling a different part of the shower thickness. Portions of the air shower which are less dense are composed of late particles, and hence PMTs which sample this portion of the shower will register arrival times which are late compared to the times which are registered by PMTs sampling a denser portion of the shower.

After estimating the core location and correcting the raw arrival times for shower curvature and pulse height dependence, the corrected arrival times of light at the PMTs and the positions of the PMTs were used to reconstruct a planar shower front as follows: The expected time of arrival, t_{ei}, of light at each PMT is given by (see Fig. 4.10),

$$t_{ei} = T_o + \frac{D_i(\theta, \phi, T_o)}{c} \quad , \tag{4.1}$$

where T_o is a time offset common to all the PMTs hit, (θ, ϕ) are the unknown angular coordinates which give the arrival direction of the primary particle, $D_i(\theta, \phi, T_o)$ is the distance from the planar shower front, which is normal to the vector defined by (θ, ϕ), to the surface of the water at time T_o, measured along a line perpendicular to the planar shower front and connecting the shower front to the i_{th} PMT hit. The difference between the corrected measured arrival time, t_{mi}, and the expected arrival time of light at each PMT is then used in a chi-square minimization algorithm in order to estimate the unknown parameters θ, ϕ, and T_o,

$$\chi^2 = \sum_{i=1}^{N_{hit}} \left(\frac{t_{mi} - t_{ei}(\theta, \phi, T_o)}{\sigma_i} \right)^2 \quad , \tag{4.2}$$

where the sum is over all the PMTs hit by Cherenkov light. The uncertainty, σ_i, in the measured arrival time is pulse height dependent and is derived from the study of the pulse height dependence of arrival times explained above. The smaller the pulse height registered by a PMT, the larger the uncertainty assigned to the arrival time that PMT registered.

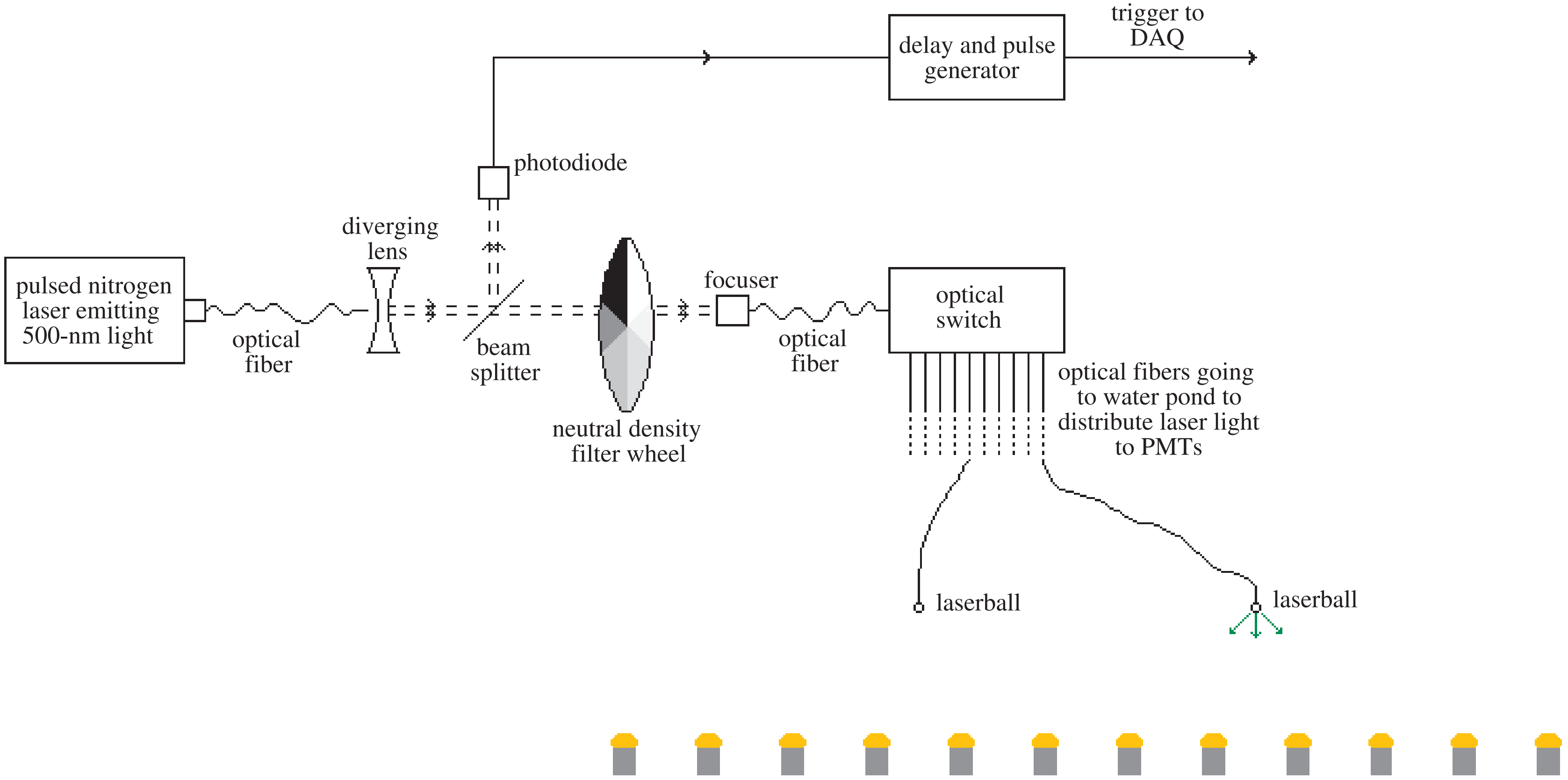

Figure 4.11: Schematic of calibration setup.

4.2.2 Calibration of the Milagrito detector Before reconstruction of the air shower events triggering Milagrito could be done, it was necessary to calibrate the Milagrito detector. The purpose of the calibration procedure was to determine the following quantities for each PMT:

(a) the amount of time slewing as a function of anode pulse size;

(b) the transition threshold for the high TOT;

(c) the time offset or pedestal contributed by the PMT, the cables, and the electronics;

(d) the number of PEs corresponding to a given anode pulse size.

These will be discussed in turn in the paragraphs that follow.

A schamatic of the equipment used in calibrating Milagrito is shown in Fig. 4.11. A pulsed nitrogen laser served as a source of 500-nm (green) light. This light was incident on a beam splitter so that half of the light intensity was available for distribution to the PMTs in the pond. The light was distributed to the PMTs through a bank of ten optical fibers running from the calibration setup to the water pond. The laser light could be diverted to any one of these ten fibers by means of an optical switch. At the end of each fiber was a small bead of epoxy, nicknamed a *laserball*, whose purpose was to diffuse the laser light so that the emitted light was approximately isotropic. The ten laserballs were more or less located at regular intervals at the water surface.

The amount of light emitted from each laserball was regulated by means of a neutral density filter wheel whose transmission property ranged from completely opaque to completely transparent. The logarithm of the relative transmittance, i.e. the relative optical density, between these two extremes of the filter wheel was 4.0. As a result, the amount of light to which the PMTs were exposed could be varied from a light intensity effecting single-PE signals, to a light intensity effecting thousands of PEs. During data-taking for calibration purposes, the laser, which generatad light pulses at a rate of ~ 20 Hz, was fired ~ 4000 times at each of 12 different filter wheel optical densities, ensuring enough statistics for a wide range of light intensities delivered to the PMTs. The PMT signals generated as a result of the detection of laser light then went through the same electronics scheme presented in Section 4.1.4.

The other half of the laser light coming from the beam splitter was directed to a photodiode. The photodiode signal was then sent to a pulse and delay generator which generated a trigger signal for the data acquisition system. Each time a trigger was generated, TDC information from the different PMT channels were recorded by the DAQ system. These information were then processed offline to determine the quantities (a), (b), and (c) listed above.

(a) Slewing

PMT signals generated at the same time but which are of different sizes cross a discriminator threshold at different times, resulting in different start times. This pulse size dependence of the start time is referred to as time *slewing*. This effect is caused by the electronics and by the PMTs themselves, and the amount of time slewing as a function of pulse size is slightly different for each PMT. Figure 4.12 shows the ideal but unrealistic case where no slewing is present. In this case, anode pulses crossing the discriminator threshold will have the same start times (vertical line in the figure) even when the pulse sizes are different, and thus the start times will reflect a horizontal shower front. Figure 4.13 shows what happens in the real world. The small pulses tend to have delayed start times relative to the start times of the large pulses. A proper reconstruction of the primary particle direction requires taking into account the time offset introduced by slewing.

Figure 4.14 shows the variation of the low start time as a function of the low TOT width for four PMTs, as derived from laser light data. Note that the TDCs used in Milagrito employed a common stop, so a larger y-axis number in the plots indicates an earlier start time. The start times shown are relative to an arbitrary time which is the same for all the PMTs. As mentioned in Section 4.1.4, the TOT value is a measure of a PMT anode

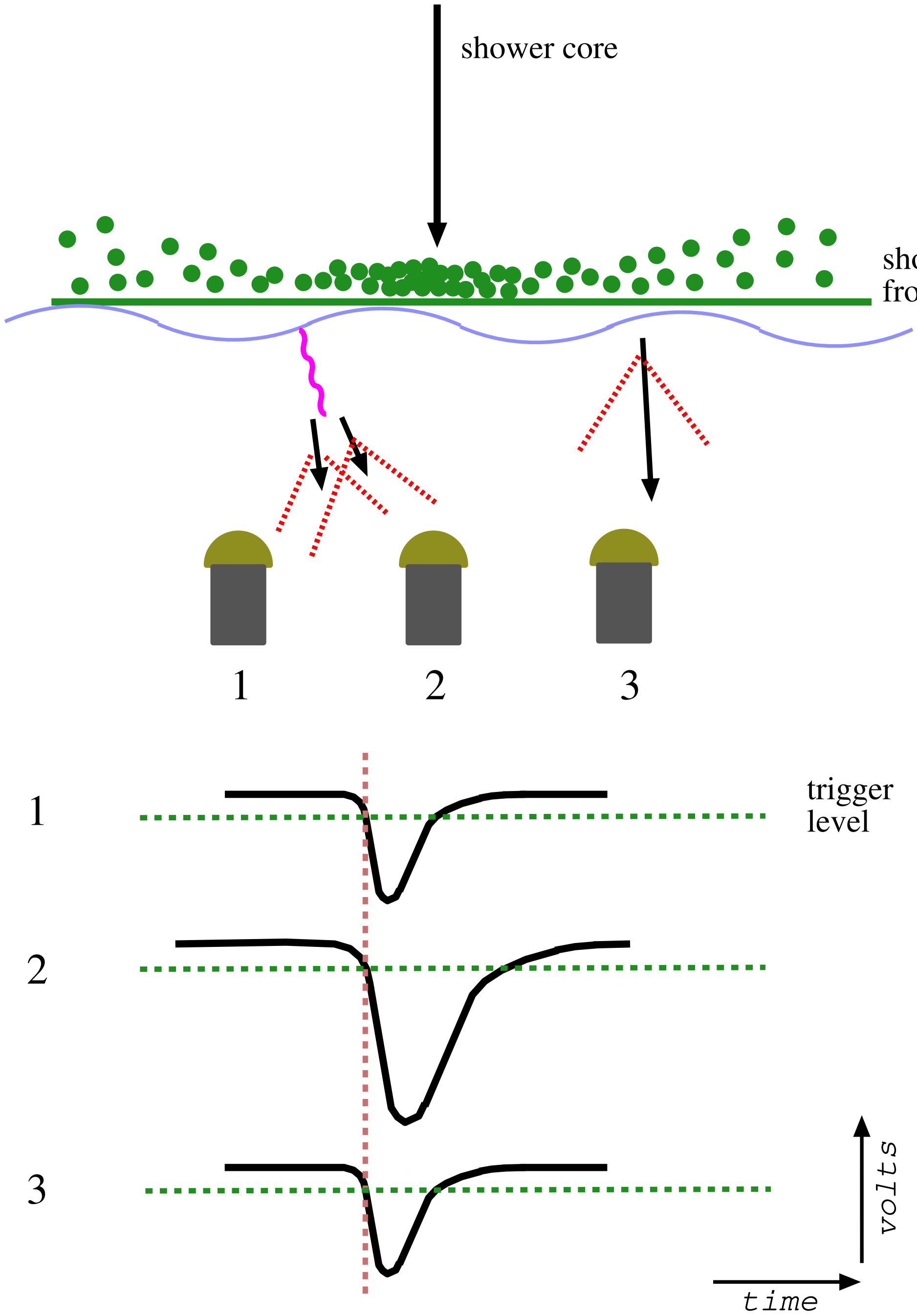

Figure 4.12: No slewing.

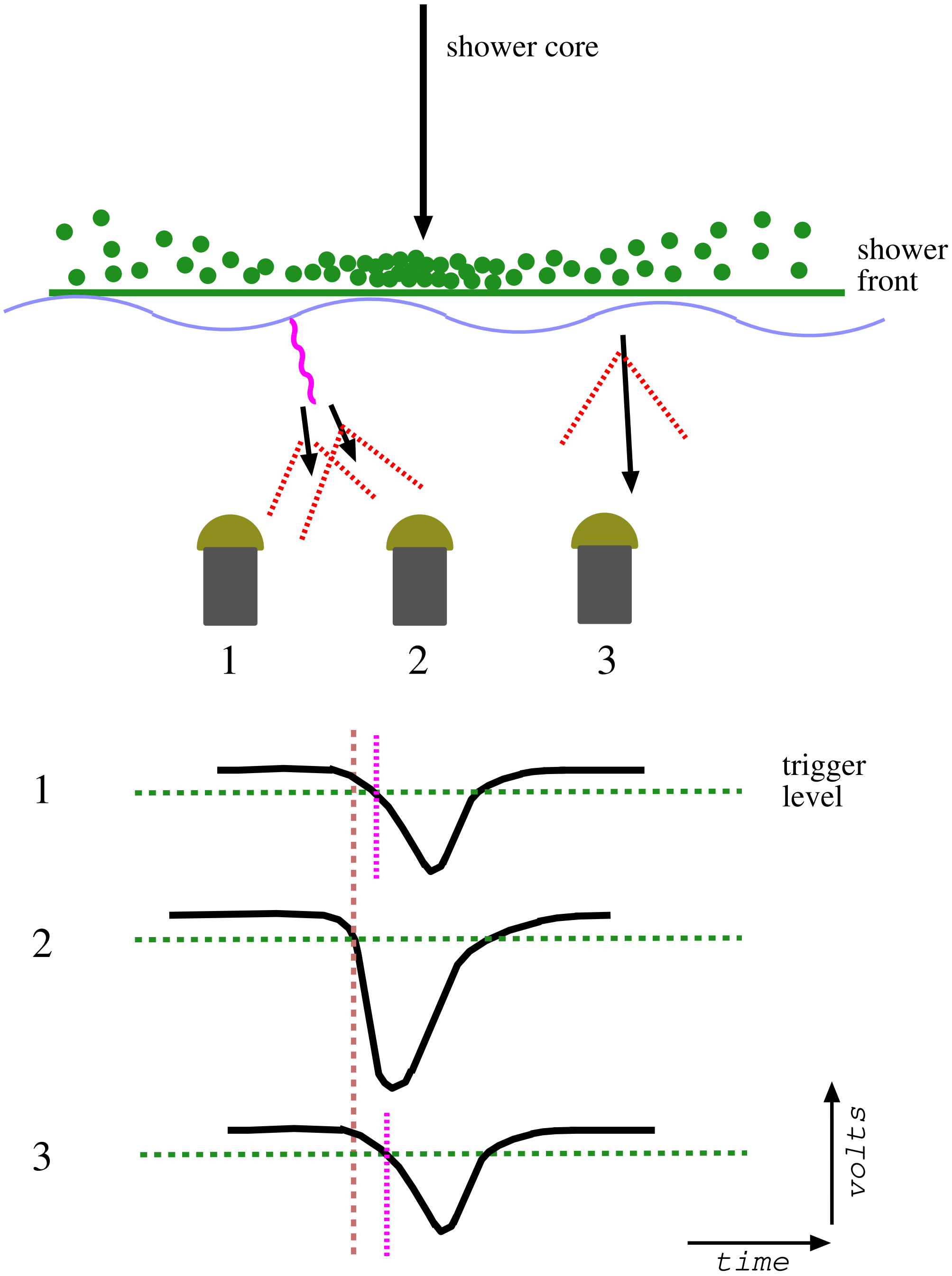

Figure 4.13: Slewing.

signal's size. The range of PEs corresponding to the low TOT range shown in the plots is also indicated for each PMT. As can be seen from the plots, the amount of slewing varies slightly from PMT to PMT, but the start time generally becomes earlier by roughly 3 to 7 ns per 10-PE increase in the number of PEs.

Similarly, Fig. 4.15 shows the variation of the low start time as a function of high TOT for the same four PMTs. Again, the amount of slewing varies slightly from PMT to PMT, but the start time generally becomes earlier by $\lesssim 1$ ns per 100 PE increase in the number of PEs.

(b) Transition threshold for high TOT

Another quantity which had to be determined for each PMT, using data derived from the use of laser light, was the transition threshold for the high TOT, i.e. the value of the high TOT at which the high start time should be used, instead of the low start time, for reconstruction purposes. As noted in Section 4.1.4, the high TOT was implemented because when large light intensities are incident on a PMT, the resulting increase in the incidence of prepulsing affects the low TOT values and the low start times. Large light intensities also lead to saturation of the high gain amplifier and, therefore, of the low TOT values.

The transition threshold for the high TOT for each PMT was determined by examining the widths of the low start time and high start time distributions as a function of laser light level, which could be represented by the high TOT value. Distributions of low start time and high start time for different values of the high TOT for one particular PMT are shown in Fig. 4.16. The high TOT value at which the width of the high start time distribution gets as good as, or better than, the width of the low start time distribution, was selected as the transition high TOT. Thus, whenever the high TOT of a PMT signal which was induced by air shower particles was equal to or larger than the predetermined transition high TOT for that PMT, the corresponding low start time was not used for reconstruction

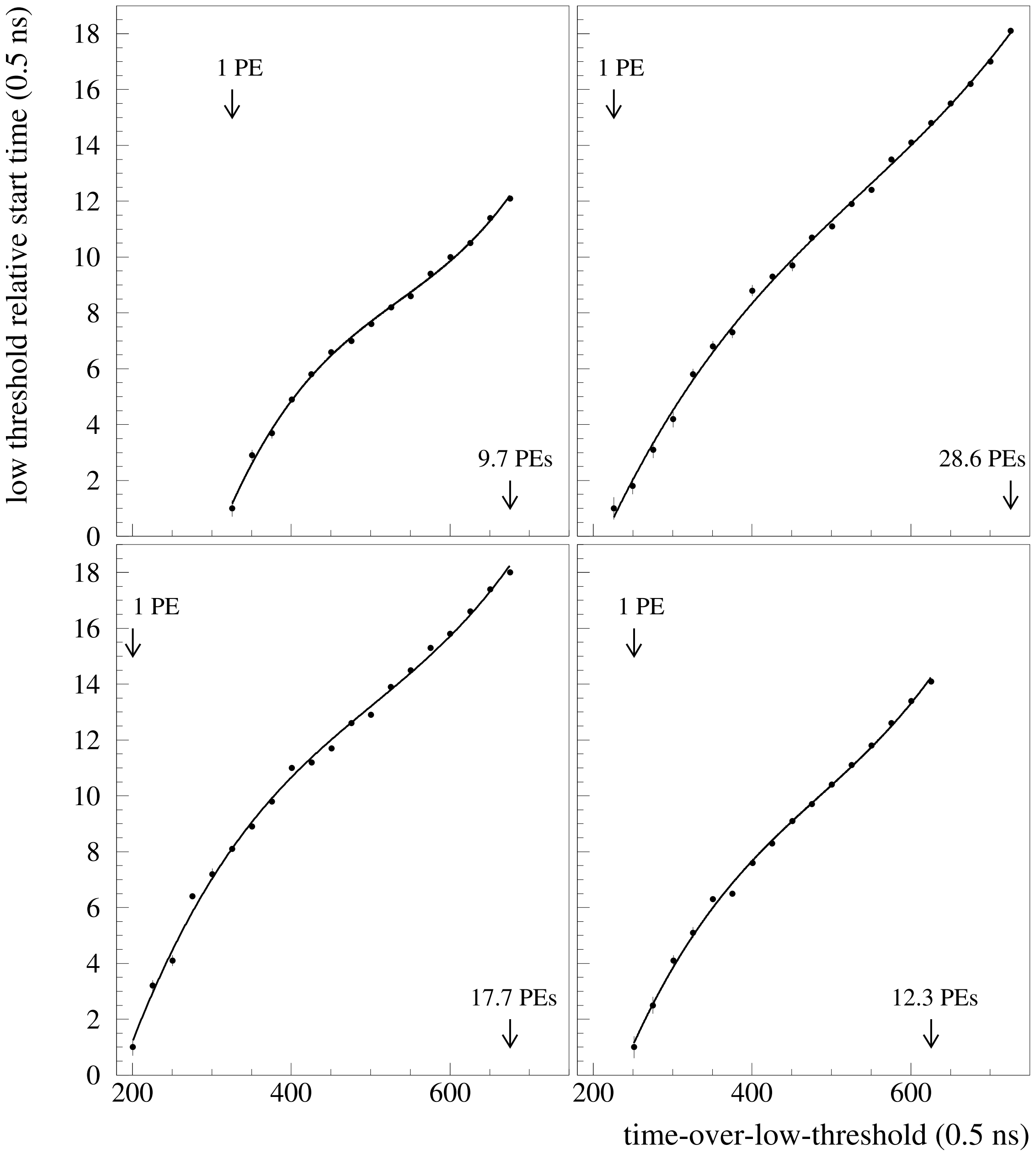

Figure 4.14: Low TOT slewing curves of four PMTs. The dots are data using laser light, the lines are fitted polynomials. To make the y-axis uniform for the four plots, the low start for each curve was shifted by an amount such that the four curves started at the same point on the y-axis. Also shown for each PMT is the range of PEs corresponding to the range of low TOT values shown in the plots.

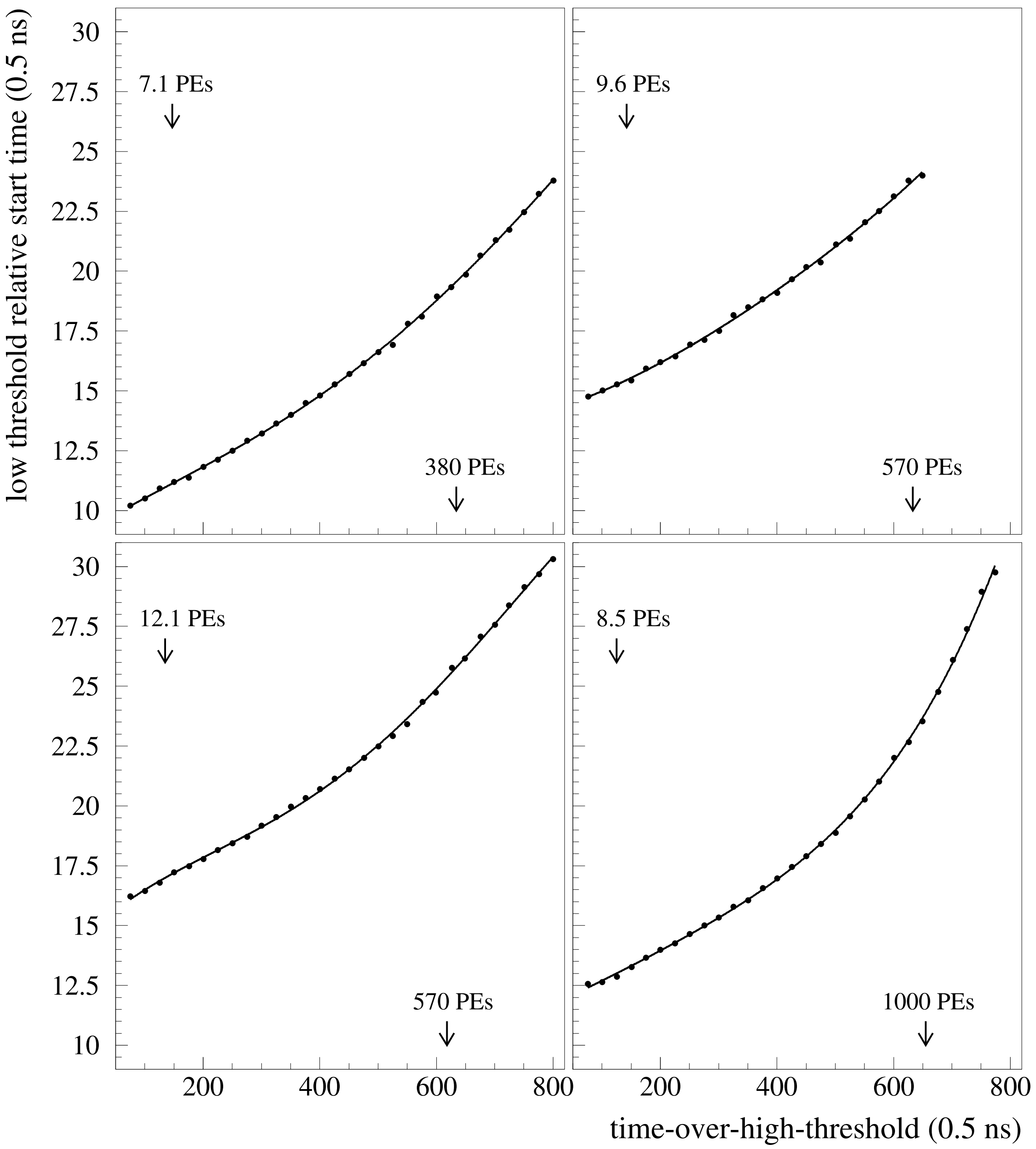

Figure 4.15: High TOT slewing curves of four PMTs. The dots are data using laser light, the lines are fitted polynomials. The y-axis is an extension of the y-axis of the low TOT slewing curves in Fig. 4.14. The PEs corresponding to the high TOT values are also shown for each PMT.

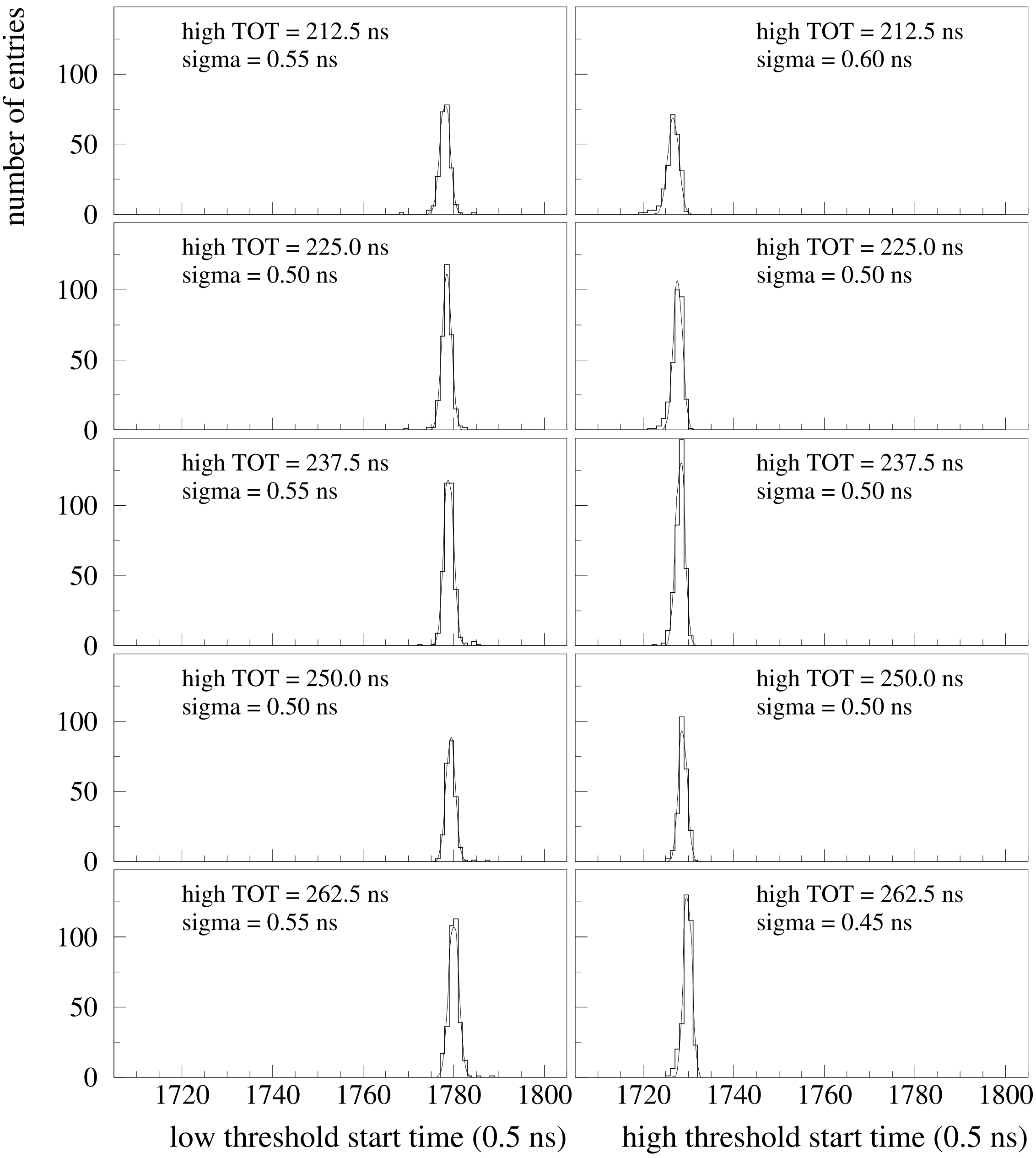

Figure 4.16: Low and high start time distributions and Gaussian fits for different values of the time-over-high-threshold for one of the PMTs. The plot shows that as the high TOT value increases, the width of the high start time distribution eventually gets as good as, or better than, the width of the low start time distribution. At the value of the high TOT at which the high start width becomes comparable to the low start width – 225.0 ns in the case of this PMT – the measured high start of a PMT output signal is chosen for reconstruction purposes to ensure that prepulsing will not affect the reconstruction of a shower event.

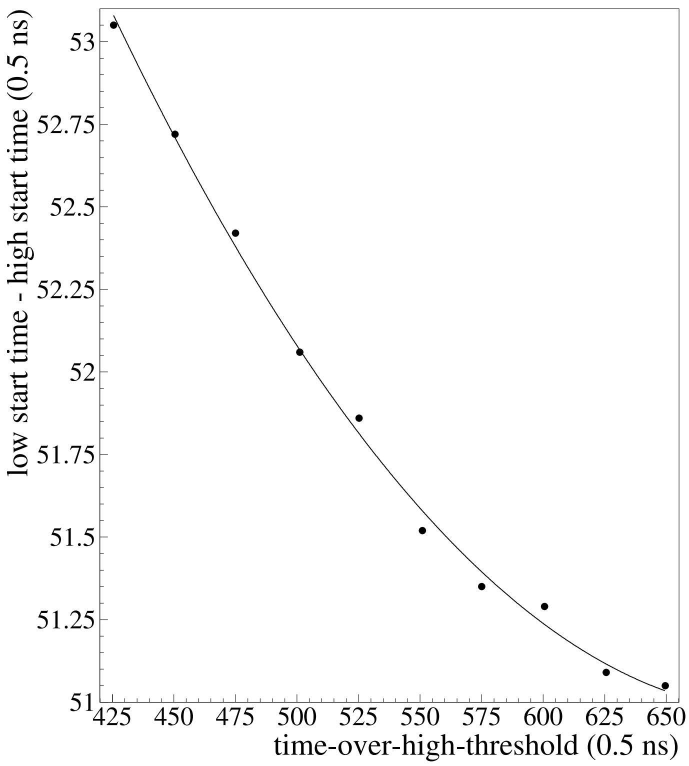

Figure 4.17: Difference between low start time and high start time as a function of high TOT for one of the PMTs. The line is the fit to the data points, and is used to convert high start time to low start time when the high TOT of a PMT output is large enough so that prepulsing starts affecting the low start time. When the low TOT is saturated, the difference between the low start time and the high start time is a constant value of $\approx$ 25 ns.

purposes. Instead, the measured high start time corresponding to the measured high TOT was converted into a prepulsing-free low start time by using the known average difference between the low and high start times as a function of high TOT for that PMT. This start time difference as a function of high TOT, an example of which is shown in Fig. 4.17, was also derived from laser data.

(c) Time pedestal

The time information which is of interest to one reconstructing air showers is the relative time of arrival of Cherenkov light at each PMT. Any time offset common to all the PMTs can be incorporated into the constant T_o in equation (4.1). However, the time information that is extracted from the TDC includes a time offset, different for each PMT, in addition to the relative time of arrival of Cherenkov light at each PMT. The origin of this time offset is a combination of the electron transit time in a PMT, and the time it takes for the PMT signal to traverse the signal cable and the electronics. This time offset is called a *time pedestal*, and its value is slightly different for each PMT. A PMT's time pedestal has to be subtracted from any start time information extracted from that PMT's TDC channel before the time information can be used for reconstruction purposes. Only the relative time pedestals of the PMTs are needed.

The relative time pedestals of the PMTs were determined by first determining the unknown positions of the laserballs and the unknown time differences in the propagation time of light in the optical fibers due to their different lengths. The expected time difference between the time a PMT receives light from one laserball and the time the same PMT receives light from another laserball is,

$$\Delta t = \Delta t_f + \frac{R_a}{c_w} - \frac{R_b}{c_w} \quad , \tag{4.3}$$

where Δt_f is a time difference brought about by different propagation times of light in the two optical fibers due to the different fiber lengths, R_a is the distance between the PMT and the first laserball, R_b is the distance between the PMT and the second laserball, and c_w is the group velocity of green light in water. Note that equation (4.3) does not depend on the PMT's time pedestal since it cancelled out when the time difference was taken. There are, thus, six unknown parameters to be determined: Δt_f, the x and y coordinates of each of the two laserballs, and c_w. Equation (4.3) and the corresponding measured (low start) time difference given by the TDC, for a number of PMTs, can be used in a χ^2 minimization to yield these unknown parameters. In practice, 20 PMTs were used in the minimization [125]. This procedure can be repeated for different pairs of laserballs to obtain the coordinates of all the laserballs, as well as Δt_f for different pairs of laserballs.

Once all the laserballs' coordinates and the fibers' relative time delays have been determined, the relative time pedestal between the i_{th} and j_{th} PMTs can be calculated using,

$$t_{pi} - t_{pj} = t_{mi} - t_{mj} - \Delta t_{fab} - \frac{R_{ai}}{c_w} + \frac{R_{bj}}{c_w} \quad , \tag{4.4}$$

where t_{mi} (t_{mj}) is the registered TDC time, relative to the trigger time, for the detection of the laser light from laserball a (b) by the i_{th} (j_{th}) PMT, Δt_{fab} is the difference between the light propagation times in fibers a and b, and R_{ai} (R_{bj}) is the distance between the i_{th} (j_{th}) PMT and laserball a (b). In practice, all the PMT pedestals were given relative to one particular PMT's pedestal. The measured relative time pedestals of the Milagrito PMTs are shown in Fig. 4.18. The spread of the distribution is ~ 2 ns.

It should also be noted that all of the measured TDC times mentioned in the preceding discussion were corrected for slewing before being used in the calculations. All of the start times, due to laser light detection, extracted from a PMT's TDC were adjusted so that the times were all equivalent, within experimental error, to the start time that a signal with a high TOT of 125 ns from that PMT had. In other words, a PMT's slewing curve was reduced to a horizontal line with a start time value equal to that measured for a 125-ns high TOT signal. Since this reference high TOT of 125 ns was used in determining the time pedestals, the same reference high TOT was used in reconstructing air showers. That is, before being used in reconstructing a shower, a measured start time from a PMT's TDC effected by air shower particles had to be slewing corrected to a start time equivalent to that which a 125-ns high TOT signal from that PMT would have, and the PMT's relative pedestal subtracted from this corrected start time.

As a bonus, the procedure outlined above resulted in the measurement of the speed of light in water, c_w. The measured speed of light in water was 22.1 ± 0.1 cm/ns, consistent with the expected group velocity of 22.04 cm/ns [125].

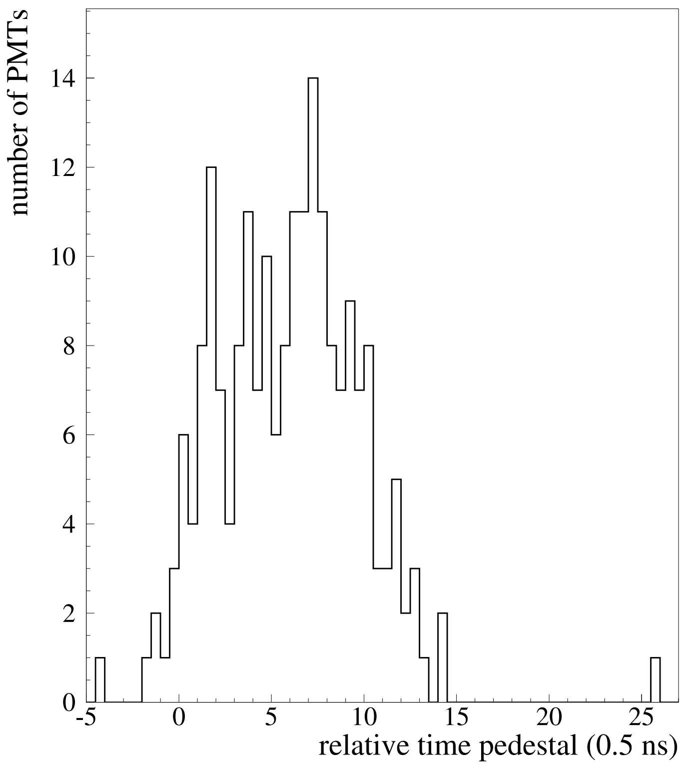

Figure 4.18: Measured relative time pedestals of the PMTs.

(d) Number of PEs

The number of PEs emitted from a PMT's photocathode is a measure of the intensity of light incident on the PMT, so the number of PEs reflected in an anode signal's size also had to be calibrated. This was accomplished by making use of ADCs and PMT signals induced by air shower particles. Figure 4.19 is an example of an ADC distribution from one of the PMTs. Each entry in the distribution was generated when a shower event triggered Milagrito. Evident in the plot is the ADC pedestal, and a hump which is due to single photoelectrons being emitted from the PMT's photocathode. The ADC is calibrated simply by measuring the number of ADC channels between the single-PE peak and the ADC pedestal. Once the number of ADC channels corresponding to a single-PE is known for a particular PMT, it is straightforward to convert any ADC channel to number of PEs. The

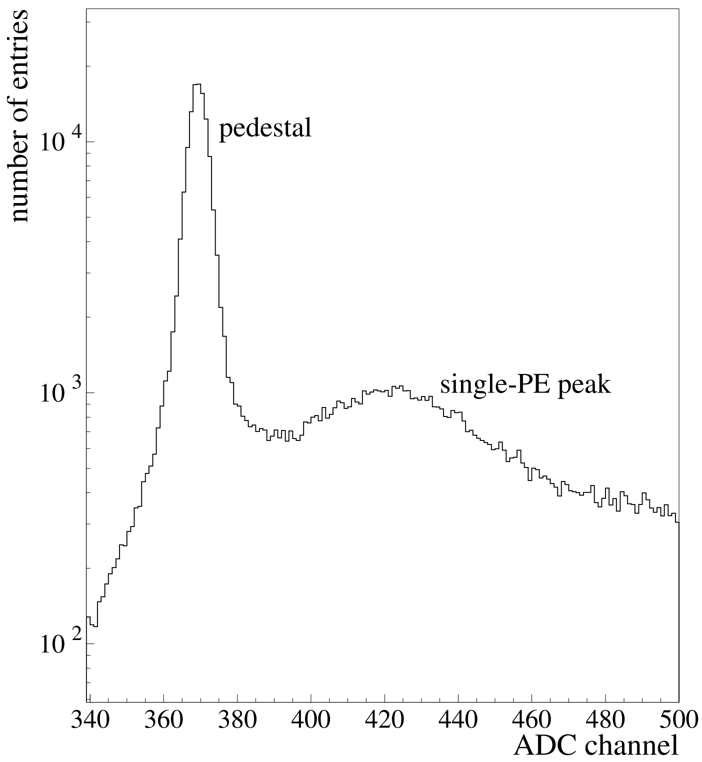

Figure 4.19: ADC distribution for one PMT showing the single-PE peak and the ADC pedestal.

ADC pedestal is simply subtracted from the ADC channel, and the difference is divided by the predetermined number of ADC channels per PE. Since the ADC channel as a function of low TOT or high TOT is easily determined from the air shower data, one can also determine PEs as a function of low TOT or high TOT for each PMT. Once this calibration has been carried out, the low TOT or high TOT of an anode signal can then be used to determine the corresponding number of PEs without the use of an ADC.

4.3 Performance of the Milagrito Detector

The Milagrito experiment was in operation from February 8, 1997 to May 7, 1998. It was functional and took data for ~ 80 % of this 15-month period. It detected air shower events at a rate of 300 to 400 events/second (see Fig. 4.6), and detected a total of ~ 8.9 billion air shower events during its lifetime.

The Milagrito detector's sensitivity to photon-initiated air shower cascades, and its capability for resolving the angular directions of the primary particles can be studied through computer simulations. An understanding of the detector's sensitivity and angular resolution is necessary before any useful science can be derived from its existence. And with a detector which exploits a multitude of particle interactions, employing computer simulations is most often the only way of quantitatively understanding the detector's capabilities. Although this path is not necessarily the most innervating one for a graduate student of physics, one nevertheless wills oneself to take this path given the promise of useful end results.

The simulations for these studies involve a two-step process: First, the development of an air shower down to Milagrito's depth is simulated, and, second, the simulated air shower particles' interactions with the water, the subsequent production of Cherenkov light, and the PMTs' response to the Cherenkov light, are simulated. The simulation package used for the shower development phase was a package called CORSIKA, and the simulation package used for the detection phase was GEANT.

The accuracy of the simulations can be tested by comparing the simulated and observed cosmic ray detection rates. A comparison of the simulated and observed rates reveals that they agree to within 20% [123].

4.3.1 Milagrito effective area The *effective area* is a measure of the sensitivity of Milagrito to air showers of different sizes. It is the area that an air shower of a certain size "sees," and gives an idea of how far a shower core can be from the pond center with the air shower still being detected by Milagrito, given the trigger condition of at least 100 tubes being hit. Since the effective area depends on shower size, it also depends on both the primary photon energy and zenith angle. The effective area can be calculated using simulation results, and is given by,

$$A_{eff}(E,\theta) = \frac{N_{trig}(E,\theta)}{N_{throw}} A_{throw} \quad , \tag{4.5}$$

where A_{throw} is the physical area where shower cores of simulated primaries of a certain energy, E, and zenith angle, θ, are randomly positioned or *thrown*, N_{throw} is the number of air showers thrown into the area A_{throw}, and $N_{trig}(E,\theta)$ is the number of these showers which trigger the Milagrito detector. Given a primary particle of energy E, the effective area for this particle, on the average, decreases as the zenith angle increases because of the increasing atmospheric overburden and, hence, decreasing shower size. Figure 4.20 plots the Milagrito effective area for gamma-rays as a function of the primary photon energy, for a 1-meter layer of water above the PMTs, and for different zenith angles. The Milagrito effective area for cosmic rays can be found in [123]. The use of the calculated effective area for estimating the Milagrito detector's sensitivity to GRBs can be found in Section 6.4.

Given a known TeV gamma-ray source with a measured flux at the top of the Earth's atmosphere, the number of air showers from this flux which can be detected by Milagrito can be calculated by convoluting the known flux with the effective area. The flux is simply the number of gamma-ray particles per unit area per unit time per unit energy incident on the top of the atmosphere. It is often observed in nature that this flux, as a function of the primary particle's energy, obeys a power law spectrum, i.e.,

$$\frac{dF}{dE} \propto E^{-\eta} \quad , \tag{4.6}$$

where η is a positive constant. The number of air showers which can be detected by Milagrito is then,

$$N_s \propto \int_{E_1}^{E_2} E^{-\eta} A_{eff}(E,\theta) dE \quad , \tag{4.7}$$

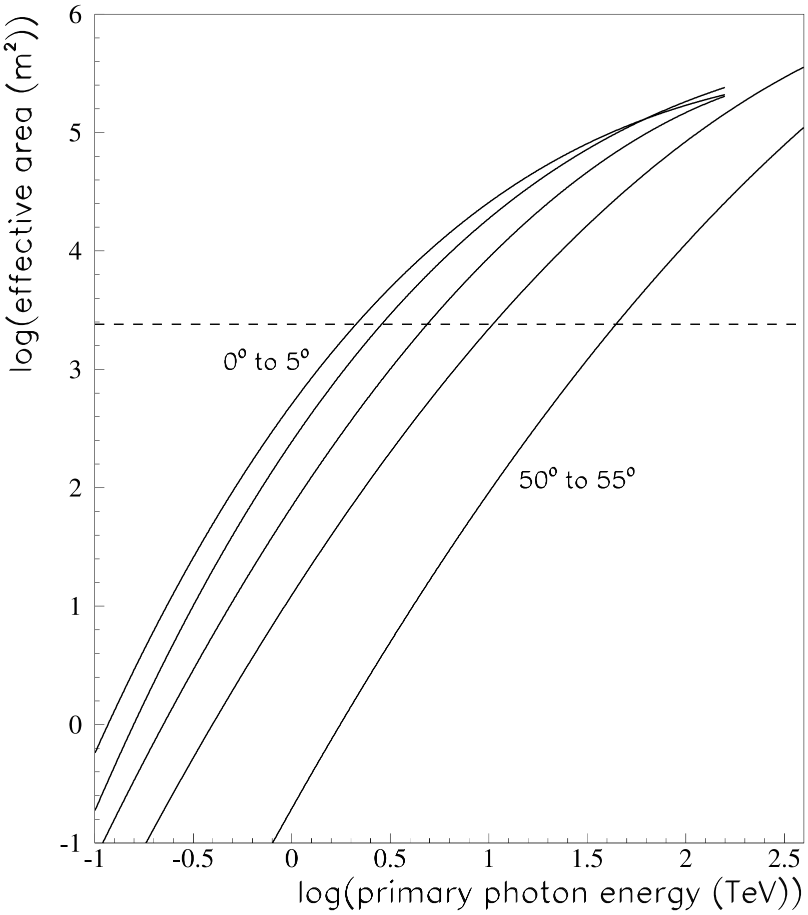

Figure 4.20: Milagrito effective area for primary photons of different energies, for different zenith angles and a 1-meter layer of water above the PMTs. From top to bottom, the zenith angles are: $0^o - 5^o$, $20^o - 25^o$, $30^o - 35^o$, $40^o - 45^o$, and $50^o - 55^o$. The dashed line indicates the physical area of the Milagrito detector at the water surface.

where E_1, E_2 define the range of TeV energies of the gamma-rays from the source. Often, the source has to be tracked through different zenith angles, so equation (4.7) has to be integrated over the different zenith angles as well.

Figure 4.21 shows plots of $E^{-2}A_{eff}(E,\theta)$ as a function of primary energy, for different zenith angles. It can be seen that as the zenith angle increases, the sensitivity of Milagrito shifts toward higher primary energies. However, since the area under a curve decreases as the zenith angle increases, Milagrito becomes a less sensitive detector of air shower events as the zenith angle of the source increases.

Of course, one has to compare the number of detectable gamma-initiated air showers calculated through equation (4.7) to the expected number of cosmic ray background events in order to ascertain if Milagrito is sensitive enough to detect a significant number of gamma-ray source events above background.

4.3.2 Milagrito point spread function and angular resolution The occurrence of random errors in the measurement of the time of arrival and amount of Cherenkov light, and in the parameters which are used in reconstructing air showers, e.g. calibration parameters, gives rise to Milagrito's finite angular resolution. This means that gamma-initiated air shower events coming from a point source and which, therefore, come from the same direction in space will have reconstructed directions which differ from the common direction.

Additionally, there existed for Milagrito a systematic pointing error. The origin of this systematic error was predominantly the large emission angle of Cherenkov radiation in water (42^o). This large emission angle meant that it was possible for a PMT which was far from a charged particle's track to be hit by the produced Cherenkov light. Thus, this PMT would register a time which was late compared to the time registered by a PMT which was close to the particle's track, and this late light would tend to bias the reconstructed zenith angle toward one which was larger than the actual zenith angle. The effect gets worse as the zenith angle increases, as PMTs which are even farther from particles' tracks can be

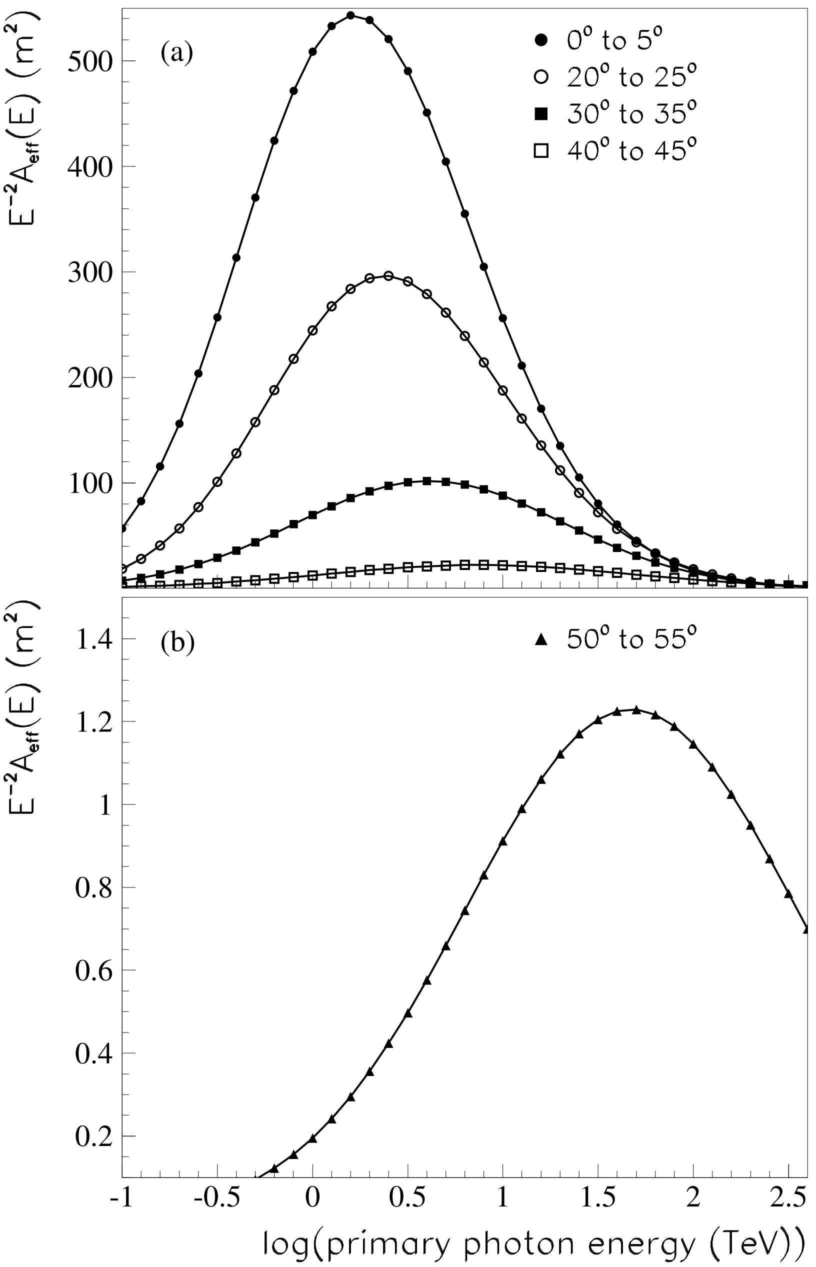

Figure 4.21: Plots of $E^{-2}A_{eff}(E,\theta)$ as a function of primary photon energy, for different zenith angles.

hit. It is estimated that the systematic pointing error produced by this effect is $\sim 1^o$ at a zenith angle of 45^o [123].

Other sources of measured late times are Cherenkov light which gets scattered in the detector, and delta-rays which are produced in the water and which give rise to Cherenkov radiation as well.

Figure 4.22(a) is a histogram of the space angle between a simulated primary photon's true source direction and the reconstructed direction, for primary gamma-rays with energies between 0.2 TeV and 50 TeV. Figure 4.22(b) plots the integral form of Fig. 4.22(a), i.e. the number of occurrences of a space angle or less in Fig. 4.22(a), normalized to the total number of entries in the histogram. The line in Fig. 4.22(b) is a fitted line and is given by,

$$P_s(\gamma) = A_1(1 - exp(-\gamma^2/2\sigma_1^2)) + A_2(1 - exp(-\gamma^2/2\sigma_2^2)) \quad , \tag{4.8}$$

where γ is the space angle between the true primary direction and the reconstructed direction, $\sigma_1 = 2.10^o$, $\sigma_2 = 0.77^o$, and $A_1 \approx A_2 \approx 0.5$. Equation (4.8) gives the probability, on the average, for finding a reconstructed primary gamma-ray direction between 0 and γ.

The probability distribution given by equation (4.8) can be differentiated to obtain the corresponding probability density function:

$$\begin{aligned} f_s(\gamma) &= \frac{1}{2\pi}\frac{dP_s(\gamma)}{d\gamma} & (4.9) \\ &= A_1\frac{\gamma}{2\pi\sigma_1^2}exp(-\gamma^2/2\sigma_1^2) + A_2\frac{\gamma}{2\pi\sigma_2^2}exp(-\gamma^2/2\sigma_2^2) \quad . & (4.10) \end{aligned}$$

Equation (4.10), like Fig. 4.22(a), characterizes Milagrito's point spread function, on the average. That is, it describes how the distribution of reconstructed directions of gamma-ray primaries from a point source looks like. From it can be extracted information about Milagrito's angular resolution. It can be seen that equation (4.10) is the sum of two Gaussian distributions on the sphere (cf. Section 5.3.1), with the first term having a peak at $\gamma = \sigma_1 = 2.10^o$, and the second term having a peak at $\gamma = \sigma_2 = 0.77^o$. These are plotted in Fig. 4.23.

4.3.3 Sources detected by Milagrito Milagrito's ability to detect sources of TeV gamma-rays of sufficient flux was demonstrated by its detection of the blazar Markarian 501 at a significance of 3.7 standard deviations [126] (see Section 5.3.3 for a discussion of the significance of a measurement).

The shadow of the Moon $-$ which is caused by the occultation of cosmic rays by the Moon, thus causing a deficit in the observed cosmic ray count $-$ was also observed by Milagrito at a significance of ≈ 10 standard deviations. In a similar fashion, the shadow of the Sun was observed by Milagrito at ≈ 8 standard deviations [127, 123].

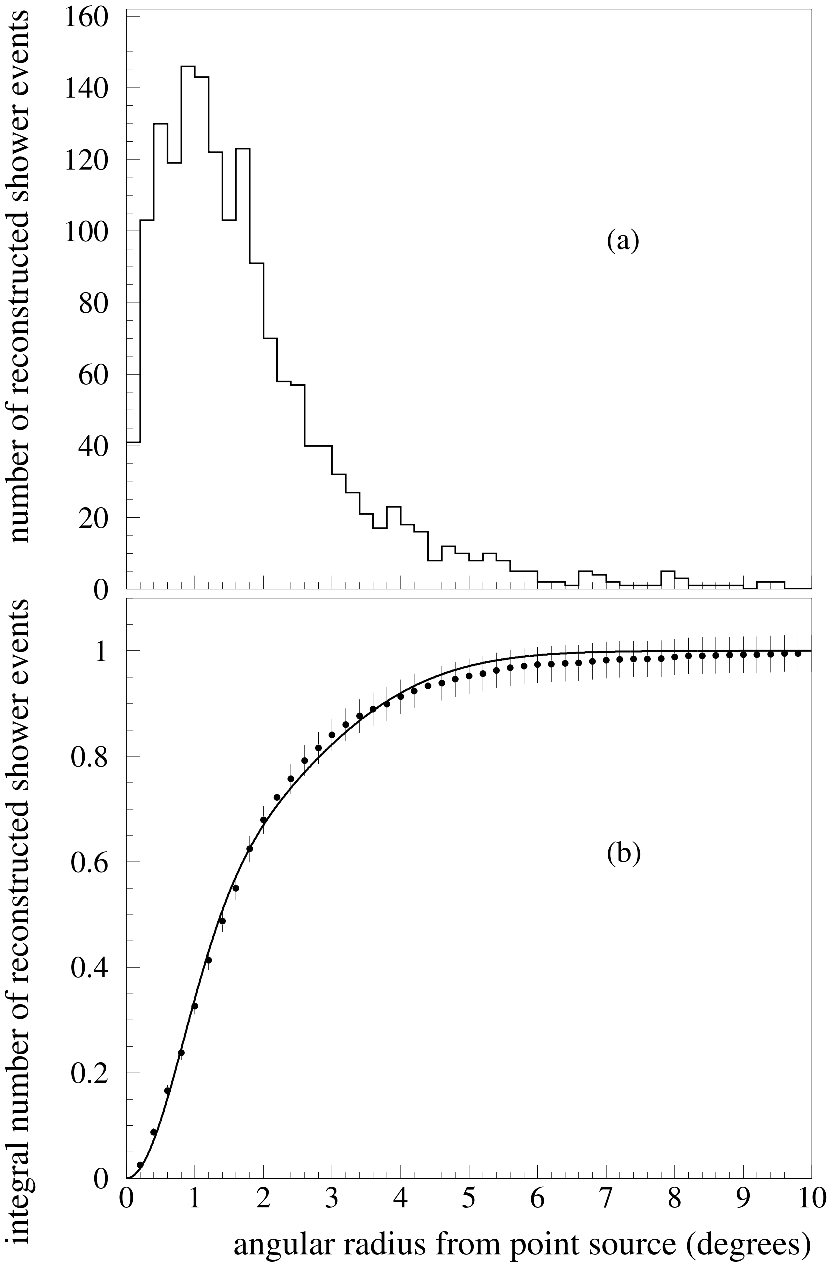

Figure 4.22: (a) Distribution of space angle between a simulated primary gamma-ray's true direction and the reconstructed direction, for primary energies between 0.2 TeV and 50 TeV. (b) The integral number of reconstructed gamma-initiated air shower events as a function of space angle, derived from plot (a). The fitted line is given by equation (4.8).

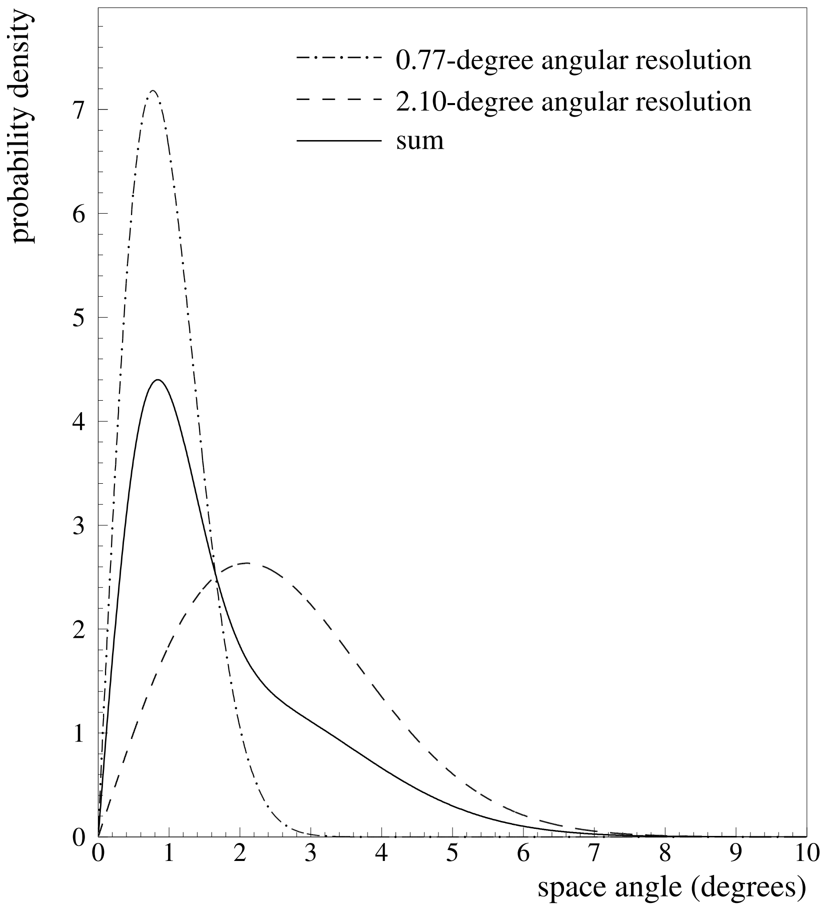

Figure 4.23: Probability density function for a Gaussian distribution on the sphere with $\sigma = 0.77^o$, $\sigma = 2.10^o$, and for the sum of the two distributions, i.e. that given by equation (4.10). The functions are normalized so that the area under each one of them is equal to unity.

Chapter 5

Data Analysis Technique

This chapter describes the analysis technique which was used in searching for a TeV component of GRBs. The search technique was a simple and straightforward binned counting analysis in which coordinate bins were used to cover an appropriate area of the sky, and events falling in each bin during an appropriate time interval were counted. The chapter starts off with definitions of the coordinate systems used, then describes the BATSE GRB sample used in this analysis, as well as the search area and search duration parameters. The foundation is then laid for understanding general counting techniques in gamma-ray astronomy, including estimating the significance of what is counted. Finally, details of choosing the appropriate bin size and estimating background are discussed.

5.1 Astrometry: Coordinate Systems on the Celestial Sphere

Two coordinate systems were used in the search analysis: the *equatorial* coordinate system, and the *local* coordinate system. These coordinate systems define a point on the *celestial sphere* (Fig. 5.1), which is an imaginary sphere infinitely larger than the Earth on which we can imagine celestial objects such as stars and gamma-ray bursts to lie. The celestial sphere has the observer at its center and, because of the Earth's rotation, the celestial sphere appears to this observer to rotate about an axis of rotation which is parallel to the Earth's axis of rotation. Important points and great circles on the celestial sphere are [128]:

> *North and south celestial poles:* The respective points of intersection of the celestial sphere with the northward and southward prolongations of the Earth's axis of rotation.
>
> *Zenith and nadir:* The respective points of intersection of the celestial sphere with the upward and downward prolongations of the observer's plumb line.

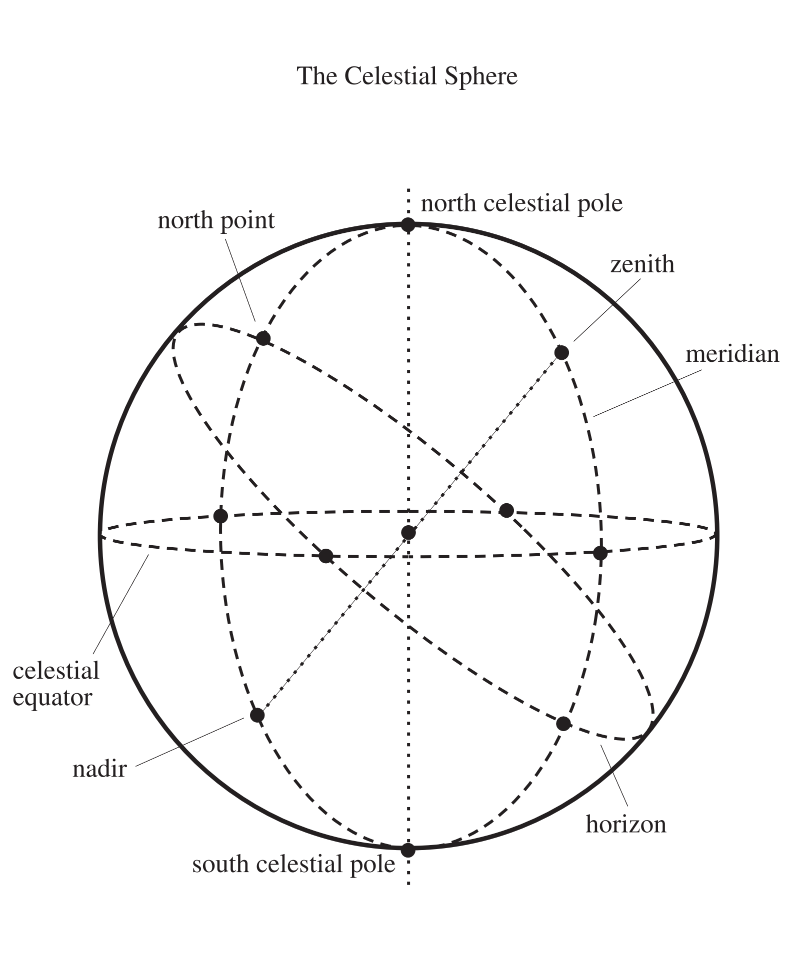

Figure 5.1: The Celestial Sphere. The observer is at the center of the sphere.

Celestial equator: The great circle defined by the intersection of the celestial sphere and the projection of the plane of the Earth's equator.

Ecliptic: The apparent great-circle path of the Sun on the celestial sphere during the course of a year. The plane of the ecliptic is inclined at an angle of about $23^o27'$ to the plane of the celestial equator.

Vernal equinox: That point of intersection of the ecliptic and the celestial equator which occurs when the Sun is going from south to north.

Horizon: the great circle defined by the intersection of the celestial sphere and that plane which is perpendicular to the observer's plumb line at the position of the observer.

Meridian: The great circle which is perpendicular to the horizon and passes through the zenith and the north celestial pole.

North point: The northward point of intersection of the meridian and the horizon.

Vertical circle: Any great circle which passes through the zenith and nadir and is therefore perpendicular to the horizon.

Hour circle: Any great circle which passes through the north and south celestial poles and is therefore perpendicular to the celestial equator.

5.1.1 Equatorial coordinate system In this coordinate system, a point on the celestial sphere is given by (δ,α) (Fig. 5.2), where δ is the *declination*, and α is the *right ascension* of the celestial object. Declination is the angle from the celestial equator to the position of the celestial object of interest, measured along the hour circle which passes through the celestial object. Declination is positive when measured north of the celestial equator, and negative south of the celestial equator; it's value ranges from -90^o to +90^o. Right ascension is the angle from the vernal equinox to the hour circle which passes through the celestial object, measured eastwardly along the celestial equator. It's value ranges from 0^o to 360^o.

Additionally, the *hour angle*, h, is defined as the angle from the meridian to the hour circle which passes through the celestial object, measured westwardly along the celestial equator.

The reference epoch for all equatorial coordinates in this dissertation is J2000.

5.1.2 Local coordinate system This coordinate system is very closely related to the *horizon coordinate system*. In the horizon coordinate system, a point on the celestial sphere is given by (a,A) (Fig. 5.3), where a is the *altitude*, and A is the *azimuth* of the celestial object. Altitude is the angle from the horizon to the position of the celestial object, measured along the vertical circle which passes through the object. It's value ranges from 0^o to 90^o. Azimuth is the angle from the north point to the vertical circle which passes through the object, measured eastwardly along the horizon. It's value ranges from 0^o to 360^o. It is

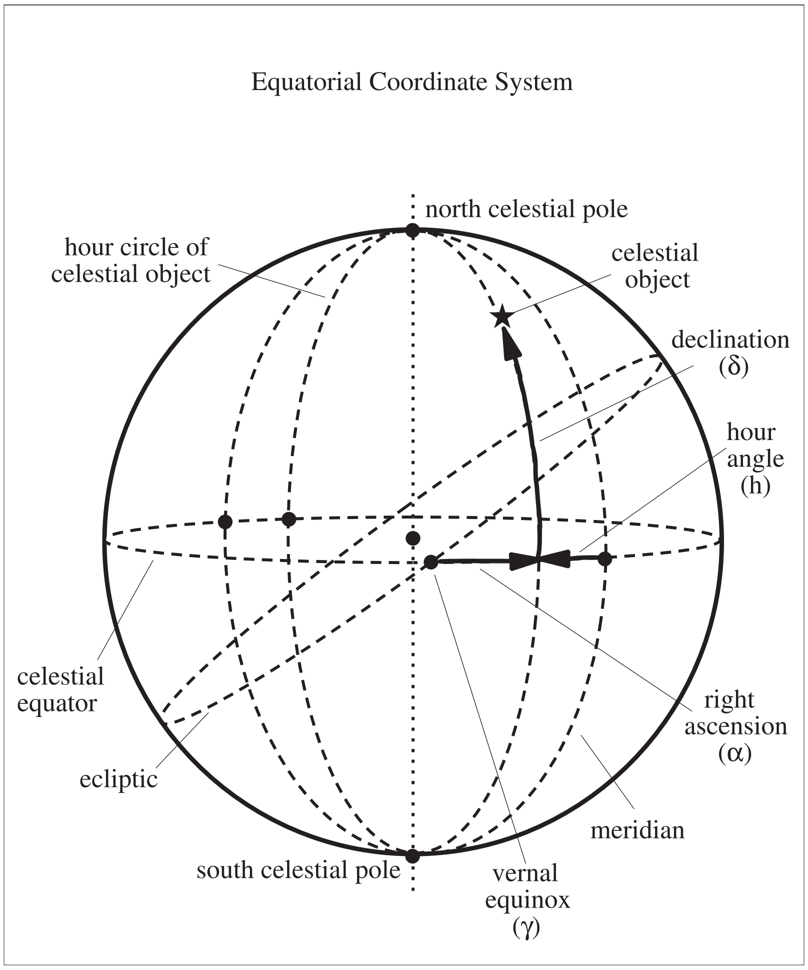

Figure 5.2: The equatorial coordinate system. The celestial object of interest is symbolized by a star. Its equatorial coordinates are given by (δ,α).

obvious that the horizon coordinates of the same celestial object are different for observers at different locations on the Earth's surface.

For the purpose of reconstructing Milagrito air shower events, it is convenient to indentify a point on the celestial sphere by the local coordinates (θ,ϕ), where θ is called the *zenith angle* of the celestial object. θ and ϕ are related to altitude and azimuth by:

$$\begin{aligned} \theta &= 90^o - altitude \\ \phi &= 90^o - azimuth \quad . \end{aligned} \tag{5.1}$$

Unlike equatorial coordinates, the local coordinates of a celestial object changes

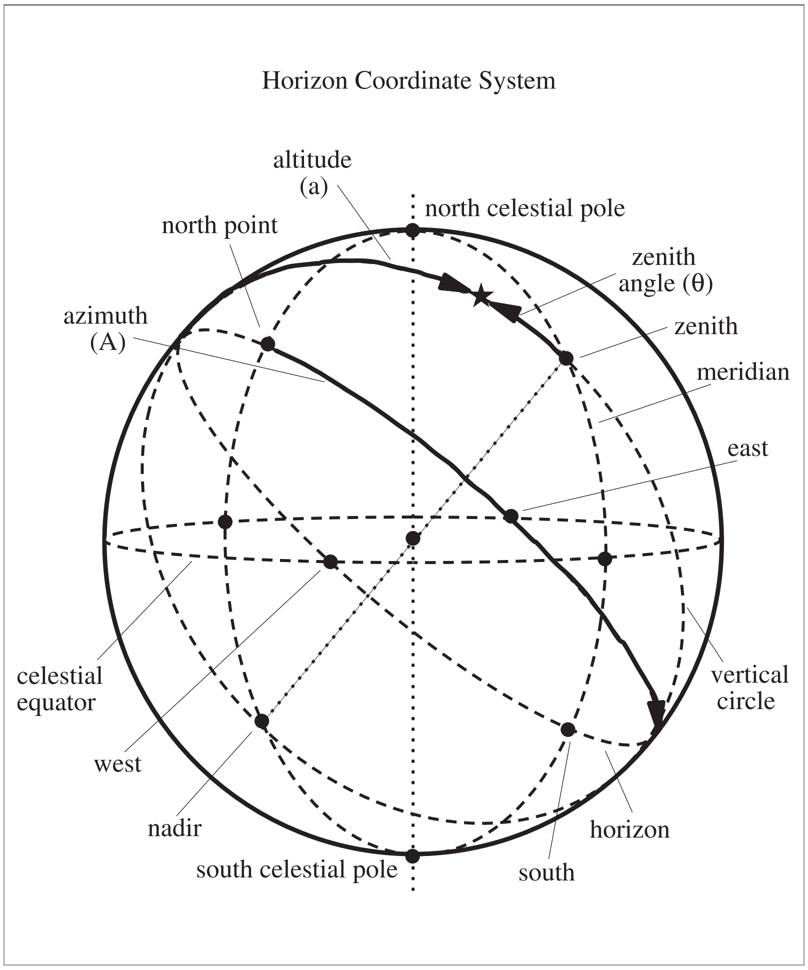

Figure 5.3: The horizon coordinate system. The celestial object of interest is symbolized by a star. Its horizon coordinates are given by (a,A).

with time, as the celestial sphere apparently rotates, relative to the local sky, about its axis. At an instant of time t, a pair of local coordinates ($\theta(t)$,$\phi(t)$) corresponds to a pair of equatorial coordinates (δ,α). Thus, once (θ,ϕ) for a reconstructed event has been determined, the time information enables the transformation to the (δ,α) coordinates of the event. Formulae connecting horizon coordinates to equatorial coordinates are found in reference [128].

5.2 The BATSE GRB Sample

During Milagrito's lifetime, 400 GRBs were detected by the BATSE detector. Out of these, there were 54 GRBs within Milagrito's field of view of $\approx 45^o$ from zenith, and for which Milagrito data existed. The 54 GRBs used in this analysis and relevant information about them are listed in Table 5.1 at the end of this chapter.

5.2.1 Search area One of the parameters which had to be defined in this analysis was the area of the sky which had to be searched for a GRB. The definition of this parameter was dependent solely on the degree of confidence that was associated with the nominal BATSE position of each GRB. BATSE determined directions to burst sources by using the relative count rates from the brightest four or six LAD detectors [129] . The BATSE burst location algorithm, LOCBURST, fitted modeled count rates to observed count rates to obtain the final burst location. The modeled count rates were the outcome of a series of complex algorithms which modeled each LAD's response as a function of source angle, incident photon energy, and source spectral index and intensity. Scattering of source photons off the Earth's atmosphere and detection of the scattered photons was also modeled. Poisson fluctuations from the real event count gave rise to a statistical uncertainty in the location of a burst. Statistical uncertainties for BATSE GRB locations ranged from $\sim$0.1^o to $\sim$25^o.

The total error for an estimated BATSE GRB location is a combination of the statistical uncertainty and a systematic error. Sources of systematic errors for BATSE are [130]: inaccuracies in the assignment of energies to channel boundaries, inaccuracies in the dead-time correction of high count rates, the approximations of the statistical and total error boxes as circles, inaccuracies in the detector response model as a function of photon energy or direction, including inaccuracies in the model of scattering from the spacecraft and the Earth's atmosphere, deviations of the actual GRB spectra from the power law assumed in most cases, and inaccuracies in background subraction.

The BATSE collaboration has quantified total errors by making error models obtained by statistical comparison of BATSE GRB locations with locations or arcs obtained

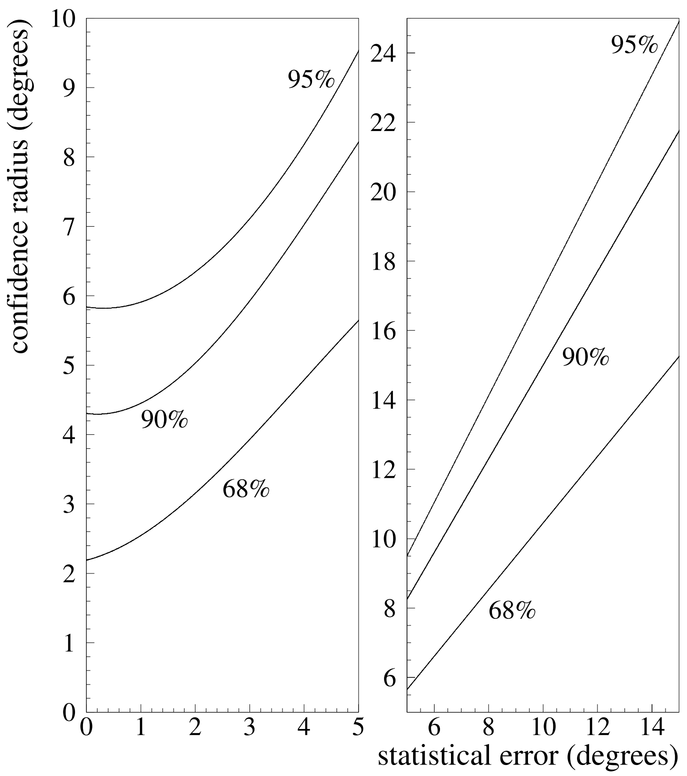

Figure 5.4: BATSE GRB confidence radius as a function of statistical error. Shown are the 68%, 90%, and 95% confidence radii using BATSE's error Model 2. This figure reproduces a plot from reference [130] with an accuracy of $\pm 0.1^o$.

by the InterPlanetary Network (IPN) [130]. One such model, Model 2 or the "core-plus-tail" model, represents the total error distribution of BATSE GRB locations as a Gaussian-like distribution with an extended tail. This model is in excellent agreement with the distribution of angular separations between BATSE locations and IPN locations or arcs. The confidence radii predicted by Model 2 as a function of the statistical uncertainty are given in Fig. 5.4. For this GRB search, the Model 2 95% confidence radii of the GRBs were used to define the search areas. A histogram of these confidence radii, which range from $\approx 6^o$ to $\approx 30^o$, is shown in Fig. 5.5(a).

5.2.2 Search time duration Another search parameter which had to be defined was the search time duration, i.e. the length of time during which events from a pre-defined GRB search area were counted. The search time duration used in this analysis was the measured BATSE T90 for each GRB, with the start time of the search duration coincident with the start time of the BATSE T90 interval.

If the process of synchrotron self-Compton, or inverse Compton (IC), scattering occurs in internal shocks which produce gamma-ray bursts, then it most likely that the emitted IC photons will be observed in the GeV or TeV energy range and that the emission will be prompt, accompanying the lower-energy emission [2, 90]. Also, in the internal-external shocks scenario of GRBs, the observed time duration reflects the duration of time during which the inner engine is active. Therefore, a natural and intuitive choice for a time to use in the search for a TeV component of GRBs, assuming that this component is produced through sychrotron self-Compton scattering within internal shocks, is that which is coincident with the observed lower-energy emission, and a natural time duration to consider is the duration during which the lower-energy emission is observed, i.e. the BATSE T90.

A histogram of the T90 durations for the 54 GRBs is shown in Fig. 5.5(b). T90 values for the sample ranged from ≈ 0.2 seconds to ≈ 200 seconds. For 12 GRBs, no T90 is given in the current BATSE catalog, so a search duration of 30 seconds was instead used in the analysis, which explains the peak in the T90 histogram.

BATSE time profiles for 46 of the 54 GRBs can be found in the Appendix.

5.3 Point Sources, Background, and Determining the Significance of a Measurement

5.3.1 Characterizing point source and background density functions Gamma-ray bursts are compact objects and are treated as point sources in this analysis. When point sources are detected by measuring instruments, the detector's finite angular resolution smears out the point source, resulting in a point spread distribution on the celestial sphere. A unimodal, rotationally symmetric distribution of directions resulting from random errors is modeled by the Fisher distribution [131] . For small space angles, the Fisher distribution

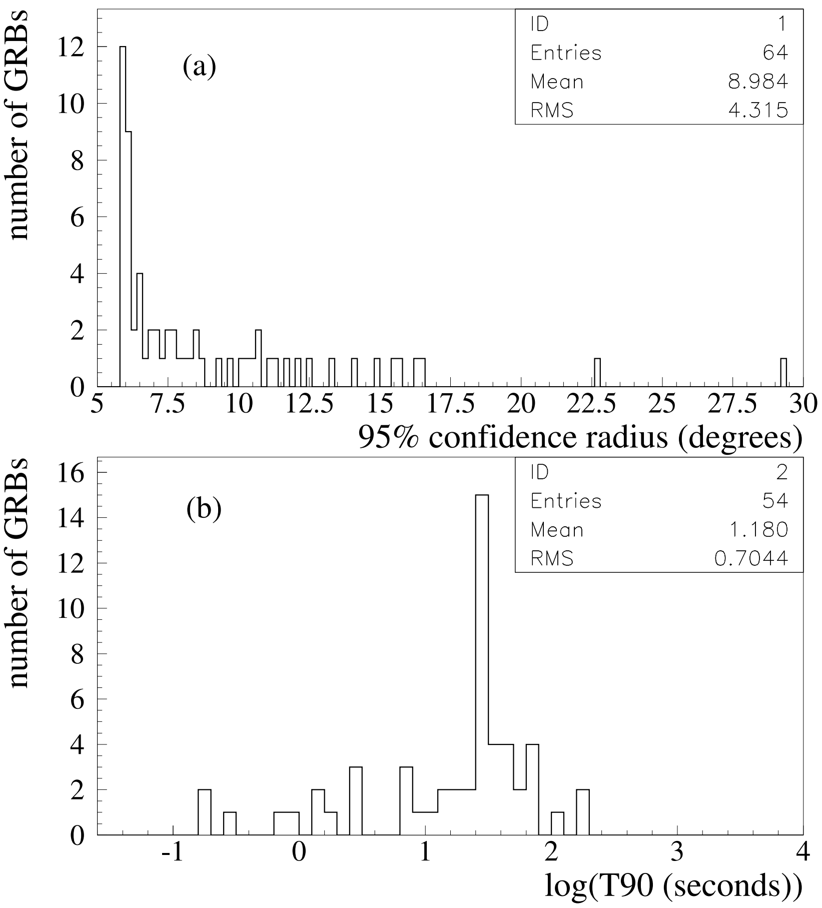

Figure 5.5: (a) The distribution of search radius for the 54 GRBs used in this analysis. (b) The T90 distribution for the GRB sample.

becomes the Gaussian distribution on the sphere. The probability density function (PDF) for this distribution is:

$$f_s(\gamma) = \frac{\gamma}{2\pi\sigma^2} exp(-\gamma^2/2\sigma^2) \quad , \qquad \gamma, \sigma \ll 1 \tag{5.2}$$

where γ is the space angle between the measured event direction and the true point source direction, and σ is the detector's angular resolution, both in radians. This distribution is plotted in Fig. 5.6.

Note that, as discussed in Chapter 4, the average point spread distribution of Mi-

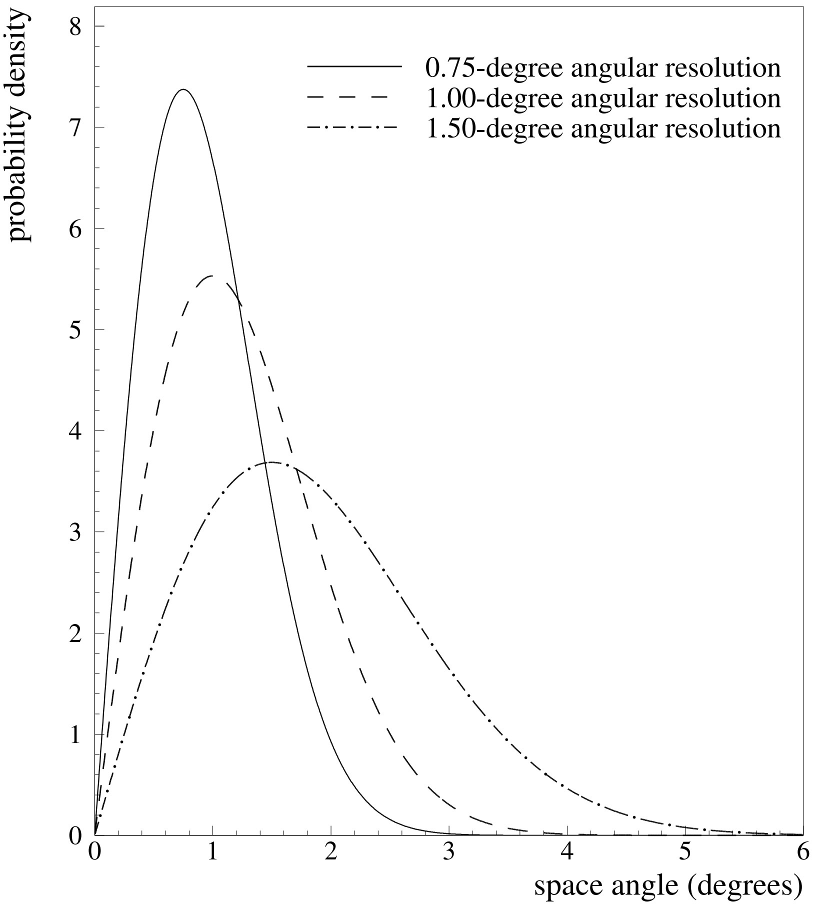

Figure 5.6: Probability density function, equation (5.2), for a Gaussian distribution on a sphere.

lagrito reconstructed events is actually a sum of two density functions, each given by equation (5.2) but with different angular resolutions σ. For the purposes of this chapter, equation (5.2) will thus serve only as an approximation to the real point spread distribution. Choosing an angular resolution for equation (5.2) which is $\approx 0.77^o$ will bias any calculation in favor of those events which contribute to the core of the real point spread distribution, and choosing an angular resolution which is $\approx 2.10^o$ will result in a bias in favor of events which contribute to the tail of the real distribution (see also Section 7.2).

The probability for finding a source event between γ and γ+dγ is:

$$dP_s = 2\pi f_s(\gamma) d\gamma \quad , \tag{5.3}$$

and the probability for finding a source event over all space, i.e. from γ = 0 to γ = π/2, is unity. The total probability for finding an event between space angles 0 and γ is then:

$$P_s(\gamma) = 2\pi \int_0^\gamma f_s(\gamma) d\gamma \tag{5.4}$$
$$P_s(\gamma) = 1 - exp(-\gamma^2/2\sigma^2) \quad . \tag{5.5}$$

Serving as background noise to gamma-ray events are cosmic ray particles. Ignoring the effect of atmospheric overburden for the moment, cosmic ray particle directions are isotropically distributed and can, therefore, be described by the following PDF:

$$f_b(\gamma) = A\gamma \quad , \tag{5.6}$$

where γ is the space angle between the measured cosmic ray particle direction and a chosen origin on the celestial sphere, and A is a normalization constant. This PDF is normalized so that

$$P_b(\gamma) = 2\pi \int_0^{\gamma_o} f_b(\gamma) d\gamma = 1 \tag{5.7}$$

$$\Rightarrow \qquad A = \frac{1}{\pi {\gamma_o}^2} \quad , \tag{5.8}$$

where γ_o defines the region of interest of a search. Then the total probability for finding a background event between space angles 0 and γ is,

$$P_b(\gamma) = 2\pi \int_0^{\gamma} f_b(\gamma) d\gamma \tag{5.9}$$

$$P_b(\gamma) = \left(\frac{\gamma}{\gamma_o}\right)^2 \quad . \tag{5.10}$$

5.3.2 General counting technique in gamma-ray astronomy Analyzing data in gamma-ray astronomy usually involves counting the number of air shower events detected by a measuring instrument during a predetermined time interval, and originating from a predetermined area of the sky − a *celestial bin*. If the source is known to exist, e.g. through previous detections of the source by other experiments, the search time interval or duration, not surprisingly, usually coincides with the time duration during which it is believed that a gamma-ray source is active or flaring or, if one is observing a steady source, the time during which the source is within the detector's field of view. Of course, one can also monitor the quiet phases of a source and be on the lookout for surprises. If the position of the source is known accurately, e.g. through localization of the source at radio, optical, or x-ray wavelengths, then, assuming that the detector has no systematic pointing error, the size of the celestial bin examined will depend on the detector's angular resolution, and, as will be discussed in a later section, on the expected background count coming from the bin during the search time interval.

In the jargon of gamma-ray astronomy, the number of events counted during the search time interval and coming from the celestial bin being examined is called the *on-source count*, N_{on}. N_{on} is obviously the sum of the gamma-ray event count and the cosmic ray background event count.

To estimate the number of background events included in N_{on}, there is a need to measure another quantity called the *off-source count*, N_{off}. In very general terms, the procedure for determining N_{off} usually calls for counting the total number of events detected during the search time interval coming from off-source bins surrounding the on-source celestial bin. Alternatively, background events can be simulated by associating the time of each real event detected within the search time interval and coming from any part of the sky, random local coordinates (θ, ϕ) generated from the measured distributions of these local coordinates. The local coordinates and time of the simulated background event is then transformed into equatorial coordinates from which it can be determined if the simulated background event falls into the on-source bin. This procedure is repeated several times for each real event time, and the total number of simulated events, N_{off}, falling into the on-source bin counted. Whichever method is chosen, a parameter α can be calculated which is equal to the the ratio of the number of on-source bins to off-source bins in the former method, and to the inverse of the number of simulated background events generated per real event in the case of the latter method. The expected background count included in N_{on} is then,

$$N_b = \alpha N_{off} \quad , \tag{5.11}$$

and the estimated number of excess events, N_s, over background is therefore,

$$N_s = N_{on} - \alpha N_{off} \quad . \tag{5.12}$$

N_{on} and N_{off} are random variables which are each described by a Poisson distribution and, in the case of large observed counts, by a normal distribution. With N_{on} and N_{off} measured, and with the experimental parameter α known, one proceeds to determine the significance of an estimated excess (or deficit), and from there decide, with a degree of confidence, either to accept the null hypothesis that no source was detected, or to reject it.

5.3.3 The significance of a measurement The significance of an excess count, N_s, over background is defined as the ratio of the excess count over its standard deviation, $\hat{\sigma}(N_s)$:

$$S = \frac{N_s}{\hat{\sigma}(N_s)} \quad . \tag{5.13}$$

For measured counts which are distributed normally, and under a null hypothesis, i.e. if no source exists, the significance given by equation (5.13), to be useful, should also be normally distributed with zero mean and unit variance, i.e. a standard normal variable.

If the measured background count, N_{off}, is large enough so that fluctuations in this background count is normally distributed and, additionally, if N_{off} is much larger than N_{on} (or, equivalently, if the uncertainty in N_b is small compared to the uncertainty in N_{on}), then the significance of an excess can be given as,

$$S = \frac{N_s}{\sqrt{N_b}} = \frac{N_s}{\sqrt{\alpha N_{off}}} \quad . \tag{5.14}$$

Using equations (5.5) and (5.10), one can write an analytical form of equation (5.14) which gives the significance as a function of the angular radius, γ, of the bin used, as,

$$S(\gamma) = \frac{N_{s,tot} P_s(\gamma)}{\sqrt{< N_{off} > P_b(\gamma)}} \tag{5.15}$$

$$= \frac{N_{s,tot}}{\sqrt{< N_{off} >}} \frac{1 - exp(-\gamma^2/2\sigma^2)}{\gamma/\gamma_o} \quad , \tag{5.16}$$

where $N_{s,tot}$ is the total number of source events in all space, $< N_{off} >$ is the expectation of the total number of background events within a space angle γ_o, and $P_b(\gamma)$ plays the role of the parameter α.

It cannot be emphasized enough that the significance given by equation (5.14) is only useful under the conditions specified in the preceding paragraph. When those conditions are not present, the significance given by equation (5.14), and consequently by equation (5.16), grossly overestimates the significance of a measurement and loses the important characteristic of being a standard normal variable. A more robust procedure for calculating significances was put forward by Li and Ma [132] and will be discussed in the paragraphs that follow.

The Li and Ma procedure for deriving a useful formula for the significance of a measurement involved calculating the likelihood ratio, λ, of the likelihood for measuring the observed counts, N_{on} and N_{off}, under the null hypothesis to the likelihood for measuring the observed counts under the alternative, non-null hypothesis. The restricted parameter is the number of expected signal events, N_s, which is restricted to be zero under the null hypothesis, and non-zero under the alternative hypothesis. Asymptotically, when N_{on} and N_{off} are not too few, the statistic $-2ln\lambda$ is distributed as a central chi-square distribution with one degree of freedom under the null hypothesis. The quantity $\sqrt{-2ln\lambda}$ is therefore a standard normal variable which could be a measure of the significance. The significance formula resulting from this procedure is,

$$S = \sqrt{-2ln\lambda} \tag{5.17}$$

$$= \sqrt{2}\sqrt{N_{on}ln\left[\frac{1+\alpha}{\alpha}\left(\frac{N_{on}}{N_{on}+N_{off}}\right)\right] + N_{off}ln\left[(1+\alpha)\left(\frac{N_{off}}{N_{on}+N_{off}}\right)\right]} \tag{5.18}$$

Although the Li-Ma prescription requires that N_{on} and N_{off} be $\gtrsim 10$, one can see from Fig. 5.7 that, for quantifying excesses, the Li-Ma significance follows a standard normal distribution quite well even in the case of a small expected background count in an on-source bin. The prescription does not work that well for quantifying deficits when the expected background count is small.

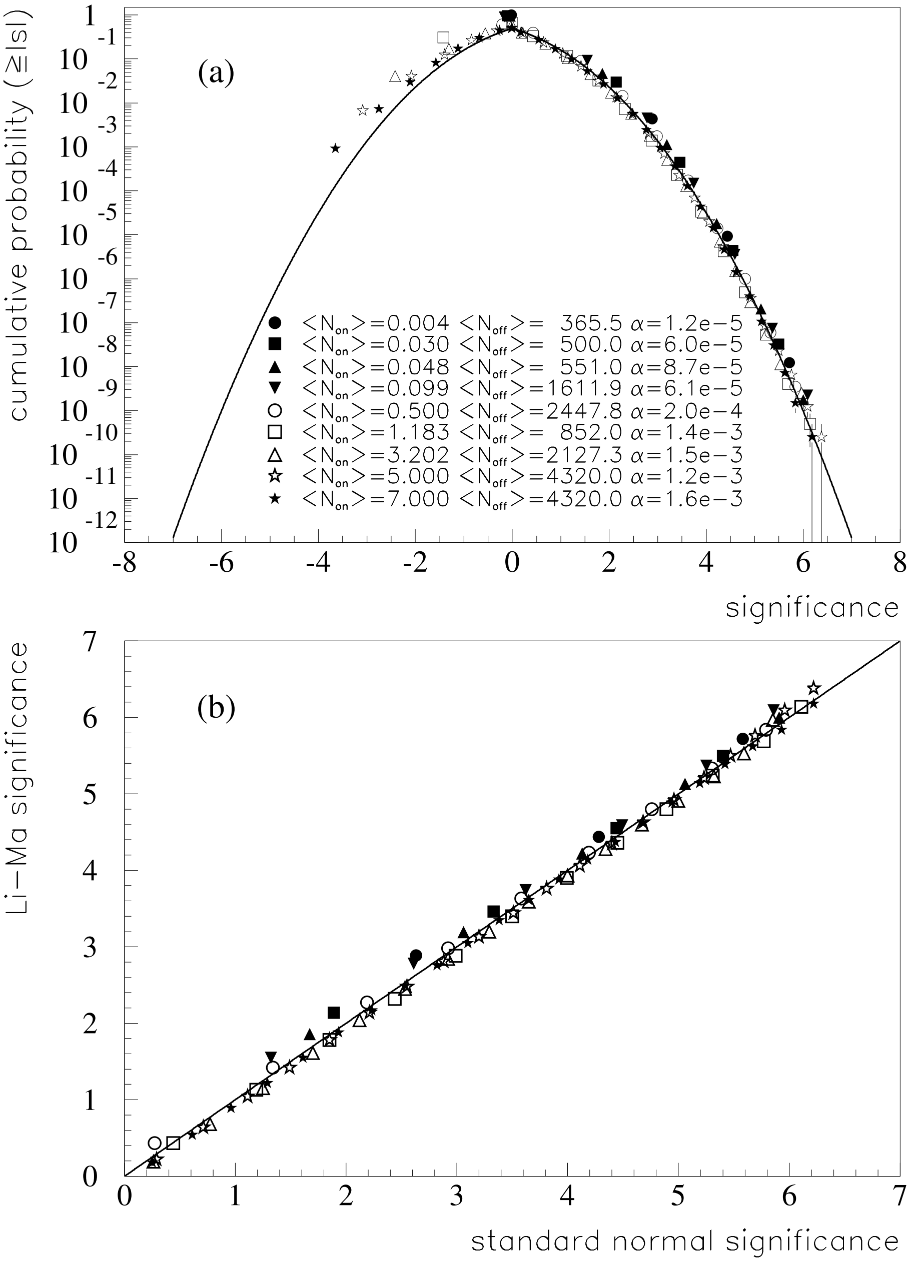

Figure 5.7: (a) The different data points plot the cumulative probability for the occurrence of a measured Li-Ma significance due to background fluctuations for small expected background. The values of $< N_{on} >$, $< N_{off} >$, and α used in the simulations are representative of some of the values measured in this GRB analysis. The solid curve is the distribution of a standard normal significance. For excesses, the Li-Ma significance follows a standard normal distribution well even for small expected background in an on-source bin. (b) Li-Ma significances from part (a) plotted versus the expected standard normal significance.

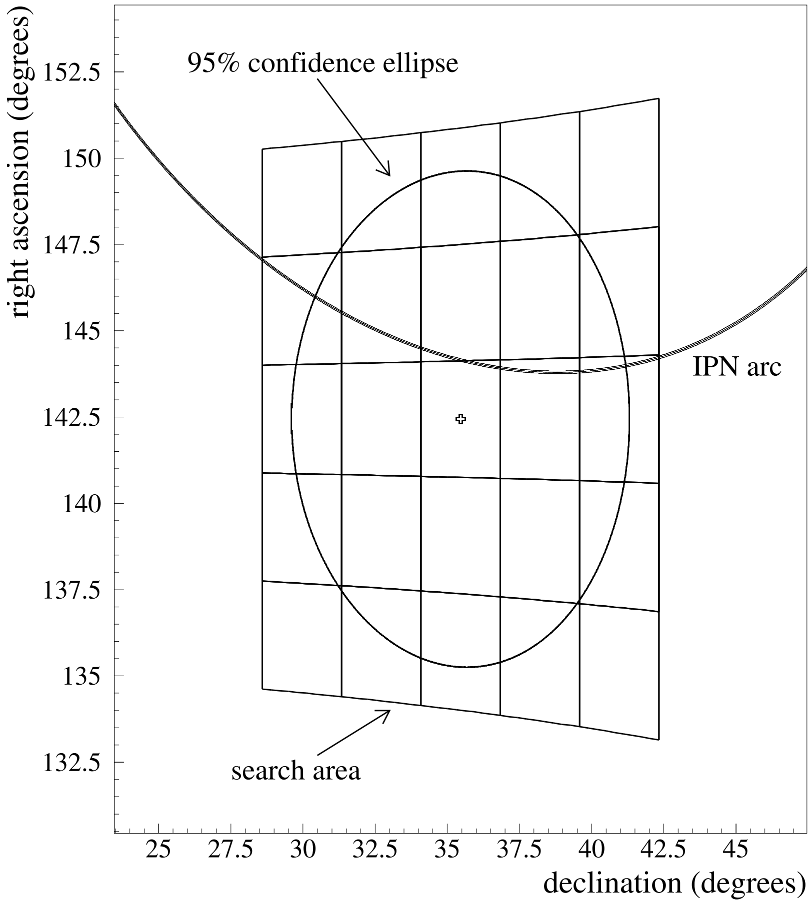

Figure 5.8: Search area and bin configuration used for one of the GRBs examined. The nominal GRB position given in the current BATSE catalog is at the center of the plot.

5.4 Search Area Configuration and Optimal Bin Size

5.4.1 Search area configuration It was shown in Section 5.2 that, owing to large uncertainties in BATSE's measured GRB positions, the search areas used in this analysis were quite large. Clearly, using a single bin on the celestial sphere to search for a source whose position was not accurately known would not have sufficed. Rather, a collection of bins which covered the search area was needed. Figure 5.8 shows the search area configuration for one of the GRBs examined. The 95% confidence area of each GRB was covered with a grid subdivided into bins of a predetermined size. The significance of an excess, if any, measured for each of the bins was then determined. To be efficient at detecting potential sources which lie near bin edges, the method called for shifting the grid half a bin-width in declination, then half a bin width in right ascension, then half a bin-width in both directions. Significance calculations were repeated for the bins at each of these grid configurations.

5.4.2 Trials: A digression into coin-tossing Using several bins to search an extended area of the sky complicates the determination of the significance of an excess. After all, while the odds for finding a needle in a haystack may be quite small, if one looks at enough haystacks one is bound to find the proverbial needle, and would think that the odds were not really small in the first place!

The effect on a significance measurement of using several bins to a search for a source can be understood by considering the simple game of coin-tossing. If the coin volunteered for this game is true, then the probability that heads will show in one toss is one-half,

$$p_o = 0.5 \quad . \tag{5.19}$$

If the coin is tossed N times, then the probability for observing n successes $-$ in this case heads showing n times $-$ is dictated by the binomial distribution,

$$P_n = \frac{N!}{n!(N-n)!} {p_o}^n (1-p_o)^{N-n} \tag{5.20}$$

and the probability for observing one or more successes in N tosses is, therefore,

$$\begin{aligned} P_{n \geq 1} &= P_{n=1} + P_{n=2} + \quad ... \quad + P_{n=N} \\ &= 1 - P_{n=0} \\ &= 1 - (1-p_o)^N \quad . \end{aligned} \tag{5.21}$$

Thus, the probability that heads will show *at least once* in two tosses is 0.75, 0.875 in three tosses, 0.9375 in four tosses, and so on, provided that equation (5.19) holds for each toss.

In an analysis using several non-overlapping bins, the number of bins N can be thought of as analogous to the number of tosses, the cumulative probability for detecting an excess of a certain significance in a bin as p_o, and the the probability for detecting an excess at least as significant as this in at least one bin when N bins are searched, as $P_{n\geq 1}$. Again in the jargon, N is called the number of *trials* in the search, p_o is called the *pre-trials probability*, and $P_{n\geq 1}$ the *post-trials probability*.

However, when the search method described in the previous subsection is used, calculating the post-trials probability is not as simple as using equation (5.21), since the method of shifting the grid results in a collection of overlapping bins and, thus, in non-independent measurements of excesses. The method used in this analysis to determine post-trials probabilities will be discussed further in Chapter 6.

5.4.3 Optimal bin size If there were no detected events due to background, then determining the appropriate bin size to use in the search for a TeV component of a point source whose position is well-localized, say through the detection of the source at another energy regime, would be a trivial matter. The search could utilize as large a bin size as is needed to spatially encompass as much of the source given by equation (5.5) as the searcher wants. But the reality of having to deal with cosmic ray background particles makes the choice of an appropriate bin size a less trivial matter than that. The addition of background to gamma-ray source events limits the bin size that could be used for the search. A needless increase in bin size will result merely in increasing the background event count while only marginally increasing the gamma-ray source event count, if at all. On the other hand, a bin size which is too small will not be very efficient at detecting source events. The goal, therefore, is to find a bin size which will maximize the significance of a measurement.

To find the optimal size of a round bin appropriate for the analysis of a well-localized point source and a normally distributed background measurement, the significance given by equation (5.16) can be maximized,

$$\frac{dS(\gamma)}{d\gamma} = 0 \tag{5.22}$$

$$\Rightarrow \quad \left(1 + \frac{\gamma^2}{\sigma^2}\right) exp(-\gamma^2/2\sigma^2) - 1 = 0 \quad . \tag{5.23}$$

Equation (5.23) has a root at $\gamma/\sigma \approx 1.6$, and thus the optimal bin size in the case of a well-localized source, and in the limit of a large measured background, is:

$$\gamma_{opt} \approx 1.6\sigma \quad . \tag{5.24}$$

Figure 5.9 shows the significance of the excess count for different values of γ/σ in the case of a well-localized point source and normally distributed background fluctuations.

The argute reader who is still awake at this point will note that the optimal radius given by equation (5.24) cannot be used in this analysis because: (1) The GRBs examined in this search do not have accurately-known positions; and, (2) for the short search time intervals used in this analysis, the number of background events expected in a bin is small, so that equation (5.14) is not valid.

The result of using a collection of bins of a certain width to search for a non-localized source is – since the source will not always fall in the center of a bin – to decrease the efficiency of a bin, defined as the ratio of the number of source events which fall into the bin to the total number of source events. Figure 5.10 compares the efficiencies of a round bin centered at a well-localized source, a square bin centered at a well-localized source, and that of a configuration of overlapping grids of square bins in a search for a non-localized source – the configuration used in this analysis. Furthermore, as noted in the previous subsection, using several bins means that the number of trials will have to be considerd in determining a post-trials significance. A bin that is too small might increase the trials considerably and result in a smaller post-trials significance compared to that resulting from a search with larger bins covering the same search area, thus resulting in less trials.

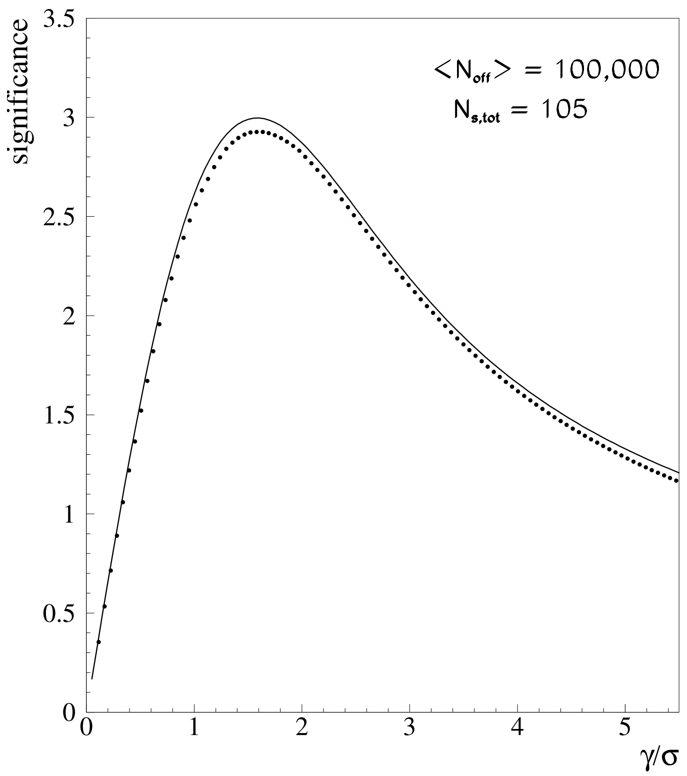

Figure 5.9: Calculated significance as a function of the normalized angular radius, γ/σ, of excess in a round bin used in examining a simulated, well-localized source. The solid line is significance derived from equation (5.16), the dotted line is that derived from equation (5.18). For this plot, the expectation of the background count, $< N_{off} >$, is 100,000 events within a space angle of $\gamma_o = 20\sigma$, and the actual total number of source events from all space, $N_{s,tot}$, is 105.

The small background count expected in a bin means that the bin size can be increased from that given by equation (5.24), since opening up a bin will make it more efficient at detecting source events while only marginally increasing the background count in the bin.

Simulations have been done to study the combined effect of these factors on the optimal bin size. For each bin size considered, the simulation duplicated the bin configuration used in the actual analysis, and assumed a search area of radius 12σ over which a simulated source of known strength was thrown several times. The expectation of the

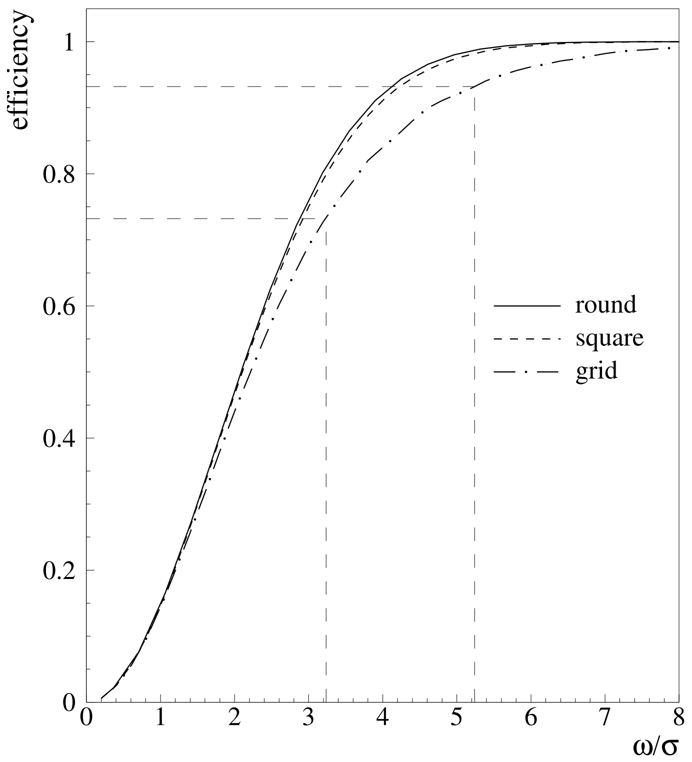

Figure 5.10: Efficiency of a bin configuration as a function of bin width normalized to the angular resolution. The solid curve is for a round bin centered at a well-localized source, and whose radius is converted to the width of a square bin with the same area as the round bin. The short-dashed curve is for a square bin centered at a well-localized source, and the long-dashed-dot curve is for a configuration of overlapping grids of square bins. The guide lines indicate the range of optimal bin widths and the corresponding (ideal) efficiencies of the bins used in this analysis.

background count in an area of size $\approx 35\sigma \times 35\sigma$ was fixed at a certain value and background count fluctuations from the expectation value were generated. The pre-trials Li-Ma significance of the excess in the bin whose center was closest to the source position was calculated. The post-trials significance was determined by generating a background count fluctuation from the expectation value, throwing this number of background events into the $35\sigma \times 35\sigma$ area, and ascertaining if there was at least one bin with an excess which corresponded to a significance larger than the pre-trials significance. The procedure was repeated numerous times and the ratio of the total number of throws which gave rise to at least one significance larger than the pre-trials significance to the total number of throws gave the probability, given the bin configuration, for getting a significance at least as large as the pre-trials significance due to background fluctuations alone. This probability was converted into the corresponding standard normal significance of a single-trial measurement with the same probability of occurrence. The pre-trials and post-trials significances as a function of the bin width for different values of the expected background in a round bin of radius equal to the detector's angular resolution are plotted in Fig. 5.11.

The optimal bin width as a function of expected background in a round bin of radius equal to the detector's assumed angular resolution has been studied in detail and parametrized by Richard Schnee [133] . His parametrization is,

$$\frac{\omega_{opt}}{\sigma} = 3.016 + \frac{2.82 - 0.13ln(< N_b(\sigma) >)}{1 + 3.1\times < N_b(\sigma) >^{0.40}} \quad . \tag{5.25}$$

This is plotted in Fig. 5.12, along with optimal bin sizes obtained from simulations as described in the previous paragraph. Equation (5.25) was used in obtaining the optimal bin widths for this GRB search. The normalized optimal bin widths appropriate for the estimated background counts in this search range from 3.4 to 5.2. The Milagrito angular resolution used was $\sigma = 0.75^o$, a value which biases the search in favor of those events which contribute to the core of the point spread distribution (cf. Section 5.3.1), resulting in optimal bin widths from 2.4^o to 3.9^o. The average Milagrito point spread distribution determined from simulations indicates that the source detection efficiencies of bins in this size range are typically ≈ 0.5 (cf. Fig. 4.22(b)).

5.5 Putting It All Together: Looking for a GRB Signal

The previous sections described much of the logistics required for searching for a TeV component of GRBs: coordinate systems, search area, search duration or time interval, bin configuration and optimal bin size, trials, significance estimation. It remains to

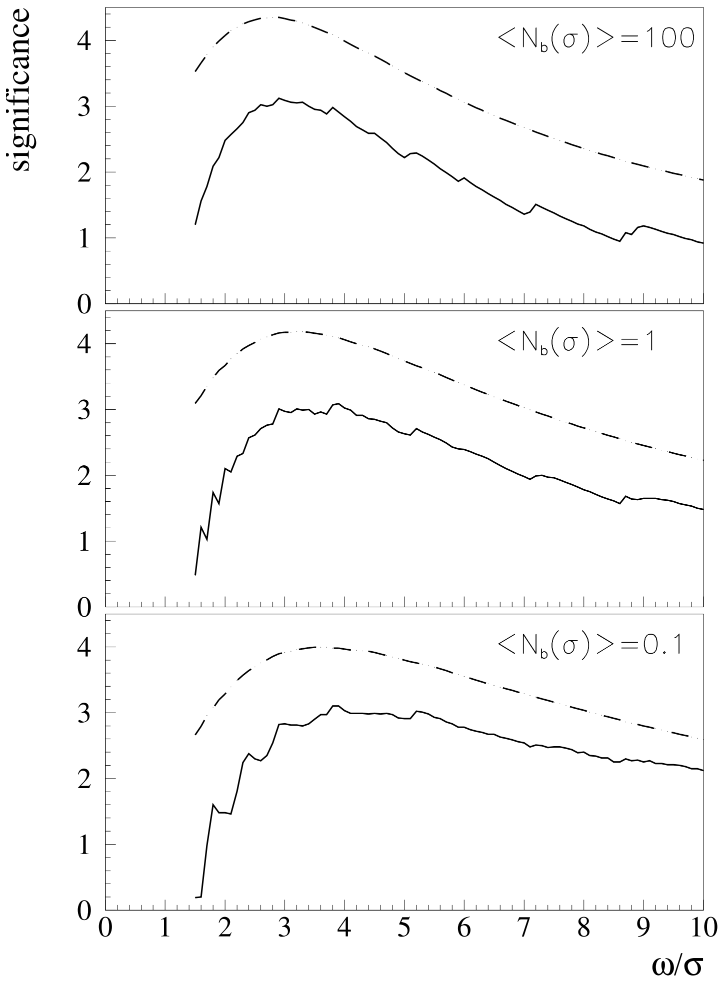

Figure 5.11: Results of simulations showing the increasing optimal bin size as the expected background in a round bin of radius equal to σ decreases. The grid configuration used in the simulations was the same as that used in the search analysis. The dashed curves give the pre-trials significance of the excess in the bin whose center was closest to the source position. The solid curves give the corresponding post-trials significance after taking into account that several non-independent bins were used. The discontinuities in the curves reflect the coarseness of the bins (e.g. as the number of bins in the search area jumped from 49 bins to 25 bins as the bin size increased from one value to the next).

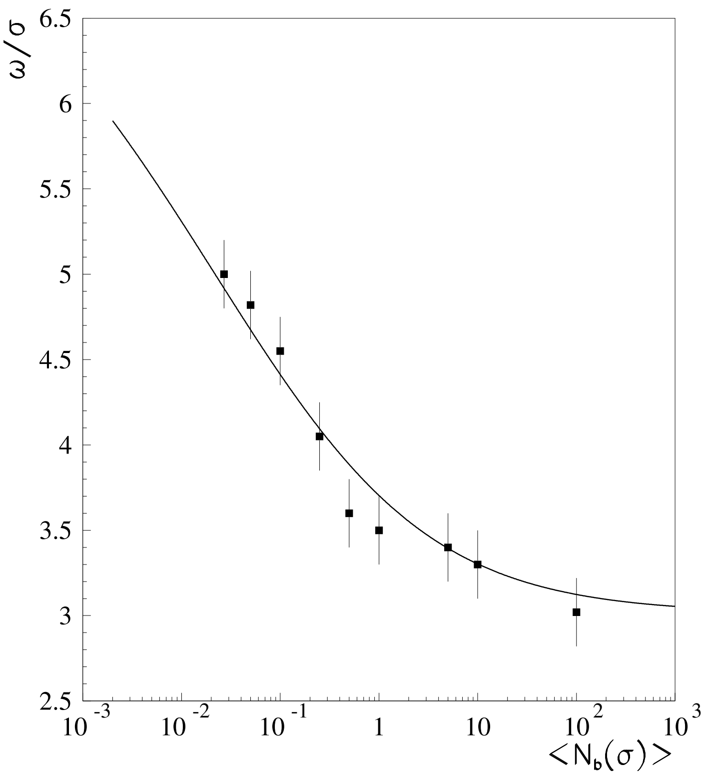

Figure 5.12: Normalized optimal bin width for a search technique utilizing overlapping grids of square bins, as a function of the number of background events, $< N_b(\sigma) >$, expected in a round bin with radius σ, the angular resolution of the detector. The line is from equation (5.25), and the square markers are from simulations.

be seen how an important experimental quantity – the expected average number of background events in each bin – was estimated. As could have been gleaned from the previous sections, an accurate determination of the expected average number of background events in each bin is essential in searches like this in which the existence or non-existence of a signal is decided by tallying the number of events detected above the background level, and comparing this count to the expected background. Details of the procedure used in this analysis for background estimation will now be described.

5.5.1 Background estimation Figure 5.8 shows how a celestial search area for a GRB was covered by a grid of non-overlapping bins. The center of each of these bins was located through its equatorial coordinates (δ,α). At the middle of the GRB T90 search time interval $-$ which shall be called the "burst time" $-$ each of these (δ,α) bins was mapped onto the corresponding local (θ,ϕ) bin of the sky, and an estimate of the expected background count during T90 made for each of these (θ,ϕ) bins. In this procedure, the motion of the celestial sphere relative to the local sky during T90 was ignored, an approximation which is valid in the limit of short time intervals, since the celestial sphere rotates about its axis at a slow rate of $\approx 0.25^o$ per minute.

Milagrito air shower events occurring within a six-hour interval centered at the burst time, but excluding events occurring during the T90 search time interval, were put into time bins of duration T90 each. At the center of each time bin, the equatorial (δ,α) bin corresponding to each local (θ,ϕ) bin was calculated. This can be imagined as moving the celestial sphere relative to the local sky by an amount $\approx (0.25^o/minute)T90$ after every T90 time increment, and resetting the (δ,α) bin center locations to those which overlap the local (θ,ϕ) bin centers. Thus, there was only one set of local (θ,ϕ) bins, but several sets of equatorial (δ,α) bins $-$ one set for each time bin. Each event from the current time bin was examined and it was determined if the event came from any of the current equatorial (δ,α) bins. If so, the event count for the corresponding (θ,ϕ) bin was incremented. Finally, the total number of events from the six-hour interval falling into each local (θ,ϕ) bin, $N_{off}(\theta,\phi)$, was tallied. The background estimate for each (θ,ϕ) bin during the T90 search time interval was then calculated using,

$$N_b(\theta,\phi,t) = \frac{N_{off}(\theta,\phi)}{N_{tot}} \begin{cases} R(t)T90 & \text{if T90} < \text{10 seconds} \quad , \\ N_{T90}(t) & \text{if T90} > \text{10 seconds} \quad ; \end{cases} \tag{5.26}$$

where N_{tot} was the total number of events detected from the entire sky during the six-hour period, $R(t)$ was the measured average all-sky event rate during a two-minute time interval centered at the burst time, and N_{T90} was the all-sky event count during T90 centered at the burst time. It will be noted that the ratio $N_{off}(\theta,\phi)/N_{tot}$ is the efficiency of the (θ,ϕ) bin for detecting cosmic-ray events. The use of the all-sky event rate for the background calculation in the case of $T90 < 10$ seconds was protection against large statistical uncertainties which result when the event count is low. This background estimation procedure was repeated for each of the four grids used in the search (see Section 5.4.1 for a description of the grids).

In essence, the background estimation procedure just described assumes an isotropic distribution of cosmic ray events on the celestial sphere, and that this isotropic distribution gets weighted by atmospheric overburden to result in a zenith-dependent, and probably azimuth-dependent, background distribution. It also assumes that the spatial dependence and time dependence of the background distribution can be completely separated.

Given a GRB search area and search time interval, the appropriate optimal bin size was determined by covering the search area by a grid of square bins of width 3^o each. The expected background in each bin during the T90 search time interval was estimated using the procedure described above. The average expected background in a 3^o-width square bin was then calculated, converted into an average expected background in a 0.75^o-radius round bin, which was in turn used in equation (5.25) to calculate an optimal bin width for that search area and search time interval.

5.5.2 Looking for the signal Once the expected average background count for each (δ,α) bin during T90 was determined, it remained to count the actual total number of air shower events, $N_{on}(\delta, \alpha)$, which came from each (δ,α) bin in the search area during the T90 search time interval. When this was accomplished, the Li-Ma significance of any excess was calculated, and the significance of the most significant excess from a GRB search area was taken as the pre-trials significance for that GRB.

Results of the search for TeV emission from the 54 BATSE GRBs are presented in the next chapter.

Table 5.1: The 54 BATSE GRBs used in this analysis. Data are from the current BATSE catalog [10], except for the zenith angles.

BATSE GRB	BATSE trigger number	BATSE truncated[a] Julian date	BATSE UT time[b] (seconds)	BATSE declination[c] (degrees)	BATSE right[c] ascension (degrees)	Milagrito zenith angle (degrees)	BATSE T90[d] (seconds)	BATSE total[d] fluence (E>20 KeV) (ergs/cm^2)
970223	6100	10502	30377.6735	35.46	142.44	24.89	16.256	7.85×10^{-5}
970317	6128	10524	84027.8495	68.90	111.75	43.65	69.952	4.00×10^{-6}
970318	6129	10525	30240.2015	56.24	135.24	44.61	–	–
970330	6148	10537	51074.7615	2.26	304.60	34.99	–	4.23×10^{-6}
970408	6165	10546	7575.2415	10.69	162.62	45.02	68.032	3.76×10^{-6}
970408	6166	10546	21449.6735	7.39	167.97	30.29	0.192	7.97×10^{-8}
970409	6167	10547	67689.1615	36.30	15.07	1.37	61.696	9.21×10^{-6}
970417	6188	10555	50016.7135	55.77	295.66	21.45	7.936	3.95×10^{-7}
970426	6209	10564	43113.6735	59.43	312.70	28.65	–	3.37×10^{-6}
970429	6213	10567	25909.3215	11.04	225.39	25.58	–	–
970503	6219	10571	20769.3535	70.18	170.66	37.99	2.752	1.47×10^{-7}
970511	6229	10579	54007.8815	19.69	0.50	19.66	26.368	–
970523	6240	10591	82890.4415	43.87	111.08	10.68	–	2.19×10^{-5}
970603	6251	10602	84900.2975	62.31	177.05	35.15	3.008	4.45×10^{-6}
970612	6265	10611	26311.1775	8.42	272.62	28.66	0.199	7.81×10^{-7}
970612	6267	10611	74290.8895	62.15	117.57	27.59	12.864	1.06×10^{-6}

[a] Truncated Julian Date = Julian Date - 2440000.5.

[b] Time of BATSE trigger.

[c] J2000 epoch.

[d] A dash indicates that no data was available from the current BATSE catalog.

Table 5.1 continuation.

BATSE GRB	BATSE trigger number	BATSE truncated[a] Julian date	BATSE UT time[b] (seconds)	BATSE declination[c] (degrees)	BATSE right[c] ascension (degrees)	Milagrito zenith angle (degrees)	BATSE T90[d] (seconds)	BATSE total[d] fluence (E>20 KeV) (ergs/cm^2)
970627	6279	10626	3865.2895	39.98	227.74	33.91	32.512	7.14×10^{-6}
970629	6288	10628	51399.8815	25.04	29.62	11.49	13.184	2.38×10^{-6}
970707	6295	10636	7855.5855	7.38	191.97	33.47	180.480	6.59×10^{-6}
970709	6300	10638	24908.5135	32.62	263.03	17.91	63.168	4.53×10^{-7}
970713	6305	10642	75437.7935	58.45	127.12	24.00	25.792	7.76×10^{-7}
970725	6317	10654	17470.9455	48.97	286.42	18.22	7.744	8.33×10^{-7}
970802	6323	10662	60901.0895	-1.98	101.97	38.00	20.352	2.00×10^{-6}
970803	6325	10663	66536.8655	59.80	146.37	28.29	–	–
970817	6338	10677	86288.6735	50.50	246.11	24.21	0.768	5.46×10^{-7}
970903	6358	10694	41929.0575	13.89	17.60	36.92	1.856	–
970906	6366	10697	9999.0735	57.61	220.33	44.56	–	1.86×10^{-5}
970910	6376	10701	41169.0575	32.14	100.51	38.03	1.320	2.10×10^{-7}
970918	6385	10709	34886.0495	40.18	31.49	5.60	0.896	2.29×10^{-7}
970925	6396	10716	25445.0895	54.60	346.97	21.92	52.672	2.83×10^{-6}
971015	6437	10736	78236.1295	28.43	192.63	43.45	9.408	4.56×10^{-7}
971016	6439	10737	41696.6095	49.32	51.78	32.11	0.256	9.58×10^{-8}
971021	6443	10742	61697.1855	3.41	147.03	44.86	6.592	1.07×10^{-6}
971110	6472	10762	68006.8815	50.37	241.67	18.09	195.200	2.67×10^{-4}
971122	6492	10774	77351.6495	78.47	300.49	43.66	–	–

Table 5.1 continuation.

BATSE GRB	BATSE trigger number	BATSE truncated[a] Julian date	BATSE UT time[b] (seconds)	BATSE declination[c] (degrees)	BATSE right[c] ascension (degrees)	Milagrito zenith angle (degrees)	BATSE T90[d] (seconds)	BATSE total[d] fluence (E>20 KeV) ($ergs/cm^2$)
971207	6523	10789	37493.4735	3.38	95.07	43.13	36.288	2.79×10^{-6}
971210	6529	10792	77005.5375	32.71	253.48	33.26	37.184	9.00×10^{-7}
971225	6545	10807	64834.0175	64.65	265.12	29.11	–	3.56×10^{-6}
980124	6577	10837	70176.2255	45.51	8.69	44.74	22.784	1.96×10^{-6}
980125	6581	10838	74368.7375	35.81	350.68	18.21	–	4.88×10^{-5}
980207	6590	10851	17052.3855	5.80	101.27	30.08	114.112	1.16×10^{-5}
980213	6599	10857	60363.4895	68.09	251.84	38.12	–	4.22×10^{-6}
980222	6610	10866	8734.9455	28.51	31.21	42.76	71.936	4.36×10^{-6}
980223	6613	10867	45882.0815	27.94	219.85	17.08	42.368	5.91×10^{-7}
980301	6619	10873	22018.7855	34.88	148.36	3.73	35.968	6.16×10^{-6}
980315	6641	10887	10197.9215	20.36	75.84	32.39	2.624	5.94×10^{-7}
980329	6665	10901	13478.4974	39.44	105.58	24.12	18.560	8.26×10^{-5}
980329	6666	10901	37860.3214	59.15	273.69	32.93	11.008	1.48×10^{-6}
980401	6672	10904	16313.9534	18.27	125.70	28.20	27.904	7.81×10^{-6}
980404	6679	10907	68090.2094	11.80	0.00	25.71	1.408	2.62×10^{-6}
980420	6694	10923	36412.3854	26.56	292.81	34.75	39.936	2.48×10^{-5}
980424	6702	10927	5523.1694	5.18	93.33	44.39	44.736	1.03×10^{-5}
980430	6716	10933	28910.3054	28.93	241.23	10.51	–	1.53×10^{-6}
980503	6720	10936	7588.5774	15.11	115.96	33.73	40.256	1.49×10^{-6}

Chapter 6

Results of Search for a TeV Component of GRBs

The results of the analysis of the 54 BATSE GRBs for TeV gamma-ray emission coincident with the keV-MeV emission observed by BATSE will be presented in this chapter. The pre-trials and post-trials probability distributions for the most significant excesses will be shown, from which it will be seen that one GRB search area resulted in an outlier from the main distribution. The final significances of the measured excesses will then be calculated and presented, together with a preemptive guide to the meaning of the presented significances. Finally, the procedure for calculating flux limits will be outlined and the resulting limits given.

6.1 Pre-Trials and Post-Trials Significance

6.1.1 Pre-trials significance: Most significant bin excess Figure 6.1(a) is the distribution of the significance of the most significant measured excess from each GRB search area. Figure 6.1(b) gives the distribution of the cumulative Poisson probability for the occurrence of the measured on-source count or larger in the most significant bin from each GRB search area, given the expected background in that bin. Details of the measurements for each bin are given in Table 6.1.

It can be seen from the distributions that one GRB search area, that of GRB 970417a, gave rise to a bin which had an excess with a pre-trials significance of 5.2 standard deviations. For the search time interval of 7.9 seconds, this particular bin had an on-source count of 17 events, off-source count of 9229 events, $\alpha = 3.689 \times 10^{-4}$, and an estimated background of 3.41 events. This means that the cumulative Poisson probability for the occurrence of the on-source count or larger given the estimated background is 1.3×10^{-7}. More details about the analysis of this GRB will be given in Chapter 7. Much of the remainder of this current chapter will be spent discussing the procedure for determining the final significance of this most significant excess from GRB 970417a, as well as that of the other excesses measured.

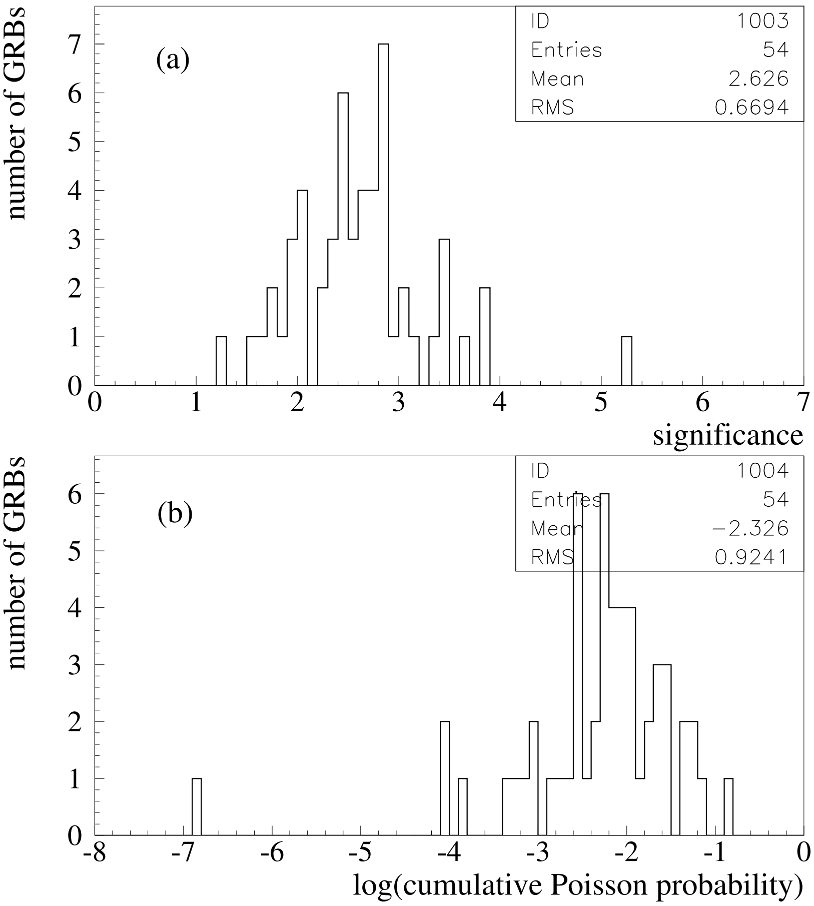

Figure 6.1: (a) Distribution of significance of the most significant excess from each GRB search area. The Li-Ma significance, equation (5.18), was used. (b) Distribution of cumulative Poisson probability for the occurrence of the measured on-source count or larger in the most significant bin given the estimated background in that bin. The most significant measurement has a significance of 5.2 standard deviations and a cumulative Poisson probability of 1.3×10^{-7}.

Table 6.1: Most significant bin from each GRB search area.

BATSE GRB	BATSE trigger number	declination[a] (degrees)	right[a] ascension (degrees)	T90[b] (seconds)	N_b[c]	N_{on}[d]	S[e]	cumulative[f] Poisson probability
970223	6100	36.83	140.72	16.256	4.65 ± 0.10	12	2.84	3.1×10^{-3}
970317	6128	70.28	124.04	69.952	3.24 ± 0.15	7	1.80	4.7×10^{-2}
970318	6129	47.54	152.42	30.000	5.13 ± 0.11	11	2.24	1.6×10^{-2}
970330	6148	7.75	300.44	30.000	7.07 ± 0.13	13	1.99	2.9×10^{-2}
970408	6165	13.39	157.06	68.032	9.7 ± 0.2	15	1.56	7.0×10^{-2}
970408	6166	9.34	171.92	0.192	0.133 ± 0.002	2	2.66	8.1×10^{-3}
970409	6167	41.30	16.73	61.696	27.2 ± 0.4	43	2.79	3.1×10^{-3}
970417	6188	54.34	290.77	7.936	3.41 ± 0.04	17	5.24	1.3×10^{-7}
970426	6209	64.77	306.43	30.000	7.63 ± 0.13	16	2.64	5.4×10^{-3}
970429	6213	20.26	218.37	30.000	12.8 ± 0.2	23	2.57	6.2×10^{-3}
970503	6219	70.18	185.12	2.752	0.844 ± 0.011	4	2.48	1.09×10^{-2}
970511	6229	26.24	9.26	26.368	10.4 ± 0.2	21	2.88	2.5×10^{-3}
970523	6240	52.98	100.27	30.000	9.5 ± 0.2	18	2.44	9.0×10^{-3}
970603	6251	67.14	168.76	3.008	0.865 ± 0.012	3	1.79	5.7×10^{-2}
970612	6265	18.17	272.62	0.199	0.1548 ± 0.0015	3	3.48	5.5×10^{-4}
970612	6267	66.37	114.06	12.864	3.43 ± 0.08	7	1.69	6.0×10^{-2}

[a] Coordinates of center of bin with the most significant excess (J2000 epoch).

[b] Search time interval. For GRBs with no T90 specified in the BATSE catalog, a search time interval of 30 seconds was used.

[c] Estimated mean number of background events in most significant bin. The given errors are statistical uncertainties.

[d] On-source count in most significant bin.

[e] Significance of excess count in most significant bin.

[f] Cumulative Poisson probability for count to fluctuate to N_{on} or larger given N_b.

Table 6.1 continuation.

BATSE GRB	BATSE trigger number	declination (degrees)	right ascension (degrees)	T90 (seconds)	N_b	N_{on}	S	cumulative Poisson probability
970627	6279	41.33	216.97	32.512	10.3±0.2	23	3.41	4.2×10^{-4}
970629	6288	30.48	35.93	13.184	5.86±0.12	13	2.54	7.4×10^{-3}
970707	6295	14.79	190.69	180.480	45.2±0.7	60	2.09	2.0×10^{-2}
970709	6300	32.62	273.51	63.168	26.2±0.3	43	2.99	1.6×10^{-3}
970713	6305	62.45	112.72	25.792	6.41±0.12	12	1.96	3.1×10^{-2}
970725	6317	56.15	278.69	7.744	2.91±0.04	9	2.85	3.2×10^{-3}
970802	6323	0.83	100.56	20.352	4.28±0.09	10	2.35	1.2×10^{-2}
970803	6325	55.76	163.13	30.000	5.49±0.11	11	2.06	2.5×10^{-2}
970817	6338	68.00	278.81	0.768	0.108±0.002	2	2.81	5.5×10^{-3}
970903	6358	20.65	37.47	1.856	1.030±0.011	7	3.86	1.00×10^{-4}
970906	6366	54.79	227.66	30.000	4.70±0.12	11	2.46	9.1×10^{-3}
970910	6376	42.62	86.27	1.320	0.708±0.008	5	3.31	8.3×10^{-4}
970918	6385	33.56	37.45	0.896	0.674±0.006	4	2.76	5.0×10^{-3}
970925	6396	63.54	4.17	52.672	14.6±0.2	23	2.04	2.5×10^{-2}
971015	6437	39.05	184.82	9.408	1.02±0.02	7	3.87	9.4×10^{-5}
971016	6439	82.73	129.48	0.256	0.0387±0.0007	2	3.44	7.3×10^{-4}
971021	6443	−2.80	148.58	6.592	0.68±0.02	4	2.74	5.3×10^{-3}
971110	6472	51.58	235.81	195.200	69.3±1.1	91	2.47	7.0×10^{-3}
971122	6492	75.65	323.26	30.000	3.40±0.08	6	1.27	1.3×10^{-1}

Table 6.1 continuation.

BATSE GRB	BATSE trigger number	declination (degrees)	right ascension (degrees)	T90 (seconds)	N_b	N_{on}	S	cumulative Poisson probability
971207	6523	10.34	96.49	36.288	6.03 ± 0.12	11	1.81	4.4×10^{-2}
971210	6529	24.71	257.88	37.184	7.96 ± 0.14	16	2.50	7.9×10^{-3}
971225	6545	56.65	260.27	30.000	11.3 ± 0.2	20	2.32	1.2×10^{-2}
980124	6577	39.74	19.95	22.784	1.02 ± 0.04	5	2.81	4.1×10^{-3}
980125	6581	34.51	341.22	30.000	14.6 ± 0.2	25	2.48	8.0×10^{-3}
980207	6590	2.09	101.27	114.112	28.2 ± 0.4	46	3.05	1.3×10^{-3}
980213	6599	72.15	247.43	30.000	4.97 ± 0.10	10	1.98	3.1×10^{-2}
980222	6610	33.75	26.49	71.936	8.1 ± 0.2	17	2.70	4.4×10^{-3}
980223	6613	43.21	239.05	42.368	23.3 ± 0.3	43	3.65	1.6×10^{-4}
980301	6619	41.38	157.02	35.968	11.6 ± 0.2	24	3.17	9.5×10^{-4}
980315	6641	25.09	70.62	2.624	0.877 ± 0.011	5	3.03	2.1×10^{-3}
980329	6665	32.84	108.72	18.560	9.8 ± 0.2	18	2.33	1.2×10^{-2}
980329	6666	52.12	259.95	11.008	6.45 ± 0.11	15	2.87	2.7×10^{-3}
980401	6672	13.07	132.37	27.904	12.1 ± 0.2	22	2.54	6.8×10^{-3}
980404	6679	16.55	358.35	1.408	1.113 ± 0.010	5	2.69	5.7×10^{-3}
980420	6694	35.74	289.58	39.936	14.6 ± 0.2	23	2.04	2.5×10^{-2}
980424	6702	3.83	90.62	44.736	4.41 ± 0.10	10	2.28	1.5×10^{-2}
980430	6716	40.48	231.11	30.000	17.0 ± 0.2	30	2.84	2.7×10^{-3}
980503	6720	6.89	109.06	40.256	2.46 ± 0.07	8	2.79	3.9×10^{-3}

6.1.2 Post-trials significance The post-trials significance of the most significant excess from each GRB search area was determined by applying the GRB search analysis to Milagrito data using the same local area of the sky as in the real search, but using different "burst times." That is, the local (θ,ϕ) coordinates of the bins used in the fake search were the same as in the real search, but portions of the celestial sphere which were different from the actual area used in the real search were examined. For each fake GRB search, the size of the search area, the number of bins, the search time interval, were all kept the same as in the real search. And for each fake search, the most significant excess from the search area was taken and histogrammed. The resulting histograms of the largest significances found from fake searches for six of the GRBs are shown in Figure 6.2. The arrows in the histograms point to the pre-trials significance for the GRBs from the real search.

Given a GRB search configuration – i.e. the size of the search area, the number of bins, the search time interval, the background distribution (which varies with time) in the local area of the sky searched – the probability that background fluctuations would give rise to a significance at least as significant as the GRB's pre-trials significance was given by the ratio of the number of fake searches resulting in a most significant excess larger than or equal to the pre-trials significance, to the total number of fake searches done for that GRB search configuration. Since actual data was used for this calculation, it also served as a check for any systematic errors in the data. These probabilities are plotted in Figure 6.3.

It can be seen from Figure 6.3 that, after considering the search configuration used in the analysis of GRB 970417a, the probability for getting a pre-trials significance of 5.2 standard deviations or larger due to background fluctuations is 2.6×10^{-5}. A single-trial measurement with this probability corresponds to a significance of 4.2 standard deviations.

Note that the probability for getting a pre-trials significance of at least 5.2 using a search configuration different from that of GRB 970417a will not necessarily be the same as the one obtained above. To determine the final probabilities, one has to factor in the fact that there were 54 different search configurations used in the real analysis.

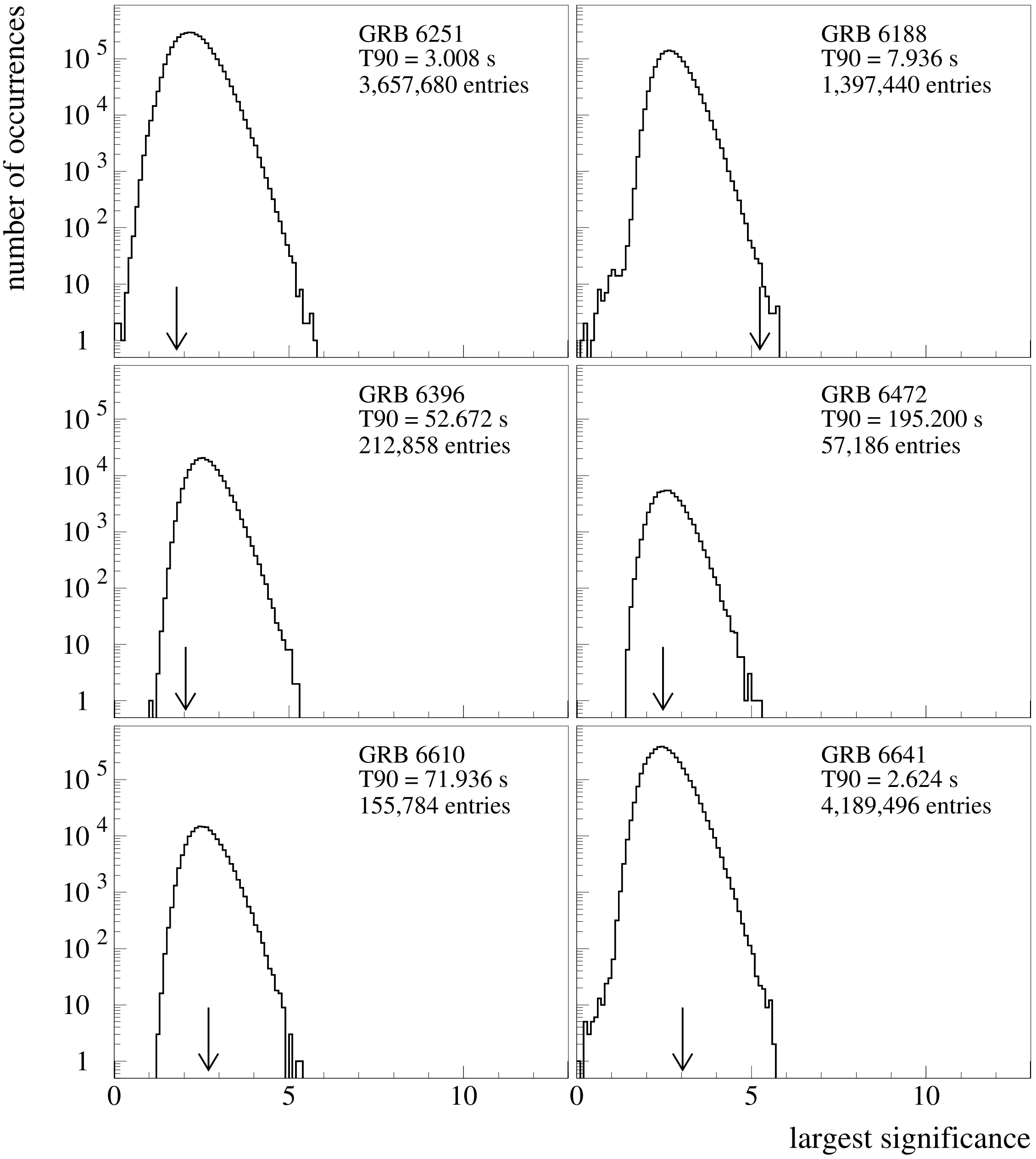

Figure 6.2: Histograms of largest significances found in performing fake searches using six GRB search configurations. An arrow indicates the pre-trials significance for each GRB from the real search. A histogram per GRB search configuration was generated to determine post-trials probabilities.

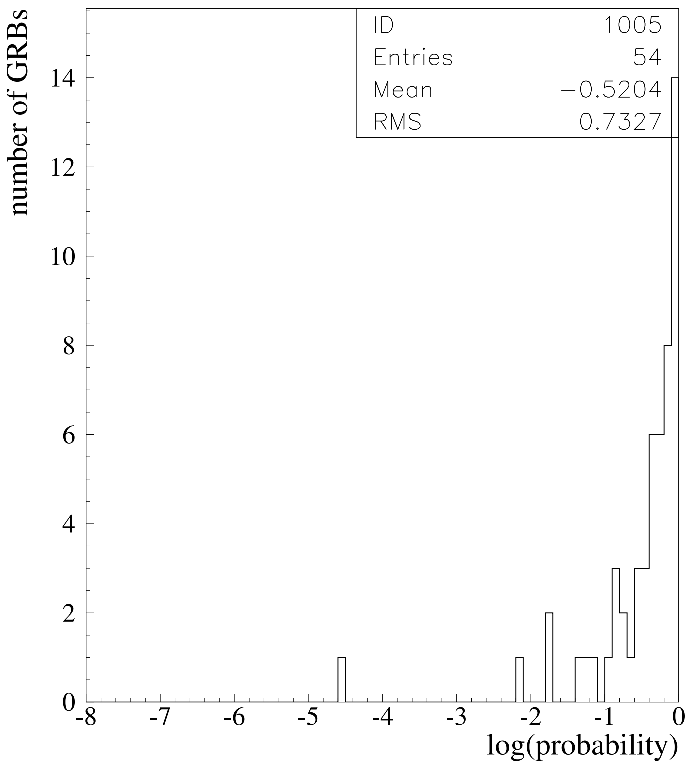

Figure 6.3: Post-trials probabilities for the occurrence of the pre-trials significances due to background fluctuations.

6.2 Final Significance

If one repeated the search analysis several times using 54 search configurations each time, one would expect that, under the null hypothesis, the resulting post-trials probabilities from the 54 search configurations would be uniformly distributed between zero and one. The log-log plot of integral number of occurrences of a post-trials probability versus the post-trials probability would thus be a line with a slope of 1.0 and a y-intercept equal to log(54). This is shown in Fig. 6.4 (dashed line). That is, the integral number of post-trials probabilities is $n(\leq p) = 54p$.

Also shown in Fig. 6.4 (solid line) is the integral number of occurrences of post-

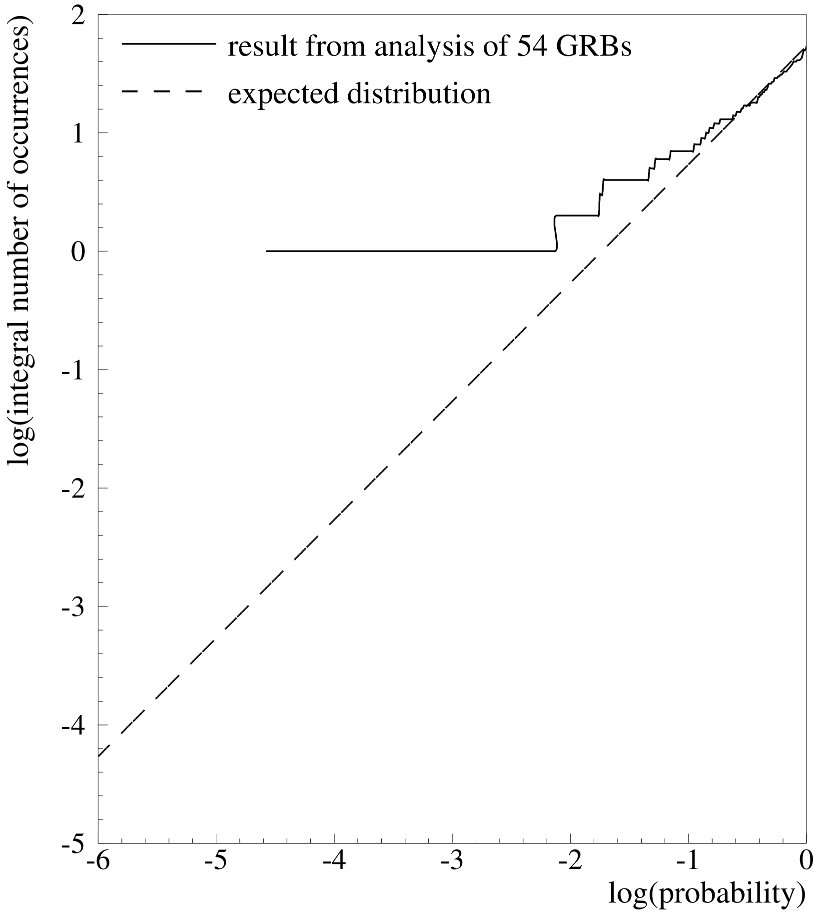

Figure 6.4: Integral distribution of post-trials probabilities.

trials probabilities from the real search (cf. Fig. 6.3). It can be seen that the tail of this line deviates from the expected distribution. Since the expected distribution is known, the final probabilities of the measured excesses can be calculated. The plot shows that the probability of occurrence from a search configuration of a post-trials probability p or less due to background fluctuations is $n(\leq p)/54 = p$, *regardless of which search configuration is considered*. Since there were 54 search configurations considered, the final probability for "success" (getting a post-trials probability of p or less) in at least one search configuration is given by the binomial distribution,

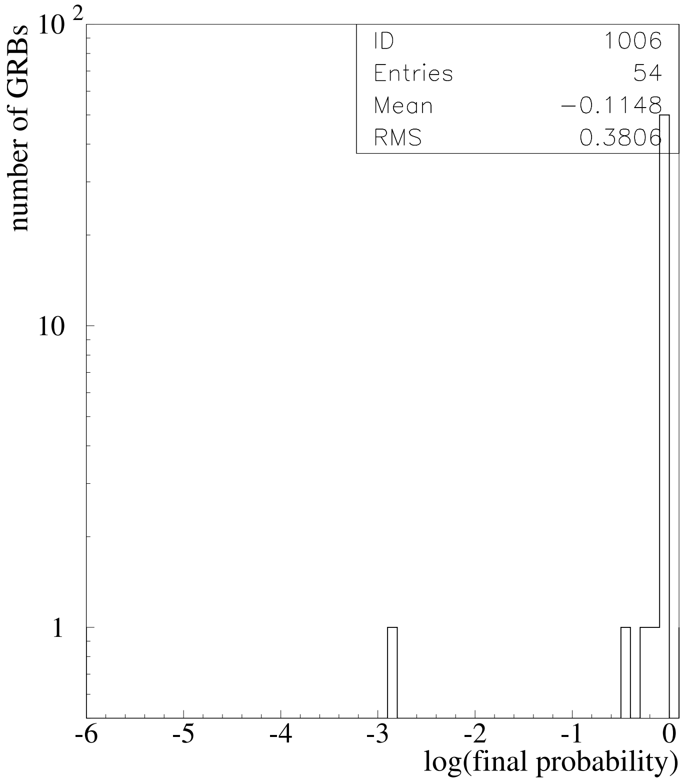

Figure 6.5: Final probabilities of the most significant excesses.

$$P_f(\leq p) = 1 - (1 - p)^{54} \tag{6.1}$$

The corresponding final probabilities of the most significant excesses found from the GRB search areas are plotted in Figure 6.5.

It can be seen from Figure 6.5 that, after considering the trials used, almost all of the most significant excesses found from the GRB search configurations have final probabilities close to or equal to unity, or a significance of zero. The most significant excess from the search configuration of GRB 970417a has a final probability of 1.4×10^{-3}. A single-trial measurement with this probability corresponds to a significance of 3.2 standard deviations.

6.3 What All The Numbers Mean

The coin was tossed and it was tossed several times. Ten tosses of a true coin ensures a large probability that one will see heads.

In the case of this GRB analysis, it has been seen that, given the number of degrees of freedom (or, one might say, the amount of effort) used, excesses with significances up to 4.0 standard deviations were not difficult to find, and that most of these initial significances were just as easily reduced to zero after considering the liberties that were allowed in the analysis. Certainly, after all the trials were counted, only one measured excess – the one from GRB 970417a's search area – was left with a final significance of note.

It was shown that the initial significance of 5.2 standard deviations for the excess found in the search configuration of GRB 970417a was reduced to a significance of 4.2 after considering the non-independent trials in the search configuration. It was also shown that one in ~ 700 analyses of 54 search configurations will give rise to at least one occurrence of a significance of 4.2 or larger due to backround fluctuations, making the final significance of the most significant excess measured equal to 3.2 standard deviations.

6.4 Upper Limits on GRB Flux at the Top of the Atmosphere

When no significant excess from a potential gamma-ray source is detected by an air-shower detector such as Milagrito, determining an upper limit on the gamma-ray flux or fluence at the top of the atmosphere for the source serves to quantify the sensitivity of the detector. An upper limit on gamma-ray flux or fluence for a particular type of source by a certain detector is a number which can be directly compared to that of other experiments, provided that the experiments converge on the definition of an upper limit. This section will outline the procedure used for determing Milagrito 90% upper limits on GRB flux, and will present the results.

6.4.1 Method of calculating GRB flux upper limits The differential flux of gamma-ray particles at the top of the atmosphere is defined as the number of gamma-ray particles per unit area per unit time per unit photon energy,

$$\frac{dF}{dE} = \frac{dN}{dA\,dt\,dE} \quad . \tag{6.2}$$

For the purpose of calculating flux limits, it shall be assumed that a GRB flux at the top of the atmosphere at TeV energies follows a power law, that is,

$$\frac{dF}{dE} = F_o E^{-\eta} \quad , \tag{6.3}$$

where F_o and η are constants, i.e. the flux normalization and the spectral shape are assumed to be constant with time. For each bin with an excess in a GRB search area, a 90% upper limit on the flux normalization F_o can be set by using the measured on-source count and estimated background for that bin during T90 to calculate a 90% upper limit on the possible number of signal events, N_{90}. N_{90} and the corresponding 90% upper limit on F_o are related by,

$$N_{90}(\theta,\phi) = \epsilon \Delta T \int_{E_o}^{E_c} \frac{dF}{dE} A_{eff}(E,\theta) dE \tag{6.4}$$

$$= \epsilon \Delta T F_o(\theta,\phi) \int_{E_o}^{E_c} E^{-\eta} A_{eff}(E,\theta) dE \quad , \tag{6.5}$$

where ϵ is the efficiency of the bin for detecting source events (cf. Fig. 4.22(b) of Chapter 4), ΔT is the burst duration (i.e. T90), A_{eff} is the effective area of the Milagrito detector, which is a function of both primary energy and zenith angle (cf. Fig. 4.20 of Chapter 4), E_o is the threshold energy for the Milagrito detector, and E_c is an assumed cutoff energy for the GRB flux at the top of the atmosphere. For most GRB search areas, the bin size used was such that $\epsilon \approx 0.5$. The threshold energy of Milagrito for small zenith angles, $\theta \lesssim 25^o$, and for a 100-tube trigger requirement, was $E_o \sim 0.3$ TeV, and increased with increasing zenith angle (cf. Fig. 4.20 of Chapter 4).

The flux upper limit will clearly depend on the chosen cutoff energy, E_c, and on the chosen differential spectral index, η. The smaller the cutoff energy, or the larger η is, the larger the flux upper limit will be, since either trend will effectively preclude using the entire range of gamma-ray energies to which the Milagrito detector is sensitive. Thus, Milagrito effectively becomes a less sensitive detector with small energy cutoffs or large spectral indices. In this analysis, cutoff energies of $E_c = \infty$ (no cutoff or, more accurately, $E_c = 10^6$ TeV was used in the numerical integration) and $E_c = 5$ TeV, and spectral indices of $\eta = 2.0$ and $\eta = 2.5$ are used. These are sufficient for calculating representative flux limits.

The 90% upper limit on the number of signal events, N_{90}, is defined as that number which satisfies [134]

$$1 - CL = 0.1 = A_{norm} \int_{N_{90}}^{\infty} \int_{0}^{\infty} p(N_{on}|N, B) f(B) dB dN \quad , \tag{6.6}$$

where

$CL = 0.9$ is the desired confidence level,

B is a possible value of the mean background count in the bin during T90,

N_{on} is the on-source count for the bin during T90,

N is a possible value of the number of signal events during T90,

$p(N_{on}|N, B)$ is the Poisson probability for observing N_{on} counts given N and B,

$f(B)$ is the probability density function for the mean background count in the bin during T90, and

A_{norm} is a normalization constant.

Typically, the relative uncertainty in the estimated mean background count N_b, σ_B/N_b, is about 2% and less than 5% (cf. Table 6.2). Then,

$$\frac{\sigma_B^2}{N_{on}} < \frac{\sigma_B^2}{N_b} \approx 0.02\sigma_B < 0.02 \tag{6.7}$$

$$\implies \quad \frac{\sigma_B^2}{N_{on}} \ll 1 \quad . \tag{6.8}$$

The second inequality in equation (6.7) holds since for the background measurements made in this work, $\sigma_B \lesssim 1$ (see Tables 6.1 and 6.2). Since equation (6.8) holds, equation (6.6) can be well approximated by,

$$1 - CL = 0.1 \approx A_{norm} \int_{N_{90}}^{\infty} p(N_{on}|N, N_b)dN \quad . \tag{6.9}$$

In other words, the uncertainties in the estimated background counts are small enough such that the distribution of B has a negligible width compared to $\sqrt{N_{on}}$, and has a well-defined peak at N_b.

Normalizing such that the probability is unity for observing N_{on}, given all the possible values of the number of signal events, gives A_{norm},

$$A_{norm} \int_{0}^{\infty} p(N_{on}|N, N_b)dN = 1 \tag{6.10}$$

$$\implies \quad A_{norm} = \frac{1}{\sum_{n=0}^{N_{on}} p(n|N_b)} = \frac{1}{e^{-N_b} \sum_{n=0}^{N_{on}} \frac{N_b^n}{n!}} \quad . \tag{6.11}$$

And integrating equation (6.9) gives,

$$1 - CL = 0.1 = \frac{\sum_{n=0}^{N_{on}} p(n|N_{90}, N_b)}{\sum_{n=0}^{N_{on}} p(n|N_b)} \tag{6.12}$$

$$= \frac{e^{-(N_b+N_{90})} \sum_{n=0}^{N_{on}} \frac{(N_b + N_{90})^n}{n!}}{e^{-N_b} \sum_{n=0}^{N_{on}} \frac{{N_b}^n}{n!}} \quad . \tag{6.13}$$

Defined as in equation (6.13), N_{90} is the number of signal events for which the measured on-source count will be larger than N_{on}, and the actual number of background events less than N_{on}, for a fraction CL of repetitions of the experiment, with N_b the same for all the repetitions. This can be turned around and it can be said that when the measured number of on-source counts is N_{on} (with N_{on} larger than the actual number of background events) and the estimated background is N_b, then the number of signal events will be less than N_{90} for a fraction CL of the experiments. In actuality, because of the discrete nature of the Poisson distribution, the number of signal events will be less than N_{90} for a fraction of the experiments larger than CL. The upper limit is then said to *overcover* the actual number of signal events, and it is said to be *conservative* (apparently an oft-misunderstood term).

Once N_{90} for each (θ, ϕ) bin with an excess in a GRB search area has been determined using equation (6.13), the corresponding flux 90% upper limits can be calculated using equation (6.5). The largest flux upper limit found in a GRB search area is then considered the flux upper limit for that GRB.

6.4.2 Results of differential flux 90% upper limit calculations The 90% upper limits on the flux normalizations at 1 TeV for 44 GRBs are given in Table 6.2 at the end of this chapter. Flux upper limits were not determined for all 53 GRBs because some GRB search areas had bins located at zenith angles larger than 60^o, for which the effective area of Milagrito could not be easily determined (except through throwing a ludicrously large number of simulated showers).

Figure 6.6 shows the flux limits as a function of burst duration and zenith angle for $\eta = 2.0$, with no high energy cutoff (left panel), and with a 5-TeV high energy cutoff (right panel). For $\eta = 2.0$, the range of upper limits on the flux normalization at 1 TeV is:

$4 \times 10^{-9} - 10^{-6}$ $\gamma s\ cm^{-2}s^{-1}TeV^{-1}$, with no energy cutoff;

$4 \times 10^{-8} - 5 \times 10^{-5}$ $\gamma s\ cm^{-2}s^{-1}TeV^{-1}$, with 5-TeV cutoff.

And for $\eta = 2.5$,

$2 \times 10^{-8} - 10^{-5}$ $\gamma s\ cm^{-2} s^{-1} TeV^{-1}$, with no energy cutoff;

$5 \times 10^{-8} - 8 \times 10^{-5}$ $\gamma s\ cm^{-2} s^{-1} TeV^{-1}$, with 5-TeV cutoff.

It can be seen from Fig. 6.6 that the zenith angle dependence of Milagrito's sensitivity is more readily apparent in the case of having a 5-TeV cutoff than in the case of having no energy cutoff. This can be explained by the fact that as the zenith angle increases, the more likely air showers produced by low-energy primary photons will be absorbed by the atmosphere and will, therefore, not be detected. This fact is reflected in the behavior of Milagrito's effective area as a function of zenith angle (cf. Section 4.3.1). Thus, the peak of the function $E^{-\eta} A_{eff}(E, \theta)$, which appears in equation (6.5), shifts to higher energies as the zenith angle increases. So if a limit is placed on the upper limit of integration, the percentage of the area under $E^{-\eta} A_{eff}(E, \theta)$ which is tossed out increases as the zenith angle gets larger, and the sensitivity of Milagrito decreases dramatically.

Although there is a marked decrease in the area under $E^{-\eta} A_{eff}(E, \theta)$ as the atmospheric overburden increases even with no energy cutoff (cf. Section 4.3.1), the fact that the background count rate also decreases with increasing zenith angle results in N_{90} being smaller at larger zenith angles. This effect partly cancels the effect of the smaller Milagrito effective area at larger zenith angles, thus resulting in flux limits, in the case of no energy cutoff, which are flatter as a function of zenith angle than those in the case of having an energy cutoff.

Figure 6.7 attempts to depict the representative Milagrito GRB flux upper limits in the TeV regime in relation to measured GRB spectra at keV-GeV energies. The three BATSE spectra shown are those of GRB 970223 (a strong burst in terms of fluence), GRB 970603b, and GRB 970627a (both average bursts in fluence), all of which were included in this GRB analysis and from which no TeV emission was detected. The black dashed lines are blind extensions of the BATSE spectra, and the average slope of the extensions is ≈ -2.1. Also shown is the EGRET spectra for the prompt and delayed emissions from the powerful GRB 940217b, fondly nicknamed the ”Superbowl burst” [16]. It can be seen that the flux spectrum at MeV-GeV energies for the prompt emission is larger and has a flatter slope (≈ -2.1) than the spectrum for the delayed emission (slope ≈ -2.8). In general, Fig. 6.7 suggests that if the prompt emission spectra of some of the GRBs analyzed in this work had extended to TeV energies without steepening of the corresponding spectral slopes, Milagrito would have had a good chance of detecting the TeV emission. That it did not detect TeV emission from the analyzed GRBs, but for one candidate GRB, means that the prompt emission spectrum for most of the 53 GRBs must have had an effective energy cutoff at MeV or GeV energies, possibly due to absorbtion at the source or absorption by cosmic infrared radiation (cf. Chapter 8).

6.4.3 Experimental uncertainty The effective area of Milagrito, A_{eff}, used in equation (6.5) reflects average experimental conditions – i.e. average shower size, average PMT response, average water conditions, and average atmospheric overburden – and does not take into account changes in experimental conditions. In a complicated experiment like Milagrito, it is difficult to quantify how such changes translate into uncertainties in measured quantities, particularly the measured number of signal events, and such changes are not directly reflected in A_{eff}. However, since the effective area obtained from Monte Carlo simulations is used in calculating flux upper limits and in predicting the sensitivity of Milagrito given a gamma-ray source with known flux, it is important to estimate the uncertainty in the calculated effective area of Milagrito in order to give an estimate of the uncertainties in the derived quantities. An estimate of the uncertainty in the effective area is equivalent to an estimate of experimental uncertainty using Milagrito, since the effective area essentially summarizes the detector performance.

The uncertainty in the effective area will be estimated by using results from Milagrito’s observation of Markarian 501 [126]. The spectrum of Mrk 501 in the TeV region has been well measured by air Cherenkov experiments [81, 82, 84]. The observed spectral shape of Mrk 501 is constant with time, but the flux normalization is highly variable with

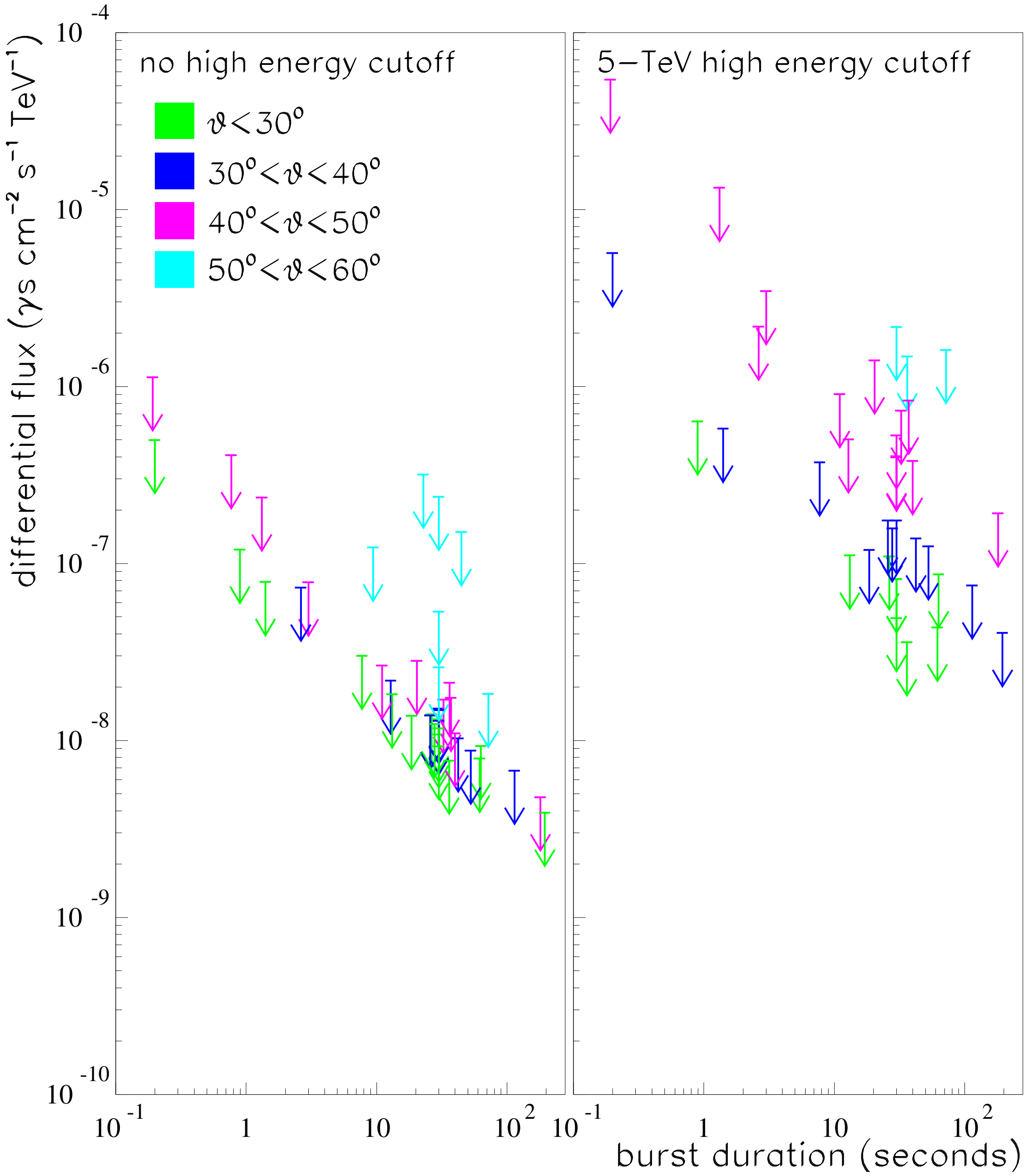

Figure 6.6: 90% upper limits on the flux normalizations at 1 TeV for the GRBs investigated, as a function of burst duration and zenith angle of the bin with the worst (i.e. largest) flux found in a GRB search area. The left panel shows flux limits assuming no high energy cutoff, while the right panel shows flux limits assuming a 5-TeV high energy cutoff. The assumed differential spectral slope was -2.0.

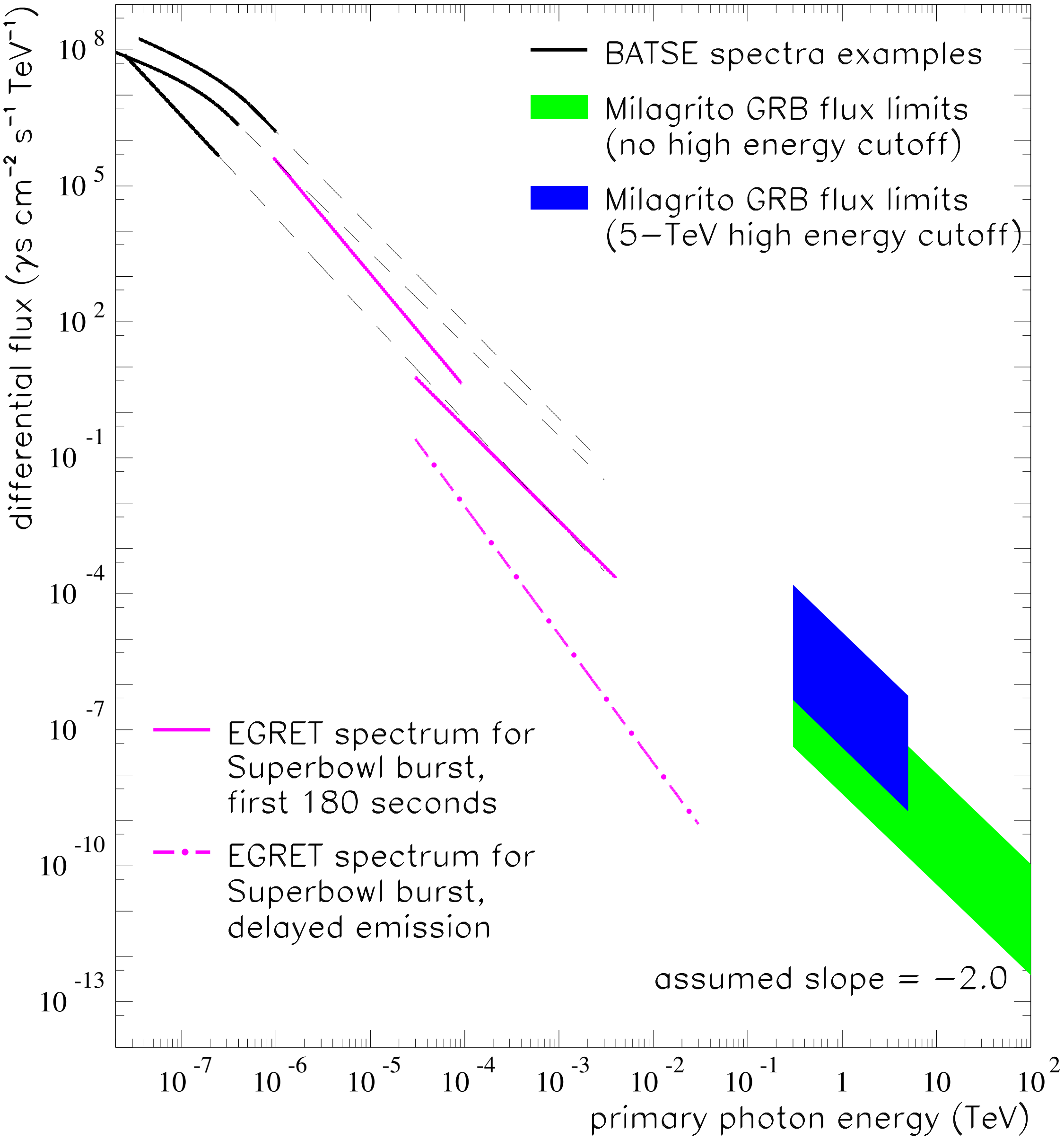

Figure 6.7: Milagrito GRB flux 90% upper limits in the TeV regime in relation to typical BATSE flux in the keV-MeV regime. The two lower BATSE spectra shown here were average bursts in fluence, while the highest BATSE specrum shown was a strong burst in fluence. The black dashed lines are blind extensions of the BATSE spectra. Also shown are the EGRET spectra for the prompt and delayed emissions from the Superbowl burst (GRB 940217b).

time, the variability time scale being between 5 to 15 hours [81]. Using cumulative counts from February to October 1997, during which Mrk 501 was active, Milagrito detected an excess corresponding to a significance of $S = 3.3$ standard deviations from the direction of Mrk 501 [126]. Using the measured Mrk 501 spectrum and the calculated effective area of Milagrito, the number of signal events that would be detected by Milagrito is given by,

$$N_s = \Delta T\, \overline{F}_o \int_{E_1}^{E_2} f(E)\, A_{eff}(E)\, dE \quad , \tag{6.14}$$

where $\overline{F}_o$ is the average flux normalization of Mrk 501, $f(E)$ is a function which quantifies the spectral shape of Mrk 501, and ΔT is the time duration of the counting experiment. The zenith angle dependence of A_{eff} has not been explicitly written in equation (6.14), but has to be taken into account in the calculations as Mrk 501 makes its transit through Milagrito's field of view. The number of signal events coming from Mrk 501 during the period February to October 1997, as predicted by equation (6.14), agrees with the measured event count to within 5% [126], signifying that the average effective area obtained through simulations reflects the average Milagrito performance well.

The uncertainty in the measured number of signal events from Mrk 501 comes from two sources: Experimental uncertainty in Milagrito's performance, and an uncertainty due to the varying flux normalization of Mrk 501 with time. That is,

$$\frac{\delta N_s}{N_s} = \sqrt{\left(\frac{\delta \overline{F}_o}{\overline{F}_o}\right)^2 + \left(\frac{\delta A_{eff}}{A_{eff}}\right)^2} \quad . \tag{6.15}$$

Since Milagrito detected excess with a significance of $S = 3.3$ standard deviations from Mrk 501, the fractional uncertainty in the measured number of signal events is (see Section 5.3.3 for the definition of significance),

$$\frac{\delta N_s}{N_s} = \frac{1}{S} = 0.3 \quad . \tag{6.16}$$

It is difficult, if not impossible, to estimate the contribution of the varying flux normalization to the uncertainty in the observed number of signal events. However, it is probably safe to assume, given that the measurement of N_s was made using data spanning several months, long enough so that the average flux normalization, $\overline{F}_o$, is well defined, that the fractional uncertainty in A_{eff} dominates the fractional uncertainty in $\overline{F}_o$. Thus, using equation (6.16) in equation (6.15),

$$\frac{\delta A_{eff}}{A_{eff}} \approx 0.3 \quad . \tag{6.17}$$

This can be directly translated into an uncertainty in the calculated flux upper limits, so that the uncertainty in the flux upper limits given in Table 6.2 is about 30%. For upper limits obtained without an energy cutoff, there is also an uncertainty, estimated to be about 20%, due to the uncertainty in extrapolating the effective area at high energies, $E \gtrsim 200\ TeV$. Adding the two uncertainties in quadrature, the total uncertainty in the flux upper limits for the case of no energy cutoff is estimated to be about 40%.

Table 6.2: Milagrito 90% confidence upper limits on GRB flux at the top of the atmosphere.

BATSE GRB	BATSE trigger number	T90[a] (seconds)	differential spectral index (η)	energy cutoff (TeV)	zenith[b] angle (degrees)	N_b[c]	N_{on}[d]	N_{90}[e]	differential flux[f] upper limit ($\gamma s\ cm^{-2} s^{-1} TeV^{-1}$)
970408	6166	0.192	2.0	∞	45.8	0.0397±0.0008	1	3.86	1.1×10^{-6}
			2.0	5.0	45.8	0.0397±0.0008	1	3.86	5.4×10^{-5}
			2.5	∞	45.8	0.0397±0.0008	1	3.86	1.0×10^{-5}
			2.5	5.0	45.8	0.0397±0.0008	1	3.86	8.2×10^{-5}
970409	6167	61.696	2.0	∞	6.0	27.2±0.4	43	25.50	7.9×10^{-9}
			2.0	5.0	9.9	26.6±0.4	41	23.90	4.3×10^{-8}
			2.5	∞	9.9	26.6±0.4	41	23.90	2.7×10^{-8}
			2.5	5.0	9.9	26.6±0.4	41	23.90	6.0×10^{-8}
970426	6209	30.000	2.0	∞	31.0	7.63±0.13	16	14.83	1.5×10^{-8}
			2.0	5.0	43.0	3.28±0.08	5	6.22	5.3×10^{-7}
			2.5	∞	43.0	3.28±0.08	5	6.22	1.0×10^{-7}
			2.5	5.0	43.0	3.28±0.08	5	6.22	8.0×10^{-7}
970429	6213	30.000	2.0	∞	29.2	8.45±0.14	16	14.02	1.3×10^{-8}
			2.0	5.0	33.5	6.68±0.12	11	10.02	1.7×10^{-7}
			2.5	∞	33.5	6.68±0.12	11	10.02	6.3×10^{-8}
			2.5	5.0	33.5	6.68±0.12	11	10.02	2.6×10^{-7}

[a] Search time interval. For GRBs with no T90 specified in the BATSE catalog, a search time interval of 30 seconds was used.

[b] Zenith angle of bin with largest flux in the GRB's search area.

[c] Estimated mean number of background events in bin. The given errors are statistical uncertainties.

[d] On-source count in bin.

[e] 90% confidence upper limit on the number of signal events.

[f] Uncertainty is 30% to 40% (see Section 6.4.3).

Table 6.2 continuation.

BATSE GRB	BATSE trigger number	T90 (seconds)	differential spectral index (η)	energy cutoff (TeV)	zenith angle (degrees)	N_b	N_{on}	N_{90}	differential flux upper limit ($\gamma s\ cm^{-2}s^{-1}TeV^{-1}$)
970511	6229	26.368	2.0	∞	20.6	10.4±0.2	21	17.77	1.4×10^{-8}
			2.0	5.0	27.6	8.33±0.14	14	11.86	1.1×10^{-7}
			2.5	∞	20.6	10.4±0.2	21	17.77	5.5×10^{-8}
			2.5	5.0	27.6	8.33±0.14	14	11.86	1.6×10^{-7}
970523	6240	30.000	2.0	∞	22.2	9.5±0.2	18	15.26	1.1×10^{-8}
			2.0	5.0	22.2	9.5±0.2	18	15.26	8.2×10^{-8}
			2.5	∞	22.2	9.5±0.2	18	15.26	4.3×10^{-8}
			2.5	5.0	22.2	9.5±0.2	18	15.26	1.2×10^{-7}
970603	6251	3.008	2.0	∞	42.5	0.517±0.009	2	4.83	7.8×10^{-8}
			2.0	5.0	45.5	0.395±0.008	1	3.57	3.5×10^{-6}
			2.5	∞	42.5	0.517±0.009	2	4.83	6.6×10^{-7}
			2.5	5.0	45.5	0.395±0.008	1	3.57	5.2×10^{-6}
970612	6265	0.199	2.0	∞	19.4	0.1548±0.0015	3	6.53	5.0×10^{-7}
			2.0	5.0	31.5	0.1022±0.0011	1	3.80	5.7×10^{-6}
			2.5	∞	31.5	0.1022±0.0011	1	3.80	2.3×10^{-6}
			2.5	5.0	31.5	0.1022±0.0011	1	3.80	8.3×10^{-6}
970612	6267	12.864	2.0	∞	37.4	2.30±0.05	5	7.03	2.2×10^{-8}
			2.0	5.0	41.5	1.79±0.05	2	3.98	5.0×10^{-7}
			2.5	∞	37.4	2.30±0.05	5	7.03	1.3×10^{-7}
			2.5	5.0	41.5	1.79±0.05	2	3.98	7.6×10^{-7}

Table 6.2 continuation.

BATSE GRB	BATSE trigger number	T90 (seconds)	differential spectral index (η)	energy cutoff (TeV)	zenith angle (degrees)	N_b	N_{on}	N_{90}	differential flux upper limit ($\gamma s\ cm^{-2} s^{-1} TeV^{-1}$)
970627	6279	32.512	2.0	∞	43.0	3.56±0.08	8	9.46	1.7×10^{-8}
			2.0	5.0	43.0	3.56±0.08	8	9.46	7.3×10^{-7}
			2.5	∞	43.0	3.56±0.08	8	9.46	1.4×10^{-7}
			2.5	5.0	43.0	3.56±0.08	8	9.46	1.1×10^{-6}
970629	6288	13.184	2.0	∞	10.4	5.86±0.12	13	13.11	1.8×10^{-8}
			2.0	5.0	17.7	5.42±0.11	11	11.21	1.1×10^{-7}
			2.5	∞	10.4	5.86±0.12	13	13.11	6.4×10^{-8}
			2.5	5.0	17.7	5.42±0.11	11	11.21	1.6×10^{-7}
970707	6295	180.480	2.0	∞	41.8	20.4±0.4	27	14.79	4.8×10^{-9}
			2.0	5.0	42.4	20.3±0.4	26	13.89	1.9×10^{-7}
			2.5	∞	42.4	20.3±0.4	26	13.89	3.9×10^{-8}
			2.5	5.0	42.4	20.3±0.4	26	13.89	2.9×10^{-7}
970709	6300	63.168	2.0	∞	27.6	16.7±0.3	30	21.61	9.3×10^{-9}
			2.0	5.0	27.6	16.7±0.3	30	21.61	8.7×10^{-8}
			2.5	∞	27.6	16.7±0.3	30	21.61	4.1×10^{-8}
			2.5	5.0	27.6	16.7±0.3	30	21.61	1.3×10^{-7}
970713	6305	25.792	2.0	∞	31.3	6.41±0.12	12	11.41	1.4×10^{-8}
			2.0	5.0	32.5	6.07±0.11	10	9.45	1.7×10^{-7}
			2.5	∞	31.3	6.41±0.12	12	11.41	6.9×10^{-8}
			2.5	5.0	32.5	6.07±0.11	10	9.45	2.6×10^{-7}

Table 6.2 continuation.

BATSE GRB	BATSE trigger number	T90 (seconds)	differential spectral index (η)	energy cutoff (TeV)	zenith angle (degrees)	N_b	N_{on}	N_{90}	differential flux upper limit ($\gamma s\ cm^{-2}s^{-1}TeV^{-1}$)
970725	6317	7.744	2.0	∞	25.7	2.51±0.03	8	10.49	3.0×10^{-8}
			2.0	5.0	36.9	1.41±0.02	2	4.18	3.7×10^{-7}
			2.5	∞	25.7	2.51±0.03	8	10.49	1.3×10^{-7}
			2.5	5.0	36.9	1.41±0.02	2	4.18	5.6×10^{-7}
970802	6323	20.352	2.0	∞	46.5	1.80±0.05	5	7.50	2.8×10^{-8}
			2.0	5.0	46.5	1.80±0.05	5	7.50	1.4×10^{-6}
			2.5	∞	46.5	1.80±0.05	5	7.50	2.6×10^{-7}
			2.5	5.0	46.5	1.80±0.05	5	7.50	2.1×10^{-6}
970803	6325	30.000	2.0	∞	33.6	5.49±0.11	11	11.13	1.3×10^{-8}
			2.0	5.0	41.8	3.08±0.08	5	6.37	4.0×10^{-7}
			2.5	∞	41.8	3.08±0.08	5	6.37	9.1×10^{-8}
			2.5	5.0	41.8	3.08±0.08	5	6.37	6.0×10^{-7}
970817	6338	0.768	2.0	∞	45.8	0.108±0.002	2	5.22	4.1×10^{-7}
			2.0	5.0	–	–	–	–	–
			2.5	∞	–	–	–	–	–
			2.5	5.0	–	–	–	–	–
970906	6366	30.000	2.0	∞	53.4	1.47±0.06	4	6.55	5.4×10^{-8}
			2.0	5.0	–	–	–	–	–
			2.5	∞	54.0	1.26±0.06	2	4.27	1.0×10^{-5}
			2.5	5.0	–	–	–	–	–

Table 6.2 continuation.

BATSE GRB	BATSE trigger number	T90 (seconds)	differential spectral index (η)	energy cutoff (TeV)	zenith angle (degrees)	N_b	N_{on}	N_{90}	differential flux upper limit ($\gamma s\ cm^{-2}s^{-1}TeV^{-1}$)
970910	6376	1.320	2.0	∞	48.7	0.149±0.003	1	3.76	2.4×10^{-7}
			2.0	5.0	48.5	0.153±0.003	1	3.75	1.3×10^{-5}
			2.5	∞	48.7	0.149±0.003	1	3.76	2.4×10^{-6}
			2.5	5.0	48.5	0.153±0.003	1	3.75	2.0×10^{-5}
970918	6385	0.896	2.0	∞	2.6	0.674±0.006	4	7.32	1.2×10^{-7}
			2.0	5.0	19.4	0.540±0.006	2	4.81	6.3×10^{-7}
			2.5	∞	2.6	0.674±0.006	4	7.32	4.0×10^{-7}
			2.5	5.0	19.4	0.540±0.006	2	4.81	9.0×10^{-7}
970925	6396	52.672	2.0	∞	32.5	11.5±0.2	18	13.32	8.8×10^{-9}
			2.0	5.0	32.5	11.5±0.2	18	13.32	1.3×10^{-7}
			2.5	∞	32.5	11.5±0.2	18	13.32	4.6×10^{-8}
			2.5	5.0	32.5	11.5±0.2	18	13.32	1.9×10^{-7}
971015	6437	9.408	2.0	∞	53.5	0.51±0.02	2	4.83	1.2×10^{-7}
			2.0	5.0	–	–	–	–	–
			2.5	∞	47.6	0.95±0.02	6	9.59	7.8×10^{-7}
			2.5	5.0	–	–	–	–	–
971110	6472	195.200	2.0	∞	16.9	69.3±1.1	91	35.26	3.9×10^{-9}
			2.0	5.0	30.6	45.1±0.9	55	21.03	4.1×10^{-8}
			2.5	∞	30.6	45.1±0.9	55	21.03	1.7×10^{-8}
			2.5	5.0	30.6	45.1±0.9	55	21.03	5.9×10^{-8}

Table 6.2 continuation.

BATSE GRB	BATSE trigger number	T90 (seconds)	differential spectral index (η)	energy cutoff (TeV)	zenith angle (degrees)	N_b	N_{on}	N_{90}	differential flux upper limit ($\gamma s\ cm^{-2} s^{-1} TeV^{-1}$)
971122	6492	30.000	2.0	∞	56.0	1.18±0.04	2	4.32	2.4×10^{-7}
			2.0	5.0	–	–	–	–	–
			2.5	∞	–	–	–	–	–
			2.5	5.0	–	–	–	–	–
971207	6523	36.288	2.0	∞	49.3	2.09±0.06	5	7.22	2.1×10^{-8}
			2.0	5.0	51.0	1.75±0.06	2	4.00	1.5×10^{-6}
			2.5	∞	49.3	2.09±0.06	5	7.22	2.2×10^{-7}
			2.5	5.0	51.0	1.75±0.06	2	4.00	2.3×10^{-6}
971210	6529	37.184	2.0	∞	45.8	3.12±0.08	7	8.69	1.7×10^{-8}
			2.0	5.0	45.8	3.12±0.08	7	8.69	8.3×10^{-7}
			2.5	∞	45.8	3.12±0.08	7	8.69	1.6×10^{-7}
			2.5	5.0	45.8	3.12±0.08	7	8.69	1.3×10^{-6}
971225	6545	30.000	2.0	∞	37.9	5.11±0.10	10	10.34	1.5×10^{-8}
			2.0	5.0	41.6	3.81±0.08	6	6.92	4.0×10^{-7}
			2.5	∞	41.6	3.81±0.08	6	6.92	9.6×10^{-8}
			2.5	5.0	41.6	3.81±0.08	6	6.92	6.1×10^{-7}
980124	6577	22.784	2.0	∞	55.9	0.88±0.03	3	5.82	3.2×10^{-7}
			2.0	5.0	–	–	–	–	–
			2.5	∞	–	–	–	–	–
			2.5	5.0	–	–	–	–	–

Table 6.2 continuation.

BATSE GRB	BATSE trigger number	T90 (seconds)	differential spectral index (η)	energy cutoff (TeV)	zenith angle (degrees)	N_b	N_{on}	N_{90}	differential flux upper limit ($\gamma s\ cm^{-2} s^{-1} TeV^{-1}$)
980125	6581	30.000	2.0	∞	19.5	12.4±0.2	22	16.92	1.2×10^{-8}
			2.0	5.0	19.5	12.4±0.2	22	16.92	8.2×10^{-8}
			2.5	∞	19.5	12.4±0.2	22	16.92	4.5×10^{-8}
			2.5	5.0	19.5	12.4±0.2	22	16.92	1.2×10^{-7}
980207	6590	114.112	2.0	∞	33.8	28.2±0.4	46	27.75	6.8×10^{-9}
			2.0	5.0	33.8	28.2±0.4	46	27.75	7.5×10^{-8}
			2.5	∞	33.8	28.2±0.4	46	27.75	3.1×10^{-8}
			2.5	5.0	33.8	28.2±0.4	46	27.75	1.1×10^{-7}
980213	6599	30.000	2.0	∞	50.4	2.24±0.06	5	7.09	2.6×10^{-8}
			2.0	5.0	51.7	1.93±0.06	2	3.91	2.2×10^{-6}
			2.5	∞	50.4	2.24±0.06	5	7.09	2.8×10^{-7}
			2.5	5.0	51.7	1.93±0.06	2	3.91	3.3×10^{-6}
980222	6610	71.936	2.0	∞	50.2	4.71±0.13	11	11.90	1.8×10^{-8}
			2.0	5.0	52.0	3.86±0.12	4	4.85	1.6×10^{-6}
			2.5	∞	50.2	4.71±0.13	11	11.90	1.9×10^{-7}
			2.5	5.0	52.0	3.86±0.12	4	4.85	2.5×10^{-6}
980223	6613	42.368	2.0	∞	37.3	8.28±0.15	15	13.05	1.0×10^{-8}
			2.0	5.0	37.3	8.28±0.15	15	13.05	1.4×10^{-7}
			2.5	∞	37.3	8.28±0.15	15	13.05	5.3×10^{-8}
			2.5	5.0	37.3	8.28±0.15	15	13.05	2.0×10^{-7}

Table 6.2 continuation.

BATSE GRB	BATSE trigger number	T90 (seconds)	differential spectral index (η)	energy cutoff (TeV)	zenith angle (degrees)	N_b	N_{on}	N_{90}	differential flux upper limit ($\gamma s\ cm^{-2}s^{-1}TeV^{-1}$)
980301	6619	35.968	2.0	∞	11.5	11.6±0.2	24	19.98	7.7×10^{-9}
			2.0	5.0	11.5	11.6±0.2	24	19.98	3.6×10^{-8}
			2.5	∞	11.5	11.6±0.2	24	19.98	2.4×10^{-8}
			2.5	5.0	11.5	11.6±0.2	24	19.98	4.8×10^{-8}
980315	6641	2.624	2.0	∞	34.0	0.877±0.011	5	8.40	7.3×10^{-8}
			2.0	5.0	43.6	0.428±0.008	1	3.55	2.2×10^{-6}
			2.5	∞	43.6	0.428±0.008	1	3.55	4.8×10^{-7}
			2.5	5.0	43.6	0.428±0.008	1	3.55	3.3×10^{-6}
980329	6665	18.560	2.0	∞	29.9	7.11±0.12	13	11.89	1.4×10^{-8}
			2.0	5.0	32.2	6.52±0.11	10	9.05	1.2×10^{-7}
			2.5	∞	29.9	7.11±0.12	13	11.89	5.7×10^{-8}
			2.5	5.0	32.2	6.52±0.11	10	9.05	1.7×10^{-7}
980329	6666	11.008	2.0	∞	42.8	1.98±0.04	4	6.11	2.7×10^{-8}
			2.0	5.0	42.8	1.98±0.04	4	6.11	9.1×10^{-7}
			2.5	∞	42.8	1.98±0.04	4	6.11	2.0×10^{-7}
			2.5	5.0	42.8	1.98±0.04	4	6.11	1.4×10^{-6}
980401	6672	27.904	2.0	∞	28.1	12.1±0.2	22	17.22	1.2×10^{-8}
			2.0	5.0	39.2	6.05±0.11	8	7.32	1.6×10^{-7}
			2.5	∞	39.2	6.05±0.11	8	7.32	5.5×10^{-8}
			2.5	5.0	39.2	6.05±0.11	8	7.32	2.3×10^{-7}

Table 6.2 continuation.

BATSE GRB	BATSE trigger number	T90 (seconds)	differential spectral index (η)	energy cutoff (TeV)	zenith angle (degrees)	N_b	N_{on}	N_{90}	differential flux upper limit ($\gamma s\ cm^{-2}s^{-1}TeV^{-1}$)
980404	6679	1.408	2.0	∞	21.9	1.113±0.010	5	8.17	7.9×10^{-8}
			2.0	5.0	33.3	0.683±0.007	1	3.41	5.8×10^{-7}
			2.5	∞	21.9	1.113±0.010	5	8.17	2.8×10^{-7}
			2.5	5.0	33.3	0.683±0.007	1	3.41	8.4×10^{-7}
980420	6694	39.936	2.0	∞	41.1	6.60±0.12	11	10.10	1.1×10^{-8}
			2.0	5.0	44.5	4.75±0.10	7	7.26	3.8×10^{-7}
			2.5	∞	44.5	4.75±0.10	7	7.26	8.2×10^{-8}
			2.5	5.0	44.5	4.75±0.10	7	7.26	5.8×10^{-7}
980424	6702	44.736	2.0	∞	55.9	1.76±0.06	4	6.29	1.5×10^{-7}
			2.0	5.0	–	–	–	–	–
			2.5	∞	–	–	–	–	–
			2.5	5.0	–	–	–	–	–
980430	6716	30.000	2.0	∞	17.4	14.4±0.2	25	18.31	9.3×10^{-9}
			2.0	5.0	17.4	14.4±0.2	25	18.31	4.9×10^{-8}
			2.5	∞	17.4	14.4±0.2	25	18.31	3.1×10^{-8}
			2.5	5.0	17.4	14.4±0.2	25	18.31	6.6×10^{-8}

Chapter 7

Details of Search for GRB 970417a

It was seen in Chapter 6 that, of the 54 BATSE GRBs examined for TeV emission coincident with keV-MeV emission, only GRB 970417a gave rise to an excess above background with a significance of note after all the trials were counted. This chapter will both summarize and present more details about the search for TeV emission from GRB 970417a. Aside from the results of the original binned analysis, a maximum likelihood analysis of the events found in the GRB's search area during T90 will also be presented. The chapter will be concluded by presenting lower limits on the primary energies of the events attributed to the candidate GRB.

7.1 GRB 970417a Binned Search

Table 7.1 summarizes the parameters for, and results from, the binned search of GRB 970417a for TeV emission. Figures 7.1 to 7.5 are plots pertaining to the search results and are explained in the following paragraphs.

Figure 7.1 shows the spatial distribution of cumulative Poisson probabilities for the occurrence of the on-source counts, or larger, measured in the bins in GRB 970417a's search area. The bin coordinates are given relative to the nominal BATSE position of GRB 970417a, symbolized as (dec0,ra0) in the plot axes. The angular distance between this position and the hottest bin found in the search area is 3.2^o.

Figure 7.2 shows the spatial distribution of Milagrito events found in the search area of GRB 970417a during the T90 search time interval. Each dot represents a reconstructed air shower event direction, and the ellipses represent the BATSE 68% and 95% confidence ellipses, the latter used as the search area for this GRB analysis. The box is the hottest bin found in the search and contains 17 events. The apparent decrease in the density of events in the (δ, α) plane as the declination increases reflects the fact that equal areas on the celestial sphere, over which the density of isotropic background events is constant, means that the length of the right ascension arc goes as $1/cos(\delta)$, and that, therefore, the density of events in the (δ, α) plane goes as $cos(\delta)$.

Figure 7.3 is the time history of Milagrito events in the local hot bin during six hours surrounding the burst time, i.e. it shows the event count in a local (θ,ϕ) bin over time. It should not be misinterpreted as tracking a source over time, and should not be used to visually search for early or delayed bursts. The time is given relative to the BATSE trigger time for GRB 970417a, and the time bins are each of length T90. The horizontal line is the expected mean background count in the local bin. The on-source count of 17 events is clearly seen coincident with the BATSE trigger.

Figure 7.4(a) is a close-up look at the time distribution of Milagrito events in the local hot bin during 30 seconds surrounding the burst time. The time is relative to the BATSE trigger time, and the time bins are each of one second length. Figure 7.4(b) is the BATSE count rate for the same time interval. The guide lines delineate the BATSE T90 interval for GRB 970417a.

Figure 7.5 shows the BATSE total fluence for 1807 GRBs, and the rank of GRB 970417a's total fluence in the population. It can be seen that this particular GRB has a relatively small fluence in the keV-MeV energy regime.

Table 7.1: Parameters for, and results from, GRB 970417a search.

BATSE T90	7.936 ± 0.630 seconds
BATSE total fluence (> 20 keV)	$(3.95 \pm 1.94) \times 10^{-7}$ ergs/cm^2
BATSE position (J2000)	55.8^o declination 295.7^o right ascension
BATSE 1σ statistical error radius	6.2^o
search area (BATSE 95% confidence radius)	11.4^o
bin width used in search	2.851^o in declination
total number of bins used in the search	324
coordinates of center of bin with most significant excess (J2000)	54.3^o declination 290.8^o right ascension
zenith angle of most significant bin	21.8^o
estimated background count in most significant bin	3.41 ± 0.04
on-source count[a] in most significant bin	17
off-source count[a] in most significant bin	9229
off-source to on-source exposure ratio (α)[a]	3.689×10^{-4}
pre-trials cumulative Poisson probability[b] of most significant excess	$(1.3 \pm 0.2) \times 10^{-7}$
pre-trials significance[b] of most significant excess	5.2 standard deviations
post-trials significance[b] of most significant excess	4.2 standard deviations
final significance[b] of most significant excess	3.2 standard deviations

[a] See Section 5.3.2 for definitions.

[b] See Sections 6.1 to 6.3 for explanations.

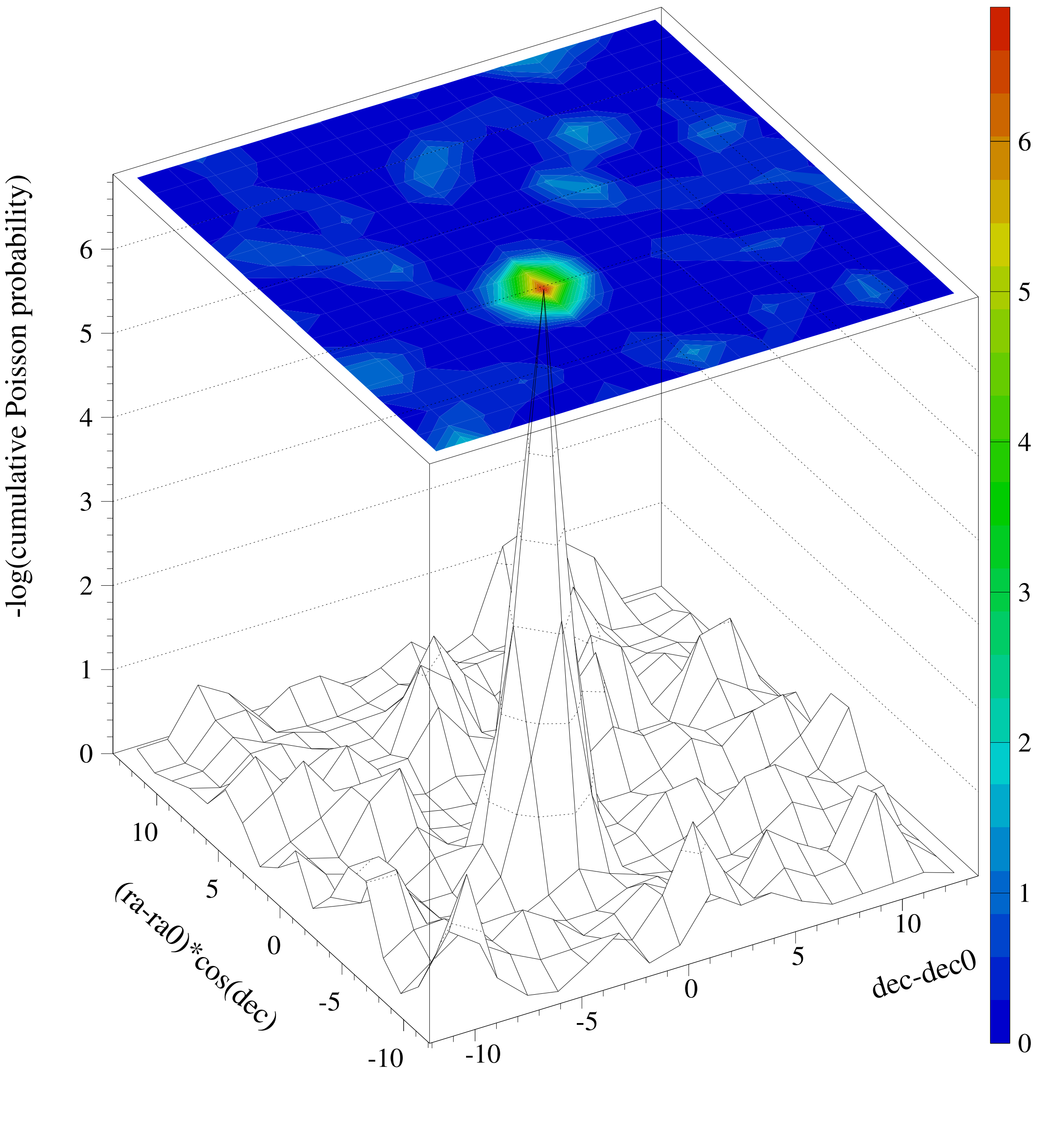

Figure 7.1: Spatial distribution of cumulative Poisson probability in GRB 970417a's search area.

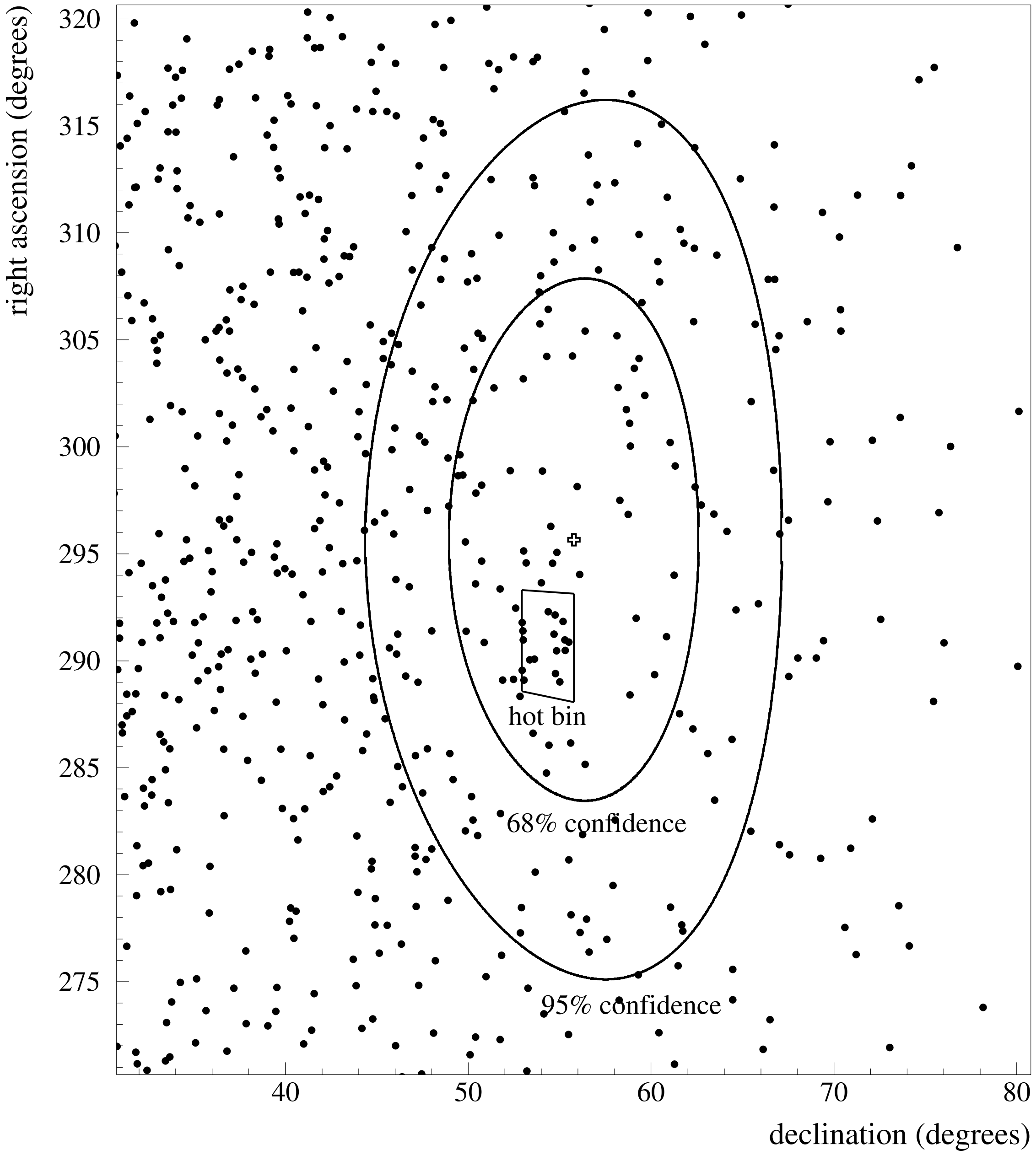

Figure 7.2: Spatial distribution of Milagrito events during the search interval, T90, for GRB 970417a. The ellipses are the BATSE 68% and 95% confidence ellipses for this GRB. The ”hot bin” is the bin with the most significant excess found in the search area.

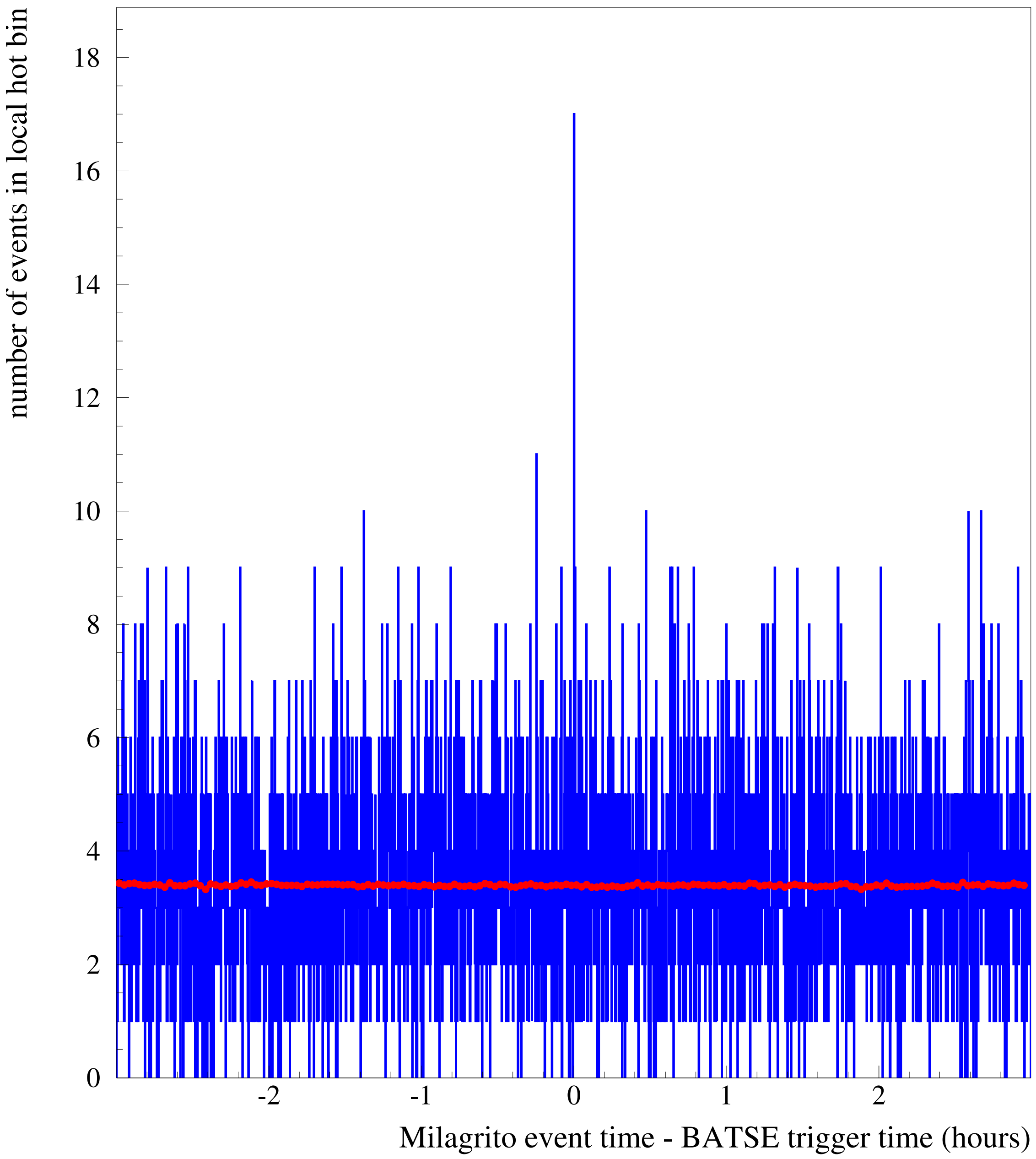

Figure 7.3: Time history of Milagrito events in local hot bin found in GRB 970417a's search area.

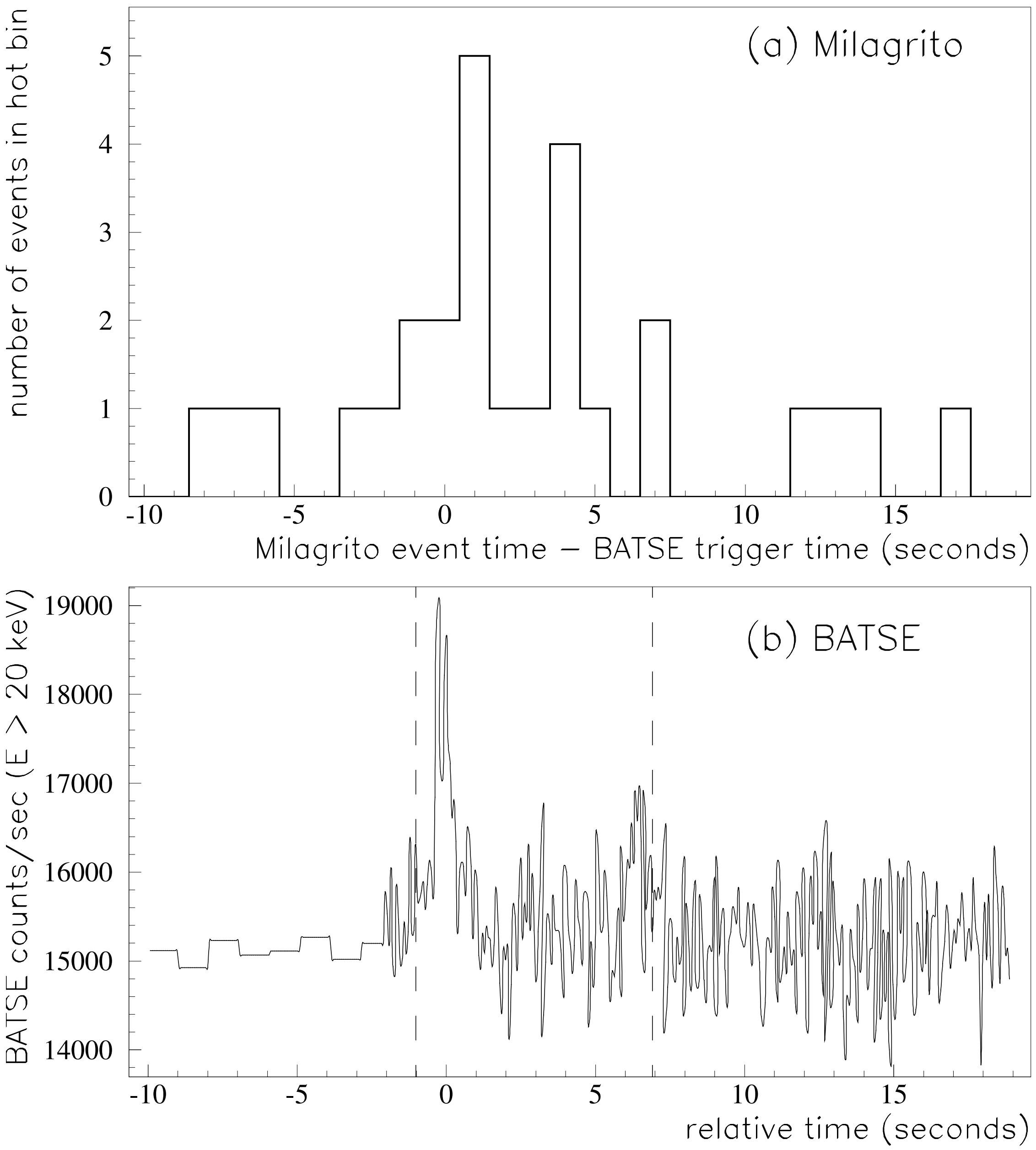

Figure 7.4: (a) Milagrito event time distribution in GRB 970417a hot bin. (b) BATSE event rate for GRB 970417a.

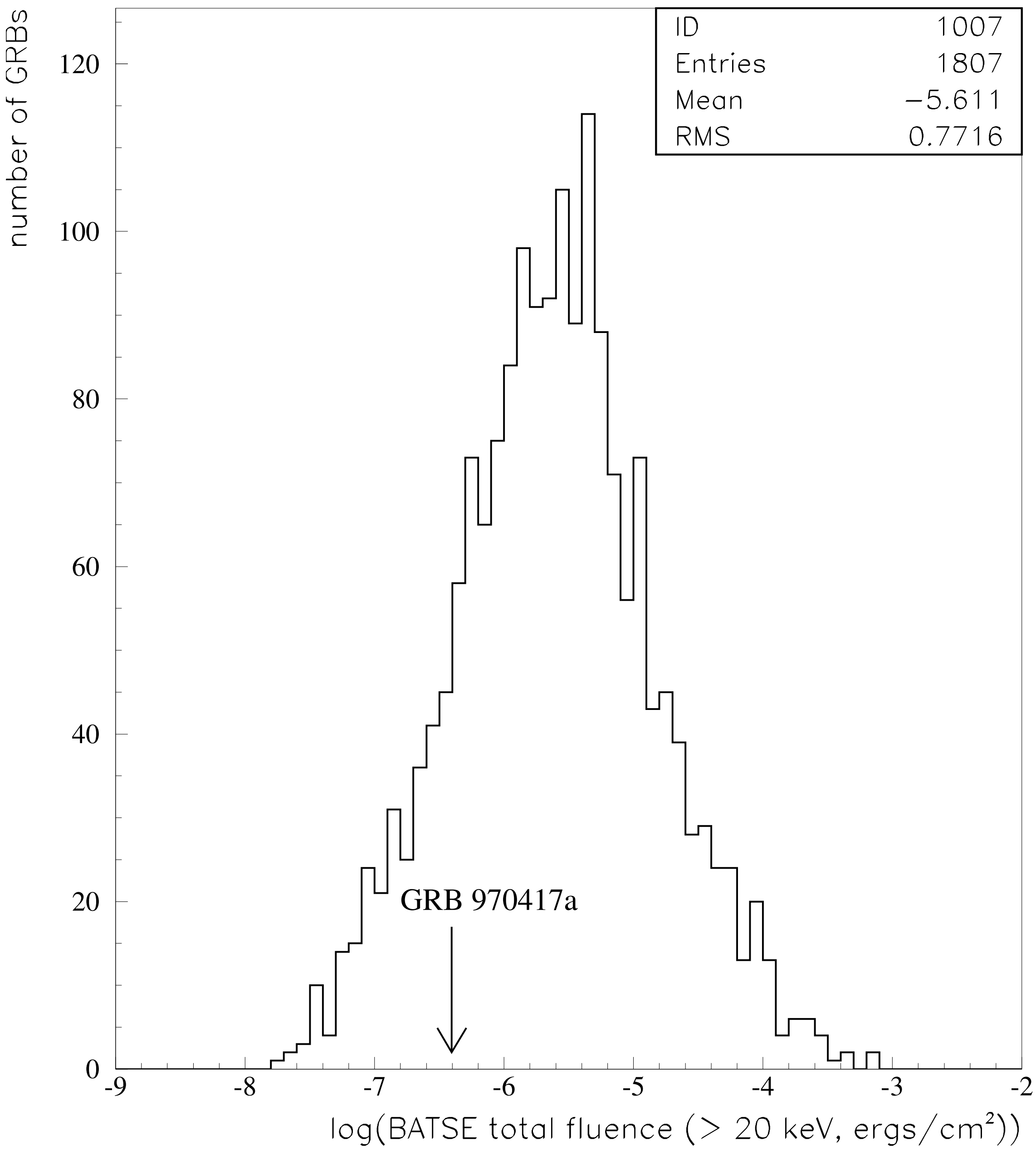

Figure 7.5: BATSE total fluence for a sample of 1807 bursts.

7.2 Maximum Likelihood Approach to the Search for GRB 970417a

The original binned analysis of the 54 GRBs was meant to be a fast, efficient way to search for non-localized sources in large search areas using a minimum of trials. However, the coarseness of the bin overlap – half a bin width – precludes the accurate determination of the location of a source and, therefore, of the number of signal events. The ideal is then to supplement a possible source detection from this type of analysis with a more robust analysis which has the ability to make an accurate estimate of the unknown parameters, namely source position and number of signal events. The *maximum likelihood method* is one such technique. Aside from providing a means for parameter estimation, this method can also be used for testing hypotheses and for estimating confidence intervals. (See, for example, reference [135] for a discussion of the maximum likelihood method.) With these benefits as its goals, and without intending to discard the conclusion of Chapter 6 regarding the final significance of the excess measured in GRB 970417a's search area in the original analysis, this section will be devoted to applying the maximum likelihood method to search for a TeV signal in GRB 970417a's search area.

7.2.1 The likelihood function for Milagrito data reduction In the endeavor to find a TeV source from Milagrito data, there are three unknown parameters to be estimated:

N_s : The number of signal events from the source.

δ_s : The declination of the source.

α_s : The right ascension of the source.

The measured random variables are (δ_i,α_i), the coordinates of the reconstructed directions of air shower events. Given N events, i.e. N independent measurements of the random variables, the probability density function (PDF) of the random variables (δ_i,α_i) is,

$$f(\delta_i, \alpha_i | N_s, \delta_s, \alpha_s) = \frac{1}{N}[N_s f_s(\delta_i, \alpha_i | \delta_s, \alpha_s) + (N - N_s) f_b(\delta_i, \alpha_i | \delta_s, \alpha_s)] \tag{7.1}$$

where f_s is the PDF for source events and f_b is the PDF for background events (cf. Section 5.3.1):

$$f_s(\delta_i, \alpha_i|\delta_s, \alpha_s) = A_1 \frac{\gamma}{2\pi\sigma_1^2} exp(-\gamma^2/2\sigma_1^2) + A_2 \frac{\gamma}{2\pi\sigma_2^2} exp(-\gamma^2/2\sigma_2^2) \quad (7.2)$$

$$f_b(\delta_i, \alpha_i|\delta_s, \alpha_s) \approx \frac{\gamma}{\pi\gamma_o^2} \quad , \quad (7.3)$$

where γ is the space angle between (δ_s,α_s) and (δ_i,α_i), $\sigma_1 = 2.10^o = 0.0367\ rad$, $\sigma_2 = 0.77^o = 0.0134\ rad$, and $A_1 \approx A_2 \approx 0.5$. The maximum likelihood function is then,

$$L(\underline{\delta}, \underline{\alpha}|N_s, \delta_s, \alpha_s) = L(\delta_1, ..., \delta_N, \alpha_1, ..., \alpha_N|N_s, \delta_s, \alpha_s) = \prod_{i=1}^{N} f(\delta_i, \alpha_i|N_s, \delta_s, \alpha_s) \quad (7.4)$$

The background distribution used in this maximum likelihood analysis was obtained by counting the number of background events falling within varying angular distances from the center of the search area, and occurring within a six-hour window centered at the burst time. The dotted line in Fig. 7.6 shows this measurement, normalized to the total number of background events detected within the 11.4^o search radius during the six-hour period. The y-axis thus gives the probability for finding a background event within an angular distance from the chosen origin. This measurement was repeated using different locations in the search area as the origin, and the resulting background probability distributions were found to differ by about 1% only. Thus, the background probability distribution shown in Fig. 7.6 can be used regardless of which location in the search area is chosen as the origin. Figure 7.6 also shows the expected background distribution from equation (7.3) (dashed line). The measured and expected background distributions differ by about 2%. Using the measured background distribution and equation (5.9), it was possible to obtain the PDF for background events. This PDF is shown in Fig. 7.7(a) (solid line).

The effect of atmospheric overburden on the background distribution was taken into account by weighting the probability density, as determined above, of an event at a given

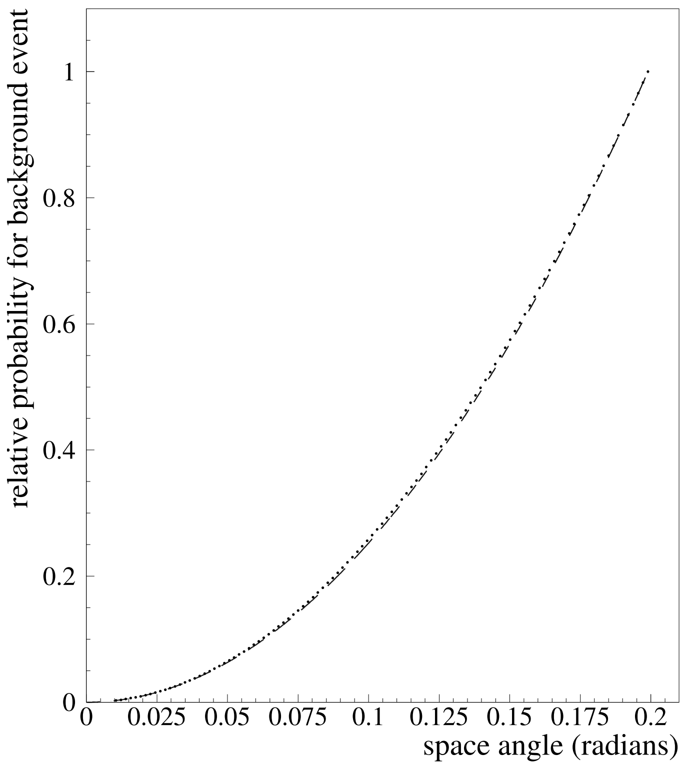

Figure 7.6: Relative probability for finding a background event within a given space angle from the center of the search area. The dots represent background measured from Milagrito data, and the dashed line is the expected background distribution from equation (7.3). The measured and expected distributions differ by about 2% on the average.

location in the search area by a factor which depended on the event's zenith angle. The relative weights came from the expected mean background count as a function of zenith angle in GRB 970417a's search area at the time of the burst. The basic idea is that, given two background events at different zenith angles but at the same angular distance from the origin, the event with the smaller zenith angle has a larger effective background probability density than the other event at the larger zenith angle. This effect is shown in Fig. 7.7(a). The line is the properly normalized PDF obtained through the procedure discussed in the preceding paragraph, that is, the resulting PDF if the background distribution had no zenith angle dependence. The dots, representing the 175 events detected in GRB 970417a's search area during T90, show how events at the same space angle from the origin get weighted dif-

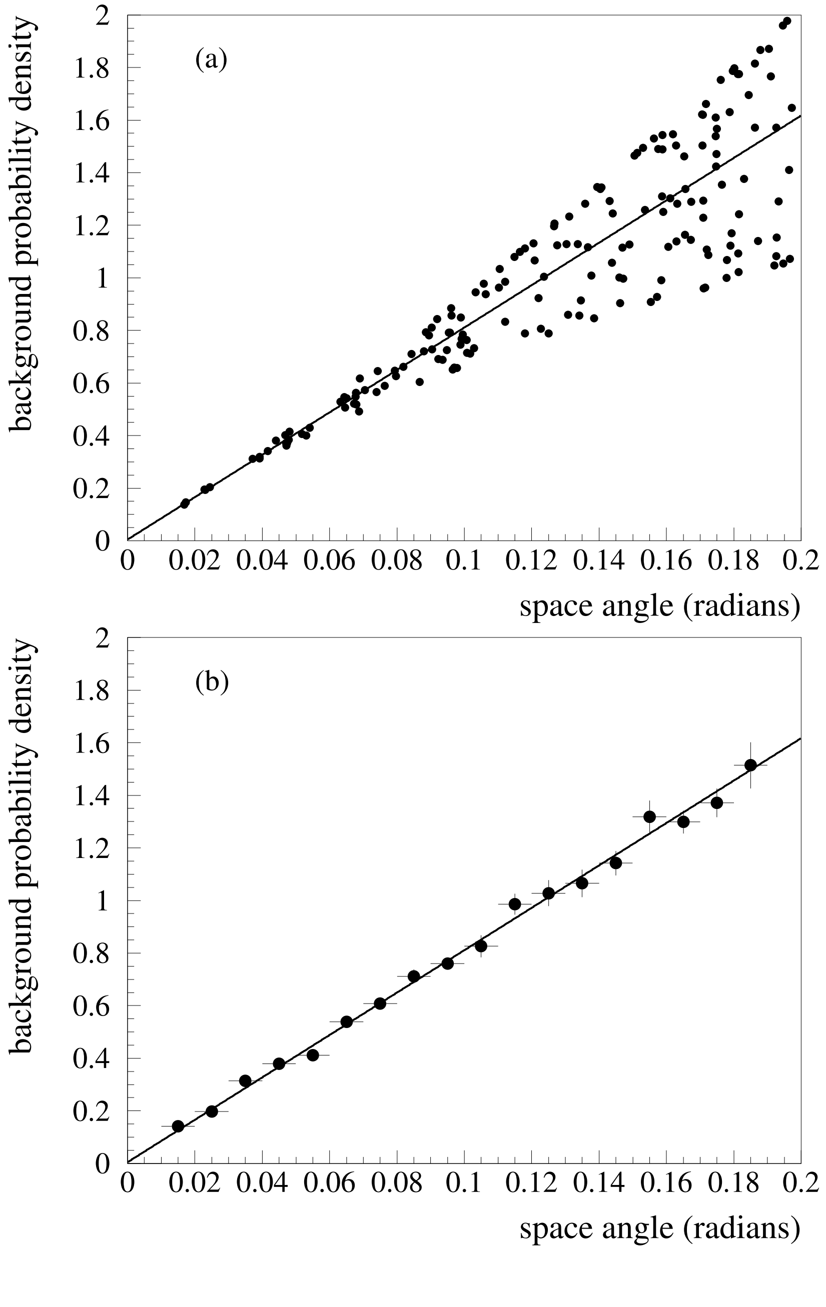

Figure 7.7: (a) The line is the properly normalized background PDF as a function of space angle without taking into account the zenith angle dependence of the background distribution. The dots represent the background probability density of the events in GRB 970417a's search area after taking into account the zenith angle dependence. Events at the same space angle but at different zenith angles get weighted differently and thus get distributed around the original PDF. (b) The dots represent the average weighted probability density of the events as a function of space angle. These match the unweighted PDF so that the probability for finding a background event within the 11.4^o search area is still equal to unity.

ferently depending on their zenith angle. Small zenith angle events have more background weight than large zenith angle events. The dots splay out more with increasing space angle simply because the corresponding area on the celestial sphere gets larger and the range of possible zenith angle values increases with increasing space angle. The weights were normalized such that the probability for finding a background event within the 11.4^o search area was still equal to unity. This was accomplished by finding a normalization such that the average weighted probability density as a function of space angle, using the 175 events, matched the original unweighted PDF, shown in Fig. 7.7(b).

7.2.2 Likelihood ratio A powerful method for testing hypotheses makes use of a ratio of likelihoods. Consider the ratio of the likelihood for the null hypothesis (no source exists) to be true to the likelihood for the alternative hypothesis (a source exists) to be true,

$$\lambda = \frac{L(\underline{\delta}, \underline{\alpha}|N_s = 0, \delta_s, \alpha_s)}{L(\underline{\delta}, \underline{\alpha}|N_s, \delta_s, \alpha_s)} \quad . \tag{7.5}$$

For a given set of measured random variables ($\underline{\delta}$,$\underline{\alpha}$) and maximum likelihood estimators $\widehat{N}_s$, $\widehat{\delta}_s$, $\widehat{\alpha}_s$, this ratio clearly takes on a value from 0 to 1. A value of λ close to 1 indicates a large probability that no source exists and, at the other end of this continuum, a value of λ close to 0 points to a large probability that a source exists. To find estimates for the unknown parameters, and at the same time test the alternative hypothesis against the null hypothesis, maximizing the likelihood for the alternative hypothesis relative to the likelihood for the null hypothesis is necessary. In other words, equation (7.5) or, equivalently, its natural logarithm, has to be minimized.

Asymptotically, under the null hypothesis, $-2ln\lambda(\widehat{N_s}, \widehat{\delta_s}, \widehat{\alpha_s})$ is distributed as a central χ^2 distribution with one degree of freedom. Thus, its square root is distributed as a standard normal variable and can be used to quantify the significance of a measured excess, i.e.,

$$S = \sqrt{-2ln\lambda(\widehat{N_s}, \widehat{\delta_s}, \widehat{\alpha_s})} \quad . \tag{7.6}$$

On the other hand, under the alternative hypothesis, $-2ln\lambda(\widehat{N_s}, \widehat{\delta_s}, \widehat{\alpha_s})$ is asymptotically distributed as a non-central χ^2 distribution with one degree of freedom and non-centrality parameter,

$$K = N_s^2 I_{N_s} \quad , \tag{7.7}$$

where I_{N_s} is the inverse of the variance of the distribution of $\widehat{N_s}$ and is given asymptotically as,

$$I_{N_s} = -\frac{\partial^2 L}{\partial N_s^2}\bigg|_{\widehat{N_s}, \widehat{\delta_s}, \widehat{\alpha_s}} \quad . \tag{7.8}$$

Knowledge of this asymptotic behavior under the alternative hypothesis is useful in calculating the power of the test.

The efficacy of the maximum likelihood technique in estimating the unknown parameters was tested by performing simulations in which the real values of the parameters were known. Source events distributed according to equation (7.2), and background events uniformly distributed over the celestial sphere were generated. The actual number of source events was 20 and the background level was similar to the background level found in GRB 970417a's search area during T90, i.e. 155 events over an area of radius 11.4^o. The real position of the simulated source was similar to the position of the hot bin found in the search area using the binned analysis, i.e. about 3^o from the nominal BATSE position which was used as the center of the search area. The values of the unknown parameters N_s, δ_s, and α_s which minimized the likelihood ratio, equation (7.5), were found and the significance calculated using equation (7.6). The results of the simulations are shown in Fig. 7.8. Figure 7.8(a) is a plot of the average significance as a function of search area radius used in

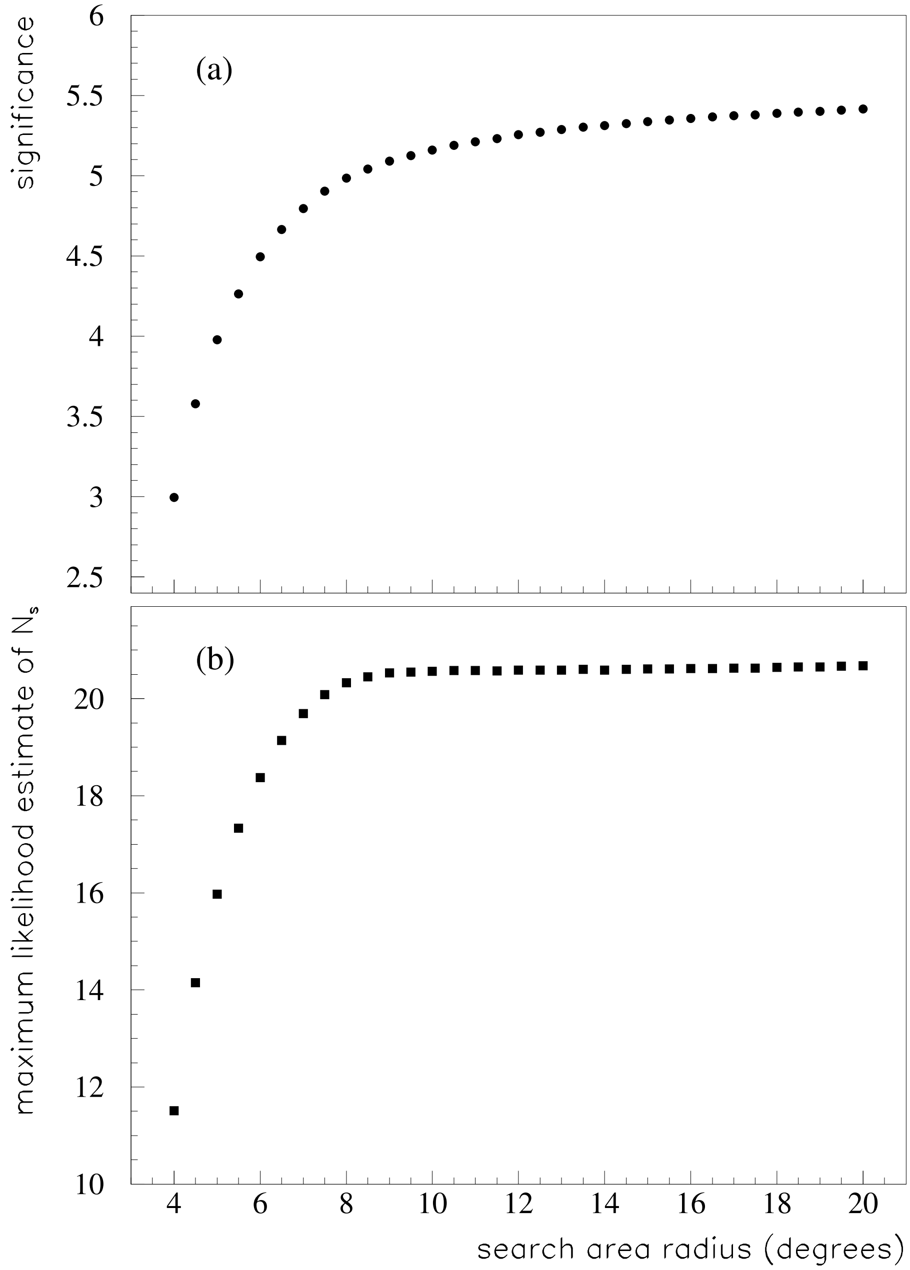

Figure 7.8: (a) Average significance, as a function of search area radius, resulting from a maximum likelihood analysis of simulated source and background events. (b) Average total number of signal events, N_s, as a function of search area radius, estimated through the maximum likelihood method. The actual number of source events used in the simulations was 20.

the simulations, and Fig. 7.8(b) is a plot of the maximum likelihood estimate of the total number of source events as a function of search area radius. It can be seen that, given the source point spread function used, as long as the search area radius is larger than 7^o, the maximum likelihood technique estimates the number of signal events quite well. This is also true for the estimated coordinates of the source position, which were both estimated with an accuracy of $\approx 0.01^o$.

In this analysis, the set of ($\underline{\delta}$,$\underline{\alpha}$) used to calculate the likelihood ratio consisted of the coordinates of 175 air shower events reconstructed as coming from GRB 970417a's search area of radius 11.4^o during the T90 duration of 7.936 seconds.

7.2.3 Confidence intervals By invoking the asymptotic properties of the likelihood ratio, it is possible to estimate confidence intervals for the unknown parameters. Let the set of measured random variables be symbolized by $\underline{x}$, and the set of $r+s$ unknown parameters by $\underline{\theta}$, with $\underline{\theta}_r$ representing the r restricted parameters, and $\underline{\theta}_s$ representing the s unrestricted parameters. Then, as in equation (7.5), define the following likelihood ratio:

$$\lambda(\underline{\theta}) = \frac{L(\underline{x}|\underline{\theta}_{ro}, \underline{\theta}_s)}{L(\underline{x}|\underline{\theta})} \quad , \tag{7.9}$$

where $\underline{\theta}_{ro}$ symbolizes the values of the constrained parameters under the null (H_0) hypothesis. If $\widehat{\underline{\theta}}$ is the set of maximum likelihood estimators, and $\underset{\sim}{I}$ is the information matrix for the parameters $\underline{\theta}$ [135], then, asymptotically,

$$-2ln\lambda(\widehat{\underline{\theta}}) + 2ln\lambda(\underline{\theta}) = (\widehat{\underline{\theta}} - \underline{\theta})^T \underset{\sim}{I}(\widehat{\underline{\theta}} - \underline{\theta}) \quad . \tag{7.10}$$

Since, asymptotically, $\widehat{\underline{\theta}}$ is distributed as a multi-normal variable with covariance matrix $\underset{\sim}{I}^{-1}$, it follows that equation (7.10), which gives the difference between the value of $-2ln\lambda$ at the estimator $\widehat{\underline{\theta}}$ and its value at the true value $\underline{\theta}$, is distributed as a central χ^2 with $r+s$ degrees of freedom [135] . Knowing how this difference is distributed makes possible the estimation of confidence intervals for the unknown parameters.

In other words, if χ^2_β is the value at which the area under the central $\chi^2(r+s)$ distribution is β, then the probability that the difference given by equation (7.10) is less than or equal this value is β,

$$P(-2ln\lambda(\widehat{\underline{\theta}}) + 2ln\lambda(\underline{\theta}) \leq \chi^2_\beta) = \beta \tag{7.11}$$

$$\Longrightarrow \qquad P(-2ln\lambda(\widehat{\underline{\theta}}) - \chi^2_\beta \leq 2ln\lambda(\underline{\theta})) = \beta \quad . \tag{7.12}$$

When the value of $-2ln\lambda$ is known at different possible values of the unknown parameters, given the set of measured random variables, then equation (7.12) makes possible the estimation of confidence intervals.

7.2.4 Results of maximum likelihood analysis The maximum likelihood analysis resulted in finding a possible source in the search area of GRB 970417a, with the maximum likelihood estimators being $\widehat{\delta_s} = 54.1^o$, $\widehat{\alpha_s} = 290.9^o$, and $\widehat{N_s} = 19.7$. The angular distance between this position and the center of the bin with the most significant excess in the binned analysis is 0.21^o. The average angular radii of the 68%, 95%, and 99% confidence contours for the position of the source are 0.5^o, 0.9^o, and 1.2^o, respectively. The confidence contours for the position of the source were determined using equation (7.12), using a central χ^2 with two degrees of freedom since N_s was kept at the constant value of 19.7 in the calculations of $-2ln\lambda$. Figure 7.9 is a significance map for the search area, for which the significance was calculated using equation (7.6). The large ellipse is the BATSE 95% confidence ellipse, and the dashed lines around the best source position are the maximum likelihood confidence contours for the position of the source. Figure 7.10 shows the confidence intervals for the number of signal events, obtained by keeping (δ_s,α_s) constant at the maximum likelihood estimators and using $\chi^2(1)$ in equation (7.12).

The maximum likelihood ratio, equation (7.5), at the maximum likelihood estimators has a value of 6.0×10^{-6}, corresponding to a significance of 4.9 standard deviations. Although this value is close to the significance of 5.2 standard deviations obtained from

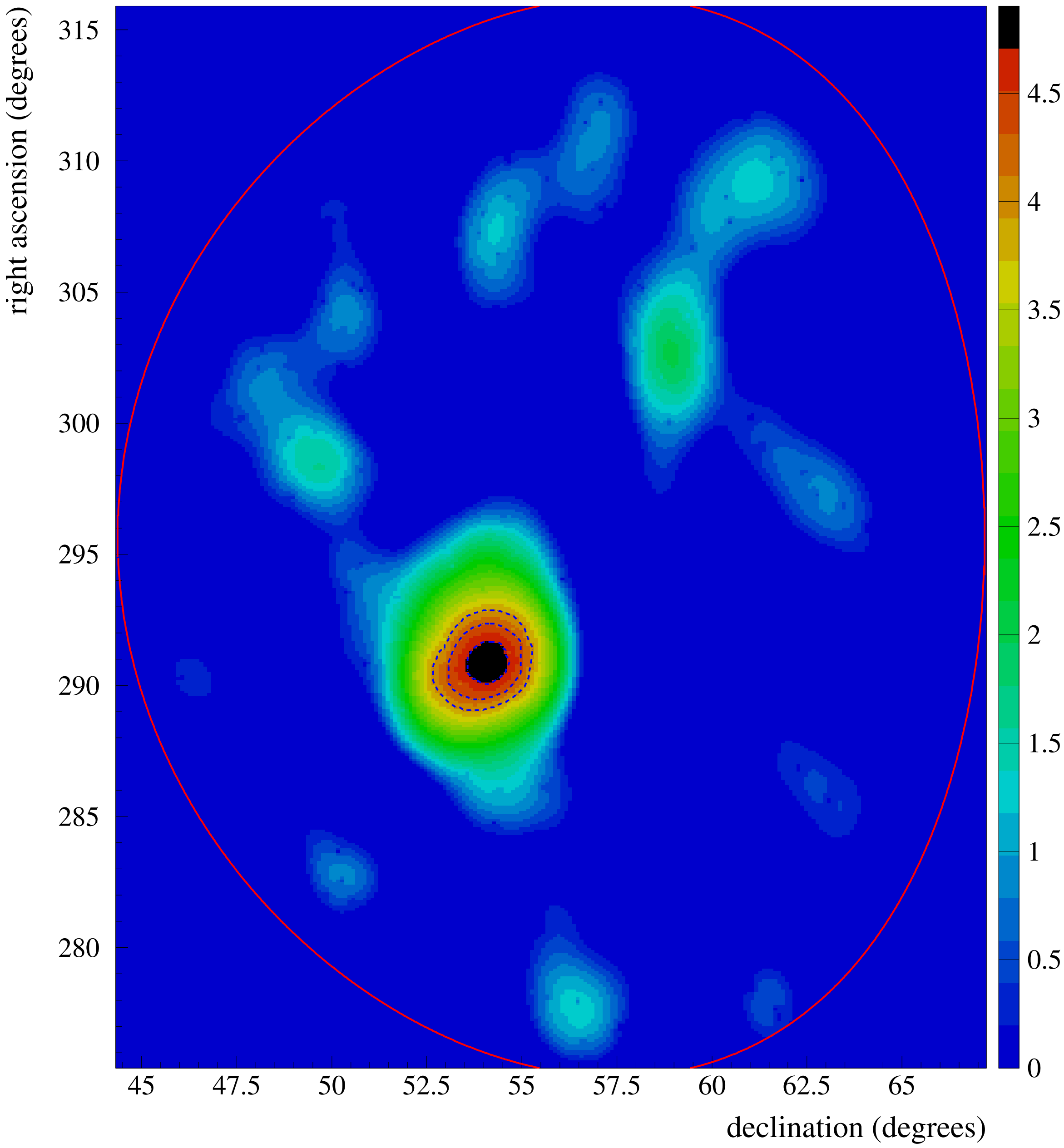

Figure 7.9: Significance map for GRB 970417a's search area, for which the significance was calculated using equation (7.6). The maximum likelihood estimators for the position of the source are $\widehat{\delta_s} = 54.1^o$, $\widehat{\alpha_s} = 290.9^o$. The significance at this position is 4.9 standard deviations. The large ellipse is the BATSE 95% confidence ellipse, and the dashed lines are, from smallest to largest, the 68%, 95%, and 99% confidence contours from this maximum likelihood analysis.

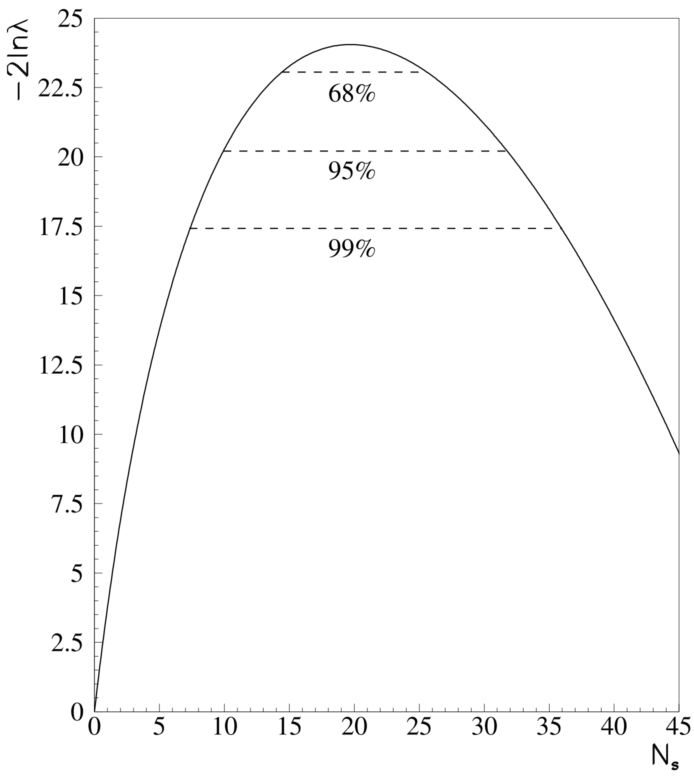

Figure 7.10: Plot of $-2ln\lambda$ vs. N_s, the possible number of signal events, using the estimators $\widehat{\delta_s} = 54.1^o$, $\widehat{\alpha_s} = 290.9^o$ as the position of the source. Confidence intervals for N_s are obtained from this plot by using equation (7.12) and $\chi^2(1)$.

the binned analysis, it is not really reasonable to compare the two numbers, since there is a fundamental and obvious difference between the procedures used to obtain the two significances, namely that the measured random variables used in the maximum likelihood analysis were the (δ_i,α_i) coordinates of each of the 175 events found in the search area during T90, whereas in the binned analysis the measured random variables were the event counts N_{on} and N_{off}. In essence, this difference results in different methods of measuring background and the number of source events. The maximum likelihood approach, as implemented in this analysis, estimates background and the number of source events by examining the spatial distribution of events in the search area during T90, while the binned approach estimates background in a bin through a statistical averaging of the background event count, and measures N_{on} by counting the number of events falling in a bin during T90, without taking into account, on an event by event basis, the spatial distribution of the events (see also [136]).

A final quantity which can be examined is the power of the test. The power of the test is the probability that the alternative hypothesis will be accepted when it is true. It is therefore desirable that this quantity be as close to unity as possible. This quantity can be calculated if the probability density functions of the statistic $-2ln\lambda$ under the two hypotheses being tested are known. It was discussed in Section 7.2.2 that under the null hypothesis, when $N_s = 0$, $-2ln\lambda$ is distributed as a central $\chi^2(1)$. This is shown in Fig. 7.11 (solid line).

Under the alternative hypothesis, when $N_s = \widehat{N_s} = 19.7$, $-2ln\lambda$ is distributed as a non-central chi-square distribution, $\chi^2(1, K)$, with non-centrality parameter K given by equation (7.7). A non-central chi-square with r degrees of freedom, $\chi^2(r, K)$, can be approximated by a variable which is proportional to a central chi-square, such that the variable has the same mean and variance as $\chi^2(r, K)$ [135], i.e.,

$$\chi^2(r, K) = \xi\chi^2(M) \quad , \tag{7.13}$$

where

$$\xi = \frac{r + 2K}{r + K} \tag{7.14}$$

$$M = \frac{(r + K)^2}{r + 2K} \quad . \tag{7.15}$$

For this analysis, $r = 1$ and, using the maximum likelihood estimators obtained, $K = 12.36$. Thus,

$$\chi^2(r = 1, K = 12.36) \approx 1.93\chi^2(7) \quad . \tag{7.16}$$

This distribution is shown in Fig. 7.11 (dashed line).

The usefulness of a test performed to discriminate between two hypotheses is visu-

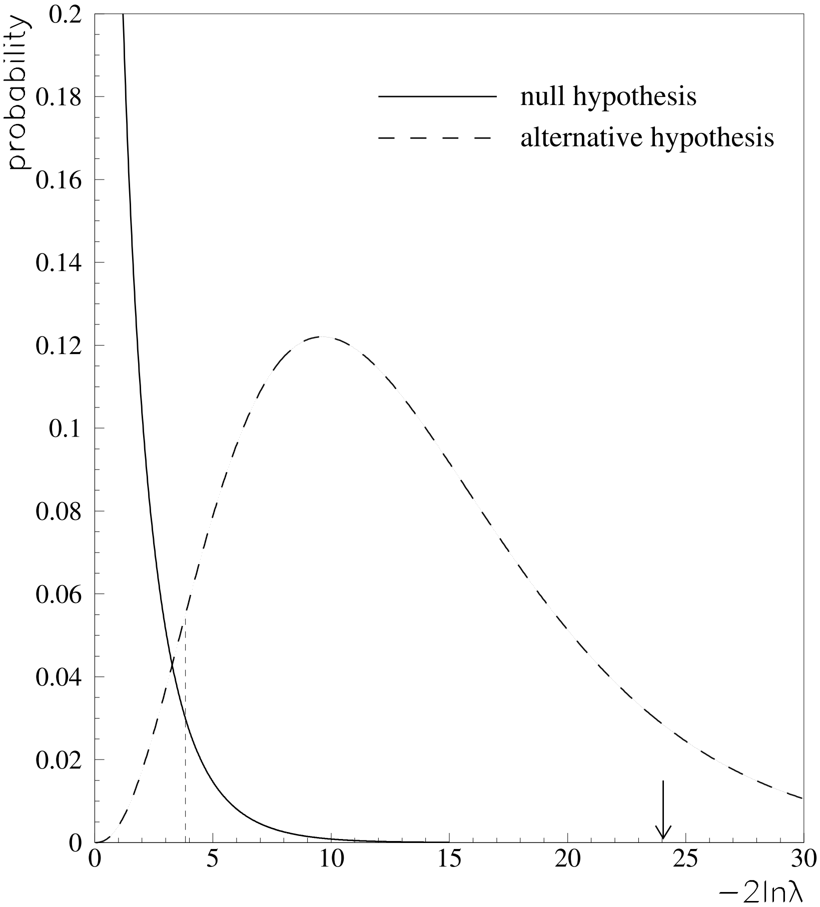

Figure 7.11: The probability density functions, or resolution functions, for $-2ln\lambda$ under the null hypothesis when $N_s = 0$ (solid line), and under the alternative hypothesis when $N_s = 19.7$ (dashed line). The vertical line indicates the critical value of $-2ln\lambda$, chosen such that the significance level, or size of the test, is 0.05. The acceptance region for the null hypothesis is to the left of this value, and the critical region is to the right. With this choice, the power of the test is 0.96. The arrow indicates the value of $-2ln\lambda$ at the maximum likelihood estimators.

ally summarized in the probability density functions, or so-called resolution functions, of the test statistic under the two hypotheses. A sound decision about which hypothesis to accept is based on resolution functions which are distinct enough to minimize the occurrence of erroneous conclusions. Resolution functions which overlap too much give rise to large probabilities for making the error of rejecting the null hypothesis when it is true and for making the error of accepting the null hypothesis when it is false.

Choosing a significance level, or size of test, of 0.05, the critical value of $-2ln\lambda$ is $-2ln\lambda_c = \chi_c^2(1) = 3.842$. The critical region is then comprised of $-2ln\lambda > -2ln\lambda_c$. This choice for the size of the test means that the probability for making the error of rejecting the null hypothesis when it is true is 0.05. For this choice, the power of the test is,

$$P = \int_{\frac{\chi_c^2(1)}{\beta}}^{\infty} dF(\chi^2(M)) \tag{7.17}$$

$$= 0.96 \quad , \tag{7.18}$$

where $F(\chi^2(M))$ is the cumulative distribution function of the central $\chi^2(M)$ variable. Thus, given the choice of the critical region, the probability for accepting the alternative hypothesis when it is true is 0.96. Note that with the maximum likelihood estimators obtained, the value of $-2ln\lambda$ is 24.0 $-$ well within the critical region. The probability of $-2ln\lambda$ being at least this large when the null hypothesis is true is 9.4×10^{-7}.

7.3 Lower Limits on Primary Energies of Events from Candidate GRB 970417a

If the analysis results presented in this and the previous chapter point to TeV emission by a gamma-ray burst, then information about the energies of the primary gamma-ray particles attributed to this GRB, and whose electromagnetic cascades were probably detected by Milagrito, would provide a means for determining the distance scale of this GRB from its most human and insignificant observers and, therefore, of the magnitude of the energy it released in the form of TeV gamma-rays in the short span of eight seconds. As discussed in Chapter 4, Milagrito did not have the capability to determine the energy of a primary particle initiating a detected air shower, a consequence primarily of the poor core location capability of Milagrito. It might, however, be possible to put a lower limit on this primary particle energy, using information from observational data and from computer simulations. This section asserts this possibility and puts forward a method for placing a lower limit on the energy of a primary photon which initiates an air shower which is detected by Milagrito.

The method for determining energy lower limits presented here utilizes the number of PMTs hit by Cherenkov light, produced as a result of an air shower incident on the Milagrito pond. On the average, an air shower initiated by a primary particle of a certain energy and zenith angle, and whose core lands a certain distance from the pond center, will effect a larger number of tubes hit than will an air shower initiated by a primary with a smaller energy but coming from the same direction, and whose core lands at the same position as that of the first shower core. On the other hand, as it often happens, a small shower whose core lands in the pond can result in a larger number of tubes hit compared to that produced by a big shower whose core lands a great distance from the pond. Knowledge of the real core position is most certainly useful in determining the energy of a primary particle. Nevertheless, the most will be done with the information that is available.

7.3.1 Data on reconstructed cores and number of tubes hit Figure 7.12 shows the reconstructed core positions for the 17 air shower events ascribed to GRB 970417a. As expected, the reconstructed cores all lie inside the pond. The average uncertainty in the reconstructed core positions is 17 meters, which is about half the width of the bottom of the pond. (The dimensions of the bottom of the pond is 30 meters by 50 meters.) The number of tubes hit for each air shower is also given. The number of tubes hit for the 17 air showers ranges from 97 to 182.

Figure 7.13(a) gives the number of tubes hit resulting from air showers triggering

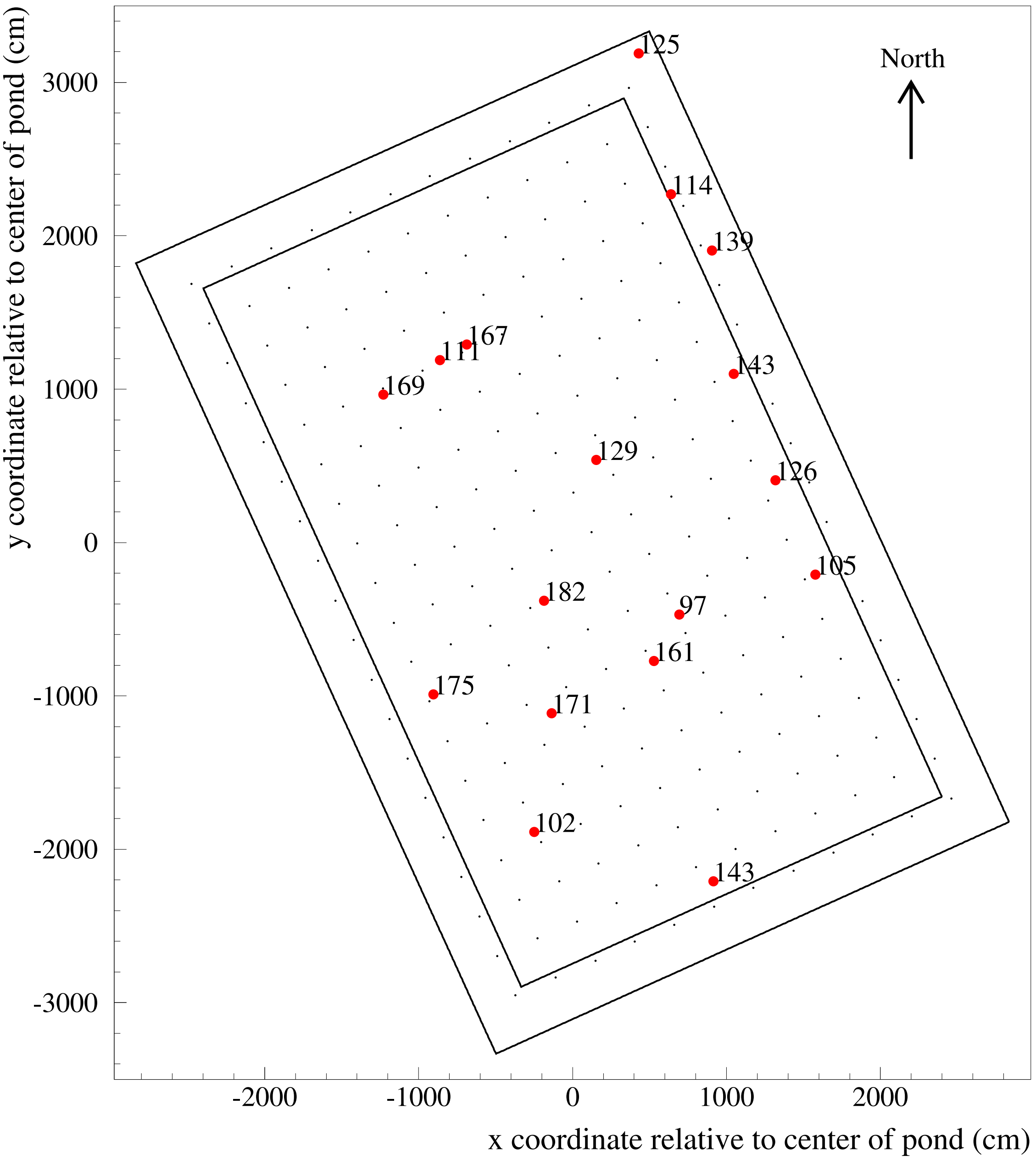

Figure 7.12: Reconstructed core positions of the 17 air shower events which fell in the T90 window, and whose reconstructed directions were in the hot bin found in GRB 970417a's search area. The number of tubes hit for each air shower is also given. The inner rectangle delineates the bottom of the pond, and the outer rectangle delineates the water surface. The small dots give the positions of the PMTs, including that of dead tubes.

Milagrito and having reconstructed directions falling in the local hot bin found in GRB 970417a's search area, plotted as a function of time relative to the BATSE trigger time for GRB 970417a. The 17 events detected during T90 are bunched at relative time zero. The largest number of tubes hit for these 17 events is 182. Figure 7.13(b) gives the number of detected air showers, for every 17 events shown in (a), which resulted in more than 182 tubes being hit, as a function of relative time. So for the 17 candidate signal events, this number is zero (since none of the events resulted in more than 182 tubes being hit), and for the next 17 events detected by Milagrito in the local hot bin, this number is four, and so on. The relative absence of a large number of tubes hit during T90 might be indicative of the relative absence of cosmic ray initiated showers during T90. As Milagrito did not have gamma-hadron separation capabilities, this hypothesis cannot otherwise be proven.

7.3.2 Upper limit on the number of tubes hit The proposed method for placing a lower limit on a primary particle's energy begins with determining a 99.7% confidence upper limit on the number of tubes hit resulting from simulated air showers produced by primary photons of a fixed energy, and coming from a source located at the center of the local hot bin found in GRB 970417a's search area. Since the goal is to determine energy lower limits using the observed number of tubes hit, and since the nearer a shower core is to the pond the larger the number of tubes hit on the average, the cores of the simulated showers were thrown only within the area defined by the water surface, i.e. 36.6 meters by 56.6 meters. A 1-meter layer of water above the PMTs, the depth at the time of GRB 970417a's activity, was used in the simulations. PMTs which were not used in the actual reconstructions were not included in the simulations.

The results of the simulations are shown in Fig. 7.14. The figure plots the ratio of the number of shower events resulting in a given number of tubes or less being hit to the total number of showers thrown, for different primary energies. For a given primary photon energy, the corresponding curve gives the probability that an air shower produced by the

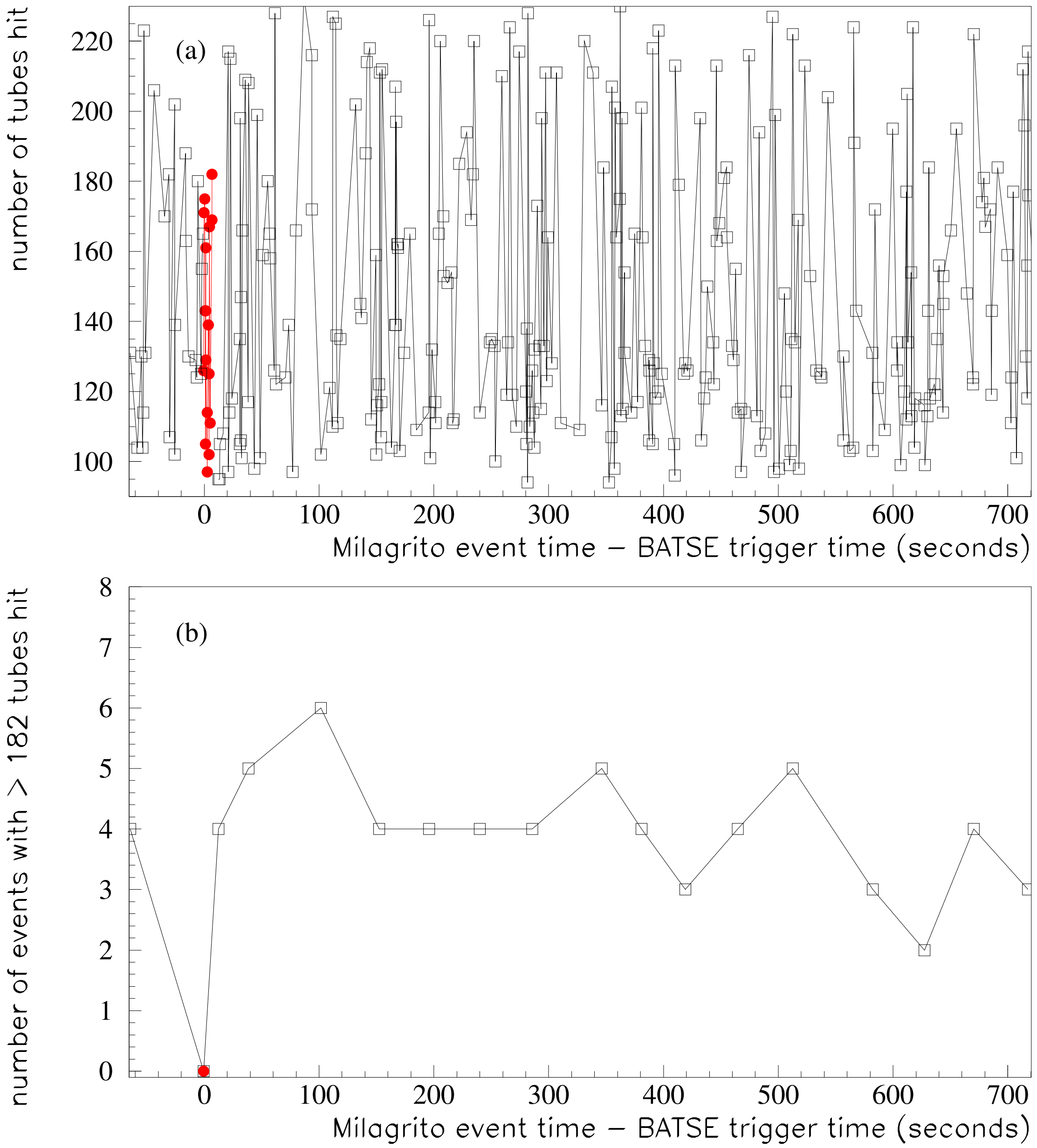

Figure 7.13: (a) Number of tubes hit as a result of air showers, with reconstructed directions falling in the local hot bin found in GRB 970417a's search area, triggering Milagrito, as a function of time relative to the BATSE trigger time for GRB 970417a. The 17 events which were detected during T90 are symbolized by dots, and can be found near relative time zero. (b) The number of detected air shower events, for every 17 events, which resulted in more than 182 tubes being hit. The relative absence of a large number of tubes being hit during T90 might be indicative of the relative absence of cosmic ray initiated shower events during T90.

primary, and whose core lands within the area delineated by the water surface, will result in a given number of tubes or less being hit. Using these results, an upper limit on the number of tubes hit due to primary photons of a given energy, defined as that number of tubes for which the probability for obtaining this number or less is 99.7%, can be determined. The resulting plot of primary photon energy versus upper limit on the number of tubes hit is shown in Fig. 7.15. This same information is then turned around to obtain a lower limit on the primary photon energy given an observed number of tubes hit. For real air showers whose cores land inside the pond, the energy lower limit obtained through this method will be a 99.7% (3σ) confidence lower limit. For showers with cores landing outside the pond, the energy lower limit obtained through this method will be at a higher confidence level.

Nondetection of a significant excess in the Milagrito scaler counts during T90 [137] rules out the possibility that the 17 events ascribed to GRB 970417a were due to a large flux of low-energy primary photons or, for that matter, a large flux of any energy. This finding makes reasonable the use of the method outlined above to set lower limits on the primary energies, since ruling out a large photon flux of a certain energy severely limits the occurrence of shower events which give rise to a number of tubes hit which is larger than the upper limit set for that energy.

7.3.3 Lower limits on the energies of primary photons attributed to GRB 970417a

The lower limits on the primary photon energies corresponding to the detected air shower events attributed to GRB 970417a can be found in Table 7.2. The number of tubes hit for each air shower, and each event's time, are also given. The energy lower limits range from 343 GeV (97 tubes hit) to 920 GeV (182 tubes hit). Figure 7.16(b) plots the energy lower limit versus the event time relative to the BATSE trigger time. In understanding these results, one has to remember that the average background count expected in the hot bin during T90 was 3.4.

With these energy lower limits, one can place an upper limit on the fluence of TeV gamma-rays incident at the top of the atmosphere at the time of the burst. Using energy

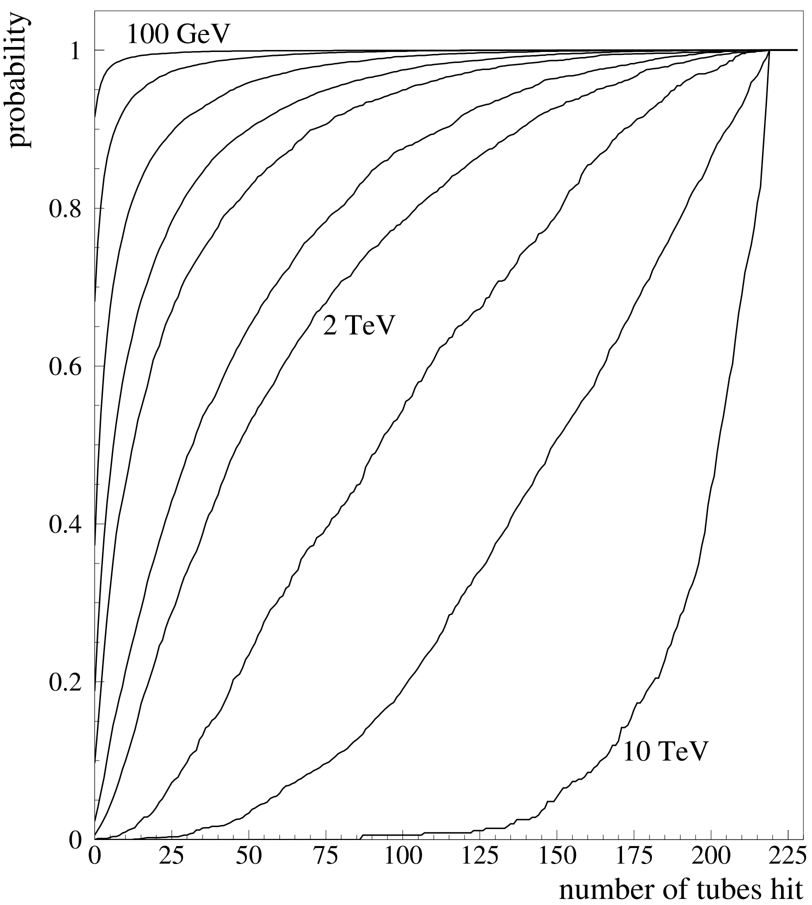

Figure 7.14: Integral distribution of number of tubes hit for different primary photon energies, valid for a source located at the center of the local hot bin found in GRB 970417a's search area, and for 1 meter of water above the PMTs. For a given primary photon energy and a given number of tubes, the corresponding curve gives the probability that an air shower produced by the primary, and whose core lands within the area delineated by the water surface, will result in that number of tubes or smaller being hit. From left to right, the curves correspond to the following primary photon energies: 100 GeV, 250 GeV, 500 GeV, 750 GeV, 1 TeV, 1.5 TeV, 2 TeV, 3 TeV, 5 TeV, and 10 TeV.

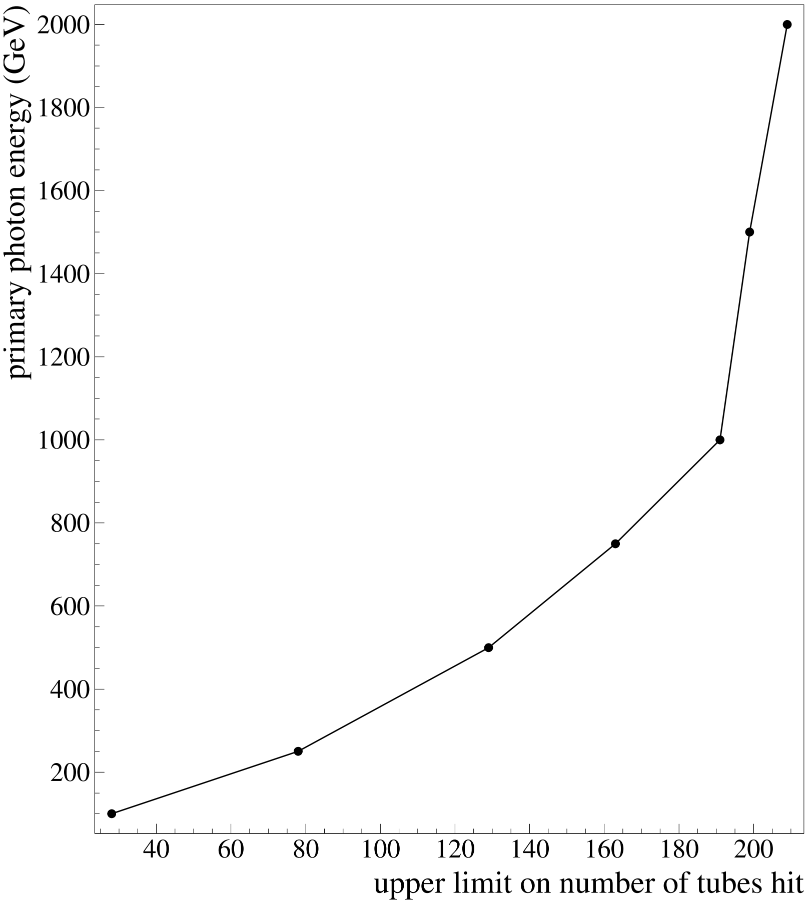

Figure 7.15: Plot of 3σ upper limit on the number of tubes hit for different primary photon energies, derived from Fig. 7.14. The same plot is used to determine a lower limit on the energy of each of the primary photons initiating the detected air shower events attributed to GRB 970417a, using the observed number of tubes hit for each event.

lower limits results in an upper limit on the fluence because Milagrito is less sensitive to low-energy photons than to high-energy ones, which means that the total energy incident on Earth due to the GRB has to be concentrated over a smaller area in order for Milagrito to detect low-energy photons. If the energies of the photons were larger than the lower limits, as they might well be, then the same total incident energy could be spread out over a larger area, that is, the fluence could be lower and Milagrito would still be able to detect the photons (see Fig. 8.4 for a plot of fluence, derived from Milagrito's effective area, as a function of primary gamma-ray energy). The fluence upper limit is calculated thus,

$$\Phi_{max} = \sum_{i=1}^{17} \frac{E_{min,i}}{A_{eff,i}} \tag{7.19}$$

$$= 4.7 \times 10^{-5} \quad ergs/cm^2 \quad , \tag{7.20}$$

where $E_{min,i}$ is the energy lower limit for a primary event, and $A_{eff,i}$ is the Milagrito effective area for that energy, for a source located at the center of the local hot bin, and for a 1-meter layer of water above the PMTs. A fluence of this magnitude is comparable with the largest GRB fluences which have been measured by BATSE.

7.3.4 Experimental uncertainties In Section 6.4.3, it was estimated that the average fractional uncertainty in the Milagrito effective area, A_{eff} was about 30%. Since the effective area is derived by using the number of tubes hit (cf. Section 4.3.1), it will be assumed that the uncertainty in the number of tubes hit plotted in Fig. 7.15 is also about 30%. By using Fig. 7.15, this means that the lower limits on the event energies are uncertain by about 35% or, more precisely, the lower limits on the event energies can be lower than the lower limits given in Table 7.2 by about 35%. Thus, the upper limit on the fluence can be larger than the upper limit given by equation (7.20) by about 45%.

Table 7.2: Lower limits on the energies of the detected events.

event time (UT seconds)	relative[a] event time (seconds)	number of tubes hit	energy lower limit (GeV)
50015.9980	-0.7155	126	485.3
50016.3561	-0.3574	171	821.4
50017.0804	0.3669	175	857.1
50017.2716	0.5581	143	602.9
50017.8051	1.0916	105	382.3
50017.9435	1.2300	143	602.9
50018.1029	1.3894	161	735.3
50018.1911	1.4776	129	500.0
50019.2018	2.4883	97	343.1
50019.2507	2.5372	114	426.5
50020.2730	3.5595	139	573.5
50020.8108	4.0973	102	367.6
50020.9167	4.2032	125	480.4
50021.0978	4.3843	167	785.7
50021.8089	5.0954	111	411.8
50023.4320	6.7185	169	803.6
50023.4660	6.7525	182	919.6

[a] Event time relative to the BATSE trigger time for GRB 970417a.

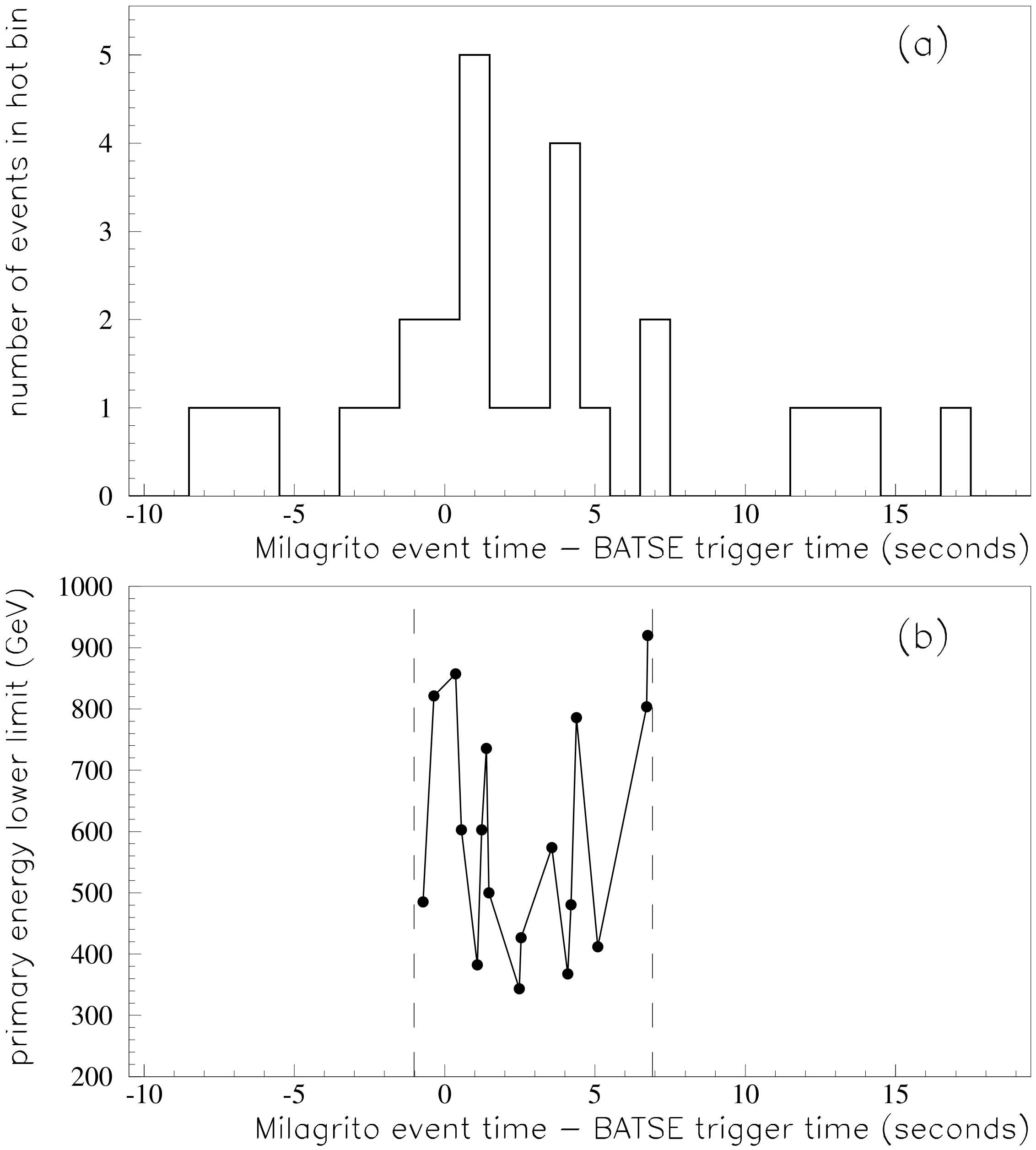

Figure 7.16: (a) Milagrito event time distribution in GRB 970417a hot bin. (b) Lower limits on the energies of the candidate primary photons giving rise to the shower events attributed to GRB 970417a, as a function of time. The dashed vertical lines border the T90 interval.

7.4 Comments on Upper Limit of Event Energies

Like the task of setting lower limits on the event energies, it is difficult to set upper limits on the event energies, again mainly due to the unknown core positions of the detected showers. Even for showers with cores located at very large distances from the pond, it is still possible to trigger Milagrito if the air showers are due to primary photons of sufficiently large energies. Nevertheless, some conclusions can be made by examining the distribution of number of tubes hit. Figure 7.17 shows the probability for getting a certain number of tubes hit or smaller for the case of 10-TeV primary photons and 20-TeV primary photons coming from the direction of the local hot bin, and for one meter of water above the PMTs. In the simulations used to derive the plot, the shower cores were thrown over an area of 400 meters by 400 meters, which is the effective area of Milagrito at energies $E \gtrsim 100\ TeV$ (see Fig. 4.20). It can be seen from the plot that for 10-TeV primaries, the probability that the number of tubes hit is 182 or smaller is about 97%, and for 20-TeV primaries, this probability is about 92%. As the primary energy increases from this, the probability decreases, i.e. getting 182 or fewer tubes hit becomes less probable as the primary energy increases.

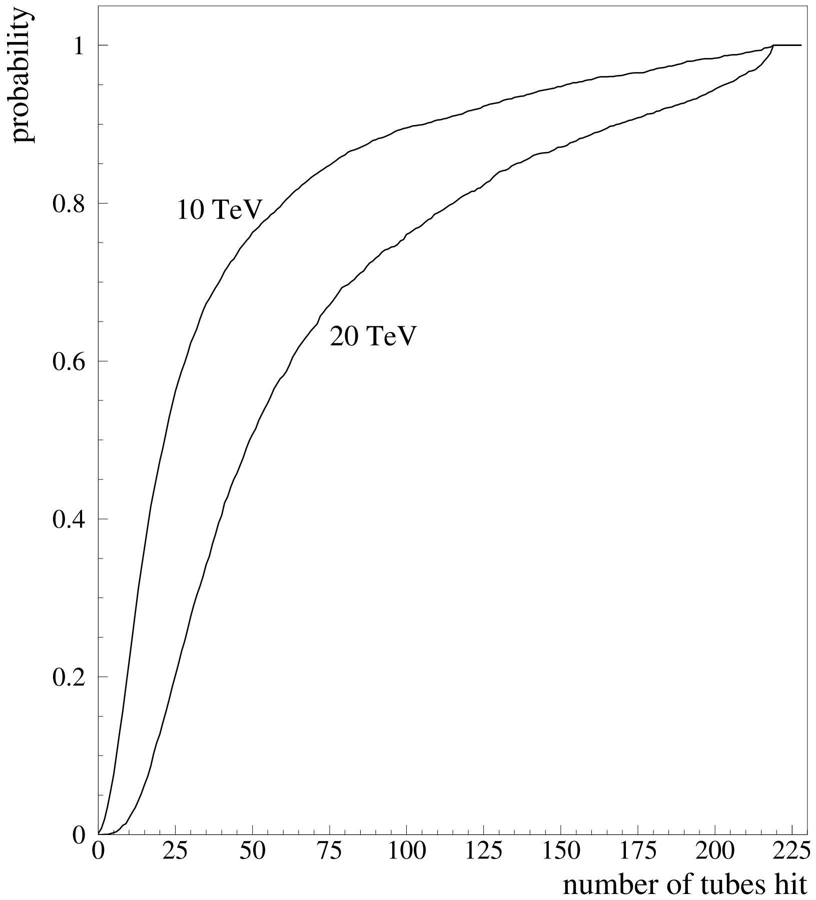

Figure 7.17: Integral distribution of number of tubes hit for 10-TeV and 20-TeV primary photon energies. The simulated source was located at the center of the local hot bin, and the shower cores were thrown over an area of 400 meters by 400 meters. A 1-meter layer of water above the PMTs was used.

Chapter 8

Starlight, Dust, and GRB 970417a

Radiation permeates the Universe. This cosmic radiation, called *extragalactic background light* (EBL), is a record of the processes which took place during the history of the Universe, including the epoch when rapid star formation in galaxies took place, the epoch when the first stars formed, and the epoch when the Universe first became transparent to radiation produced in the Big Bang. The presence of this isotropic radiation at epochs past and present has significant consequences on the study of gamma-ray sources in the TeV regime, since cosmic TeV gamma-rays, as they travel from the past to the present epoch, are expected to interact with the cosmic background photons via the electron-positron pair production mechanism. For example, interaction of gamma-rays of energy $\gtrsim 100\ TeV$ with the microwave component of the cosmic background radiation, the component which overwhelmingly dominates the EBL spectrum, makes the Universe opaque to gamma-ray photons with energies $\gtrsim 100\ TeV$ and, thus, leaves little motivation for the study of cosmic, ultra-high energy (UHE), gamma-ray sources [69]. The Universe is more transparent to gamma-rays of lower energies, i.e. of energies $\sim 0.1\ TeV$ to $\sim 10\ TeV$, thus allowing for the study of gamma-ray sources at these energies by ground-based experiments. In contrast, the effect of the EBL on extragalactic gamma-rays with energies $\lesssim 10\ GeV$, the energy range of satellite experiments, is negligible at redshifts $z \lesssim 3$ [138]. This chapter examines the implications of the interaction of the TeV photons attributed to GRB 970417a with the EBL, specifically its infrared (IR) component, on the distance scale and energy release of the GRB.

8.1 Extragalactic Background Light

As the term asserts, extragalactic background light refers to diffuse, isotropic radiation originating beyond the Milky Way galaxy. The extragalactic background light present at the current epoch can be decomposed into three components, depending on the wavelength of the radiation, with the three components having different origins. Radiation in the wavelength range from $\sim 0.1\ \mu m$ to $\sim 10\ \mu m$ (ultraviolet to near infrared), the so-called *starlight component*, is primarily the cumulative energy released in nucleosynthetic processes in stars in all the galaxies which existed in the Universe. Where there was a dusty interstellar environment, this starlight component heated the dust and was subsequently re-radiated or scattered by the dust at longer infrared wavelengths. This reprocessing of the radiation by the dust is the primary origin of the so-called *dust component* of the EBL, observed at the present epoch at wavelengths of $\sim 10\ \mu m$ to $\sim 300\ \mu m$ (mid to far infrared). Active galactic nuclei (AGN), black holes, gravitationally collapsing systems could also contribute to the infrared component of the EBL [139, 140]. A third component, observed at $\gtrsim 300\ \mu m$ (sub-millimeter to millimeter), is the *cosmic microwave background* (CMB), a remnant of the radiation created in the Big Bang. The wavelengths of all three components of the EBL have been redshifted to their present-day values from the original wavelengths at the time of the radiation's creation in the past.

Figure 8.1 plots the limits and recent detections which have been made of the EBL spectral energy density (SED), which gives the energy of the background radiation per unit area per unit solid angle observed per second at the present epoch as a function of radiation wavelength. The general shape of the EBL SED is outlined in this figure, and the starlight, dust, and CMB components are plainly seen. In studying this figure, it is important to be aware of the difficulties involved in detecting and measuring the EBL at infrared wavelenghts. The CMB component has been precisely measured, obeying a blackbody spectrum at a temperature of $T = 2.73\ K$ [152] (thin, solid line in Fig. 8.1). However, the task of measuring the IR component of the EBL is beset with problems relating to the proper sub-

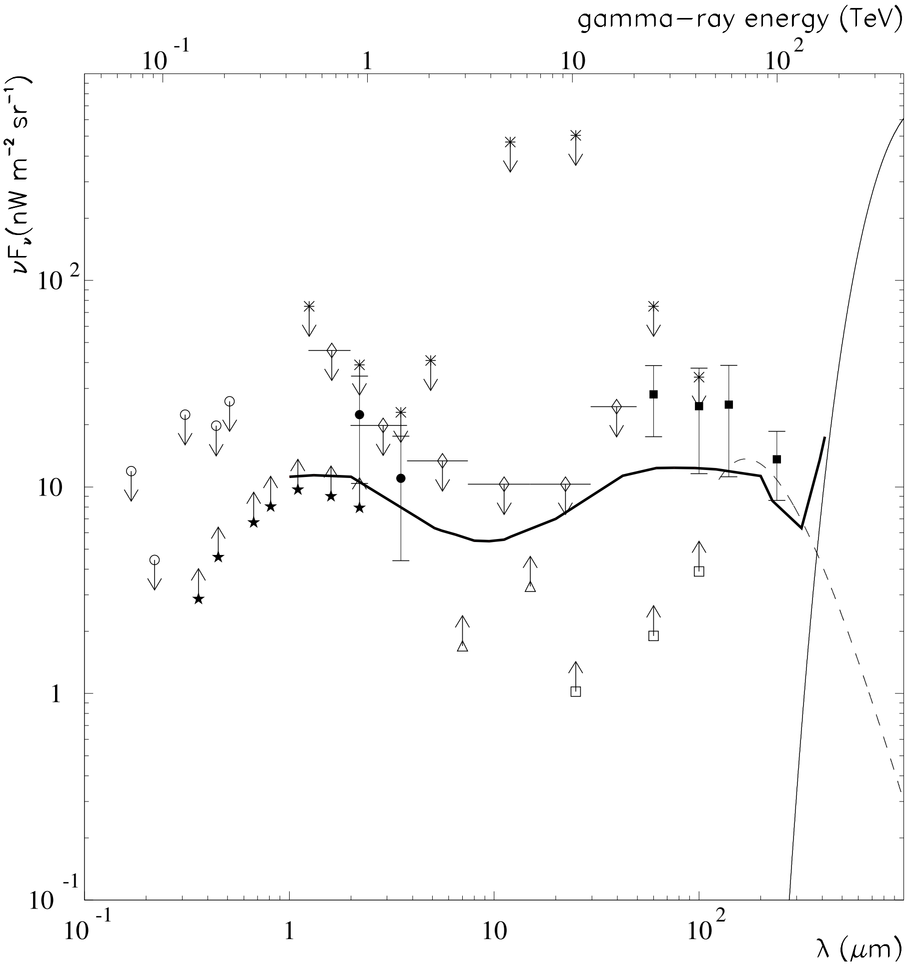

Figure 8.1: Limits on, and detections of, the EBL SED. • and ■ symbols are excesses found in DIRBE data, shown with 2σ error bars [141, 140, 142]; $*$ symbols are upper limits by DIRBE [142]; $\Diamond$ symbols are upper limits derived by Biller, et. al. from Mrk 421 and Mrk 501 energy spectra [143]; $\circ$ symbols are upper limits from photometry measurements [144, 145, 146]; ★ symbols are lower limits from Hubble Deep Field and ground-based galaxy counts [147]; $\triangle$ symbols are lower limits by ISO [148]; □ symbols are lower limits by IRAS [149]. The thin, dashed line is the average EBL SED measured by FIRAS [150], and the thin, solid line is the CMB spectrum. The thick, solid line is the EBL model used by Stecker and de Jager 1997 [151] for calculating optical depths due to electron-positron pair production.

traction of bright foreground radiation. There are basically three sources of this foreground radiation: (1) Zodiacal light is due to scattering and emission of light, from the ultraviolet to the infrared, by interplanetary dust $-$ dust from asteroids and comets $-$ which extends out to the asteroid belt [141]. The bright zodiacal emission peaks at $\sim 25\ \mu m$ [140], which explains the large upper limits on the EBL around this wavelength shown in Fig. 8.1. (2) Emission from dust in the Galactic interstellar medium contributes to the foreground at far infrared wavelengths [141, 140]. (3) Emission from Galactic stars is the main source of foreground at $1\ \mu m$ to $5\ \mu m$ [141, 140].

The *Cosmic Background Explorer* (COBE) [152] is a spacecraft devoted to cosmology, and whose mission is the measurement of the EBL SED at $1.2\ \mu m$ to $1\ cm$. On board are three complementary instruments dedicated to this mission: The Far-Infrared Absolute Spectrometer (FIRAS), the Differential Microwave Radiometers (DMR), and the Diffuse Infrared Background Experiment (DIRBE). The average EBL SED measured by FIRAS [150] at the far infrared region is shown as a dashed line in Fig. 8.1. DIRBE has likewise claimed detections of the EBL at $140\ \mu m$ and $240\ \mu m$ [142]. Recently, analysis of DIRBE data also revealed excesses at $60\ \mu m$ and $100\ \mu m$, excesses which were claimed to be possible detections of the EBL at these wavelengths [140]. At the near infrared region, at wavelengths of $2.2\ \mu m$ and $3.5\ \mu m$, detections of the EBL, using DIRBE data as well as ground-based imaging to estimate the contribution of Galactic stars to the DIRBE data set, have also been recently reported [141]. All of these detections are plotted in Fig. 8.1 with their respective 2σ error bars. Upper limits by DIRBE [142] are also shown as asterisk ($*$) symbols.

Lower limits on the EBL SED obtained by counting galaxies observed at different wavelengths are also given in Fig. 8.1. Lower limits from $0.36\ \mu m$ to $2.2\ \mu m$ are from the *Hubble Deep Field* (HDF) as well as ground-based galaxy counts [147]; lower limits at $7\ \mu m$ and $15\ \mu m$ are from ultra-deep galaxy observations by the *Infrared Space Observatory* (ISO) satellite [148]; and lower limits at $25\ \mu m$, $60\ \mu m$, and $100\ \mu m$ wavelengths are from observations of nearby galaxies by the *Infrared Astronomical Satellite* (IRAS) [149]. In general, lower limits on the EBL SED are obtained from galaxy counts by integrating the convolution of the measured differential galaxy count with the corresponding flux down to the detection limit of the experiment.

It was pointed out at the beginning of this chapter that the interaction of TeV photons with the EBL has significant consequences on the study of cosmic gamma-ray sources at TeV energies. Because of this coupled relationship, it has been realized that it is possible to put constraints on the EBL density by examining the measured energy spectra of known astrophysical TeV gamma-ray sources for evidence of absorption by the EBL. Several efforts toward this goal uses, in particular, the energy spectra of Markarian 421 ($z = 0.031$) and Markarian 501 ($z = 0.033$), two well-studied active galactic nuclei which are also the nearest AGN to Earth, to put constraints on the EBL density at IR wavelengths [143, 153, 154, 155]. Although this particular method of putting constraints on the EBL has not gained wide acceptance in the astrophysics community, it is a sound technique which logically follows from the expected interactions of gamma-ray and EBL photons, and warrants consideration when trying to obtain knowledge about the EBL. Upper limits on the EBL using this method obtained by Biller, et. al. [143] is shown as open diamonds in Fig. 8.1.

Upper limits on the EBL SED at UV and optical wavelengths ($0.17\ \mu m$ to $0.51\ \mu m$) shown in Fig. 8.1 are from photometry measurements [144, 145, 146].

8.2 Interaction of TeV Photons with Extragalactic Background Light

As a TeV photon travels from its source in the past to detectors in the present epoch, it encounters the diffuse cosmic background radiation, and a finite probability exists for the TeV photon and a background photon to interact and produce an electron-positron pair. The cross-section for this interaction [153, 156, 157] is non-zero when

$$\frac{2(m_e c^2)^2}{E\varepsilon(1+z)^2 x} < 1 \quad , \tag{8.1}$$

where E is the TeV gamma-ray energy at the present epoch, ε is the EBL photon energy at the present epoch, z is the redshift at which the interaction takes place, $x \equiv (1 - cos\theta)$, where θ is the angle between the two photons, m_e is the electron rest mass, and c is the speed of light. The cross-section is maximum when

$$\frac{2(m_e c^2)^2}{E\varepsilon(1+z)^2 x} = 0.508 \quad . \tag{8.2}$$

For a head-on collission ($\theta = \pi$), the interaction takes place at EBL photon energies

$$\varepsilon(eV) > \frac{0.26}{E(TeV)\,(1+z)^2} \quad , \tag{8.3}$$

or at wavelengths

$$\lambda(\mu m) < 4.75\, E(TeV)\,(1+z)^2 \quad . \tag{8.4}$$

The cross-section peaks in the case of head-on collissions at the EBL energy

$$\varepsilon(eV) = \frac{0.51}{E(TeV)\,(1+z)^2} \quad , \tag{8.5}$$

or at wavelength

$$\lambda(\mu m) = 2.41\, E(TeV)\,(1+z)^2 \quad . \tag{8.6}$$

So at $z = 0$, a 1-TeV gamma-ray photon interacts mainly with EBL photons with wavelength $\lambda \approx 2.41\ \mu m$ ($\varepsilon \approx 0.51\ eV$), and a 10-TeV gamma-ray photon interacts mainly with EBL photons with wavelength $\lambda \approx 24.1\ \mu m$ ($\varepsilon \approx 0.051\ eV$). Characteristic gamma-ray energies, E, given by equation (8.6) are given on the top axis of Fig. 8.1.

The opacity of the Universe to photons of TeV energies has been estimated by several authors using different models of the EBL SED [158, 151, 156, 159, 155]. This opacity, or optical depth, is a measure of the average number of EBL photons which could interact

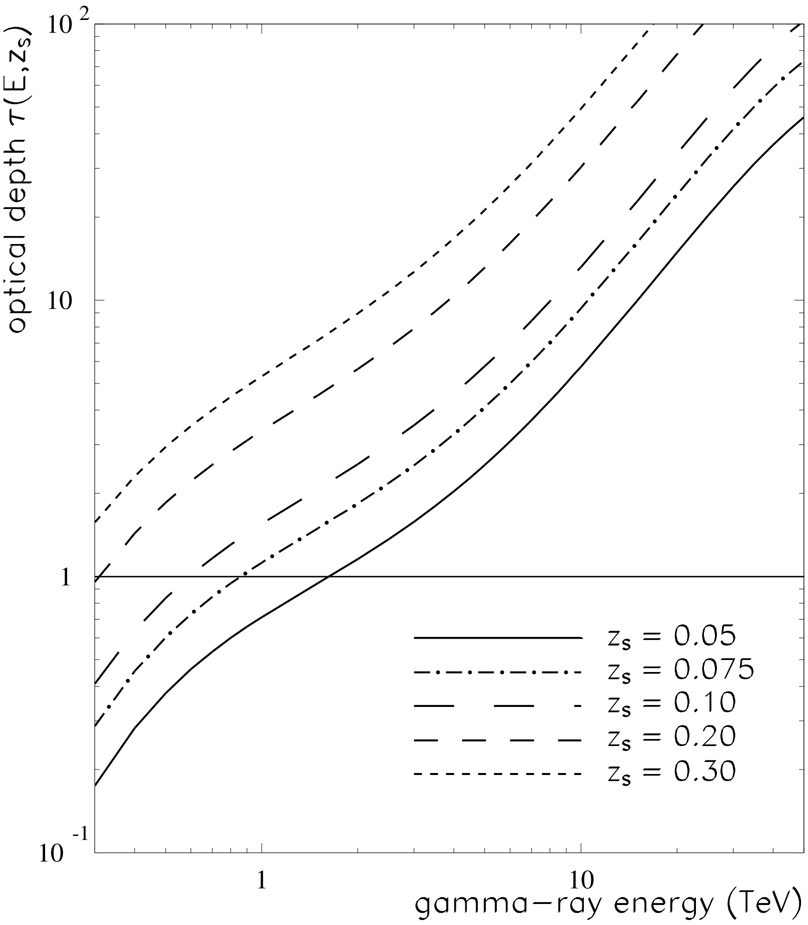

Figure 8.2: Optical depth, calculated by SJ97, due to EBL as a function of gamma-ray energy, for different source redshifts.

with a TeV photon as the TeV photon makes its way from the past to the present. The larger the optical depth, the lesser the chance the TeV photon has for surviving up to the present epoch. The opacity, τ, is thus a function of both the TeV photon energy and the redshift of the source of the TeV photon, $\tau = \tau(E, z_s)$.

For this work, the opacity calculations of Stecker and de Jager 1997 [151] (hereafter SJ97) have been adopted. The model EBL SED which these authors used in their calculation is given as a bold, solid line in Fig. 8.1. Given the measured values of the EBL SED by DIRBE, the model seems to lie on the low side of the measured DIRBE excesses, but is still consistent with the observations, some of which are preliminary, and with the various limits on the EBL SED. Nevertheless, there still exists a large uncertainty in the current knowledge about the EBL SED. The optical depth values of SJ97 are given in Fig. 8.2, which plots optical depth as a function of gamma-ray energy for different source redshifts, and in Fig. 8.3, which plots optical depth as a function of source redshift for different gamma-ray energies.

The probability that a TeV photon of energy E coming from a source redshift z_s will be unabsorbed by the EBL and survive up to the present epoch is given by $exp(-\tau(E, z_s))$. An opacity of unity, for example, would mean a 37% probability for survival. If the differential flux of TeV photons from a gamma-ray source has been measured, then the unattenuated differential flux, corrected for EBL attenuation, would be given by,

$$\left(\frac{dF(E)}{dE}\right)_{unattenuated} = \left(\frac{dF(E)}{dE}\right)_{observed} exp(\tau(E, z_s)) \quad . \tag{8.7}$$

8.3 Implications of TeV Absorption on the Redshift and Energetics of GRB 970417a

In Section 7.3, a lower limit was determined for the energy of each of the 17 primary particles which were detected by Milagrito and ascribed to GRB 970417a. The five largest lower limits obtained ranged from $E \approx 0.8\ TeV$ to $E \approx 0.9\ TeV$ (cf. Table 7.2). Knowledge of these energy lower limits allows the estimate of an upper limit to the distance scale of the GRB. From Fig. 8.3(a), it can be seen that gamma-rays with energies $E \approx 0.8\ TeV$ to $E \approx 0.9\ TeV$ have optical depths $\tau \approx 1$, corresponding to a 37% survival probability, if the GRB source redshift is $z_s \lesssim 0.1$. The same conclusion is obtained if the optical depth calculations of Primack, et. al. [158] are used.

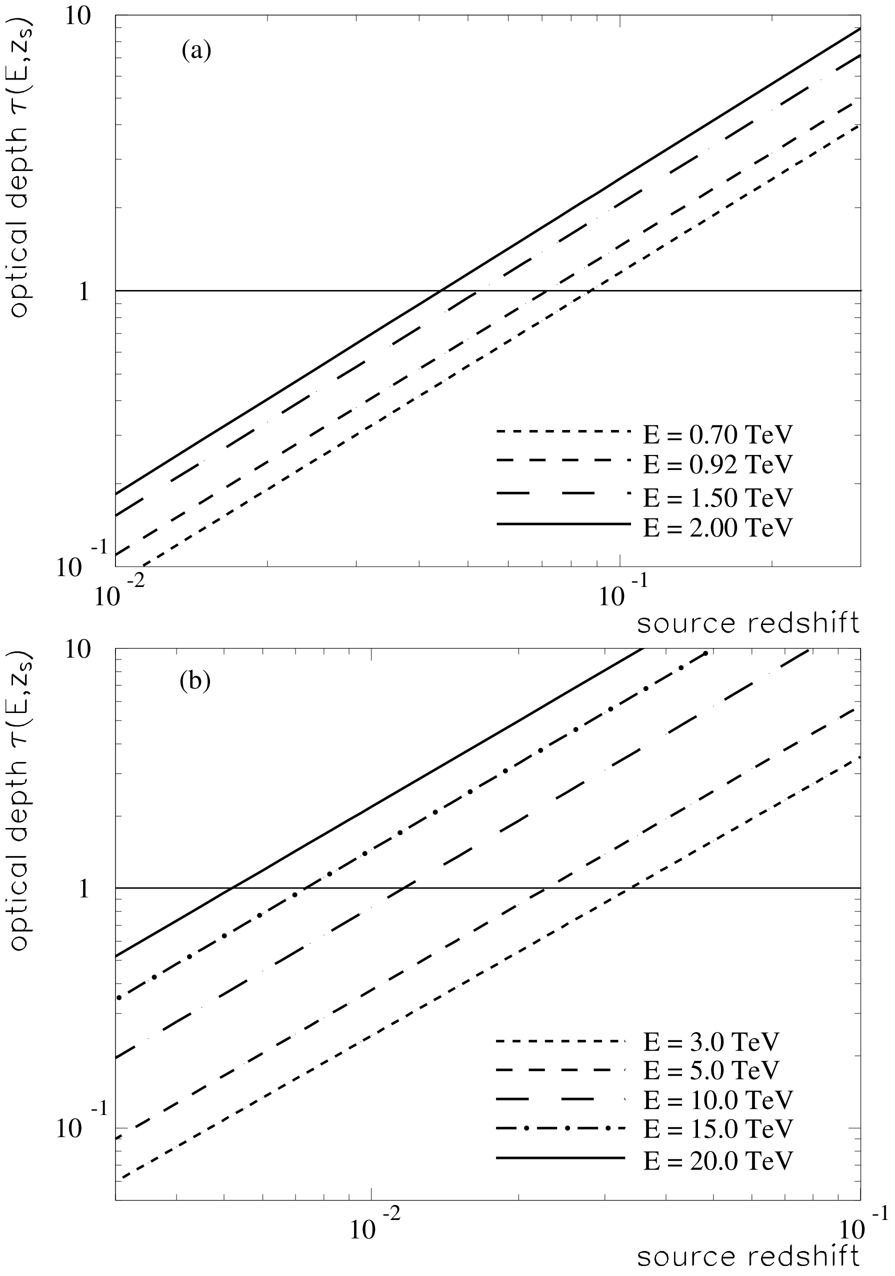

Figure 8.3: Optical depth, from SJ97, due to EBL as a function of source redshift, for different gamma-ray energies.

The energy lower limits given in Section 7.3 can also be used to obtain an upper limit on the energy release of GRB 970417a in the TeV waveband. The upper limit on the isotropic energy release by GRB 970417a in the TeV regime as a function of GRB redshift is calculated using,

$$E_{iso}(z_s) = \frac{4\pi d_L^2}{1+z_s} \sum_{i=1}^{17} \Phi(E_{min,i})\ exp(\tau(E_{min,i}, z_s)) \quad , \tag{8.8}$$

where $E_{min,i}$ is the energy lower limit for the i_{th} event, $\Phi(E_{min,i})$ is the fluence corresponding to this energy, and d_L is the luminosity distance given by equation (2.8), assuming a cosmology with $\Omega_m = 1, \Lambda = 0$, and Hubble parameter $H_o = 65\ km\ s^{-1}\ Mpc^{-1}$. In terms of Milagrito's effective area, equation (8.8) is equal to,

$$E_{iso}(z_s) = \frac{4\pi d_L^2}{1+z_s} \sum_{i=1}^{17} \frac{E_{min,i}}{A_{eff,i}}\ exp(\tau(E_{min,i}, z_s)) \quad . \tag{8.9}$$

Since the effective area of Milagrito for different primary gamma-ray energies is known, it is also possible to set lower limits on the GRB's energy release as a function of redshift, independent of the unknown, actual energy of the highest-energy gamma-ray detected. The basis for determining these lower limits is Fig. 8.4, which plots the fluence implied by the detection of Milagrito of one primary gamma-ray of a particular energy from the zenith angle of the excess count attributed to GRB 970417a, and for a 1-meter layer of water above the PMTs. The fluence implied by the detection of a photon of energy E is given by $E/A_{eff}(E)$ (in $ergs/cm^2$). Figure 8.4 shows that for $E \lesssim 20\ TeV$, as the energy increases, the implied fluence decreases. In other words, Milagrito becomes more sensitive as the primary energy increases because of the corresponding increase in effective area. For $E \gtrsim 20\ TeV$, the effective area does not change very much with increasing primary energy and, thus, the implied fluence increases beyond $E \gtrsim 20\ TeV$. Convoluting this fluence with $exp(\tau(E, z_s))$ to correct for attenuation by the EBL gives Fig. 8.5, where z_s

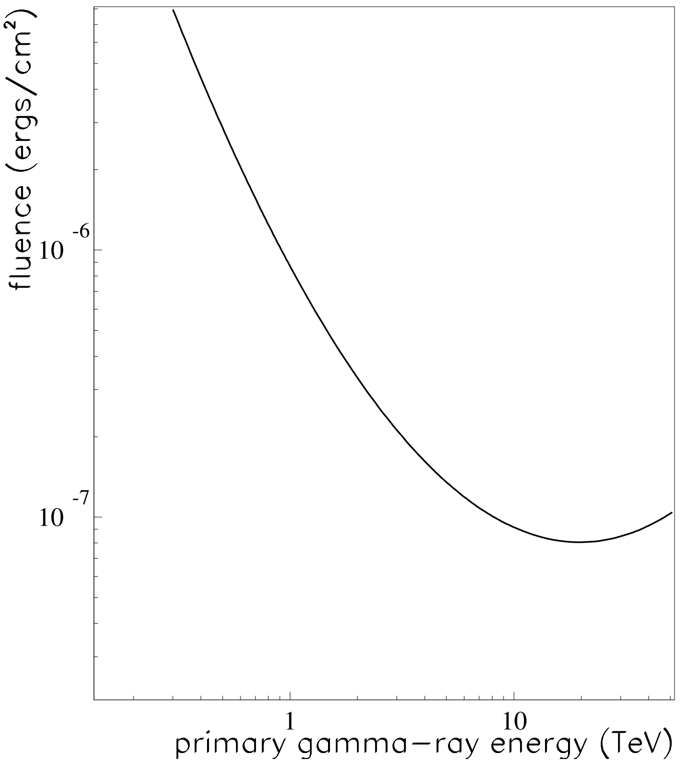

Figure 8.4: Fluence implied by the Milagrito detection of one primary gamma-ray particle of a certain energy, valid for gamma-ray primaries originating from the zenith angle where the excess count attributed to GRB 970417a was found, and for a 1-meter layer of water above the PMTs.

is an assumed source redshift. It can be seen from Fig. 8.5 that the curves corresponding to different assumed source redshifts have minimum values. The lower limit on the isotropic energy release of GRB 970417a in the TeV waveband can thus be obtained by using these minimum values in equation (8.8) for each of the 17 events. Note that the energy release lower limit obtained in this manner is independent of any energy estimates of the primary gamma-ray energies.

Figure 8.6 plots the upper and lower limits on the energy release by GRB 970417a in the TeV waveband as a function of GRB redshift (bold, solid lines), using the procedure given in the preceding paragraphs. At the redshift upper limit of $z_s \approx 0.1$, the energy

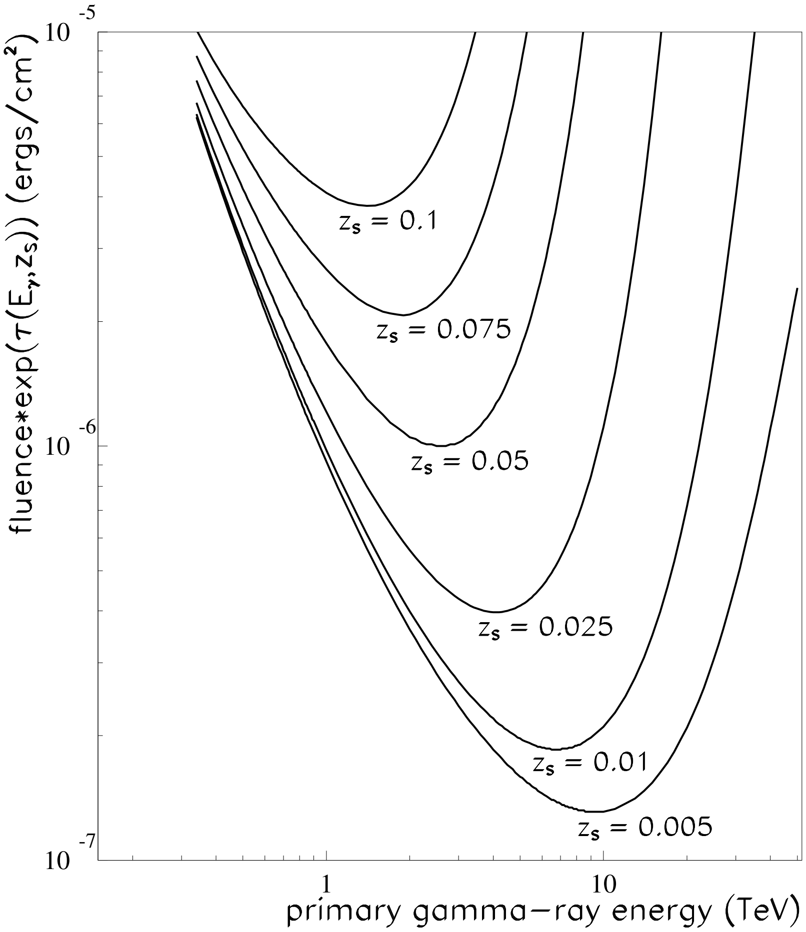

Figure 8.5: The fluence implied by the Milagrito detection of a primary gamma-ray (cf. Fig. 8.4) after correcting for attenuation by the EBL, assuming different source redshifts z_s.

upper and lower limits constrain the energy release to be $E_{iso} \approx 2 \times 10^{51}\ ergs$. Since Fig. 8.1 suggests that the EBL model used by SJ97 could be at the low side of the actual EBL SED, a check was made on the effect on the energy calculations of doubling the value of the EBL density from the SJ97 model. The resulting effect is shown as short-dashed lines in Fig. 8.6. As expected, doubling the optical depth lowers the upper limit on the source redshift, but the effect on the energy upper limits is small. Also plotted in Fig. 8.6 is the implied energy release at BATSE's waveband (long-dashed line), i.e. using the total fluence measured by BATSE in the soft gamma-ray energy regime. The black dots and the filled

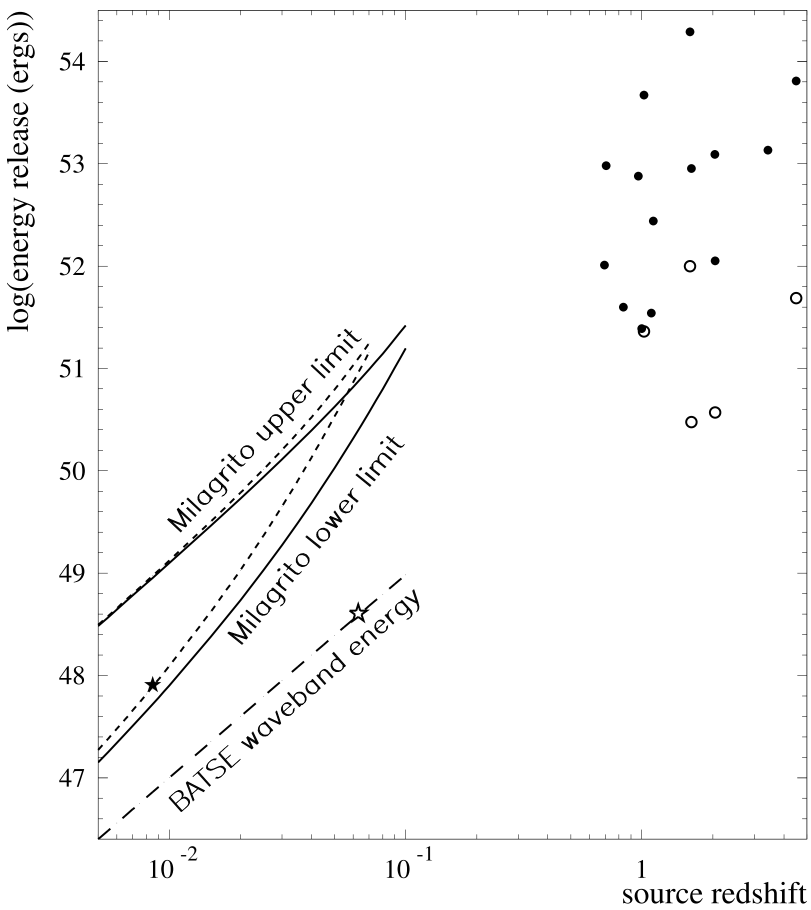

Figure 8.6: Upper and lower limits (thick, solid lines) on the isotropic energy release of GRB 970417a in the TeV waveband, as a function of assumed source redshift, using optical depths of SJ97. The short-dashed lines show the effect on the upper and lower limits of doubling the optical depths from that given by SJ97. The long-dashed line is the energy release of GRB 970417a in soft, keV-MeV gamma-rays, i.e. BATSE's waveband. Also shown are estimates of energy released in the soft gamma-rays by GRBs with known redshifts. The filled circles, filled star, and open star assume isotropic geometry. The open circles show the energy estimates for five of the GRBs when beaming is considered. The filled star is GRB 980425/SN 1997bw, and the open star is GRB 970514/SN 1997cy.

star in Fig. 8.6 give the implied isotropic energy release in the soft gamma-ray waveband for GRBs with known redshifts (cf. Table 2.1). The open circles give the estimated energy release in soft gamma-rays for five of the GRBs if beaming is considered (cf. Section 2.5.4). The filled star is GRB 980425, the GRB which was found spatially and temporally coincident with supernova SN 1997bw, and the open star is GRB 970514, a GRB which has been suggested to be associated with supernova SN 1997cy (cf. Section 2.4.4). Using an alternative cosmology, e.g. with $\Omega_m = 0.3$, $\Omega_\Lambda = 0.7$, is expected to increase these energy estimates by factors of order unity.

Using the same argument used in Section 7.3.4, the upper limit on the isotropic energy release in the TeV waveband can be larger than the upper limits shown in Fig. 8.6 by about 45%, due to the uncertainty in the lower limits on the event energies and the uncertainty in the effective area. The uncertainty, due to the uncertainty in the effective area, in the Milagrito lower limits on the isotropic energy release in the TeV waveband is about 30%.

Chapter 9

Final Thoughts

Out of 54 GRBs which were examined for TeV emission, only one, GRB 970417a, was found to be a candidate for releasing such emission. If one considers the final significance of 3.2 standard deviations of the excess found in this GRB's search area, then it is decidedly a marginal excess. On the other hand, closer inspection of the data presented in Chapter 7 does not force one to readily conclude that the excess was merely due to a background fluctuation. It is not the smoking gun which provides evidence of the production of TeV photons in GRBs, but it is, nevertheless, a compelling reason to believe that it is only a matter of time, and more sensitive instruments, before convincing proof of the existence of such TeV photons in GRBs is found. This is especially true in light of the fact that the relativistic fireball model of GRBs anticipates a TeV component of GRBs.

Without assuming anything about the unknown spectral shape of the TeV emission from the candidate GRB, and relying a great extent on the fact that the observed events attributed to the candidate GRB could not have been due to a large flux of low-energy primary gamma-rays, it is determined that there is a good probability that the event energies are at least in the energy range of ~ 0.3 to ~ 1 TeV, and that the event energies could be larger than this range. Consideration of the interaction of extragalactic photons of TeV energies with the cosmic infrared background radiation puts an upper limit of $z \sim 0.1$ on the distance scale of the candidate GRB. This places the candidate GRB among the closest GRBs found, given that the median redshift of the GRBs with well-established redshifts is $z \approx 1$. It is noted that the redshifts of the GRBs which have been suggested to have originated "nearby", i.e. GRB 980425/SN 1997bw, GRB 970514/SN 1997cy, have not attained the same secure, non-eyebrow-raising status as the well-established redshifts of "cosmological" GRBs, due to the fact that the disputed redshifts were obtained by temporally and spatially associating the GRBs with observed supernovae. But if the distribution of GRBs traces the star formation history of the Universe, then it is expected that a small fraction of GRBs would be found at $z \ll 1$, and the detection of nearby GRBs would be consistent with the true spatial distribution of GRBs.

Due to the unknown distance to the candidate GRB, the implied isotropic energy release in the TeV waveband is hard to establish. An estimate of the isotropic energy release in the TeV waveband ranges from $E_{iso} \sim 2 \times 10^{51}$ $ergs$ at $z \approx 0.1$, which is consistent with the derived energy release by GRBs at $z \sim 1$, to $E_{iso} \sim 2 \times 10^{47}$ $ergs$ at $z \approx 0.005$, which is consistent with the implied energy release of GRB 980425/SN 1997bw. The energy released by the candidate GRB in the TeV waveband would thus be 10 to 300 times larger than the energy released by GRB 970417a in the keV-MeV waveband. Thus, this would mean that if GRB 970417a emitted TeV radiation, at least 90$\%$ of the energy released in the gamma-ray burst was in the form of TeV photons. In this case, a small measured flux or fluence in the keV-MeV energy range would not mean that the GRB is far and therefore results in a weak signal on Earth, as is usually assumed in modelling the GRB spatial distribution, but that most of the energy is found at the TeV waveband. One can then hypothesize that, perhaps, a fraction of GRBs which have small fluences in the keV-MeV waveband emit TeV radiation. Since only those TeV-emitting GRBs which are at $z \lesssim 0.1$ would be detected by ground-based detectors because of absorption by cosmic infrared backgroud radiation, the results of this work would indicate that the fraction of GRBs which emit TeV radiation is larger than 1 in 54 ($> 2\%$).

If TeV emission is a common feature of a fraction of GRBs, then GRBs will add to the list of astrophysical objects whose observed emission spans a broad spectrum from radio to TeV wavebands, a list which includes the Crab pulsar/nebula system, and the BL Lacartae Markarian 421 and Markarian 501. In these three astrophysical objects, the emitted radiation is believed to be essentially the consequence of the acceleration of electrons to relativistic speeds. Their well-established TeV component is popularly believed to be due to the inverse Compton scattering of low-energy photons off the relativistic electrons, where the low-energy photons are the synchrotron radiation from the same relativistic electrons. If these processes are paralleled in GRBs, the convincing detection of a TeV component of GRBs is one way to confirm the existence of highly relativistic electrons in GRBs and, thus, to validate the relativistic fireball model of GRBs.

Bibliography

[1] Macomb, D.J., & Gehrels, N. 1999, ApJS, 120, 335.

[2] Piran, T. 1999, PhR, 314, 575.

[3] Comprehensive Nuclear Test Ban Treaty Organization, 1999, http://www.ctbto.org/ctbto/summary.shtml.

[4] U.S. Air Force Satellite Launches, http://www.laafb.af.mil/SMC/HO/SLFACT.HTM.

[5] Strong, I.B., & Klebesadel, R.W. 1976, SciAm, 235, 66.

[6] Bonnell, J. 1995, A Brief History of the Discovery of Cosmic Gamma-Ray Bursts, http://antwrp.gsfc.nasa.gov/htmltest/jbonnell/www/grbhist.html.

[7] Klebesadel, R.W., Strong, I.B., & Olson, R.A. 1973, ApJ, 182, L85.

[8] Dingus, B.L. 1995, in Proceedings of the 1994 Snowmass Summer Study, Particle and Nuclear Astrophysics and Cosmology in the Next Millennium, ed. E.W. Kolb & R.D. Peccei (Singapore: World Scientific) 99.

[9] Appendix G to the NASA Research Announcement for the Compton Gamma Ray Observatory Guest Investigator Program, 1999, http://cossc.gsfc.nasa.gov/cossc/nra/appendix_g.html.

[10] Burst and Transient Source Experiment, 2000, http://gammaray.msfc.nasa.gov/batse.

[11] Meegan, C.A., Fishman, G.J., Wilson, R.B., Paciesas, W.S., Pendleton, G.N., Horack, J.M., Brock, M.N., & Kouveliotou, C. 1992, Nature, 355, 143.

[12] The Milky Way Galaxy, 1999, http://ftp.seds.org/messier/more/mw.html.

[13] Brainerd, J.J. 1992, Nature, 355, 522.

[14] The Burst and Trainsient Source Experiment, 2000, http://cossc.gsfc.nasa.gov/cossc/batse.

[15] Catelli, J.R., Dingus, B.L., & Schneid, E.J. 1998, in AIP Conference Proceedings 428, Gamma-Ray Bursts, 4th Huntsville Symposium, ed. C.A. Meegan, R.D. Preece, & T.M. Koshut (New York: AIP) 309.

[16] Hurley, K., et. al. 1994, Nature, 372, 652.

[17] Band, D., et. al. 1993, ApJ, 413, 281.

[18] Preece, R.D., Briggs, M.S., Mallozzi, R.S, Pendleton, G.N., & Paciesas, W.S. 2000, ApJS, 126, 19.

[19] Schaefer, B.E. 1992, in Gamma-Ray Bursts, Proceedings of the Los Alamos Workshop on Gamma-Ray Bursts, ed. C. Ho, R.I. Epstein, & E.E. Fenimore (Cambridge: Cambridge University Press) 107.

[20] Boella, G., Butler, R.C., Perola, G.C., Piro, L., Scarsi, L., & Bleeker, J.A.M. 1997, A&AS, 122, 299.

[21] Frontera, F., Costa, E., Dal Fiume, D., Feroci, M., Nicastro, L., Orlandini, M., Palazzi, E., & Zavattini, G. 1997, A&AS, 122, 357.

[22] Hurley, K. 1999, A&AS, 138, 553.

[23] Costa, E., et. al. 1997, Nature, 387, 783.

[24] van Paradijs, J. 1997, Nature, 386, 686.

[25] Bloom, J.S., Djorgovski, S.G., & Kulkarni, S.R. 2000, ApJ, submitted, astro-ph/0007244.

[26] Greiner, J. 2000, Table of well-localized GRBs, http://www.aip.de/˜jcg/grbgen.html.

[27] Levine, A.M., Bradt, H., Cui, W., Jernigan, J.G., Morgan, E.H., Remillard, R., Shirey, R.E., & Smith, D.A. 1996, ApJ, 469, L33.

[28] Costa, E., et. al. 1997, IAU Circ. 6649.

[29] Galama, T.J., et. al. 1998, ApJ, 497, L13.

[30] Bond, H.E. 1997, IAU Circ. 6654.

[31] Galama, T.J., et. al. 1997, IAU Circ. 6655.

[32] Jaunsen, A.O., et. al. 1997, IAU Circ. 6656.

[33] Piro, L., et. al. 1997, IAU Circ. 6656.

[34] Frail, D.A., et. al. 1997, IAU Circ. 6662.

[35] Metzger, M.R., Djorgovski, S.G., Steidel, C.C., Kulkarni, S.R., Adelberger, K.L., & Frail, D.A. 1997, IAU Circ. 6655.

[36] Metzger, M.R., Cohen, J.G., Chaffee, F.H., & Blandford, R.D. 1997, IAU Circ. 6676.

[37] Bloom, J.S., Djorgovski, S.G., & Kulkarni, S.R. 1998, ApJ, 507, L25.

[38] Kulkarni, S.R., Frail, D.A., Wieringa, M.H., Ekers, R.D., Sadler, E.M., Wark, R.M., Higdon, J.L., Phinney, E.S., Bloom, J.S. 1998, Nature, 395, 663.

[39] Kulkarni, S.R., et. al. 1998, Nature, 393, 35.

[40] Groot, P.J., et. al. 1998, ApJ, 502, L123.

[41] Bloom, J.S., et. al. 1999, Nature, 401, 453.

[42] Galama, T.J., et. al. 1998, Nature, 395, 670.

[43] Iwamoto, K., et. al. 1998, Nature, 395, 672.

[44] Djorgovski, S.G., Bloom, J.S., & Kulkarni, S.R. 2000, ApJL, submitted, astro-ph/0008029.

[45] Vreeswijk, P.M., et. al. 1999, ApJ, 523, 171.

[46] Djorgovski, S.G., Kulkarni, S.R., Bloom, J.S., Goodrich, R., Frail, D.A., Piro, L., & Palazzi, E. 1998, ApJ, 508, L17.

[47] Kulkarni, S.R., et. al. 1999, Nature, 398, 389.

[48] Wijers, R.A.M.J., et. al. 1999, ApJ, 523, L33.

[49] Sahu, K.C., et. al. 2000, ApJ, submitted, astro-ph/0003378.

[50] Hjorth, J., Holland, S., Courbin, F., Dar, A., Olsen, L.F., & Scodeggio, M. 2000, ApJL, submitted, astro-ph/0003383.

[51] Hurley, K., et. al. 2000, ApJ, 534, L23.

[52] Dodonov, S.N., Afanasiev, V.L., Sokolov, V.V., Moiseev, A.V., & Castro-Tirado, A.J. 1999, GCN Circ. 475.

[53] Halpern, J.P., et. al. 2000, ApJ, submitted, astro-ph/0006206.

[54] Andersen, M.I., et. al. 2000, A&A, submitted, astro-ph/0010322.

[55] Jensen, B.L., et. al. 2000, A&A, submitted, astro-ph/0005609.

[56] Klose, S., et. al. 2000, ApJ, submitted, astro-ph/0007201.

[57] Bloom, J.S., et. al. 2000, GCN Circ. 661.

[58] Hurley, K., et. al. 2000, GCN Circ. 801.

[59] Hurley, K., et. al. 2000, GCN Circ. 802.

[60] Castro, S.M., et. al. 2000, GCN Circ. 851.

[61] Reichart, D.E. 1999, ApJ, 521, L111.

[62] Galama, T.J., et. al. 2000, ApJ, 536, 185.

[63] Germany, L.M., Reiss, D.J., Sadler, E.M., Schmidt, B.P., & Stubbs, C.W. 2000, ApJ, 533, 320.

[64] Turatto, M., et. al. 2000, ApJ, 534, L57.

[65] Schmidt, M. 1999, ApJ, 523, L117.

[66] Piran, T. 2000, PhR, 333-334, 529.

[67] Fenimore, E.E., Madras, C.D., & Nayakshin, S. 1996, ApJ, 473, 998.

[68] Catanese, M., & Weekes, T.C. 1999, PASP, 111, 1193.

[69] Hoffman, C.M., Sinnis, C., Fleury, P., & Punch, M. 1999, RvMP, 71, 897.

[70] Aharonian, F.A., et. al. 2000, ApJ, 539, 317.

[71] Hillas, A.M., et. al. 1998, ApJ, 503, 744.

[72] Tanimori, T., et. al. 1998, ApJ, 492, L33.

[73] de Jager, O.C., Harding, A.K., Michelson, P.F., Nel, H.I., Nolan, P.L., Sreekumar, P., & Thompson, D.J. 1996, ApJ, 457, 253.

[74] de Jager, O.C., & Harding, A.K. 1992, ApJ, 396, 161.

[75] Takahashi, T., et. al. 2000, ApJ, 542, L105.

[76] Maraschi, L., et. al. 1999, ApJ, 526, L81.

[77] Krennrich, F., et. al. 1999, ApJ, 511, 149.

[78] Zweerink, J.A., et. al. 1997, ApJ, 490, L141.

[79] Krennrich, F., et. al. 1997, ApJ, 481, 758.

[80] Petry, D., et. al. 2000, ApJ, 536, 742.

[81] Aharonian, F.A., et. al. 1999, A&A, 342, 69.

[82] Aharonian, F., et. al. 1999, A& A, 349, 29.

[83] Quinn, J., et. al. 1999, ApJ, 518, 693.

[84] Samuelson, F.W., et. al. 1998, ApJ, 501, L17.

[85] Inoue, S., & Takahara, F. 1996, ApJ, 463, 555.

[86] Sikora, M., Begelman, M.C., & Rees, M.J. 1994, ApJ, 421, 153.

[87] Bloom, S.D., & Marscher, A.P. 1996, ApJ, 461, 657.

[88] Maraschi, L, Ghisellini, G., & Celotti, A. 1992, ApJ, 397, L5.

[89] Bednarek, W., & Protheroe, R.J. 1997, MNRAS, 287, L9.

[90] Pilla, R.P., & Loeb, A. 1998, ApJ, 494, L167.

[91] Padilla, L., et. al. 1998, A&A, 337, 43.

[92] Amenomori, M., et. al. 1996, A&A, 311, 919.

[93] Connaughton, V., et. al. 1997, ApJ, 479, 859.

[94] Aglietta, M., et. al. 1996, ApJ, 469, 305.

[95] Alexandreas, D.E., et. al. 1994, ApJ, 426, L1.

[96] Sari, R., Piran, T., & Halpern, J.P. 1999, ApJ, 519, L17.

[97] Diercks, A., et. al. 1998, ApJ, 503, L105.

[98] Halpern, J.P., Thorstensen, J.R., Helfand, D.J., & Costa, E. 1998, Nature, 393, 41.

[99] Gorosabel, J., Castro-Tirado, A.J., Pedrosa, A., Zapatero-Osorio, M.R., Fernades, A.J.L., Feroci, M., Costa, E., & Frontera, F. 1999, A&A, 347, L31.

[100] Halpern, J.P., Kemp, J., Piran, T., & Bershady, M.A. 1999, ApJ, 517, L105.

[101] Harrison, F.A., et. al. 1999, ApJ, 523, L121.

[102] Stanek, K.Z., Garnavich, P.M., Kaluzny, J., Pych, W., & Thompson, I. 1999, ApJ, 522, L39.

[103] Jensen, B.L., et. al. 1999, GCN Circ. 454.

[104] Jensen, B.L., et. al. 2000, GCN Circ, 747.

[105] Lamb, D.Q. 2000, PhR, 333-334, 505.

[106] Wijers, R.A.M.J., Bloom, J.S., Bagla, J.S., & Natarajan, P. 1998, MNRAS, 294, L13.

[107] Lamb, D.Q., & Reichart, D.E. 2000, ApJ, 536, 1.

[108] Hogg, D.W., & Fruchter, A.S. 1999, ApJ, 520, 54.

[109] Totani, T. 1999, ApJ, 511, 41.

[110] Bloom, J.S., Sigurdsson, S., & Pols, O.R. 1999, MNRAS, 305, 763.

[111] Woosley, S.E. 1993, ApJ, 405, 273.

[112] Paczynski, B. 1998, ApJ, 494, L45.

[113] Rosswog, S., Liebendorfer, M., Thielemann, F.-K., Davies, M.B., Benz, W., & Piran, T. 1999, A&A, 341, 499.

[114] Ruffert, M., & Janka, H.-Th. 1999, A&A, 344, 573.

[115] MacFadyen, A.I., & Woosley, S.E. 1999, ApJ, 524, 262.

[116] Longair, M.S. 1997, High Energy Astrophysics v. 1 (Cambridge: Cambridge University Press).

[117] Hillier, R. 1984, Gamma Ray Astronomy (New York: Oxford University Press).

[118] Di Sciascio, G., D'Ettorre Piazzoli, B., & Iacovacci, M. 1997, APh, 6, 313.

[119] Jelley, J.V. 1961, in Progress in Nuclear Physics v. 3, ed. O.R. Frisch (Pergamon Press) 84.

[120] Jackson, J.D. 1975, Classical Electrodynamics (New York: John Wiley & Sons).

[121] Galbraith, W. 1958, Extensive Air Showers (New York: Academic Press).

[122] Gaisser, T.K., & Stanev, T. 2000, in Review of Particle Physics, Eur. Phys. J. C, 15, 150.

[123] Atkins, R., et. al. 2000, NIMPA, 449, 478.

[124] Hamamatsu Photomultiplier Tube R5912 Specifications Sheet, 1998, http://usa.hamamatsu.com.

[125] Fleysher, L., Fleysher, R., Nemethy, P., & Leonor, I.R. 1997, Time Pedestals (Milagro internal memo).

[126] Atkins, R., et. al. 1999, ApJ, 525, L25.

[127] Wascko, M.O., in preparation, Ph.D. Dissertation, U.C. Riverside.

[128] Lang, K.R. 1980, Astrophysical Formulae (New York: Springer-Verlag).

[129] Pendleton, G.N., et. al. 1999, ApJ, 512, 362.

[130] Briggs, M.S., Pendleton, G.N., Kippen, R.M., Brainerd, J.J., Hurley, K., Connaughton, V., & Meegan, C.A. 1999, ApJS, 122, 503.

[131] Fisher, N.I., Lewis, T., & Embleton, B.J.J. 1987, Statistical Analysis of Spherical Data (New York: Cambridge University Press).

[132] Li, T.-P., & Ma, Y.-Q. 1983, ApJ, 272, 317.

[133] Schnee, R. 1996, Search for Higher-Energy Radiation from Gamma-Ray Bursts, Ph.D Dissertation, U.C. Santa Cruz.

[134] Helene, O. 1983, NIMPR, 212, 319.

[135] Eadie, W.T., et. al. 1971, Statistical Methods in Experimental Physics (New York: American Elsevier).

[136] Biller, S.D. 1992, A Study of Ultra High Energy Radiation Associated with Hercules X-1, Ph.D. Dissertation, U.C. Irvine.

[137] McEnery, J., & Smith, A.J. 2000, Flux, Fluence and Upper Energy Cutoff for GRB 970417a (Milagro internal memo).

[138] Stecker, F.W. 1999, astro-ph/9904416.

[139] Dwek, E., et. al. 1998, ApJ, 508, 106.

[140] Finkbeiner, D.P., Davis, M., & Schlegel, D.J. 2000, ApJ, submitted, astro-ph/0004175.

[141] Gorjian, V., Wright, E.L., & Chary, R.R. 2000, ApJ, 536, 550.

[142] Hauser, M.G., et. al. 1998, ApJ, 508, 25.

[143] Biller, S.D., et. al. 1998, PhRvL, 80, 2992.

[144] Maucherat-Joubert, M., Deharveng, J.M., & Cruvellier, P. 1980, A&A, 88, 323.

[145] Toller, G.N. 1983, ApJ, 266, L79.

[146] Dube, R.R., Wickes, W.C., & Wilkinson, D.T. 1979, ApJ, 232, 333.

[147] Madau, P., & Pozzetti, L. 2000, MNRAS, 312, L9.

[148] Altieri, B., et. al. 1999, A&A, 343, L65.

[149] Hacking, P.B., & Soifer, B.T. 1991, ApJ, 367, L49.

[150] Fixsen, D.J., Dwek, E., Mather, J.C., Bennett, C.L., & Shafer, R.A. 1998, ApJ, 508, 123.

[151] Stecker, F.W., & de Jager, O.C. 1997, ApJ, 476, 712.

[152] Boggess, N.W., et. al. 1992, ApJ, 397, 420.

[153] Vassiliev, V.V. 2000, APh, 12, 217.

[154] Stanev, T., & Franceschini, A. 1998, ApJ, 494, L159.

[155] Dwek, E., & Slavin, J. 1994, ApJ, 436, 696.

[156] Salamon, M.H., & Stecker, F.W. 1998, ApJ, 493, 547.

[157] Stecker, F.W., de Jager, O.C., & Salamon, M.H. 1992, ApJ, 390, L49.

[158] Primack, J.R., Bullock, J.S., Somerville, R.S., & MacMinn, D. 1999, APh, 11, 93.

[159] Stecker, F.W., & de Jager, O.C. 1998, A&A, 334, L85.

Appendix

BATSE Time Profiles of the GRBs

The BATSE time profiles for 46 of the 54 GRBs examined in this work are given in the plots which are found in the next pages. Data used in the plots were downloaded from the BATSE website given in reference [14]. There were no time history data found for eight of the GRBs. The identifying numbers in the plots are the BATSE trigger numbers of the GRBs. These numbers can be used to search for more information about the bursts in the BATSE online catalogs (references [10] and [14]).

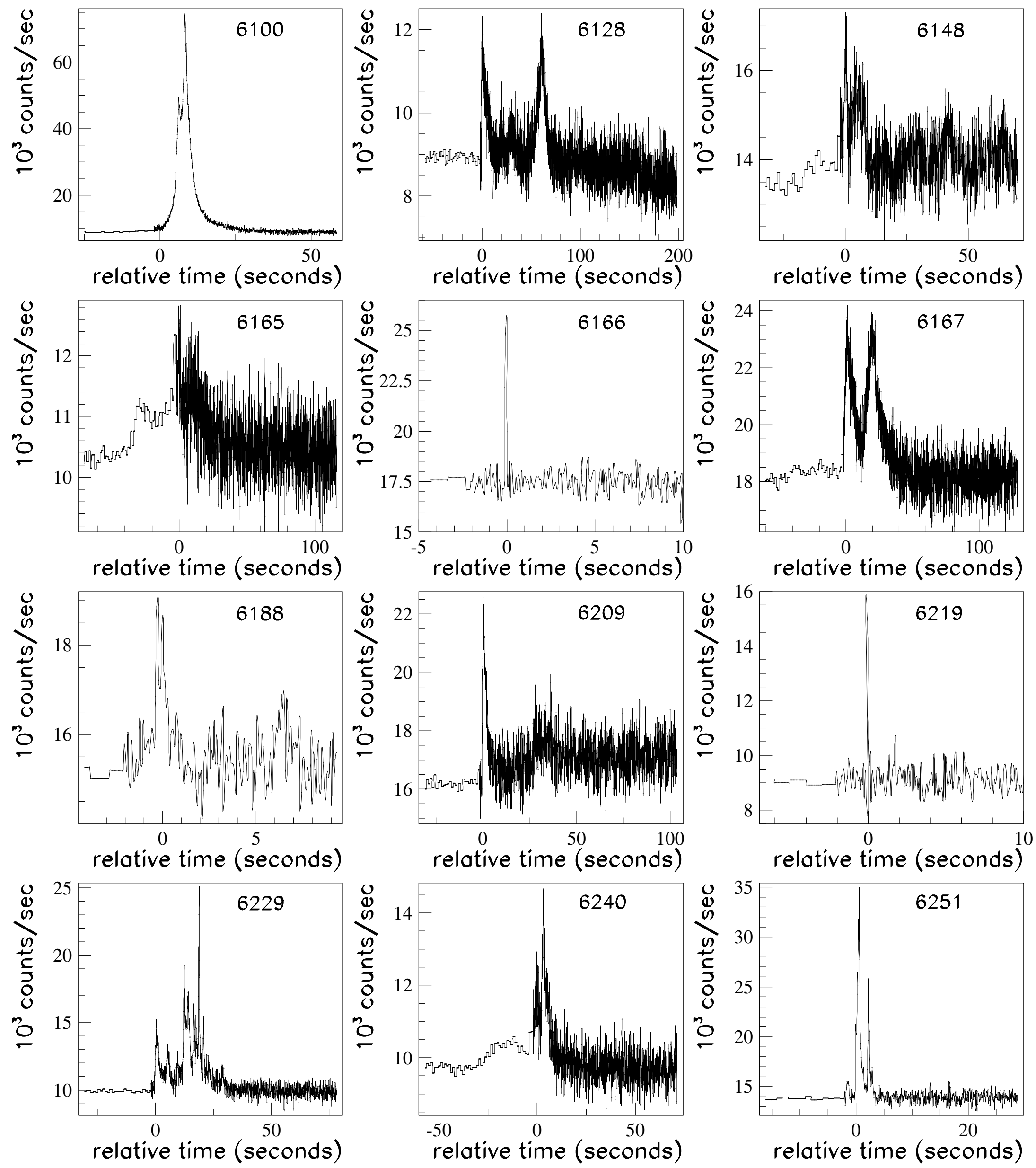

Figure A.1: GRB time profiles.

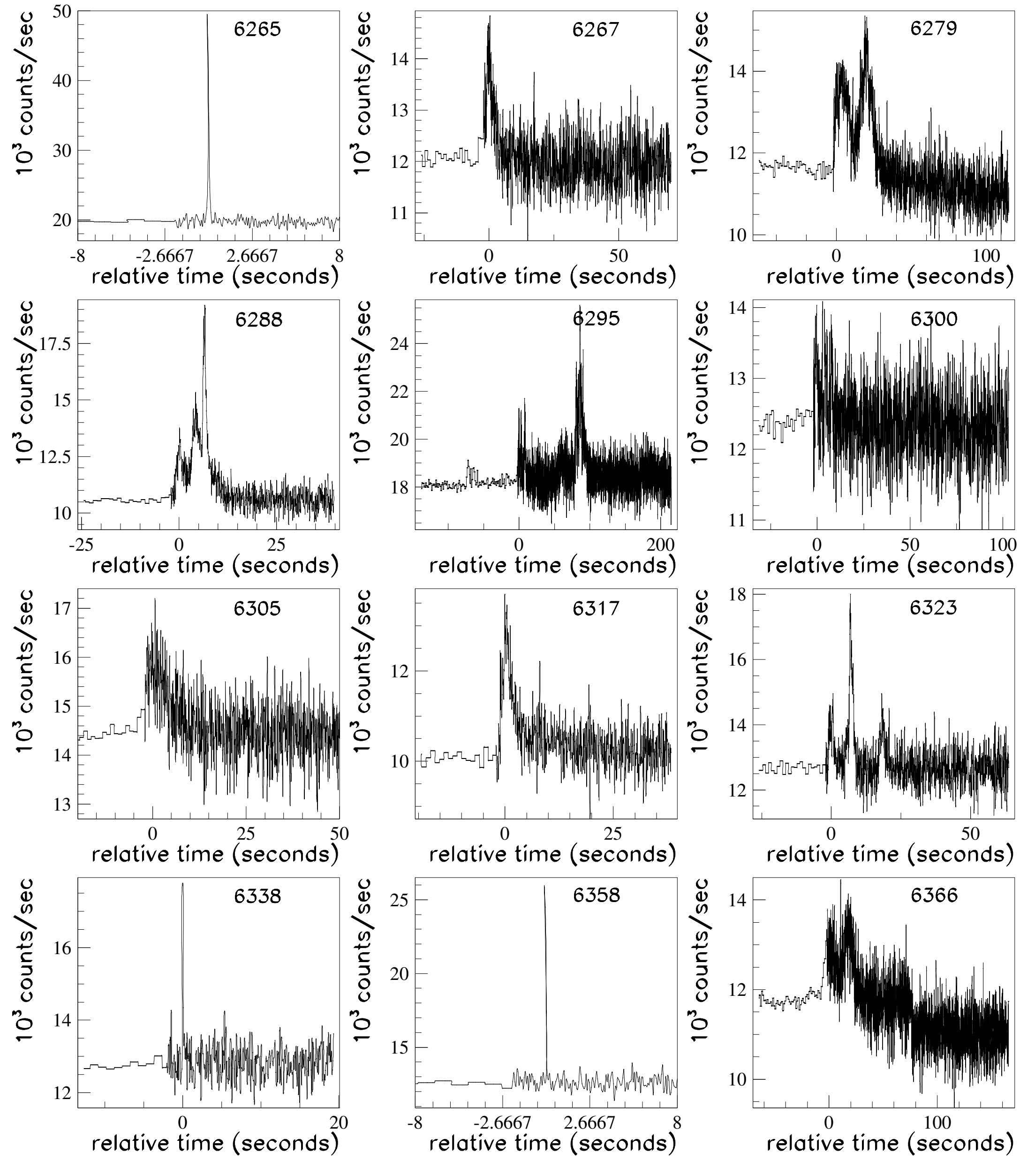

Figure A.2: GRB time profiles.

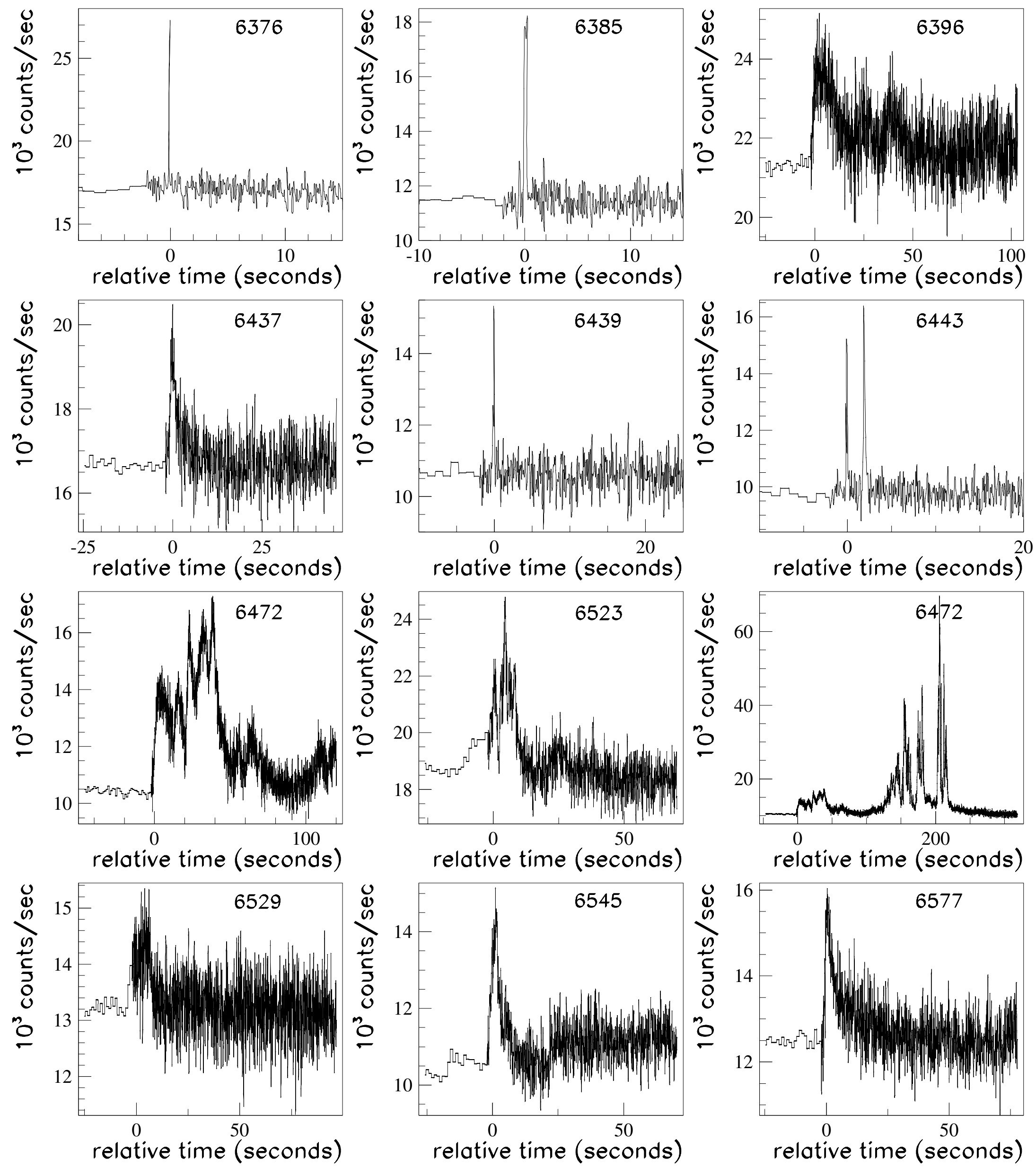

Figure A.3: GRB time profiles.

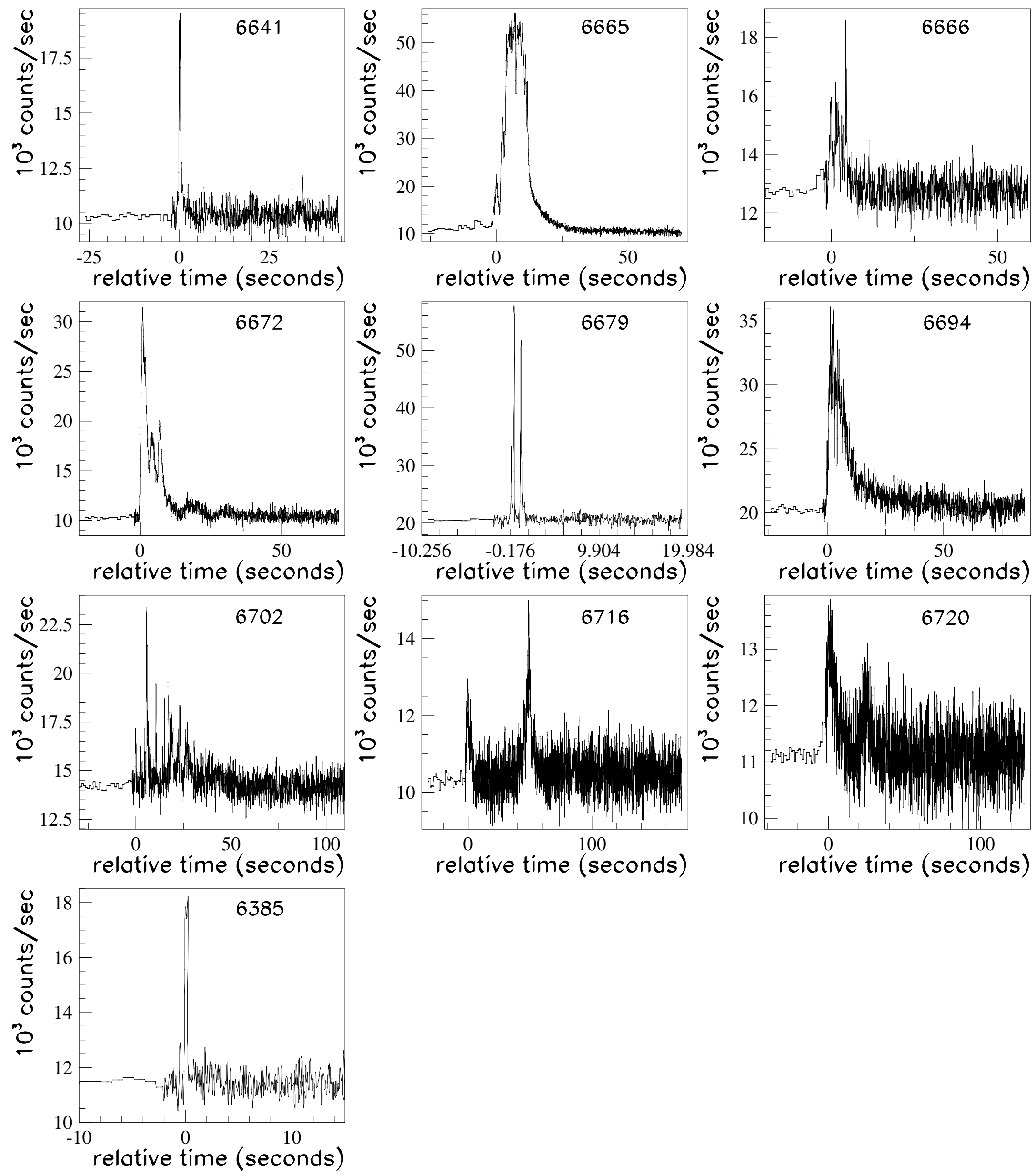

Figure A.4: GRB time profiles.